

# Dynamic self-organization phenomena in complex ionized gas systems: new paradigms and technological aspects

S.V. Vladimirov<sup>a,\*</sup>, K. Ostrikov<sup>a,b,c</sup>

<sup>a</sup>*School of Physics, The University of Sydney, Sydney, NSW 2006, Australia*

<sup>b</sup>*Plasma Sources and Applications Center, NIE, Nanyang Technological University, 637616, Singapore, Singapore*

<sup>c</sup>*School of Chemistry, Physics and Earth Sciences, The Flinders University of South Australia, GPO Box 2100, Adelaide SA 5001, Australia*

Accepted 16 December 2003

editor: J. Eichler

## Abstract

An overview of dynamic self-organization phenomena in complex ionized gas systems, associated physical phenomena, and industrial applications is presented. The most recent experimental, theoretical, and modeling efforts to understand the growth mechanisms and dynamics of nano- and micron-sized particles, as well as the unique properties of the plasma–particle systems (colloidal, or complex plasmas) and the associated physical phenomena are reviewed and the major technological applications of micro- and nanoparticles are discussed. Until recently, such particles were considered mostly as a potential hazard for the microelectronic manufacturing and significant efforts were applied to remove them from the processing volume or suppress the gas-phase coagulation. Nowadays, fine clusters and particulates find numerous challenging applications in fundamental science as well as in nanotechnology and other leading high-tech industries.

© 2003 Elsevier B.V. All rights reserved.

PACS: 51.50.+v; 52.80.–s

## Contents

|   |     |
|---|-----|
| 1. Introduction .....   | 177 |
| 1.1. Complex plasma systems in laboratory and space .....                 | 177 |
| 1.2. New paradigms in complex plasma research .....                       | 180 |
| 1.3. Colloidal “dusty” plasma—an open self-organized complex system ..... | 182 |
| 1.4. Structure of the review .....  | 183 |

\* Corresponding author.

E-mail address: [s.vladimirov@physics.usyd.edu.au](mailto:s.vladimirov@physics.usyd.edu.au) (S.V. Vladimirov).

|   |     |
|---|-----|
| 2. Origin and growth of nano- and micron-sized particles in ionized gas systems .....                                       | 186 |
| 2.1. Origin and mechanisms of growth of clusters and particulates in reactive plasmas .....                                 | 186 |
| 2.1.1. Silane plasmas .....   | 186 |
| 2.1.2. Hydrocarbon plasmas .....  | 188 |
| 2.1.3. Fluorocarbon plasmas .....   | 193 |
| 2.2. Effects of fine particles on discharge stability—self-organization and critical phenomena .....                        | 194 |
| 2.3. Particle growth in plasma-assisted sputtering facilities .....   | 198 |
| 2.4. Problems of particle diagnostics and characterization in the nanometer range .....                                     | 200 |
| 3. Technological aspects of clusters and particulates in complex ionized gas systems .....                                  | 204 |
| 3.1. Particulate powders as process contaminants and remediation methods .....  | 204 |
| 3.2. Dust particles in fusion reactors .....  | 207 |
| 3.3. Nanoparticles as precursors for plasma enhanced assembly of carbon-based nanostructures .....                          | 210 |
| 3.4. Nano-powders in PECVD of nanostructured silicon-based films .....  | 213 |
| 3.5. High-rate cluster and particulate deposition on nanostructured surfaces: a new paradigm in thin film fabrication ..... | 217 |
| 3.6. Particle size as a key factor in nano-scale technologies .....   | 220 |
| 3.7. Other industrial applications of nano- and micron-sized particles .....  | 223 |
| 4. Levitation and dynamics of fine particles .....  | 227 |
| 4.1. Charging of dust particles .....   | 227 |
| 4.2. Particle charge as a function of the grain size .....  | 235 |
| 4.3. Forces acting on the grains in the plasma .....  | 238 |
| 4.4. Dynamics and levitation of fine particles in the plasma sheath: modeling and simulation .....                          | 241 |
| 4.5. Dynamics of fine particles in chemically active plasmas .....  | 248 |
| 4.5.1. Dynamics of fine particles in silane plasmas .....   | 248 |
| 4.5.2. Levitation of submicron-sized particles in fluorocarbon plasmas .....  | 249 |
| 4.6. Fine particles as probes for plasma–surface interactions .....   | 253 |
| 4.7. Detection and characterization of dust particles .....   | 254 |
| 5. Self-organized structures and phase transitions in complex plasma systems .....  | 256 |
| 5.1. Dust–plasma sheath—a self-organized structure .....  | 257 |
| 5.2. Dust voids in plasmas .....  | 262 |
| 5.2.1. Collisionless dust voids .....   | 264 |
| 5.2.2. Voids in collision-dominated plasmas .....   | 269 |
| 5.3. Dynamics and diffusion of particles in strongly coupled complex plasmas .....  | 273 |
| 5.4. Criteria of phase transitions in the dust–plasma crystals .....  | 280 |
| 6. Collective plasma phenomena in the dust–plasma interactions: the ion wake .....  | 285 |
| 6.1. Plasma and levitated dust in the collisionless sheath region .....   | 286 |
| 6.2. Supersonic wake behind a charged spherical particle levitating in the sheath .....                                     | 288 |
| 6.3. Wakes behind dipoles and non-spherical particles .....   | 293 |
| 6.3.1. Wakes behind dipoles .....   | 293 |
| 6.3.2. Wakes behind elongated particles (rods) .....  | 296 |
| 6.4. Dust Cooper pairing: Hamiltonian description .....   | 302 |
| 6.5. Subsonic plasma wakes .....  | 306 |
| 6.6. Simulations on plasma wakes .....  | 313 |
| 6.6.1. Wake of a single test particle .....   | 314 |
| 6.6.2. Wake of two particles .....  | 315 |
| 7. Collective plasma waves in open complex plasma systems .....   | 321 |
| 7.1. Dust charging—a new channel of wave dissipation .....  | 321 |
| 7.2. Langmuir waves .....   | 325 |
| 7.3. Ion–acoustic waves .....   | 328 |
| 7.4. Dust–acoustic waves .....  | 330 |
| 7.5. Dust–acoustic and other instabilities .....  | 333 |

|   |     |
|---|-----|
| 8. Collective oscillations in arrays of colloid particles .....                                       | 337 |
| 8.1. Oscillations of a particle in the plasma sheath .....  | 338 |
| 8.2. Stability of dust particles confinement .....  | 341 |
| 8.3. Dust–lattice waves in the regular arrays of spherical particles .....                            | 347 |
| 8.3.1. Oscillation modes in one-dimensional chains of particles .....                                 | 348 |
| 8.3.2. Oscillation modes in two vertically arranged one-dimensional chains of colloid particles ..... | 350 |
| 8.4. Waves in arrays of rod-like particles .....  | 354 |
| 9. Conclusion .....   | 360 |
| Acknowledgements .....  | 365 |
| References .....  | 365 |

## 1. Introduction

### 1.1. Complex plasma systems in laboratory and space

Complex plasma systems containing colloid nano/microscopic particles (“dust”) have recently been widely discussed in the physics and chemistry of plasmas, ionized gases, space physics and astrophysics, and materials research. Particles with different sizes, from a few nanometers to tens of micrometers have been observed in various ionized gas media for many years. There are numerous reports on the occurrence of charged dust particles in interstellar space, planetary atmospheres, ring structures, cometary tails, etc. Furthermore, charged grains can play an important role in the synthesis of molecular species in diffuse nebulae [1]. Dust in planetary atmospheres and planetary ring structures has also been studied extensively [2–4].

Under terrestrial conditions, fine particles are the important parts of various colloidal suspensions, charged aerosols, high-pressure ionized gas systems, nucleation catalysts, and many others. Particulate powders with sizes in the nano-/micrometer range have also been detected in a number of experiments with low-temperature plasmas for materials synthesis and processing applications. Dust is also very common in radio-frequency (RF) gas discharges, where it was noted that dust appears in mixtures of chemically active (reactive) gases that generate electronegative free radicals [5].

The plasmas of chemically active gases have recently been of a remarkable interest in a number of high-tech industries that use various plasma-based surface modification technologies. The processes involved include but are not limited to ultra-fine surface modification and microstructuring, patterning and selective etching, plasma enhanced chemical vapor deposition (PECVD) of protective and wear-resistant coatings and interlayers, data storage, sensing, guiding, emitting, converting and other functionalities of the numerous optoelectronic and photonic devices, etc. It was also noted that the low-temperature plasma discharges are very efficient as electrostatic traps for both negative ions and dust grains. For example, in conventional parallel-plate reactors, where both electrodes are charged negatively due to high mobility of the plasma electrons, the inter-electrode ambipolar field also confines the dust grains.

Therefore, one should expect intense interactions between the reactive plasma environments and the fine powders being grown. Under certain conditions, dense clouds of fine powders (with the number densities of up to  $10^{11} \text{ cm}^{-3}$  and even higher) have been detected. Depending on the prevailing experimental conditions, dust grains feature various chemical organization and structure, surface morphology and bulk architecture, gas-kinetic temperature, equilibrium positions in the plasma reactor,

etc. [5]. Furthermore, the fine particles not only range in size (typically from a few nanometers to tens of micrometers) but can also be quite different because of the underlying physics and chemistry of their origin, growth, and self-organization. Accordingly, their global role in the entire colloidal (complex) plasma system can be quite different.

In this review, our major focus is on laboratory complex ionized gas systems, although many of the reviewed phenomena and results are also applicable to space dusty plasmas. For most of the cases considered, the fine particle component is able to dramatically affect the global and microscopic properties of the complex plasma system including stationary spatial profiles and temporal evolution of the electron/ion number densities and temperatures, plasma potentials, and electromagnetic fields in the reactor chamber. It is remarkable that the complex plasma systems are highly capable for the self-organization and can dynamically adjust its microscopic and global parameters through self-consistent nonlinear responses to any changes in the external control parameters (e.g. gas composition, pressure, or input power) or in the internal colloidal subsystem (e.g. dust charge and/or size variation). In particular, the effect of the dust component on the discharge strongly depends on the specific powder growth stage, with remarkably different chemical state and structure, size, shape, equilibrium electric charge, and the density of the dust grains.

The evolution of the dust component in chemically active complex plasmas usually begins with the growth of nanometer-scale protoparticles that appear as a result of homogeneous (purely gas-phase) or heterogeneous (particle/catalyst-induced) nucleation processes. The homogeneous nucleation is usually triggered by specific negative or neutral precursor radicals and proceeds through numerous chemical polymerization chains. On the other hand, the heterogeneous process can be initiated by substrate/wall flakes released as a result of reactive etching or physical sputtering or, alternatively, externally injected (e.g. metal) nanoparticles. At this stage, fine particles are usually either charge neutral or carry a positive/negative charge of up to a few elementary charges. Their number density typically exceeds  $10^8 \text{ cm}^{-3}$  and in strongly electronegative (with high densities of negative ion precursor radicals) cases can reach  $10^{11} \text{ cm}^{-3}$  and even higher.

Fine particles of the intermediate (a few tens to a few hundreds nm) size often appear as agglomerates of complex shapes, as can be seen in Fig. 1. The latter originate as a result of relatively fast gas-phase agglomeration of smaller (nm-sized) particles, followed by a significant re-distribution of the electric charge in the overall charge neutral plasma system. The number density of the grains in this size range is typically a few orders of magnitude lower ( $10^6$ – $10^8 \text{ cm}^{-3}$ ) than that of nanometer-sized particles. Furthermore, the roles of the particles with different sizes in the complex plasma system are physically different. Indeed, due to much larger surface area ( $S \propto a^2$ , where  $a$  is the particle radius), the intermediate-sized grains become capable to collect large numbers of electrons and ions from the adjacent plasma and accumulate the net negative charge of tens to hundreds of electron charges due to high electron mobility. Thus, the negative charge is re-distributed between the electron plasma and the dust components. This phenomenon can lower the electron density and, hence the rates of the prevailing electron-impact elementary processes in the plasma.

Meanwhile, the complex plasma system tends to self-organize in order to “reinstate” the number of the plasma electrons lost to the dust and re-establish the pristine charge/particle distribution. Typical changes in the plasma system include the variations of the ionization/dissociation rates, electron temperature, changes in the ambipolar (confining) electric field, electron/ion fluxes to the walls/dust, density/temperature profiles of the plasma species, dust-induced transitions of the discharge operation regimes, plasma instabilities etc. The above changes affect the number densities, energies, and fluxes

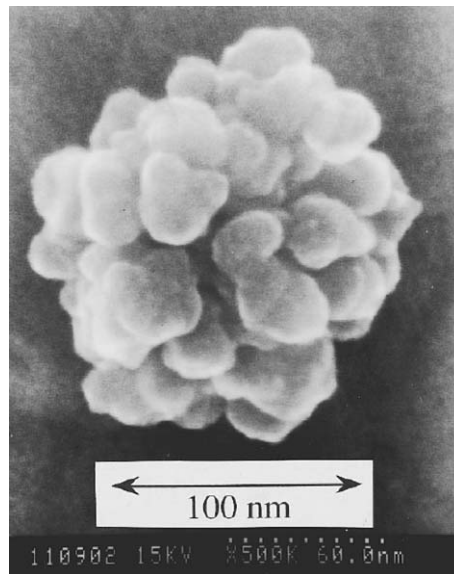


Fig. 1. High-resolution SEM micrograph of a particulate agglomerate grown in chemically active He + SiH<sub>4</sub> plasmas [6].

of the neutral/anion precursor radicals, thus modifying the basic conditions for the dust nucleation and growth. Therefore, the fine particle-plasma system is a typical example of an *open dissipative system* with the dynamically coupled sub-components. Furthermore, the variations of either the external conditions or internal parameters of the plasma and/or colloidal subsystems dynamically affect the global power and particle balance in the entire complex plasma system, which in turn influence the dust generation and growth processes.

On the other hand, larger ( $a > 1 \mu\text{m}$ ) particles are also quite common to many thin film deposition processes and laboratory experiments with externally injected organic powders. In many processing discharges, micron-sized particulates can naturally evolve from submicron-sized particles via a relatively slow process of collection of the neutrals and ions from the reactive plasma environment. This process can be regarded as a microscopic plasma-assisted CVD of thin films on a dust grain. In this range, the equilibrium particle charge is also controlled by the dynamic balance of microscopic electron/ion currents flowing onto the dust surface.

It is notable that a complex plasma with micron-sized grains is quite stable, and self-organization processes usually develop over longer time scales (e.g. associated with larger and therefore heavier colloid particles). In the micrometer size range, a relatively large (a few thousand electron charges) electric charge favors the charge-induced self-organization of the plasma–dust system into strongly coupled colloidal liquids and ordered crystal-like particle structures [7]. Some typical examples of such structures are displayed in Fig. 2.

Furthermore, under certain conditions the complex plasmas are subject to various phase transitions to liquid and crystalline states. It is important that the above phase transitions preserve the charge state and the charged components of the plasma. Hence, these systems may be regarded as new plasma states, namely “condensed plasmas”. The ordering forces are mostly electrostatic, however, dipolar effects, anisotropic pressure due the plasma shielding, focusing of ion flows, etc., can also

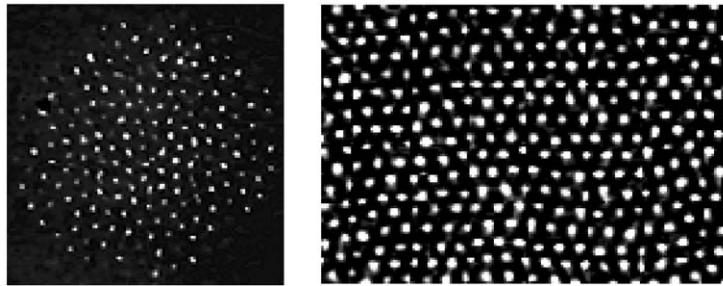


Fig. 2. Optical images of a typical dust cloud (left) and a self-organized crystal-like structure (right) in a low-pressure capacitively coupled plasma [courtesy of A. A. Samarian (unpublished), Complex Plasma Laboratory, School of Physics, The University of Sydney].

play a significant role. It is remarkable that the complex plasmas are of *fundamental interest* since the individual dust particles can be easily visualized and the collective processes can be studied at the most fundamental kinetic level [7].

Thus, the dynamic self-organization of the entire system as a result of the evolution of the colloidal subsystem or variation of external control parameters is one of the most important fundamental features of the complex plasmas. Furthermore, as detailed in the following section, the dynamic self-organization and collective phenomena in the complex ionized gas systems with nano- and micron-sized colloidal particles are becoming the most critical issues for the low-temperature plasma-based synthesis and surface modification of advanced nano-materials and are one of the key focuses of this review.

### 1.2. *New paradigms in complex plasma research*

In this review the focus is on the most important current fundamental topics and new paradigms of dynamic self-organization phenomena in the complex ionized gas systems. Such systems are usually referred to as complex systems because of the many and varied constituents, with the extensive interaction between them, as well as the space and time scales involved.

Since early nineties, the fine powder-contaminated plasmas have posed a number of challenging and yet not fully solved problems to the microelectronic industry, materials science, and gas discharge research and development areas. At that time, the particulate powders with the sizes comparable to a typical size of line features of the semiconductor integrated circuits did become a troublesome factor in the semiconductor wafer manufacturing. Above all, dust in the plasma reactors often caused unrecoverable defects and line shorts in some ultra large scale integrated (ULSI) circuits, which totally compromised the entire microchip fabrication process. However, the current accents in the fine particle research are now gradually shifting from the traditional view on them as unwelcome process “killer” contaminants to often desired elements that can dramatically affect and even improve the basic properties of plasma-made thin films.

We therefore discuss here the role of fine powders in the low-temperature processing plasmas and review some of the challenging recent applications of nano/micron-sized particles in a number of high-tech industries. For example, in the last few years the complex plasma systems have been



increasingly used for the synthesis of nano-structured materials. In particular, the nano-sized particle incorporation leads to a substantial improvement of the efficiency of amorphous solar cells, the development of the entirely new classes of nano- and bio-materials, drug delivery systems, environmental remediation technologies, advanced catalytic applications, and several others.

On the other hand, a number of nanostructure fabrication processes uses a low-energy nanocluster chemical vapor deposition [8], where the nanocluster charge appears to be a critical factor in the growth of various silicon- and carbon-based nanostructures [9]. Until recently, it was presumed that atoms and molecular complexes play a pivotal role in the assembly processes at nano- and micro-scales. However, in the last few years, the building block paradigm has shifted towards accepting the crucial role of clusters, large “molecules” that typically contain from 10 to 2000 atoms. The nanocluster scenario invokes the concept of short-range interactions between the atoms of neighboring building blocks. In this regard, the charge and size of nanoclusters are the crucial parameters for the explanation of the unique architectures of many nano-sized objects. In particular, the nanocluster charge appears to be a key reason for the highly anisotropic growth of some ordered nanostructures [9].

In the coming years, the optoelectronic, photonic, nano- and biomaterials technologies are expected to be extremely important. Thus, the *fundamental physics* of multi-scale dynamic processes in complex ionized gas systems that contain nano- and micrometer-sized solid particles is becoming a matter of the utmost importance for various industrial applications of nanoscience and nanotechnology. There is a vital demand for conceptually new approaches to the analysis of behavior and manipulation of such systems, based on advanced physical models of the interaction of the cluster/particulate matter with their ionized plasma environments.

One of the aims of such attempts is to tailor the size, composition, and architecture of the nano-sized particles as building units of various nanoscale assemblies. Therefore, our specific aim here is to review the physical foundations and insights of dynamic phenomena in low-temperature complex plasma systems leading to the origin, growth, and self-organization of micro- and nano-scale particles of the desired size and shape. The review is focused on the physics of the micro- and nanometer scale processes in the plasma that allow one to efficiently manipulate the structure and basic properties of the matter at the corresponding length scales. We systematically present the current state and the most important physical advances of the fundamental research activities. The latter include the advanced theoretical models and extensive computer simulations, complemented by the laboratory experiments specifically designed to elucidate the fundamental physics of the complex plasmas.

It is remarkable that chemically active environments of the complex ionized gas systems have proved to be very efficient in generating charged fine particles. It is expected that in the near future the systems in question will become one of the major means of producing nano-scaled particles for numerous industrial applications. However, the application of plasma-particle systems to nano-scale processes is still at an early stage, and a number of fundamental physical problems are yet to be solved before the scheme can become commercially feasible. First, the nano-assembly process cannot be reliable without a precise control of the composition, size, and architecture of the plasma-grown building units. The latter have to preserve their unique features and need to be deposited on the nanostructured substrates in a non-destructive fashion. The optimal parameters of the ionized gas phase allowing a predictable and controllable fabrication process have yet to be established and linked to the process control parameters.

Apparently, the above goals cannot be achieved without solving a number of fundamental physical problems at different space and time scales. The building blocks originate at nanometer scales as a result of the elementary gas-phase reactions, and frequently agglomerate into larger particles. The gas-phase grown nano-sized particles do affect the entire ionized gas system by distorting and sometimes destabilizing the balance of electrons and reactive species, which in turn dynamically affects the cluster/nanoparticle origin and growth conditions. Thus, the processes at multiple scales become dynamically coupled through a number of elementary processes and self-consistent plasma responses, which are yet to be properly understood.

Here, in a systematic manner, we review the most recent advances in the origin, growth, and high-tech applications of micro- and nanoparticles in various complex ionized gas systems. We also discuss a number of dynamic collective phenomena in the near-substrate transition areas, with the focus on the development of the novel methods for the soft deposition of the nano-sized building units, without compromising their integrity and unique properties. Furthermore, various physical phenomena inseparably associated with the self-organization of the particle–plasma systems are reviewed. In particular, we discuss the physics of the plasma–dust interaction, levitation and dynamics of fine particles in the near-substrate areas, new self-organized structures involving the particles and the plasma, as well as a number of collective plasma phenomena (supersonic wakes, plasma waves and oscillations, motions of arrays of charged particles in plasma sheath/pre-sheath areas) important for the particle interactions and formation of many-particle structures.

### *1.3. Colloidal “dusty” plasma—an open self-organized complex system*

When considering the basic physics of complex plasmas, a special attention is paid here to the open character of this system. This openness is related to the presence of an ionization source producing the plasma, continuous flows of electrons, ions, and radicals onto the surfaces of colloid particles. The latter appear as important sinks for the plasma species, since the electrons and ions usually recombine on the grain surfaces [10–12]. Thus, sources of ionization of plasma neutrals inside the system and/or additional transport of charged particles from outside the system are required to sustain the plasma–particle system in the dynamic equilibrium. We note that in some earlier (and sometimes even current) investigations on collective phenomena in dusty plasmas, the fact that complex plasma systems are practically always thermodynamically open was often overlooked or merely sidestepped by invoking unspecified sources of power/particles and/or similarly unspecified sinks and further assuming that their total effect is negligible. However, the details of these sources and sinks can nevertheless be important for the proper and rigorous treatment of the problem. On the other hand, sinks of the plasma electrons and ions resulting from their capture by dust should also be properly accounted for by introducing the corresponding capture processes into the electron and ion conservation equations [10–12].

However, accounting only for the plasma particle capture processes is not sufficient, since without a balancing source for the plasma particles there cannot exist a self-consistent stationary state. Generally, the energy and plasma particles have to be supplied externally to maintain the system in the equilibrium state [11]. It is therefore necessary to take into account the creation of the plasma particles, for example, by an ionization source. For most plasmas it is then also necessary to include related plasma–particle loss and transport mechanisms such as, e.g., ambipolar diffusion and volume recombination, which usually develop over the same time scale with the ionization process [13].



Since the plasma ionization, transport, and recombination are all density dependent, all electrostatic processes in the system can be strongly affected. This opens the possibility that the presence of dust can affect the entire discharge system through modification of the ionization-transport-recombination balance.

It is noteworthy that many unique self-organization phenomena in the complex plasma are affected by or originate due to the openness of the system. These phenomena include, for example, various collective excitations in the background plasma, charging and collective motions of dust grains, inter-particle interactions, dust–plasma interactions (e.g., with the plasma wakes), formation of numerous self-organized structures, such as dust–plasma sheaths, dust voids, etc., considered in this review. Thus, the openness is a remarkable intrinsic feature of complex plasma systems, which definitely qualify as a fascinating and unusual state of the matter [11].

#### *1.4. Structure of the review*

Structurally, the review consists of Introduction, 7 main sections, and Summary/Conclusion. In Sections 2 and 3, the overview of the fine particle growth in chemically active plasmas and related high-tech applications is given. In Section 2, the major processes involved in the generation and growth of micro- and nano-particles in reactive plasmas, are discussed. Basically, the growth of fine powders starts with heterogeneous and homogeneous nucleation that controls the formation of sub-nanometer/nanometer-sized protoparticles (Section 2.1). The origin of protoparticles is followed by the agglomeration and coagulation processes leading to a pronounced particulate formation with the size of a few tens of nanometers. On the other hand, quickly agglomerating fine particles strongly affect the plasma stability, giving rise to mode transitions and instabilities, which are discussed in Section 2.2. The nano/micron-sized particles of numerous materials (graphite, titanium, copper, aluminum, etc.) can also be efficiently generated in plasma-enhanced sputtering facilities, as detailed in Section 2.3. As noted in Section 2.4, modern particle detection techniques (e.g. laser scattering) allow one to successfully monitor the growth and dynamics of submicron-sized particles. However, the detection and diagnostics of the nano-sized particles as well as the investigation of the complex physical/chemical mechanisms leading to the nucleation of particle precursors, appears to be a challenging problem for the coming years.

Section 3 gives a systematic review of current technological aspects of micron- and nano-sized particles. Traditionally, plasma enhanced chemical vapor deposition (PECVD) systems for the fabrication and microstructuring of silicon films for microelectronic devices suffered from the gas-phase polymerization of fine particles. Section 3.1 reviews the most recent progress in the development of the efficient techniques to remove the micron-sized particulates from the reactor volume or suppress the nanoparticle growth processes at the initial stages. Furthermore, dust particles have recently become a serious safety concern for the design and operation of fusion reactors (Section 3.2). On the other hand, the nano-sized particles have recently found a number of applications in nanotechnology, as precursors for highly anisotropic growth of carbon-based nanostructures (Section 3.3), and building units for the synthesis of nanostructured silicon-based films for solar cells applications (Section 3.4). Most recently, the nanoparticles have emerged as the key elements of several technologies that allow one to manipulate the properties of the matter at the nanoscales and synthesize previously unknown powder-assembled materials with unique nano-scale architectures, morphologies, as well as optical, thermal, catalytic, mechanical, structural and other properties (Section 3.5).

The rapidly emerging applications of nano-sized particles include nanostructured and nanocomposite films, nanocrystalline powders and consolidated structures, nanoparticle-assembled superlattices and other 3-dimensional (3D) assemblies that represent principally new forms of supramolecular crystalline matter, nanoscale inorganic synthesis, dispersions and suspensions with the controllable fluid dynamic properties, nano-sized single/few-electron data storage units and many others. As explained in Section 3.6, the nanoparticle size appears to be a key factor that determines the basic properties of nano-scaled objects. Other numerous applications of nanoparticles in high-tech industries are discussed in Section 3.7.

Sections 4–8 overview the fundamental physical phenomena in the complex plasma systems. The discussed processes can naturally affect, in a self-consistent manner, the size, shape, and deposition of the plasma-grown nano- and micron-sized particles. On the other hand, the (highly) charged colloid particles also affect the full complex ionized gas system via a number of collective processes also discussed in the review.

Progress in studies of the dynamics and levitation of charged dust grains in the near-substrate areas of laboratory low-temperature plasmas is reviewed in Section 4, which begins with the discussion of the fundamentals of charging and motion of particles in low-temperature complex plasmas (Sections 4.1–4.3). The forces acting on the particles generally include, but are not limited to, the force of gravity, electrostatic force, ion and neutral drag forces (Section 4.3). The modeling and simulation results on the dynamics and levitation of fine particles in the transition areas of argon plasmas are discussed in Section 4.4. The transition area between the plasma and the boundary includes the sheath and pre-sheath regions where the grains can levitate due to the dynamic balance of several forces acting on them. Since the plasma parameters vary dramatically in the sheath/pre-sheath areas, so does the equilibrium electric charge on a particle, which dynamically affects the force balance while the particle moves towards the wall. Several peculiarities of the fine particle charging, dynamics, and levitation in silane and fluorocarbon plasmas are reviewed in Section 4.5. As explained in Section 4.6, the investigation of the balance of forces acting on dust particles can be instrumental in probing the interactions between the plasma-grown fine powders and the processing surface. Section 4 is concluded with the overview of the major experimental techniques currently used for the detection/characterization of fine particles and measurement of their electrostatic charge (Section 4.7).

Section 5 is devoted to the overview of the main self-organized structures observed in complex plasmas, and presents the advanced theoretical models describing these structures. The key point in theoretical understanding of the motion and interactions of dust grains in the plasma is the open character of the emerging structures, with the flows of the plasma particles onto the grains. This physical insight allows one to model the unique properties of the dust–plasma systems, effectively describe the observed and predict new phenomena. In particular, in Section 5.1 we demonstrate that dust grains levitating in the sheath area create a dissipative self-organized structure that can be called the dust–plasma sheath. Under certain conditions, the dust cloud can become unstable due to formation of dust voids, i.e. plasma regions free of dust particles (Section 5.2). When the size of dust grains becomes sufficiently large, a new strongly coupled self-organized structure, a so-called Coulomb crystal, can emerge. The dynamics and diffusion of the dust particles in the strongly coupled structures is discussed in Section 5.3, where the modeling and simulation results are presented. Furthermore, the strongly coupled structures may exhibit phase transitions to the liquid-like and gas-like phases. In Section 5.4, the criteria of phase transitions in such systems are discussed and present the related simulation results are presented.

In Section 6, collective phenomena in the background plasma in the presence of charged dust grains are reviewed. Since fine particles usually levitate in the sheath areas, with strong non-uniformities of the plasma parameters and established flows of the plasma ions towards the wall, the new collective plasma phenomena appear. The latter, in turn, strongly affect the charging, arrangements, motion, and interactions of dust grains, as described in Section 6.1. One of the most important phenomena is the formation of the plasma wake because of the plasma ion flows through the charged dust structures. Here, we review the main physical mechanisms of the plasma wake generation, starting with the seminal case of the supersonic wake of a spherical charged particle (Section 6.2). We then proceed in Section 6.3 to more complicated cases of the dust particles with dipole moments and non-spherical morphology (e.g., rod-like). An analogy with the Cooper pairing of electrons in semiconductors can be seen in Section 6.4 with the Hamiltonian model of the dust–dust interaction in the presence of the plasma wake. We then proceed to the case of subsonic plasma wakes (Section 6.5), and demonstrate that the interactions of dust grains in this case can be attributed to the inverse Landau damping. Finally, the results of molecular dynamics and particle-in-cell computer simulations of the plasma wake formation are presented in Section 6.6.

The discussion of the plasma collective phenomena in the presence of dust is continued in Section 7, where the main effects of the charged dust particles on the plasma collective excitations, such as the plasma electron and ion waves, as well as new collective excitations associated with heavy (relative to the masses of plasma ions) charged grains, are reviewed. First, it is demonstrated in Section 7.1 that the dust charging opens up a new channel of dissipation of the plasma wave energy, and the dust charge appears as a new dynamic variable in the kinetic description of a complex plasma. Thereafter, the dispersion characteristics of the plasma Langmuir (Section 7.2) and ion-acoustic (Section 7.3) waves are derived. In this derivation, we also take into account the open character of the complex plasma system, and demonstrate how this affects the plasma wave dispersion characteristics. Furthermore, new modes, such as the dust-acoustic mode associated with the motion of grains, are discussed in Section 7.4. Section 7 concludes with the discussion of the dust-acoustic instability (Section 7.5).

Section 8 introduces collective excitations in the regular arrays of dust grains levitating in the plasma sheath (such as the strongly coupled plasma crystals). Study of these phenomena relies on finding proper solutions for the particle levitation and oscillations in the sheath region. Thus we start in Section 8.1 with the simplest case of oscillations of an isolated grain. The stability of the dust particle confinement is discussed in Section 8.2, where we demonstrate that even in the case of two levitating grains, their positions and stability of levitation strongly depend on the conditions in the background plasma as well as on the external forces acting on the system. In Section 8.3, the dust–lattice waves, i.e. collective wave excitations, in the strings of regularly arranged dust particles, are described. More complicated cases of non-spherical particles of a rod-like shape are considered in Section 8.4. In this case, new rotational modes of oscillations appear. We also demonstrate that depending on the plasma and external conditions, different cases of levitation of rod-like particles, associated either with vertical or horizontal alignment of the rods, are possible. The latter might have important applications for the particle deposition.

In Conclusion, the outlook of major research directions in the area of complex plasma research for the coming few years is presented. New horizons of problems associated with the dynamic and self-organization phenomena involving the plasma-grown nanoparticles are discussed as well.

## 2. Origin and growth of nano- and micron-sized particles in ionized gas systems

Generation of fine powders, ranging in size from a few nanometers to several tens of microns has been frequently reported for various plasma processing facilities since mid-1980s. The particulate matter in the processing plasmas has numerous implications for the semiconductor micro-fabrication and materials processing, which will be discussed in detail below in Section 3. Here, the underlying physico-chemical processes involved in the origin and growth of fine particles in reactive plasmas of silane-, hydrocarbon-, and fluorocarbon-based gas mixtures, are reviewed (Section 2.1). Despite a remarkable difference in the process kinetics and the plasma chemistry involved, the growth scenario can be quite similar. Indeed, the dust growth in chemically active plasmas starts with the formation of sub-nanometer/nanometer-sized protoparticles nucleated as a result of homogeneous or heterogeneous processes. Thereafter, the agglomeration/coagulation processes result in the pronounced generation of particulates with the sizes in the few-tens of nanometers range, which quickly acquire a negative electric charge as a result of collection of the plasma electrons/ions [14]. These rapidly developing processes result in a remarkable reorganization of the entire plasma system due to the changes in the particle balance (such as a noticeable depletion of the electron number density) induced by the growing dust grains (Section 2.2). Meanwhile, the plasma system reorganizes to compensate the enhanced electron losses onto the dust grains. As a result of this self-organization, the major ionization/dissociation rates, and very often, the effective electron temperature, increase. The dust growth then usually proceeds to sub-micron and micron sizes via a relatively slow process of accretion of neutral/ionic monomers (e.g. deposition of  $\text{SiH}_x$  radicals on the grain surface in silane-based reactive plasmas). Chemical nucleation in the ionized gas phase is not the only possible mechanism of the dust growth in the processing plasmas. The particulate growth can also be induced by physical and reactive sputtering of the wall/electrode material in the plasma-assisted DC/RF magnetron and other sputtering facilities. The basic physics of the relevant processes is discussed in Section 2.3. Furthermore, since most of the fine particles feature the sizes in the nanometer or sub-micrometer range, this poses a number of apparent challenges for the in situ detection and ex situ characterization methods. Some of the most recent relevant techniques are discussed in Section 2.4.

### 2.1. Origin and mechanisms of growth of clusters and particulates in reactive plasmas

#### 2.1.1. Silane plasmas

Plasmas of pure silane ( $\text{SiH}_4$ ) and its mixtures are widely used nowadays for numerous applications in the semiconductor industry (integrated circuitry and silicon-based microchips, flat panel displays, amorphous silicon solar cells, etc.). It is believed that understanding of the fine particle generation processes in silane-based plasmas is the most comprehensive as compared to other reactive plasma chemistries [15]. In this subsection, we thus review the most recent advances and current problems of the origin and growth of fine powder particles in low-pressure silane-based discharges.

The initial stages of the particle growth in pure silane discharges can adequately be described by the steady-state homogeneous model [16,17]. The basic assumption of the model is that the particle growth process is triggered by  $\text{SiH}_3^-$  anions and/or  $\text{SiH}_m$  neutral radicals, which polymerize into  $\text{Si}_n\text{H}_m$  radicals with larger numbers  $n$  of silicon atoms. With an increase of  $n$ , large clusters, and eventually subnano-/nano-sized particles of hydrogenated silicon are generated.

The apparent puzzle for the plasma processing community in the last decade has been to identify the precursor species and dominant gas-phase/surface reactions for the growth of larger (with  $> 10^4$  silicon atoms) particulates and relate the dust growth to the discharge control parameters. At present, the above problem seems to be quite far from being solved and in most cases there is yet no consensus on the dominant catalysts for the fine particles in the plasma. However, there exist only three major classes of possible catalyst candidates in the silicon hydride clustering process [18], namely, anions (negative ions), neutrals, and cations (positive ions). Apparently, the underlying physics and chemistry of the powder origin in chemically active plasmas critically depends on the prevailing experimental conditions.

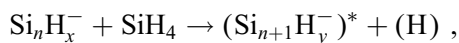
For example, the role of short lifetime neutral radicals  $\text{SiH}_2$  at several stages of particulate growth has been clarified [19]. It is notable that neutral complexes are capable to incorporate into larger saturated molecules and can thus be considered as viable candidates for the nanoparticle growth in reactive silane plasmas [15]. Hence, in the short residence time situations one could expect that short-lifetime, highly reactive neutral radicals can efficiently support numerous homogeneous nucleation processes. In particular, neutral radicals  $\text{SiH}_m$  ( $m=0-2$ ) can be responsible for the nano-powder formation in dense helium or argon-diluted silane discharges [20,21].

Likewise, positive ions can also be regarded as potential powder precursors despite high activation barriers preventing the formation of higher-mass cations. Several works report on the possibility of cationic (positively charged) silicon-based clusters. In particular, cationic silicon clusters that contain up to ten silicon atoms, have been detected in argon/hydrogen thermal plasmas by means of time-resolved mass-spectrometry [22]. Unfortunately, data on the role of positive ions in the origin of fine particulates in the low-pressure plasma glows are somewhat limited.

On the other hand, the anionic pathway is another viable route for the powder generation in silane-based plasmas. Invoking a simple argument that the formation of particulates does require critically large clusters, it was concluded that typical residence times of the neutrals are not sufficient to trigger the efficient dust growth process [23]. However, the clustering process can involve negative ions trapped by the ambipolar potential in the plasma. Furthermore, the negatively charged intermediaries can increase the average residence time of the clusters and enable their growth to the critical size [23].

Likewise, hydrosilicon anions can be efficiently confined in the near-electrode areas and participate in the plasma-assisted clustering process. Thus, a large number of negative ions can accumulate and grow towards higher masses according to the homogeneous model [17]. Relevant time-resolved mass-spectrometry data have revealed that the anionic pathway is the most likely route for the nanoparticle generation in low-pressure RF silane plasmas [15]. For example, the dust evolution from the molecular to the particulate form was studied for low-pressure silane RF capacitively coupled plasmas [24]. It was also noted that negative ions indeed play a crucial role in the powder nucleation and growth process. In the experiments, the entire range of negatively charged species, ranging from monosilicon anions through to nanometre-sized clusters, was observed [24]. Furthermore, it was shown that the anion confinement results in a pronounced particle formation. Conversely, de-trapping of the negative ions strongly inhibits the entire growth process.

In the above examples, it is likely that the negative ion clustering reaction





leads to the efficient polymerization of the higher-mass anions  $(\text{Si}_{n+1}\text{H}_y^-)^*$  in the excited state, where (H) denotes the hydrogen-bearing products [15].

The second phase of the particle growth can proceed via a rapid agglomeration of small clusters into larger (usually  $\sim 40\text{--}50$  nm-sized) particles [16]. This process is accompanied by remarkable self-organization of the plasma–dust system and is considered in more detail in Section 2.2. After the agglomeration/coagulation phase is complete, the grain size increases with the rates comparable with the relevant thin film growth rates.

We emphasize that the key dust nucleation and growth processes discussed above are most relevant to the plasmas of pure silane discharges. However, a large number of real thin film fabrication processes require a substantial dilution of silane by hydrogen and/or argon. It was noted that the offset and dynamics of the particulate growth appear quite different as compared to the pure silane case. In particular, it was observed that silane dilution complicates the discharge chemistry and elongates the time scales required for the powder detection. Thus, the particulate size, bonding states, architecture, and surface morphology of the particles grown in the pure and buffer gas diluted silane plasmas can be quite different and critically depend on the reactive gas feedstock.

Physically, by varying the gas composition one can control the residence time  $t_{\text{res}}$  of the precursor species in the discharge. Moreover,  $t_{\text{res}}$  appears to be a critical factor in the nanoparticle generation and growth. Specifically, there is a direct correlation between the residence time of the precursor radicals and the size of fine particles detected [25]. The selective trapping model [26] assumes that the neutrals should reside in the reactor volume long enough to acquire a negative charge through the electron non-dissociative attachment and/or heavy particle charge exchange collisions. If this is the case, the nano-sized particles can be trapped in the near-electrode areas, building up the minimum number density for the coagulation onset.

The critical size of the particles that can be trapped and are capable to agglomerate appears to be  $a_{\text{crit}} \sim 2$  nm for the following parameters of the experiment in Ref. [26]: the flow rates of Ar and  $\text{SiH}_4$  being 30 and 1.2 sccm (total gas pressure 117 mTorr); the gas and electron temperatures of 300–400 K and 2 eV; the electron/positive ion number density of  $3 \times 10^9$  and  $4 \times 10^9 \text{ cm}^{-3}$ , respectively. We note that under the above conditions the neutral gas residence time is approximately 150 ms. Further details of the experimental setup can be found in Ref. [27]. Finally, the formation of a dense ( $\sim 10^{10}\text{--}10^{11} \text{ cm}^{-3}$ ) powder cloud of fairly monodisperse, 2 nm-sized fine particles immediately before the coagulation onset was convincingly confirmed by the high-resolution transmission electron microscopy (TEM) complemented with the laser light scattering (LLS) measurements [26].

### 2.1.2. Hydrocarbon plasmas

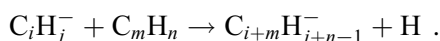
The existing understanding of the nanoparticle growth in hydrocarbon ( $\text{C}_m\text{H}_n$ , e.g. methane,  $\text{CH}_4$  or acetylene,  $\text{C}_2\text{H}_2$ ) discharges is still at an early stage as compared with the similar processes in the silane-based plasmas. However, several successful attempts to investigate the plasma chemistry and growth of nano-sized particles have recently been reported. For example, a numerical model of the nanoparticle clustering kinetics in the low-pressure RF discharge in acetylene was developed and tested experimentally [28]. The numerous gas-phase processes including the electron impact dissociation, electron attachment leading to the negative ion generation, ion–ion recombination, ion–neutral clustering, chemical reactions involving the hydrocarbon (chain and aromatic) neutrals, as well as diffusion losses of the plasma species to the discharge walls, have been included in the simulation.



Based on numerous data from the reactive plasma, aerosol and combustion literature, it was assumed in the model that the carbon hydride clustering process is triggered by the electron-impact abstraction of hydrogen from the acetylene monomer



followed by the efficient generation of  $\text{C}_m\text{H}_n$  radicals (with higher numbers of carbon and hydrogen atoms) via a chain of polymerization reactions [28]. The model allows one to predict the most probable clustering pathways as well as the temporal evolution of the number densities of the major charged and neutral species. The most likely clustering process proceeds through the addition of the anion species  $\text{C}_i\text{H}_j^-$  to the neutrals  $\text{C}_m\text{H}_n$  accompanied by the elimination of hydrogen and generation of the higher-mass anions



Eventually, the rapid chemical nucleation stage evolves into the equilibrium state, which can usually be reached when the particle loss to the walls is compensated by the production of the new species. The equilibrium state is strongly affected by the neutral gas temperature, RF power input, and working gas pressure. Similarly, depending on the external parameters, the coagulation process can either be enhanced or inhibited. It is worthwhile to mention that even though the clustering occurs mainly through the formation of linear molecules, the proportion of aromatic hydrocarbons increases and becomes significant at higher working gas temperatures.

The results of numerical modeling of the clustering processes in acetylene plasmas [28] are presented in Fig. 3, which shows a temporal evolution of the number densities of the neutral and charged species. To present the results transparently, the following notations were used [28]. The number densities of all the chain species with the same number of carbon atoms are added together and plotted as single curves. For instance, the label 2 refers to the sum of the concentrations of  $\text{C}_2\text{H}$ ,  $\text{C}_2\text{H}_2$ ,  $\text{C}_2\text{H}_3$ ,  $\text{C}_2\text{H}_4$ , etc. species. All species that have a ring structure (regardless on the number of carbon atoms) are combined together and denoted as “rings”. Species with more than 10 carbon atoms, are lumped together as “particles”.

From Fig. 3 one can see that after the initial increase in the species concentrations, the production rates slow down and eventually a steady state is reached. This indicates that a balance between the species production and diffusion losses is achieved. We note that the rates of the diffusion losses are proportional to the species concentration and this loss channel plays only a minor role at the early stages of particulate development. This certainly favors a quick initial rise of the number densities of the reactive plasma species. Eventually, the diffusion losses are balanced by the gas-phase reactions that lead to the particle production and a steady state of the discharge can be established. A comparison of the number densities of the structurally similar neutrals and anions reveals that the anion concentrations are much lower (Fig. 3). Since the density of positive ions is an upper limit for the combined anion and electron densities, the above difference can be attributed to high growth rates of the neutral particles in acetylene plasmas.

However, this does not necessarily mean that nano-sized particles are mostly neutral. In fact, one can note that most of the negative species are formed in the particle form, with the number densities of the same order of magnitude as the concentrations of the neutral particles. The ratio between the number densities of neutral and negative particles is important for the understanding of the details

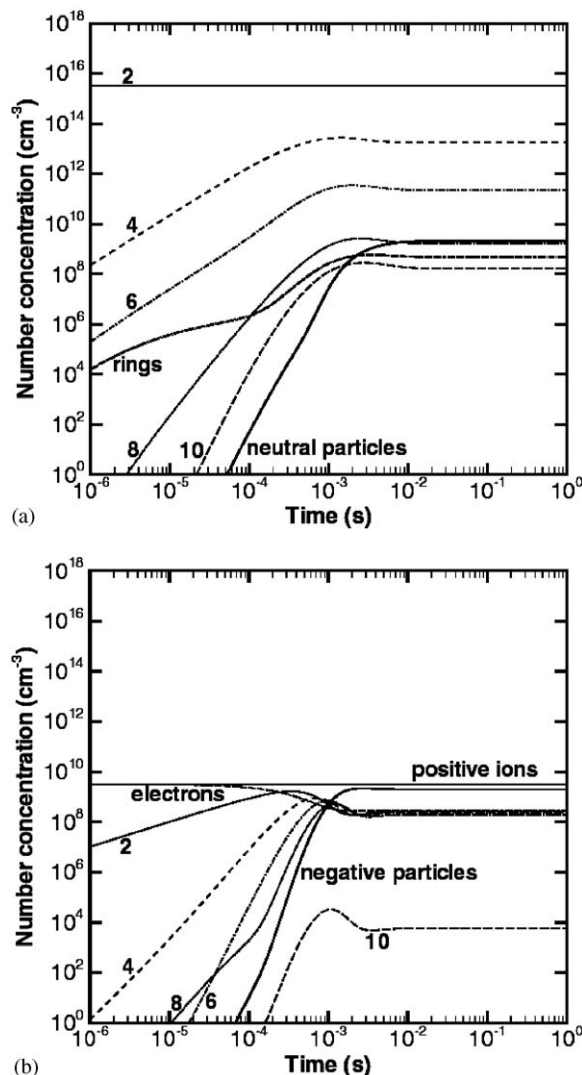


Fig. 3. Temporal dynamics of the clustering process involving neutral (a) and charged (b) species at  $T_n = 300$  K and the ionization degree of  $10^{-6}$  [28].

of the further growth processes, which are affected by the grain charge [16]. It was shown that the formation of neutral particles is favored at lower temperatures, higher degrees of ionization, and higher pressures [28]. Further details on the dependence of the ratio of the negative-to-neutral particle densities on the plasma parameters (e.g. gas temperature, degree of ionization, pressure) can be found in the original work [28].

Meanwhile, Ref. [28] also presents the experimental results on the chemical composition of nanoparticles and their aromatic hydrocarbon content in acetylene-based plasmas sustained at the

room temperatures and the 100 mTorr pressure with the 10–30 W RF powers in a 13.56 MHz capacitively coupled plasma reactor. The infrared (IR) absorption of the species was analysed in situ by comparing the IR absorption spectra of the particle-generating discharge with the reference spectra of the neutral acetylene gas feedstock. The plasma-grown nanopowders were collected from the lower electrode and analysed ex situ by the Diffuse Reflectance Infrared Fourier-Transform Spectroscopy (DRIFTS) and a Nuclear Magnetic Resonance (NMR) techniques.

It is interesting that Fourier Transform IR (FTIR) spectroscopy data collected in situ and from the powder samples confirm a predominant production of the acetylenic compounds in the ionized gas phase, although the presence of aromatic compounds appears to be non-negligible. It is notable that the recent mass spectrometry studies [29] of the RF plasma in acetylene have indicated the presence of aromatic compounds such as benzene, substituted benzenes and toluenes. The above numerical and experimental results are in agreement with the recent experiments on the dust particle generation, size-controlled growth, diagnostics and deposition in 13.56 MHz RF plasmas of Ar/CH<sub>4</sub> and Ar/C<sub>2</sub>H<sub>2</sub> gas mixtures in a Gaseous Electronic Conference (GEC) Reference Cell plasma reactor [30]. We emphasize that the most efficient dust particle generation has been reported for the elevated RF power levels, which indicates on the importance of the adequate amounts of the particle growth precursors [30].

It is also worthwhile to mention that the recent in situ FTIR spectroscopy and the plasma-ion mass spectrometry measurements evidenced the highly-monodisperse size distributions of nanoparticles grown in RF plasmas of Ar + C<sub>2</sub>H<sub>2</sub> gas mixtures [31]. This conclusion was also cross-referenced by the scanning electron microscopy of the powder samples collected during different growth phases. Measurements of the intensity of the Rayleigh/Mie scattering of the infrared signal revealed that the process of the fine particle generation, growth and disappearance is periodic (with the period of approximately 35 min under prevailing experimental conditions). It is notable that the time scales when the electron-impact ionization is enhanced and the plasma parameters in Ar + C<sub>2</sub>H<sub>2</sub> RF discharges noticeably change due to the dust growth  $\tau_{\text{C}_2\text{H}_2}$  appear to be consistently longer than the corresponding time scales  $\tau_{\text{SiH}_4}$  in silane-based plasmas (see Section 2.1.1) [31].

A simple explanation has been offered for the observed periodicity of the Rayleigh/Mie scattering signal [31]. Negatively charged particles are confined in the plasma potential as long as the different forces acting on the single particle are balanced. Since all the major forces (see Section 4.3. for details) scale differently with the grain radius, the actual particle confinement critically depends on their size. As soon as the particles reach the critical size, they are either dragged out of the plasma bulk or fall down onto the lower electrode, which results in a decrease of the scattered signal. A quick drop in the intensity of the above signal evidences a highly monodispersive character of the powder growth process in Ar + CH<sub>4</sub> plasmas.

Furthermore, the ex situ scanning electron microscopy suggests that the particles collected 10 min after the ignition of the discharge have a spheroidal shape with the particle diameter of about 150 nm and a fractal surface texture. It is thus likely that the accretion (uniform deposition of the neutral species onto the particle's surface) is probably a dominant particle growth mechanism in the relevant phase of the particle collection at the substrate [31].

A very interesting observation relevant to the plasma polymerization and dust growth processes is that the acetylene monomer was almost completely consumed for the plasma polymerization as was evidenced by the neutral mass spectrometry [31]. This is consistent with the recent findings that acetylene as a monomer plays an important role in the fine powder formation in hydrocarbon

plasmas [29,28]. This fact is highly relevant to the PECVD of various carbon-based nanostructures discussed in detail in Section 3.3.

A follow-up work of the same research group [32] details the growth precursors and dynamics of the dust grain formation in argon–methane and argon–acetylene RF plasma discharges. In particular, this work further substantiates the role of acetylenic compounds in the dust nucleation and growth processes. Indeed, in  $\text{Ar} + \text{CH}_4$  plasmas, the fine particles were formed spontaneously at consistently low discharge powers. On the other hand, the particle growth in  $\text{Ar} + \text{CH}_4$  plasmas started only after transient elevation of the RF power or quick inlet of  $\text{C}_2\text{H}_2$  monomer in the discharge volume. Therefore, the different manners in which the dust particles behave in  $\text{Ar} + \text{CH}_4$  and  $\text{Ar} + \text{C}_2\text{H}_2$  discharges can be attributed to different nucleation scenarios in both kinds of discharges.

Apparently, the procedure of adding more  $\text{C}_2\text{H}_2$  or RF power to the discharge is required to trigger the nucleation of primary clusters and protoparticles at the initial stage. Once the cluster precursors are formed, the further growth process can continue under normal discharge operation conditions.

It is very interesting to note that the elevated abundance of the  $\text{C}_2\text{H}_2$  monomer species in the  $\text{Ar} + \text{CH}_4 + \text{H}_2$  inductively coupled plasmas for the PECVD of various carbon-based nanostructures [33,34] has been achieved by operating the discharge at elevated RF powers. One can thus presume that the relevant nanostructure growth process has been strongly affected by the pronounced formation of dust in the ionized gas phase (for details, please refer to Section 3.3).

On the other hand, the dynamics of the dust formation in  $\text{Ar} + \text{C}_2\text{H}_2$  plasmas is periodic and follows the scenario: nucleation  $\Rightarrow$  further growth (agglomeration and accretion)  $\Rightarrow$  development of dust-free regions (due to the action of various forces)  $\Rightarrow$  new nucleation in the dust-free regions. A possible explanation for the differences in the dust growth dynamics in methane-based and acetylene-based reactive environments is that the nucleation process strongly depends on the concentration of  $\text{C}_2\text{H}^-$  negative ions, which are efficiently generated in the  $\text{Ar} + \text{C}_2\text{H}_2$  plasmas. Further discussion on this matter can be found in [32].

There are numerous indications that powder formation can also be induced by the surface and reactor contamination effects. For example, in pure methane discharges in a clean reactor chamber, the powder formation process takes at least a few hundred seconds. However, in a contaminated reactor, the fine particle appearance can be detected much faster. Thus, the powder formation might be affected by surface effects as is the case for SiN dusty plasmas. However, no high mass neutrals, cations or anions have been detected by the mass spectrometry, in contrast to the silane complex plasmas [15]. Hence, it is very likely that large particles are formed via heterogeneous processes. The latter processes are most common for the situations when the plasma species are non-reactive and direct gas-phase reactions leading to the clusterization are not efficient. In this case the fine particle growth can proceed via the electron-induced surface desorption of nano-sized clusters. The initially neutral clusters can migrate into the near-electrode/plasma sheath area where the probability of their excitation/ionization via collisions with high-energy electrons is quite high. Ion–molecular reactions can further contribute the particulate growth. Finally, a pronounced coagulation process can lead to the formation of the primary particles as well as larger agglomerates [15].

It is also remarkable that carbon nanoparticles can be formed in thermal plasmas of arc discharges. It has recently been proposed [35] that the shell-structured carbon clusters can be formed as a result of the same formation mechanism—the liquid cluster crystallization. In this case, both the fullerenes (one-shell structure) and the carbon nanoparticles (multi-shell structure) can be generated.

### 2.1.3. Fluorocarbon plasmas

Fluorocarbon ( $C_xF_y$ ) based plasmas have recently been widely used for ultrafine and highly selective etching of polysilicon and a number of PECVD processes including many common applications in microelectronic manufacturing industry [36]. Furthermore, many plasma etching processes of silicon and its components, as well as deposition of chemically resistant barriers, dry lubricants, etc. involve  $CF_4$ ,  $C_2F_6$  or  $CHF_3$ ,  $C_2F_4$ , aromatic fluorocarbons, etc. [37]. An early article [37] reports on a gas phase particulate formation in RF fluorocarbon plasmas of 13.56 MHz capacitive discharge between two 15 cm in diameter parallel-plate electrodes with 3 cm separation. Laser light scattering was used to monitor the appearance and trapping of particles in the discharge. In the experiment, the powder particles were collected and analyzed by the FTIR and TEM tools. In particular, a sequence of monochromatic images of particulate suspension and growth obtained from a vinylidene fluoride plasma at 27 mTorr sustained with the 30 W RF powers (Fig. 1 of Ref. [37]) reveals that the time of the initial particle detection varied in the experiments from  $\sim 10$  to 250 s. The TEM results show that the particles generated are usually non-agglomerated, of the fairly spherical shape and accumulate during extended discharge operation. The grain diameter typically ranged from 110 to 270 nm.

The particles develop in size and evolve into a spatial pattern, which is suspended in the inter-electrode space as can be seen in Fig. 1 of Ref. [37]. The time of the first appearance of particles is found quite sensitive to the total gas pressure and the discharge chemistry. Addition of hydrogen or hydrogen-containing gas (e.g.,  $CH_4$ ) to a fluorocarbon discharge resulted in a remarkable increase of the particle growth rate and shortening of the time of their first appearance. This effect could be attributed to the enhanced production of free radicals by hydrogen atom abstraction of fluorine.

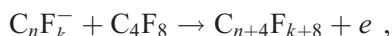
Article [37] also provides a valuable direct experimental indication on the fine particle growth rates in fluorocarbon plasmas. Specifically, the appearance time for particles in a  $C_2F_4$  plasma at 140 mTorr was measured to be 110 s. Assuming a constant radial growth rate (and a minimal diameter of 100–300 nm that can be detected by the Laser Light Scattering methods), one can obtain 0.5–1.4 nm/s for the particle growth rate. It is worth noting that the fluorocarbon film growth rate on a substrate placed on the lower electrode occur at a comparable rate of 2 nm/s.

Meanwhile, it has recently been demonstrated that RF discharges of octafluorocyclobutane ( $c-C_4F_8$ ) based gas mixtures also generate large amounts of highly polymerized molecules, which have been correlated to various polymerization processes in the gas phase [38]. It is worth noting that the chemistry behind the gas-phase nucleation processes can be quite similar in the silane and fluorocarbon based plasmas. Indeed, the higher-fluorocarbons polymerized in the ionized gas phase, can act as efficient precursors for the generation of nano-sized particles and also take part in the thin film deposition processes, which is very similar to what was described in Section 2.1.

Article [39] reports on the generation of solid grains and agglomerates in fluorocarbon plasmas for ultra-fine selective etching of  $SiO_2$  and PECVD of low-dielectric constant polymeric films. Dust generation was examined *ex situ* by the SEM technique, after deposition of the solid particles on the surface. Furthermore, the correlation between the polymerization in the ionized gas phase and the relevant surface processes has been established and the most relevant powder formation mechanisms in fluorocarbon plasmas have been proposed [39]. The fine particles were generated in a parallel plate 13.56 MHz plasma reactor, where a capacitively coupled plasma of  $c-C_4F_8$  was maintained within the pressure range from 23 to 250 mTorr. The typical RF power density in the experiments

on deposition of fluorinated amorphous carbon (*a*-C:F) thin films was 0.15 W/cm<sup>2</sup>. Under such conditions, numerous nano-/micron-sized particles and agglomerates dispersed over the wafer surface have been observed. The diameter of the gas-phase grown particles, measured by the SEM, ranged from 0.5 to 2.3 μm. In the intermediate pressure range (> 50 mTorr), a pronounced generation of the agglomerates with the size in the few tens of micrometer range and composed of the primary spherical particles, has also been detected. It is notable that the number of primary particles building up the agglomerates increases with pressure. A typical size of the fluorocarbon-based agglomerate at 250 mTorr pressure is about 30 μm.

We stress that the gas-phase particulate polymerization was inferred through the dependence of the film deposition rate on the gas feedstock pressure. Specifically, the film deposition rate decreased when the gas pressure exceeded 50 mTorr. Presumably, this can be attributed to the enhanced loss of the gas-phase polymer precursors to the particle generation processes. It is also worthwhile to mention that no significant particulate formation in the gas phase was observed in the CF<sub>4</sub> or C<sub>2</sub>F<sub>6</sub>-based discharges. Thus, it seems reasonable to conclude that stable CF<sub>4</sub> and C<sub>2</sub>F<sub>6</sub> molecules are not efficient precursors for the particle growth. Even though the trigger catalyst plasma species are yet to be conclusively identified, one can presume the nanocluster route for the fine particle growth. The following chain associative electron detachment polymerization reaction



was proposed as a basic clustering pathway in the fluorocarbon plasmas. This mechanism also appears to be consistent with the elevated particle production rates at higher gas pressures. Furthermore, there is a correlation between the clusterizing rates and the gas-phase concentrations of the source gas molecules and the main products of the first-order reactions [39].

We emphasize that similarly to SiH<sub>4</sub> (Section 2.1.1) and C<sub>m</sub>H<sub>n</sub> (Section 2.1.2) plasmas, the negative ions also play a crucial role in the clustering reactions in fluorocarbon plasmas. Thus, elucidation of the dust generation pathways, including a detailed experimental investigation of the catalyst species and gas-phase reactions for polymerization [40], is an apparent forthcoming challenge for the coming years. In particular, the particle production has recently been confirmed in the C<sub>4</sub>F<sub>8</sub> plasmas [39], which were able to generate several molecules such as CF<sub>4</sub>, C<sub>2</sub>F<sub>6</sub>, and C<sub>2</sub>F<sub>4</sub>. In particular, the C<sub>2</sub>F<sub>4</sub> molecule played an important role in the gas-phase polymerization leading to the dust particle generation [40]. The C<sub>2</sub>F<sub>4</sub> molecule can be activated and transformed to highly reactive species –CF=CF– and –CF=CF<sub>2</sub> in the plasma. Numerous branching reactions involving the above species lead to high molecular weight compounds further acting as the particle nuclei and polymer precursors. However, under prevailing experimental conditions the particle production and film deposition was not observed in CF<sub>4</sub> and C<sub>2</sub>F<sub>6</sub> plasmas [40].

At the end of this section, we note that dust growth under the plasma conditions is not merely limited by the silane-, hydrocarbon-, and fluorocarbon-based chemistries. For example, the carbon nitride particles with diameters of a few hundred nanometres, have recently been grown at the room temperatures in RF capacitive discharges of N<sub>2</sub> + CH<sub>4</sub> gas mixtures [41].

## 2.2. Effects of fine particles on discharge stability—self-organization and critical phenomena

Here, we consider critical phenomena in silane-based reactive plasmas following the selective protoparticle trapping stage. Once the density of the powder particles has exceeded a critical value,



being typically within the range of  $\sim 10^{10}$ – $10^{11}$   $\text{cm}^{-3}$  [26], the fast coagulation process starts. At this stage, the generation of new protoparticles is usually inhibited and 40–50 nm aggregates are detected. It is notable that neutral atoms/molecules can play an important role in the dynamics of the above process [43]. A number of works studied temporal dynamics of the fine particle growth. A typical diagram reflecting the temporal variation of the particle size and the number density is given in Fig. 4 of Ref. [15]. At the beginning of the process (within typically a few seconds after the plasma onset), the size increase and decline of the dust density are fairly monotonous. On the other hand, during the rapid (coagulation) phase, the plasma and dust parameters usually change dramatically. Thereafter, the process reverts to the slow growth phase.

The specific critical value of the dust concentration can possibly be explained by the competition between the clustering process and the attachment of small anions to the grown nano-sized particles [26]. We emphasize that the fine particle charging processes appear to be physically different before and after the coagulation stage. When a particle size is in a few nanometer range, the electric (usually negative) charge is acquired through the negative ion attachment process. On the other hand, larger (a few tens of nm sized) grains are usually charged by the microscopic electron/ion fluxes originated due to the potential difference between the particulate surface and adjacent plasma. In the latter case, the dust charge can be calculated using the Orbit Motion Limited (OML) approximation [3,44,45]. For more details on the dust charging mechanisms, the reader can be referred to Section 4.1. Note that the negative particle charge appears to be a strong limiting factor in the agglomeration process [15–17].

A simple estimate of the time necessary for the coagulation process to begin can be derived by comparing the rates at which the fine particles coagulate and are lost to the walls. Specifically, the characteristic time for the diffusion (which can be derived from the classical Brownian motion) losses  $\tau_D$  becomes smaller than the coagulation characteristic time  $\tau_c$ , i.e.  $\tau_c < \tau_D$ . For instance, the coagulation characteristic time can be derived from the collision rate between neutral nanoparticles:

$$\tau_c^{-1} = \sqrt{2}(8T_n/\pi m_d)^{1/2} 4\pi n_d a^2 ,$$

where  $T_n$  is the gas temperature (in energy units), and other notations are standard, namely,  $m_d$  is the mass of the dust particle,  $a$  is its radius, and  $n_d$  is the number density of the dust particles. For example, for the room temperature argon plasma at the 130 Pa pressure, the density of the 1 nm-sized nanoparticles should exceed  $n_{d,\text{crit}} = 6 \times 10^{11}$   $\text{cm}^{-3}$  for the coagulation process to start [42].

As the powder size increases, the dust number density and other discharge parameters change rapidly during the coagulation stage. This critical phenomenon leads to dramatic modifications of the power and particle balance in the discharge. The major reason for this reorganization is a newly emerged electron/ion sink channel onto the combined surface of the fine particles. In some cases, the electron/ion capture by dust can become a dominant channel of the plasma particle loss (as compared to, e.g. ambipolar diffusion losses to the electrodes/discharge walls). Thus the plasma–particle system can become unstable giving rise to so-called  $\alpha - \gamma'$  transitions [14,25,26]. Hence, the enhanced loss of the electrons/ions is to be compensated by an additional ionization. Consequently, the plasma–particle system generates a self-consistent feedback by elevating the electron temperature, which yields the remarkably higher ionization/dissociation rates. A number of the silane-based discharges have been frequently reported to feature the elevated ( $\sim 10$  eV) electron temperatures, as compared with pristine (dust-free) plasmas [14,15,25,26].

An interesting insight into the coagulation of small protoparticles into larger particulates in low-temperature plasmas is given in Ref. [16]. The agglomeration model of this work is favourably different from some other models since it takes into account the details of the dust charging. Furthermore, in addition to the (common to the OML theory) electron and ion microscopic currents, the model also includes the UV photoelectron emission (photodetachment processes). We note that it is quite typical for the rare gas discharges that up to  $\sim 50\%$  of the RF power can be transferred into optical/UV emission [46]. The latter radiation can further be trapped in the plasma, where the plasma effectively acts as an optical resonator. Typically, the UV resonance radiation features energies between 10 and 20 eV. Furthermore, nanoparticles are very sensitive to the photoelectron emission, with up to one photon emitted from the neutral nanoparticles of Ni, Cu, Ag, and Au. Thus, the intensity of the photoelectron emission from nanoparticles is approximately two orders of magnitude higher than from the respective bulk materials. The advanced charging model of Ref. [16] also includes the electron detachment from the nanoparticles due to their collisions with the excited atoms (quenching process), the secondary electron emission, the charge distribution on the nanoparticles, etc.

The key equation of the model is quite common for the aerosol science and describes the dynamics of the coagulation process

$$\frac{\partial n(v)}{\partial t} = \frac{1}{2} \int_0^v \beta(v', v-v') n(v') n(v-v') dv' - \int_0^\infty \beta(v, v') n(v) n(v') dv', \quad (2.1)$$

where the first term accounts for the gain of particles within the volume  $[v, v+dv]$  due to coagulation of smaller particles. The second term describes the loss of particles from the same element of volume due to coagulation with particles of any volume, and  $\beta(v, v')$  is the coagulation rate between the two particles with a volume  $v$  and  $v'$ . The corresponding rates can be found in the aerosol literature, see e.g. Ref. [47].

The plasma properties have been modeled by using the standard set of the positive ion and the power balance equations of the global discharge model [48]. The ion balance equation accounts for the ion loss to the walls and to the fine particles, the ion production by the electron impact, as well as the energetic electrons entering the discharge through the sheaths. The power balance equation suggests that the power provided by the RF field is dissipated in the electron collision processes and the ion acceleration to the plasma sheaths. The set of the basic equations is complemented by the overall charge neutrality  $n_i = n_d Z_d(a) + n_e$  and by the equation for the two resonant radiative levels  $^3P_1$  and  $^1P_1$ , where  $Z_d(a)$  (here it is emphasized that the grain charge is a function of the size) is the grain charge. For simplicity, the negative ions that can in reality strongly affect the major processes of the particle's formation and growth, have been neglected.

Below we summarize the main findings of Ref. [16] on the fine particle coagulation. First, the positive ion density appears to be a critical factor for the coagulation process. Specifically, the coagulation is more likely to occur in the low ion density plasma. However, the model predicts that the density of the protoparticles should be higher in high-density plasmas. Secondly, the particle coagulation in the low pressure plasma can be enhanced as compared to coagulation in neutral aerosols due to the charge effects. Finally, the coagulation of particles in a plasma follows the same time dependence as the neutral coagulation ( $n_d \propto t^{-6/5}$ ). In this sense the charged particle coagulation can be considered as the neutral coagulation of particles with an effective cross-section depending on the particle charge distribution. However, article [16] states that the details of the

charging mechanism, although affecting the plasma properties, do not have any significant effect on the coagulation dynamics.

However, recent results show that the process of particle coagulation can be even more complicated. In the recent microparticle coagulation experiments performed onboard of the International Space Station [49], the monodisperse particles of 3.4  $\mu\text{m}$  in size were injected into a chamber filled with Ar gas at 0.7 mbar pressure. The mass spectrum of the resulting particle clusters (number of clusters  $N$  containing  $k$  particles) was measured. It was shown that starting from a certain moment  $N(k) \propto k^{-\alpha_k} N(k)$ . Simultaneously, the growth of a single large agglomerate occurs, accumulating  $\sim 10^5$  particles per second. The coagulation process developed a few orders of magnitude faster than was expected. A huge agglomerate was formed while the aggregation among smaller clusters was still on the way. Further investigations showed that the clusters were charged, positively or negatively (the charge was measured by applying a sinusoidal voltage to the chamber electrodes). Note that in this case the standard coagulation equation falls short to explain the observed features of the aggregation kinetics. Presumably, this can be attributed to the pronounced dust charging effects. The coagulation equation was generalized taking into account the enhancement of the coagulation rate due to the charge-induced attraction [49]. The detailed analysis shows that the above equation allows the so-called “gelation” solution, when a particle of an infinite mass is formed at the certain (gelation) moment  $t_{\text{gel}}$ . Two phases “-gel” (infinite aggregate) and “sol” (clusters of finite size), co-exist at  $t > t_{\text{gel}}$ . The aggregation theory shows that the presence of charge on particles dramatically enhances the aggregation process and noticeably impedes the gelation onset.

The criteria for the dust agglomeration in plasmas have also been obtained in Ref. [43]. It was demonstrated that dust particle attraction in a plasma can be due to the plasma particle and neutral particle bombardment. The criteria of charged dust agglomeration where the attraction forces due to particle bombardment, exceed the dust repulsion forces due to Coulomb interaction between the like charges, have been derived [43].

We recall that the coagulation process is usually accompanied by reorganization of the discharge into another state with lower electron number density and remarkably higher electron temperature. This transition is a classic example of a self-organization process in the plasma and is commonly referred to as a  $\alpha - \gamma'$  transition [25,26]. Let us now have a semi-quantitative look at this interesting phenomenon and, following [26], estimate the critical particle radius  $a_c$  and the corresponding change in the electron temperature  $T_e - T_{e0}$ . A simplified equation for the electrons is given by

$$dn_e/dt = K_i(T_e)n_en_n - n_e D_a/R^2 - K_{\text{att}}(a)n_d n_e, \quad (2.2)$$

where  $n_n$ ,  $n_d$ , and  $n_e$ , are the number densities of the neutral gas, particulates, and electrons, respectively,  $K_i(T_e)$  is the ionization rate,  $K_{\text{att}}$  is the rate of electron attachment to nano-sized particles,  $D_a$  is the ambipolar diffusion coefficient,  $a$  is the particle radius, and  $R$  is the discharge dimension (e.g. space between the two RF electrodes in a parallel plate geometry). In a steady state ( $dn_e/dt = 0$ ), from (2.2), one can obtain

$$K_{0i} \exp(-U_i)n_n = D_a/R^2 + n_d K_{0a} a^2 \exp(-e^2/hva),$$

where  $U_i$  is the ionization potential,  $h\nu$  is a characteristic quantum that an electron can transfer by polarization to molecular vibrations of a small nano-sized particle, and the coefficient  $K_{0a}$  can be found in Ref. [26]. Before the coagulation onset, the electron temperature is determined by the balance of volume ionization and electron loss to the walls.

Physically, the  $\alpha - \gamma'$  transition happens when the electron losses on the particles become more essential than those on the walls/electrodes. The critical radius can thus be calculated from (2.2)

$$a_c = (e^2/h\nu) \ln(K_{0a}n_d R^2/D_a) ,$$

which yields the estimate  $a_c \approx 3$  nm for the experimental parameters of Ref. [26]. From (2.2), one can also get a simple and general relation for the electron temperature evolution as a function of the aggregates radius in the process of  $\alpha - \gamma'$  transition:

$$1/T_e - 1/T_{e0} = (e^2/h\nu)(1/a - 1/a_c) , \quad (2.3)$$

where  $T_{e0}$  is the value of the electron temperature immediately before the  $\alpha - \gamma'$  transition. Before the transition, when the electron attachment is much slower than the ambipolar diffusion to the walls, the electron temperature can be estimated from (2.2) as  $T_e \approx 2$  eV. Furthermore, from (2.3) one can estimate that during the particle agglomeration process the electron temperature rises and levels off at  $e^2/h\nu a_c$ , numerically being  $T_e \sim 5\text{--}7$  eV. One can also infer that in the process of the  $\alpha - \gamma'$  transition, the electron number density decreases in at least one order of magnitude, whereas the positive ion concentration slightly increases.

To summarize, the particles, trapped and survived in the plasma, play a major role in the self-organization of the plasma-powder system. This aggregate formation process resembles a phase transition and starts only when the particle density exceeds a certain threshold value. The coagulation process triggers the critical phenomenon of the  $\alpha - \gamma'$  transition, when the high rate of electron attachment to relatively big aggregates results in an essential electron temperature increase and a dramatic fall of the electron density. We also note that the main parameters like voltage/power thresholds necessary for the discharge maintenance, can be strongly affected by dust particles dispersed over the volume of the plasma [50]. Furthermore, dielectric dust grains can trigger transitions between the two different discharge states in the capacitive planar RF discharges [50]. Thus, it certainly becomes clear that further studies of the coagulation/agglomeration kinetics in low-temperature gas discharges are warranted.

### 2.3. Particle growth in plasma-assisted sputtering facilities

Nano/micron-sized particles of various materials (graphite, titanium, copper, silicon, aluminum, etc.) can also be successfully generated in plasma-enhanced sputtering facilities [51,37]. In sputtering plasmas, contaminant particles have been reported for several kinds of sputtering targets and plasma sources. In particular, generation of the silicon/silica, aluminum, copper, carbon, etc. particles in DC and RF sputtering discharges in various gas feedstocks has been extensively reported (see e.g. [52–54]).

Article [51] reports on phenomenological observations of submicron to micron-sized particles formed in the gas phase of a sputtering capacitively coupled discharge for a variety of target materials. The particulate clouds appeared after a few seconds or minutes after the discharge was switched on and were detected by a sensitive video camera. This period will further be referred as the particle detection time  $t_{\text{det}}$ . As the particles grew in size, their distribution was imaged by the laser light scattering technique (see Section 4.6 of this review). Initially, the particle cloud filled the entire volume between the electrodes except for the plasma sheaths. Furthermore, the cloud was the densest near the upper (powered) RF electrode. Once the particles grew to a critical diameter of 120 nm, the

discharge becomes unstable. Towards the end of the instability cycle there was an empty region, or void, in the particle cloud. The dust voids in complex plasmas will be discussed in detail in Section 5.2 below. The void expands as the particles grow in size until the void fills in nearly the whole interelectrode region. This marked the end of the growth cycle noted here as  $t_{\text{growth}}$ .

Typically,  $t_{\text{det}}$  varied from 15 s for copper to 10 min for aluminum, whereas  $t_{\text{growth}}$  varied from 3 min for Torr Seal epoxy to 3 h for titanium [51]. The particle diameters were measured ex situ by the Scanning Electron Microscopy (SEM). After the end of the growth stage, the sizes of the graphite, titanium, stainless steel, and tungsten particles were in the submicron range (typically 300–400 nm in diameter), whereas aluminum and copper particles grew to micrometer (typically 1–5  $\mu\text{m}$ ) sizes. Particles grown from different materials had different shapes. Some particles were filamentary fractals, like those grown from copper and aluminum. In contrast, carbon particles had a bumpy spherical shape. Other materials formed compact coagulants of a few spheres, like titanium and stainless steel. On the other hand, tungsten formed compact agglomerates.

As compared with the reactive plasmas, particle growth rates are usually lower in the sputtering discharges mostly because of the lower number densities of the reactive species. However, the sputtering discharges have an obvious advantage that they can produce particles from almost any solid material that can be sputtered without decomposition. Similar to the particle growth in chemically active plasmas, the growth process develops in several steps. However, in this case the particles originate as clusters released from the sputtering target or the walls. Afterwards, the clusters coagulate, forming the primary particles, which can further agglomerate to form particulates of various shapes and architectures (e.g. spongy and filamentary or compact and spheroidal).

Note that the electric charge is a critical factor in determining the shape of the plasma-grown nanoparticles [55]. Indeed, when particles have a small (typically negative) charge and a high velocity, they can easily overcome Coulomb repulsion and form compact or spheroidal agglomerates. On the other hand, when the charge is larger and the velocity is lower, the electrostatic repulsion is stronger and an incoming particle is more likely to strike the end of a particle chain than the middle (mostly because of the plasma shielding of the distant elements of the agglomerate), and this process tends to promote a filamentary or fractal shape, which was verified by numerical simulations [55].

The picture of the particulate growth is certainly more complex in magnetron sputtering discharges [56]. It has been demonstrated that the mechanisms for particle generation, transport and trapping during the magnetron sputter deposition are different from the mechanisms reported in previously studied etching processes in reactive plasmas, due to the inherent spatial non-uniformity of magnetically enhanced plasmas. Since the magnetron sputtering facilities are usually operated at low pressures, the contributions from the homogeneous mechanism (which is a dominant one in silane plasmas, see Section 2.1) are likely to be negligible. Hence, most of contamination problems in magnetron sputtering processes have been attributed to heterogeneous contamination sources, such as wall flaking. Furthermore, highly non-uniform plasmas typical for magnetron sputtering processes are subject to simultaneous material removal and redeposition in different target regions. Due to the above processes, a formation of filament structures can be favored. Meanwhile, the filaments can be resistively heated by intense current flows, which can cause violent mechanical failures and the removal of the filament into the plasma bulk. Combined with the repulsion between the negatively charged filament and the sheath region, this process can result in an acceleration of the filaments away from the sputter target, which can be a source of hot and fast particles capable of damaging



the substrate being processed. Further details of the particulate growth in the magnetron sputtering deposition systems can be found in Ref. [56].

We note that DC/RF sputtering belongs to a larger group of particle generation mechanisms from the surrounding solid surfaces, encompassing the reactive ion etching (RIE) [57], the filtered cathodic vacuum arc deposition [58], the hollow cathode discharges, and some other processes. In RIE systems with halogen containing species and originally small roughness, which might exist at the substrate surface, can result in a local deposition of polymer films. The latter parts are usually etched away slower than clean surfaces. In the anisotropic RIE process caused by directed ion fluxes, small columnary etch residues are formed. As a result of a slight underetching, the columns become thinner at their base and thus unstable. Since the structures are negatively charged, the Coulomb repulsion from the surface causes them to break off and to be ejected into the discharge. The splitted etch residues are finally trapped in the glow by the plasma force balance. We emphasize that the above mechanism is quite similar to the magnetically-enhanced sputtering systems discussed above [56].

Finally, we note that the results of the Transmission Electron Microscopy (TEM) of GaAs and gold nanoparticles synthesized by the RF sputtering on silica substrates [59] suggest that migration of small nanoparticles/clusters (released as a result of a target sputtering) on the substrate surface is yet another factor affecting the initial nanoparticle growth processes. Apparently, detailed investigation of the nanoparticle origin and growth mechanisms in the complex plasma systems with solid particles released from the walls/electrodes, is eagerly anticipated in the near future.

#### *2.4. Problems of particle diagnostics and characterization in the nanometer range*

At present, the most advanced common particle detection techniques (e.g. laser light scattering) (see Section 4.7) allow one to successfully monitor the growth and dynamics of submicron-sized particles. However, detection and diagnostics of nano-sized particles as well as investigation of the complex physical/chemical mechanisms leading to nucleation of particle precursors, is still an unresolved problem so far.

Some common methods for the detection of micron-sized particles in a low-temperature plasma are discussed in Section 4.7. Here, we remark that in the studies of the particulate growth in reactive plasmas (see Section 2.1) the most common methods are the Laser Light Scattering based on the Mie light scattering theory. This method can be used to detect the particles and get an insight into the dust number density. However, the accuracy of the methods based on the Mie scattering theory is restricted to very small (typically larger than 20 nm in diameter) particles, due to the  $a^6/\lambda^4$  dependence of the intensity of the scattered signal, where  $\lambda$  is the laser wavelength.

Here, we address some new in situ methods of the detection of nanosized clusters and particles grown in chemically active plasma environments. Since such environments are common for industrial manufacturing processes, it is imperative to be able to detect and control the particles in the ionized gas phase. The so-called double-pulse-discharge (DPD) method enables a highly sensitive in situ detection of very small ( $> 0.5$  nm in size) clusters and particles [21]. Using this method, one can simultaneously measure a temporal evolution of the average size and density of the clusters during the nucleation and subsequent growth phases in silane RF discharges (see Section 2.1). In the DPD method, each discharge cycle includes three discharge phases, namely, the periods of the main pulse discharge  $T_{\text{on}}$ , the cluster diffusion  $t_{\text{off}}$ , and the subpulse discharge  $t_{\text{on}}$ . The nano-clusters nucleate and grow during  $T_{\text{on}}$ , and diffuse after the main pulse discharge is turned off. In the experiments,



most of the clusters were electrically neutral [21]. In the following model [21], it was assumed that the loss of plasma electrons due to their attachment to the neutral clusters is comparable with the electron loss due to diffusion. In this case the cluster density  $n_d$  can be related to the decay rate of the electron density  $n_e$ :

$$\frac{dn_e}{dt} = -\langle\sigma_{\text{att}}v_e\rangle n_e n_d - \frac{n_e}{\tau_{\text{dif}}} , \quad (2.4)$$

where  $\sigma_{\text{att}}$  is the cross-section of the electron attachment to the clusters,  $\tau_{\text{dif}}$  is the characteristic time of the electron loss due to diffusion,  $v_e$  is the electron velocity, and the angular brackets denote the averaging over the electron distribution. The dynamics of the electron density decay provides a valuable information on the cluster diffusion during  $t_{\text{off}}$ . From Eq. (2.4) one can obtain

$$n_d(t_{\text{off}}) \propto 1/\tau(t_{\text{off}}) - 1/\tau_{\text{dif}} ,$$

where  $\tau(t_{\text{off}})$  is the characteristic time of the electron density decay after the subpulse discharge is turned off. The characteristic time of the  $n_e$  decay after turning off the main pulse discharge for  $T_{\text{on}} \sim 1$  ms was used as an estimate of  $\tau_{\text{dif}}$ . Indeed, the electron diffusion loss was dominant under the above condition. The characteristic decay time of the cluster density  $\tau_p$  was deduced from the dependence of  $\tau$  on  $t_{\text{off}}$ . Furthermore, the cluster diffusion coefficient, which is related to the cluster size, can be deduced from the value of  $\tau_p$ . The absolute value of  $n_d$  can then be calculated by using the measured cluster size and fitting (2.4) to the time evolution of  $n_e$  after the main pulse discharge.

The experiments of Ref. [21] were conducted in a parallel plate capacitively coupled plasmas of 13.56 MHz discharges sustained with RF power densities of 0.18 W/cm<sup>2</sup> in pure SiH<sub>4</sub>. The dynamics of the electron density decay (after the RF pulse was off) was measured by a 9 GHz microwave interferometry. Fig. 4 shows the nanocluster size distribution for the different main pulse durations  $T_{\text{on}} = 3, 10$ , and 100 ms. One can note that only small clusters exist for  $T_{\text{on}} = 3$  ms. For  $T_{\text{on}} = 10$  ms, the larger clusters coexist with the small ones and there is a “bottleneck” in the size distribution of Si<sub>*n*</sub>H<sub>*x*</sub> ( $n \sim 4$ ). This bottleneck clearly indicates that the large clusters are structurally different from the small ones. Presumably, the larger clusters are well nucleated. After the main discharge pulse of 100 ms is over, the large clusters grow further in a monodisperse way. On the other hand, smaller clusters with  $n \approx 4-6$  are consumed by the large clusters. It is imperative that the latter process almost completely suppresses the nucleation of new large clusters with the intermediate number of silicon atoms. Thus, it indeed appears possible to control the size and number density of the nano-clusters using the pulsed discharge arrangements. Further details of the method and detection of ultrafine ( $< 5$  nm) clusters in silane plasmas can be found in Ref. [21].

Another method of in situ particle detection is based on the analysis of the radio-frequency discharge impedance [60]. It enables one to detect the occurrence of fine powders with the size of about 2–3 nm. In this work, capacitively coupled non-symmetrical discharges in silane–argon gas mixtures were used. In such discharges the relation between the RF voltage and RF current is usually quite nonlinear [48]. Specifically, this nonlinearity generates higher harmonics in the discharge current. From the analysis of the nonlinear higher-harmonic currents one can infer a valuable information about the electron and ion dynamics. The spectral analysis of the RF current reveals two distinctive harmonics, namely, with the frequencies  $\nu_1 = 13.56$  MHz (fundamental frequency or the first harmonic) and  $\nu_3 = 40.68$  MHz (third harmonic).

In pure argon plasmas, the amplitudes of the two harmonic components remain constant. However, in a dust-forming plasma, their amplitudes start to decrease a few tens of milliseconds after the

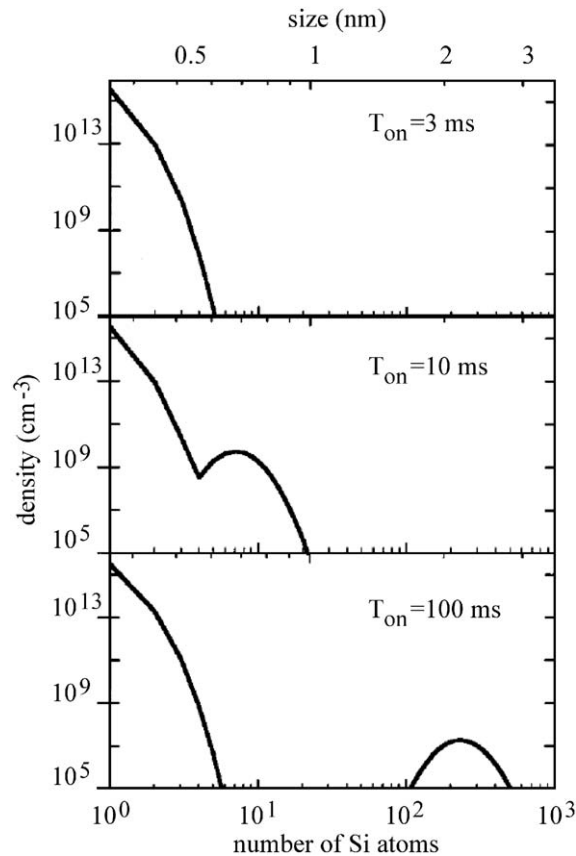


Fig. 4. Size distribution of clusters for  $T_{\text{on}} = 3, 10$ , and  $100$  ms in a  $13.56$  MHz RF discharge at  $13.3$  Pa [21].

ignition of the discharge owing to the formation of nanoparticles in the gas phase. This effect can thus be used as a powerful tool to detect the occurrence of the nano-sized powders in silane-based plasmas. Capacitive probe measurements of RF current and voltage show that in the pristine (pure argon) plasma, the intensity of the  $40.68$  MHz nonlinear signal is invariable, while it is a clearly declining function of time in  $\text{Ar} + \text{SiH}_4$  dust-forming plasmas [22]. It is notable that the time intervals when the discharge parameters change and the typical particle growth times (see Section 2.1) in similar gas mixtures are found in a remarkable correlation. In particular [22], in a room-temperature discharge in the  $30$  sccm  $\text{Ar} + 1.2$  sccm  $\text{SiH}_4$  mixture at the  $12$  Pa total pressure, the  $70$  ms interval appears to be sufficient to detect the  $2$ – $3$  nm-sized crystallites in the plasma.

Another interesting feature is that the intensity of the  $40.68$  MHz nonlinear signal after  $200$  ms diminishes linearly, revealing the linear character of the dust growth at later stages. On the other hand, the size of the initially formed particles remains constant during the first phase of the particle growth, when their number density increases up to a critical value (about  $10^{11}$ – $10^{12}$   $\text{cm}^{-3}$ ) for the coagulation phase to start. Furthermore, the observed drastic decrease in the amplitude of the nonlinear signals can be attributed not only to the higher resistance of the dust-loaded plasmas but also to the drop of the electron density as a result of the electron capture by the dust grains.

We emphasize that the above method is non-perturbative, with a temporal resolution in the microsecond range, very easy to implement, and can thus be used in industrial plasma reactors. For further details, the reader can be referred to the original work [22].

Note that even though the laser light scattering methods can be successfully used to obtain the in situ information on the growth processes and the spatial distribution of fine particles, the information regarding the size and the number density of the dust particles requires certain assumptions about the particle size distribution and the refractive index. Thus, there are problems with quantitative in situ measurements of the particle size distributions. Recently, promising results on the particle size distribution measurements at low pressures using a differential mobility analyzer (DMA) system have been obtained [61]. The DMA was coupled to a PECVD plasma reactor, where tetraethylortosilicate (TEOS) and oxygen were used as the reactants for the amorphous silica ( $\alpha$ -SiO<sub>2</sub>) film growth. The reactor was equipped with a carbon film-coated electrostatic collector of charged particles, the latter were further analyzed by the TEM.

Generally, the dust mobility measurements were carried out by applying a variable voltage to the collecting electrode of the DMA. Only the charged particles with the electrical mobility controlled by the applied voltage, can successfully pass through the slit in the collecting electrode. The mobility distribution of the charged particles was obtained by measuring their total charge using a Faraday cup electrometer [61]. In this way, the particle size can be estimated using conventional relationships between the particle mobility and the voltage applied to the DMA. This methods provides a very good qualitative agreement (with a typical discrepancy within 14–50%) between the particle sizes (in the few tens of nanometres range) obtained via the DMA and TEM [61].

Another apparent challenge in the characterization of nano-particles in reactive plasmas is to perform a real-time compositional analysis of small particles [62]. For instance, a CW laser can be used to sense a particle and fire a pulsed light. Following the laser ablation process, a complete mass spectrum of the resulting ions from a single particle was detected with a time of flight mass spectrometer. The apparent disadvantage of this method is that only particles with a size of  $> 200$  nm scatter enough light to be detected. Therefore, smaller particles cannot be detected in this way. With some modifications and without a CW laser, this technique was shown to be capable of in situ analyzing the chemical composition of the particles ranging in size from 20 nm to  $> 10$   $\mu$ m in air [62]. It is remarkable that the system can be straightforwardly adjusted to the analysis of the submicrometer and nano-sized particles in high pressure low-temperature plasmas [62].

A least direct but also quite reliable method of particle size detection is based on the use of the particle-size dependent dispersion of dust-acoustic waves [63]. Specifically, the dispersion characteristics of the dust acoustic waves (DAWs) during the nucleation phase have been analyzed. It is shown that the dispersion properties of the dust-acoustic waves depend sensitively on the particle size  $a$ . In particular, a size-dependent momentum relaxation frequency of nanoparticles, entering the dispersion relation of the DAW, can be presented as

$$v_D(a) = \frac{27}{52} \pi a^2 \frac{m_n}{m_d(a)} n_n v_{Tn} ,$$

where  $m_n$  and  $m_d$  are the masses of the neutrals and the nanoparticles, and  $n_n$  and  $v_{Tn}$  are the densities and thermal velocities of the neutral gas atoms/molecules, respectively. In the case of particle generation in silane plasmas, a Si<sub>m</sub>H<sub>n</sub> particle with the radius of  $\sim 1$  nm usually consists of approximately  $10^3$  atoms. In this case the composition ratio of Si to H atoms is  $\sim 3 : 4$  [64]. The

particle mass entering the expression for the momentum relaxation frequency is thus

$$m_d(a) = 10^3 \left( \frac{3}{4} m_{\text{Si}} + \frac{4}{7} m_{\text{H}} \right) a \text{ [nm]} ,$$

where  $m_{\text{Si}}$  and  $m_{\text{H}}$  are the masses of the silicon and hydrogen atoms, respectively [64]. Furthermore, it was demonstrated that the measurements of the dust acoustic speed should enable one to accurately characterize the size of monodisperse nanoparticles.

It should be noted that the Quadrupole Mass Spectroscopy has already been used for in situ analysis of hydrogenated nanophase silicon powders and can also be used to detect various  $\text{Si}_x\text{H}_y$  neutral and positively charged radicals that play a crucial role in fine powder growth processes [65]. For instance, typical QMS spectrometers with the range of 200 amu can accurately detect higher-silicon radicals  $\text{Si}_6\text{H}_x^{0,+}$ , where superscripts “0” and “+” denote neutral and positively charged states [65].

Finally, we stress that in the above we have focused on the fine particle growth and associated phenomena in low-temperature processing plasmas. For the peculiarities and fascinating details of dust grain growth in astrophysical plasmas the reader can be referred to a recent detailed review on this matter (see [66] and references therein).

### 3. Technological aspects of clusters and particulates in complex ionized gas systems

In this section, we review various technological implications of fine solid particles in chemically active plasmas, including deleterious (such as the process contaminants in the semiconductor micro-fabrication and safety hazard for the future fusion reactors) and useful (building units and functional embedded particles for various thin film deposition and nano-assembly processes, etc.) aspects. For a number of years, the plasma-grown powder particles have been deemed as unwelcome process contaminants in the semiconductor industry. Indeed, the grains with the sizes comparable with the typical feature sizes of the integrated circuitry elements caused line and interconnect shorts thus irrecoverably compromising the entire semiconductor wafer manufacturing process.

Therefore, a number of remediation methods have recently been developed aiming to remove the powder particulates from the processing volumes or suppress the dust growth at the initial stages (Section 3.1). Meanwhile, radioactive nuclear-induced dust has recently become a major concern for the safety of operation of the future fusion reactors. The physical mechanisms of the origin of and the major problems associated with the radioactive dust in the fusion reactors are discussed in Section 3.2. On the other hand, nano- and micron-sized clusters and particulates have recently attracted a remarkable interest for a number of applications discussed in Sections 3.3–3.7. The examples of the existing and potential applications include the self-assembly of various carbon-based nanostructures, deposition of nano-structured amorphous silicon films for solar cell manufacture, embedded particles for functional coatings, and many others.

#### 3.1. Particulate powders as process contaminants and remediation methods

We recall that our aim here is to review dynamic processes in chemically active complex plasma systems presently used by the microelectronic and other industries, e.g. for manufacturing advanced

semiconductor microchips and more complex integrated devices. Such systems are prone of fine particles, ranging in size from few nanometers to tens of microns [67]. As a result of intensive research efforts of the last decade, it was proven that the particulate matter appears in ultra-large scale integration (ULSI) fabrication processes not because of the dust remaining in the clean rooms, but emerges as a result of numerous chemical and physical processes in the ionized gas phase. The fundamental processes of the particulate formation include but are not limited to the gas-phase polymerization leading to creation of protoparticles (large molecules), release of atoms/radicals of the substrate/wall material as a result of reactive sputtering, self-organization of the atomic/molecular matter into larger clusters, typically in the nanometer range, and coagulation of fine particles into larger particulates, with the size ranging from tens of nanometers to few microns.

Presence of the solid particles in processing volumes inevitably results in compromising the product yield, e.g. limitations to plasma production of amorphous silicon ( $\alpha$ -Si:H) devices. Indeed, particles with sizes comparable to the ULSI feature size can cause the line shorts and have been termed in the literature as the “killer” particles. Moreover, dust contamination can result in pinholes, delamination and interconnection shorts or opens in ULSI circuits. Data storage disks can also be affected by read–write errors, damaged sectors, and total failure caused by excessive powder contamination. About 10 years ago, when the average feature sizes of ULSI circuits were in the micrometer range, nanoparticles appearing in the discharge volume, were simply too small to be of any concern for the semiconductor manufacture. On the other hand, an efficient solution for the contaminant micron-sized particles was found to confine them in the near-wafer areas, and subsequently remove them from the processing volume by direct pumping, gas flows or other simple means. Efficient particle confinement was possible due to the large sheath (near-wafer) potentials in capacitively coupled plasma (CCP) reactors, which were used as benchmark plasma processing tools in microelectronic industry at that time.

In the last few years, the situation has changed. First, the current typical ULSI feature sizes shrunk to 0.13  $\mu\text{m}$ , and it is expected that by 2010 they will be as small as 40–50 nm [68]. Hence, even nanometer-sized particles have to be considered now as the “killer” particles in the semiconductor technology. Secondly, the capacitively coupled RF discharges have been widely replaced by inductively coupled plasma (ICP) reactors featuring higher plasma densities and process efficiency. Unfortunately, the particle trapping capacity of ICPs is relatively weak due to smaller sheath potentials, which can result in the uncontrollable fallout of even nano-sized particles onto the wafer. Thus, the existing solution based on the discharge trapping capacity is unlikely to work in the near future, and the problem of removal of nano-sized particles from the discharge volume or controlling their growth is becoming critical for the semiconductor industry. If the problem is not solved within the next couple of years, development of the next generation of the integrated circuits can be substantially compromised [69].

Several aspects of the plasma-process-induced particle contamination have been discussed in [70], where was noted that fluorine-containing gas mixtures produce fewer particles during the silicon etching process than chlorine or bromine-containing gases do because of the generation of high-pressure volatile etch products in the fluorine-based plasmas. On the other hand, recent detection of fine powders in fluorocarbon gases discussed in detail in Section 2.1.3 suggests that a certain dust-fallout prevention strategy should also be implemented by the microelectronic industry during the fluorine-based silicon etching processes. As was mentioned in [70], the plasma etching tool design, especially the electrode, significantly affects the overall cleanliness of a plasma tool.

It is not thus surprising that during a number of years the main goal of early dusty plasma investigations was to obtain a good control of contamination in plasma-processing reactors, either by eliminating dust particles from the gas phase or by preventing them from getting into contact with the wafer surface. As a result of numerous studies of dust dynamics in plasma reactors [71–73] contamination by relatively large ( $> 100$  nm) particles at present is well under control.

Generally, dust contamination control includes the proper operation of plasma shutdown (e.g. managing the sequence of discharge “on” and “off” cycles as will be discussed below), the appropriate process chemistry (e.g., the powder growth suppression) and plasma tool (e.g., the electrode shape) design [70]. Particles suspended near the plasma/sheath boundary can be removed before shutting the plasma process off by using the proper changes in RF power, gas flow, and magnetic field near the end of the plasma etching stage. Furthermore, the fine particles can be purged to the pump line during the process by a proper tool design, whereas the dust generation and growth can be impeded or disrupted by controlling the number densities and reactivities of the dust growth precursor species [70].

More specifically, in order to minimize the deleterious effect of dust particles on the thin film deposition and etching, it is important to develop either new processes avoiding dust generation or to develop process cycles in dusty plasmas without contamination over the relevant substrate regions, which are sensitive to the dust fallout [74]. There are several options in this regard: intelligent arrangement of electrodes and substrate holders, construction of special electrode shapes (e.g. “grooved” electrodes) [71,72], square waveform plasma modulation [21], fast transport regimes of the reactive species, external electrostatic forces (e.g. Langmuir Probe induced) [75], additional forces based on the neutral drag (gas flow) or the thermophoresis (temperature gradient) by external heating [76] or the photophoresis (laser irradiation) [77].

The basic idea for introduction of the square wave plasma modulation with the “on-off” cycles is that the small and negatively charged dust precursors are not allowed to grow in size and concentration during the “on” sequence and leave the plasma volume during the “off” sequence. Introduction of the special electrode shapes and additional forces usually results in changes of the equilibrium particle trapping positions. Using the above methods, dust can be effectively pushed outwards the sensitive areas of the plasma reactor.

It is interesting that even after the fallout from the gas phase, the dust grains can still be removed from the surface, as was shown in a series of elegant experiments [78]. In situ laser light scattering measurements have shown how the particulates can be shed from the chamber walls. Using a test surface coated with micron-size particles, it was found that when the plasma is turned on, particulates are released rapidly, and when the discharge is turned off, the above release stops. Thus, the plasma exposure is likely to cause the particulate shedding. Furthermore, the rate of the dust shedding increases with the plasma density. Physically, the grains become negatively charged due to the electron and ion fluxes and are then pulled off the surface by the electric field in the plasma sheath. It was also shown that an individual dust grain is shed when its charge becomes sufficiently negative [78].

Recently, a quite similar principle has been adopted to remove the fallen particles from the semiconductor wafers by using a low-power discharge in the plasma processing tool and direct mechanical agitation of the dust grains on the wafer surface [79]. The actual process included two steps, the first one being a mechanical agitation of the particles by piezoelectrical excitation of ultrasonic surface vibrations. Once the vibrational forces overcome the sticking forces, the powder particles can be removed from the surface, acquire a negative electric charge, and eventually be directed to the pumping line by the appropriate manipulation of the discharge power [41,79].



One of the key problems of the dust confinement is to develop the appropriate particulate traps. The latter can naturally emerge near various 3D physical and electromagnetic structures in plasma processing discharges, such as internal antennas (or coils), gas injection nozzles, sub- or super-substrate topography elements, as well as single-sided vacuum pump ports. These structures contribute to azimuthal asymmetries in reactant fluxes and can also create efficient dust particle traps due to significant distortions of the electromagnetic pattern at distances well exceeding the geometrical sizes of the internal structures [80].

Meanwhile, many simple physical methods for removing charged particles from RF processing plasmas have been proposed. Generally, most of the methods adopt control of the particle dynamics by varying the input power and the working gas pressure, and applying external electrostatic or magnetic fields [81]. Variation of the RF power affects the depth of the potential wells, where the particles can be trapped. Furthermore, the power input controls the shape and location of the traps, as well as the profile of the plasma potential. Likewise, if the gas pressure increases, the sheath edge moves closer to the substrate being processed. Since the particulate traps are usually formed in the vicinity of the plasma sheaths, the dust particles will thus be confined closer to the substrate at elevated pressures.

On the other hand, a negatively biased Langmuir probe can repel the negatively charged dust grains, and attract them when the bias polarity is reversed. The probe can also distort the sheath edge when the tip resides within the sheath. Meanwhile, external magnetic fields can change the characteristics of the particle traps and also exert additional forces on the charged dust grains. Specifically,  $\mathbf{E} \times \mathbf{B}$  drift in the crossed electric and magnetic fields has been applied to remove silicon particles grown in silane plasma discharges used for preparation of large-area uniform hydrogenated amorphous silicon thin films [82]. A direct correlation between the magnitude of the external magnetic field and the efficiency of dust removal was also established [82]. Particle confinement in the particle traps in processing plasmas can also be controlled by the ultraviolet (UV) radiation, which normally reduces the negative equilibrium charge on fine particles and modifies the prevailing force balance [83]. In this article, the options to facilitate the removal of the contaminant particles from the traps by using the UV radiation are also investigated.

It was also proposed to use the thermophoretic force (experimentally implemented by an additional heating of the grounded electrode in parallel plate plasma reactors) to drive nano-sized clusters towards the RF electrode (away from the processing side). We note that this method works well even for ultra-small particles above a few nanometres in size. Alternatively, growth of large size clusters can be significantly suppressed by an extensive dilution of silane by hydrogen (e.g.  $[\text{H}_2]/[\text{SiH}_4] > 20$ ). In particular, it was found [84] that the pulse discharge modulation combined with the electrode heating is very efficient in suppressing the nanocluster growth. Most recently, the reactor, which suppresses the growth of clusters both by the thermophoretic force and by the gas flow and evacuation without stagnation, has been newly developed for the manufacturing of the device-grade amorphous silicon films [85].

### 3.2. *Dust particles in fusion reactors*

In this section, we consider the radioactive dust as a major concern for the safety of operation of fusion devices. It has been common for a number of years that small dust particles do exist in magnetic confinement fusion devices [86,87]. Their origin is mostly due to the plasma–surface

interactions. The radioactive dust contains large amounts of hydrogen isotopes, with up to 50% in tritium. The main consequence of the dust contamination is the safety hazard due to the high chemical reactivity and the mobile tritium inventory. It can also affect the plasma performance and stability, as well as the operation of fusion devices.

Physically, tritium, incorporated into the carbonaceous dust, undergoes radioactive decay, and this can lead to the dust charging and the formation of the nuclear induced plasma. In the plasma, charged dust particles can be transported and levitated. There are thus two major sets of problems related to the particulate generation in fusion devices. One of them is related to the safety of operation of the fusion reactor, the other being related to the plasma parameters and stability. Specifically, the dust-bound tritium inventory appears to be a major safety concern for future fusion reactors. The main problem in this regard is that the dust cannot be re-processed together with tritium, thus increasing the site inventory. Dust is also a potential carrier of tritium in the case of a severe reactor failure. Furthermore, if the reactor cooling systems are damaged, large amounts of hydrogen can form an explosive mixture with oxygen from the environment.

The key point of another aspect is that large amounts of dust can accumulate at the bottom of the device (which is usually a divertor area in tokamak and stellarator devices). Dust accumulation can impede the heat transfer to the cooling surfaces and can also damage the special gaps for the electrical insulation or thermal expansion purposes. Indeed, such layers can sublime when exposed to huge heat loads. On the other hand, this can lead to a source of plasma impurities adversely affecting the plasma parameters and stability.

It is thus reasonable to pose the following question: what are the sources of the origin and formation mechanisms of dust particles in fusion devices? It is notable that significant parts of the plasma-exposed surfaces (e.g. limiters, divertors, antennas for RF heating) are often coated with carbon-based materials, such as graphite or carbon fiber composites. However, carbon suffers from high erosion rates due to the intense physical sputtering and chemical erosion. As a result of the exposure to chemically active hydrogen, several forms of hydrocarbon are released from the surfaces into the plasma edge where they interact with the plasma and could be ionized or dissociated. The edge-localized modes (ELM) and the pressure-driven instabilities or disruptions (quick and uncontrollable discharge quenching that leads to the deposition of the plasma-stored energy onto the surface) at the plasma edge can lead to excessive heat fluxes onto divertor surfaces. In the International Thermonuclear Experimental Reactor (ITER) device, the thermal load from a disruption is estimated to be  $100 \text{ GW/m}^2$  during 1 ms. For this reason, many recent discharge disruption experiments included the dust as a critical component.

Thus, a detailed understanding of the mechanisms responsible for the particulate production from plasma–surface interactions in fusion devices is required. Moreover, this area has recently been highlighted by the US Fusion Safety Program as one of the priority areas of research. Recently developed plasma/fluid and aerosol models of disruption simulation experiments in the SIRENS high heat flux facility integrate the necessary mechanisms of plasma-material interactions, plasma and fluid flow, and particulate generation and transport [88]. The model successfully predicts the size distribution of primary particulates generated in SIRENS disruption-induced material immobilization experiments [88].

Meanwhile, the estimated erosion rate of the carbon material can be quite high, up to  $2 \times 10^{21} \text{ m}^{-2}/\text{s}$  in the TEXTOR (Tokamak Experiment for Technology-oriented Research) fusion device. The eroded material is usually redeposited in a form of carbon-based layers in the areas of lower heat fluxes,

and contains a large amount of radioactive hydrogen isotopes. The dust can thus become radioactive and can carry a large proportion of the tritium inventory. Above all,  $\beta$ -decay of tritium can lead to the dust charging and formation of the nuclear-induced plasmas. This can certainly affect the initiation phase of the thermonuclear plasma. Article [87] gives a simple estimate for the charge that can be accumulated by a carbon-based particle due to the radioactive decay of tritium (half-lifetime of  $t_{1/2} = 12.3$  years with the maximum electron energy of 18.6 keV). Specifically, the number of  $\beta$ -decays in a 5  $\mu\text{m}$ -sized carbon particle carrying 0.4 hydrogen isotopes (with 50% tritium) per carbon atom, can reach up to  $5 \times 10^2$  per second. Assuming that all  $\beta$ -electrons leave the particle, the secondary electron emission yield of unity, and the mean charge lifetime of 1 s, one can obtain that such a particle can accumulate a positive equilibrium charge of up to 500 elementary charges. The electric field of 38 V/cm would be sufficient to confine such a particle near the surface.

The size of particulates in fusion devices varies in broad ranges, from a few tens of nanometers to several millimeters. The estimates of the total amount of redeposited radioactive dust show that large amounts up to a few tens of kilograms can be generated in the ITER device [87]. The dust composition is mostly carbon but may also include all other materials used inside the vessel or for wall conditioning purposes (e.g. B, Si). In TEXTOR experiments, a large number of almost perfect metallic spheres with the diameters from 10  $\mu\text{m}$  to 1 mm has been identified. The most likely formation mechanism is the reactor wall flaking (one of the heterogeneous processes discussed in detail in Section 2.3) with the subsequent coagulation of metal atoms on hot and non-wetting graphite surfaces. It is also interesting to note that very small, sub-100 nm carbon particles can be formed in the fusion devices as a result of CVD processes in the carbon vapor. Several studies report formation of small globular clusters, fullerene-like materials, etc. In TEXTOR device, agglomerates of individual particles of about 100 nm diameter have been observed. Another possible mechanism is the dust growth in the scrape-off layers (detached plasmas in the proximity of divertors and limiters), where the conditions are quite similar to those in chemically active low-temperature hydrocarbon plasmas (see Section 2.1). Under such conditions, the growth will probably proceed via negative hydrocarbon ions and multiple ion-neutral reactions.

Large particles introduced into the plasma can also induce a disruption. However, usually if the discharge is fully developed, their effect on the discharge performance is weak. However, if the particles pre-exist in the vessel prior to the plasma start-up, they can release significant amounts of impurities into the plasma volume. Indeed, the intensive impurity radiation is often observed during the start-up phase and may be due to the levitated dust.

It is worth noting that the electron number density of the nuclear-induced plasmas is typically about  $5 \times 10^9 \text{cm}^{-3}$ . When the gas pressure in the vessel increases to about  $10^{-3}$  mbar, the plasma breakdown takes place and the fast  $\beta$ -electrons from T-decay ionize the gas along their track (of the order of  $10^3$  m at this pressure). In this way, about 500 electron–ion pairs per  $\beta$ -electron can be formed. Furthermore, it has recently been shown [89] that a plasma induced by radioactive particles can be formed in a simple parallel plate model reactor configuration even without any magnetic field. Meanwhile, levitation of solid particles and even formation of ordered dust structures have been observed [89]. Ref. [89] also contains the extended discussion of the possible methods to remove from or minimize the consequences of the radioactive dust in the fusion reactors. It is interesting that using the thermophoretic force (in a manner similar to what was discussed in Section 3.1) can be a viable route for the removal of the radioactive dust [90]. Finally, we note that despite a notable recent progress, the problem of the dust charging by the nuclear decay and

generation of the nuclear induced plasmas still remains an unsolved puzzle for the nuclear fusion community.

### 3.3. *Nanoparticles as precursors for plasma enhanced assembly of carbon-based nanostructures*

In this section, we address the issues relevant to the role of the plasma-grown nano-sized particles in the synthesis of various carbon-based nanostructures. One of the most common nano-structured organization of carbon-based materials are so-called carbon nanotubes (CNT). The CNTs were discovered in the early 1990s [91] and represent a new and extraordinary form of carbon. Depending on chirality and diameter, CNTs can either be metallic or semiconductor and thus can be useful for fabrication of metal–semiconductor and semiconductor–semiconductor junctions. Furthermore, they exhibit extraordinary electrical and mechanical properties and offer remarkable potential for revolutionary applications in electronic devices, computing and data storage technology, sensors, composites, storage of hydrogen or lithium for battery development, nanoelectromechanical (NEMS) systems, and as tips in scanning probe microscopy for imaging and nanolithography. Many common recipes for the synthesis of various carbon-based nanostructures are based on the plasma-enhanced CVD using the surface catalysis [92]. Note that fine particles containing single walled carbon nanotubes were originally synthesized using a carbon-arc reactor with the carbon cathode containing iron and observed in soot-like deposits on the chamber walls [93]. The length of single-walled CNTs synthesized by arc discharge methods is usually less than several hundred nanometers. Nevertheless, the nanotubes can also be grown up to a micrometer length with special arrangements for longer process duration.

It is also remarkable that different transitions between various forms of organization of nano-structured carbon are due to the reorganization of carbon-based nano-sized clusters. Furthermore, if the clusters were actually grown by the PECVD, the processes in the ionized gas phase can also critically affect self-organization of nanostructured carbon. For example, under external irradiation, carbon nanotubes can transit to the diamond state through the intermediate carbon nano-onion state [94]. The transition from the nanotube to the nano-onion structure is accompanied by a structure collapse of the tube and reorganization of the carbon clusters. This further supports the idea that nano-clusters are indeed the building units for the fabrication of various nanostructures, including the carbon nanotubes. Here we refer the reader to further discussion of the nano-cluster route of nano-materials fabrication in Section 3.5. However, the dynamics of the crystallization behavior [95] of CNTs in various (including plasma-based) CVD systems still remains a challenge. One of the common nucleation models invokes a rearrangement of the metal (e.g. Fe, Ni, or Co) catalyst from a pre-deposited nano-layer into round nanoparticles, which size appears to be a decisive factor in the nanostructure nucleation [96]. We thus remark that CNTs usually grow within narrow range of substrate temperatures, promoting the required reorganization of the catalyst layer.

We need to keep in mind however that carbon-based nanostructures is a separate and quickly emerging area of the solid-state physics and materials engineering, and thus refer the reader to the available literature (see e.g. Refs. [97–99] and references therein). Moreover, even a discussion of various plasma-based methods of the nanostructure fabrication is worth of a special review (see e.g. [100] and references therein) due to the large and continuously increasing number of publications, and we will just mention only a few relevant works. In particular, well-aligned CNTs were grown on metal nanoparticle catalyst precursors exposed to low-temperature hot-filament, microwave, and

inductively coupled plasmas of several PECVD systems [101,102]. Our specific aim here is to discuss the details of the plasma-assisted growth of carbon-based nanostructures, with the most relevance to the complex plasma systems reviewed.

As was shown in a series of experiments [103], by injecting metal nanoparticles into a microwave surface-wave sustained plasma reactor one can grow various carbon-based nanostructures directly in the reactor volume, which is quite different from many conventional methods involving solid substrates. The microwave plasma was generated with 300–800 W 2.45 GHz microwave powers deposited into the 8 cm in diameter reactor chamber through a number of slots above a dielectric window (slot-excited or surface-wave sustained plasmas [104]). The surface wave plasmas were sustained in a methane-hydrogen gas mixture within the pressure range from 1 to 20 mTorr. One of the side ports of the chamber was designed to inject fine metal particles. Particulate clouds were monitored using light scattering of a laser beam directed from another side port. A biased electrode positioned in the lower part of the plasma glow was designed to suspend fine metal particles to enable efficient gas-phase growth of carbon nanostructures. The former also acted as a collector of nano-materials in a powder form. At lower powers, the injected nickel ultra-fine particles formed a cloud in the plasma bulk between the chamber window and the electrode. As the power increased, some of the particles escaped the main cloud and moved downwards to the electrode, presumably due to the increased ion drag force (which is higher at higher RF powers and plasma densities, see Section 4.3), where they were suspended (due to the balance of forces acting on fine particles, also considered in Section 4.3) during the nanostructure growth phase with an approximate duration of 20 min. At higher microwave powers, tubular structures resembling carbon nanotubes were grown in the gas phase and further dropped on the particle collector when the generator was turned off.

The above experiments support the idea that fine nano-sized particles grown or externally dispensed in the plasma reactor volume can act as the gas-phase catalyst particles that can support the growth of the carbon nanotube-like structures in the ionized gas phase alongside with the most commonly adopted scenario of the CNT assembly on rough catalyzed surfaces. Recently, this possibility has been supported by the kinetic theory of the carbon nanotube nucleation from graphitic nanofragments [105]. In particular, it was shown that a carbon nanosheet wrapping around amorphous carbon, fullerene-like, and carbonized metal catalyst nanoparticles that are present in the gas, is the first step in the CNT nucleation process. The proposed mechanism of CNT nucleation thus invokes the so-called nanosheet–nanoparticle collision pathway, which is an alternative to the conventional carbon segregation pathway. Certainly, there is a room for speculations whether this mechanism is applicable or not for the PECVD systems with the plasma-grown nanoparticles, which is apparently an interesting but yet unresolved problem.

Another issue in the PECVD of carbon-based nanostructures (CNSs) is the actual role of the gas-phase grown nanoparticles discussed in detail in Section 2.1.2. A relevant observation from the growth of the CNSs in the  $\text{CH}_4 + \text{H}_2 + \text{Ar}$  [34] and other  $\text{CH}_4$ -based reactive chemistries [100,106,107] is that the CNSs growth is accompanied by a very strong methane conversion (the gas feedstock dissociation) of up to 95% and even higher. It is remarkable that there is direct evidence that in the dust-growth regimes, the methane dissociation can be enhanced by a factor of 6–8 as compared with the pristine plasma at the same operating conditions such as the pressure and the RF power [41]. The reason behind this is a remarkable rise of the electron temperature due to the dust generation (discussed in detail in Section 2.2), which increases the rates of dissociation of methane molecules. We emphasize that this effect is a notable illustration of the enhanced chemical efficiency



of dust-contaminated plasmas. Further examples of the outstanding chemical efficiency of dusty plasmas can be found in [41]. It is also interesting to point out that in many conventional thermal CVD processes the feedstock gas does not dissociate in the gas phase even at the temperatures commonly used for the single- and multiwalled carbon nanotube growth ( $\sim 800$ – $1000^\circ\text{C}$ ), and the nanotube production is entirely due to surface reactions of the  $\text{CH}_4$  molecules on the catalyst surfaces [106]. In contrast, significant amounts of acetylene, ethylene, a variety of  $\text{C}_x\text{H}_y$  radical and cation species, all of which contributing to the carbon nanotube assembly, are generated in low-temperature plasma reactors [100,106].

We note that PECVD of the carbon nanostructures is a complex process that involves numerous transformations of neutral and charged radical species both in the gas phase and on the surfaces of catalyzed substrates. A very interesting observation that favors the possible role of the dust grains grown in the ionized gas phase in the nano-scale assembly is that large amounts of the acetylene monomer  $\text{C}_2\text{H}_2$  are generated both during PECVD of CNSs [33,34,100,106,107] and the dust growth in  $\text{Ar} + \text{CH}_4$  plasmas [32]. Indeed, it has also been reported elsewhere that concentration of the  $\text{C}_2\text{H}_2$  species is an important factor for initiation of the dust formation [29,28]. Furthermore, in saturated and unsaturated hydrocarbon plasmas the polymerization process is triggered and proceeds at a higher rate after large enough acetylene concentrations were formed [32]. For further details of the dust grain nucleation process in the argon–methane and argon–acetylene plasmas refer to Section 2.1.2 and the original works [31,32].

One of the critical problems in the kinetics of the plasma-based growth of various CNSs is whether the gas-phase-grown carbon nanoparticles participate in the nucleation process as catalyst particles, nano-sized building blocks of the CNSs, valuable morphology elements of the nanostructured carbon films, or are just deleterious contaminants that can compromise the entire CNS assembly process. The answer to this question still remains open and will certainly depend on specific conditions of an experiment, including the gas feedstock composition, the RF power and gas pressure ranges, the substrate heating and biasing conditions, etc. Nevertheless, one of the clues for the solution of the above problem is the fact that the CNSs grown by the PECVD methods are mostly aligned vertically due to the near-substrate electrostatic fields [108], which is a preferential direction for their growth. Furthermore, the electrostatic fields near sharp tips of many CNSs (e.g. CNTs) certainly modify the deposition conditions of most of the charged particles in the plasma (including the radical and ion species, and fine powder particles) leading to the selective deposition of them onto the CNS tips rather than the lateral surfaces and the inter-structure “valleys” [109]. For example, for a carbon nanofiber with the radius of  $r_0 = 20$  nm protruding from a biased ( $V_s = -500$  V) substrate surface, the field strength at the tip  $F_{\text{em}}$  is estimated to reach  $5 \times 10^7$  V/cm from a simple calculation widely used for the CNT field emitter nanotips  $F_{\text{em}} = V_s/\alpha_g r_0$ , where the geometrical factor  $\alpha_g \approx 5$  [109]. The presence of strong electrostatic fields near the surface of CNTs does require understanding of the capacitive issues of the carbon nanotube-based systems and their ability to charge-up, store electric charge and dynamically respond to external variable fields [110]. This is very important for a number of industrial applications of CNTs as scanning probes, non-volatile memory cells, and nanoelectronic devices. In this sense the notion of the electrostatic charging of carbon nanotube-like structures is very similar to that of dust grains considered in Section 4.1.

It is important to note that surface-based methods of CNT growth usually require substrate temperatures of the order of  $600$ – $800^\circ\text{C}$ . Thus, accurate control of the gas (and hence, the catalyst particle surface) temperature by varying the RF/microwave power could be instrumental in the challenging



synthesis of nanostructured carbon powder material in the ionized gas phase by using the intrinsic ability of low-temperature plasmas to levitate colloidal particles in the near-electrode areas. It is notable that there are many forthcoming challenges in the direction of the plasma-based production of various carbon nanostructures listed in a recent review [100] (see also references therein). Here, we would pose one more important question: what is the role of the plasma-polymerized nanoparticles and plasma polymerization processes in the assembly of various CNSs? This apparent puzzle is a further argument for the need of intensive theoretical and experimental research in the area in the coming years. Finally, we believe that research in this direction should certainly continue in the near future to demonstrate the outstanding potential of the complex plasma systems in manufacturing of various nano-structured materials.

### 3.4. Nano-powders in PECVD of nanostructured silicon-based films

Design of efficient PECVD reactors for the coating of large-area glass plates ( $\sim 1 \text{ m}^2$ ) in the flat panel display or solar cell manufacturing technologies raises a number of challenging issues in physics, chemistry, materials science, mechanical, thermal, and electrical engineering. In such reactive discharge plasma glows, excited at the RF frequency from 13.56 MHz to  $\sim 100$  MHz, the uniformity of the thin film deposition is controlled by the gas flow distribution, as well as the local plasma perturbations, and other factors. Moreover, the film properties critically depend on the plasma chemistry involving formation and trapping of fine particles triggered by the homogeneous nucleation, the neutral radicals contributing to the film growth, the effect of ion bombardment, and other processes [111]. In particular, plasma assisted CVD of the amorphous silicon (*a*-Si) films is one of the most advanced methods of fabrication of thin film transistors, flat panel displays, solar cells, and other opto-electronic devices [112]. However, the characteristics of the films, and hence the deposition techniques are to be continuously upgraded in line with the increasing demands of the emerging optoelectronic industry.

It has recently been reported that several parameters (including the transport and stability) of the *a*-Si films prepared in the powder generating regime can be significantly improved as compared to those achievable in other regimes [113–115]. It is apparent that this improvement can be attributed to silicon-based nanoparticles nucleated and grown in the chemically active environment of  $\text{SiH}_4$  plasmas. Conventional thin film characterization routines do confirm that the films grown in the powder-generating regime have nano-scaled structure featuring ordered arrays of silicon nanocrystals [115]. Therefore, the efficient fine powder control is crucial for the development of viable methods of the nanostructured films deposition.

Article [116] reports on the efficient PECVD of nanostructured Si-based films in highly hydrogen-diluted silane discharges sustained at higher working pressures that promote the low ion bombardment conditions for the better surface activation and/or passivation. In this series of experiments, high-quality nanostructured silicon films with low density of states and high mobility-lifetime product were fabricated. Presumably, the film growth proceeded via gas-phase nanopowder formation and subsequent embedding of fine particles in the amorphous silicon matrix. It is worth mentioning that since in the low-pressure plasma glows the dust particles usually acquire the negative electric charge (see Section 4.1), one can predominantly deposit either positive ions/radicals or anions/dust particles by reversing polarity of the substrate bias. Specifically, the positive bias favors embedding of the gas phase-grown grains into the matrix on the substrate, while the negative one strongly impedes

this process. It is remarkable that the films fabricated under the condition of the positive bias feature higher density, smoother surface nano-morphology, more compact arrangement of the grains over the surface, as compared to the films deposited at the negative DC bias. In the latter case, the films have a pronounced porous structure. Moreover, the elements of the surface morphology appear to be distributed randomly over the surface. Above all, the positive bias promoted clearly higher deposition rates.

From the device quality point of view, the incorporation of the silicon-based nanoclusters enlarges the optical bandgap as well as lowers the density of states of the film material. Therefore, the film fabrication process can be remarkably improved by the nano-sized particles grown in the plasma and capable of embedding into the films being grown. It is thus imperative to continue investigations of the underlying mechanisms of the dust-substrate interactions and the growth kinetic of the nanoparticle-incorporated films.

We emphasize that the nanostructured hydrogenated silicon films (*ns*-Si:H), also frequently termed in the literature as polymorphous (*pm*-Si:H), feature a high degree of the nano-crystallinity due to the incorporation of nano-sized (typically in the few nanometers range) crystallites grown in the ionized gas phase [117]. The term “polymorphous” applies for the silicon-based nano-materials that consist of a two-phase mixture of the ordered and amorphous silicon material [117]. A nanostructured amorphous *a*-Si:H matrix with the embedded silicon-based nanocrystallites grown in the plasma, is a typical example of a polymorphous thin film. To control the deposition rate and ensure the device quality of the nanostructured Si films, it appears instrumental to pre-set the plasma conditions to the powder-generating regime that enables a simultaneous deposition of the plasma radicals that contribute to the formation of the amorphous matrix and the ordered plasma-grown nanoparticles that act as the nanometer-sized highly-crystalline “dopant” particles. Furthermore, the resulting crystalline structure appears quite different from the diamond-like structure of the bulk silicon [117]. However, the fact that the Si nanoparticles appear as crystallites with a specific (usually *fcc*) crystalline structure under high argon dilution of the silicon carrier gas SiH<sub>4</sub> still warrants the adequate explanation.

It should be noted that article [117] provides a comprehensive review of the results on the deposition of the nanostructured silicon-based films and growth of freestanding nanoparticles in the presence of the powder particles in the discharge. For example, one research group reported the efficient deposition of polymorphous hydrogenated silicon films under the conditions of very low particle development, which usually implied high silane dilution in the hydrogen. However, the deposition temperature, the gas pressure and the RF power could be kept at low [118] as well as high [119] levels.

Meanwhile, other researchers managed to obtain high-quality *pm*-Si:H films from square wave modulated (SWM) RF plasmas in the presence of powder particles in the ionized gas phase [120]. Plasma modulation and gas temperature were changed to control the powder development pathway [120]. The square wave modulation of the RF plasma controlled the selective incorporation of nanoparticles into the film being grown. During the plasma-on time of the modulation cycle, an amorphous Si film is deposited onto the substrate and, at the same time, nanoparticles nucleate and grow in the ionized gas phase. During the afterglow periods, the dust grains leave the plasma and are deposited onto the amorphous Si film. Therefore, after a number of cycles, the final structure will consist of silicon nanoparticles embedded in the *a*-Si:H matrix [120]. On the other hand, freestanding nanocrystalline Si particles have also been generated in the experiments [121,122]. Typically, these experiments required high silane dilution in argon, moderate pressures, and high RF power. In these

and some other experiments the nanocrystals are typically in the range of 2–10 nm in diameter, whereas larger particles appear to be either amorphous or polymorphous. Recently, the successful use of the intermediate pressure (500–800 mTorr) inductively coupled plasmas to produce the single-crystal silicon nanoparticles with diameters between 20 and 80 nm have been reported [123]. Such nanoparticles are suitable as building blocks for various single-nanoparticle electronic devices. From these studies, one can infer the following trends. First, the particle concentration is roughly proportional to the silane partial pressure. Secondly, highly oriented single-crystal particles are favored by longer plasma-on times, higher power density, and higher total gas pressure. And finally, fractal agglomerates, or even dendritic or cauliflower structure particles are found at low discharge pressures and low input powers [123].

Meanwhile, the deposition rates can be efficiently controlled by enhancing or inhibiting the dust growth in powder-generating (such as silane-based) discharges. Recently, a model for high-rate film deposition from dusty RF discharges was developed [124]. In this work, particulate generation was considered as a multi-step process: generation of negative ions by electron attachment; clustering of negative ions; and growth of clusters by parent molecule addition. Estimates for the rates of dust formation and film deposition were made for gas mixtures of silane with dichlorosilane ( $\text{SiH}_2\text{Cl}_2$ ) and tetrafluorosilane ( $\text{SiF}_4$ ). It was shown that in this way the new growth techniques of amorphous, microcrystalline and polycrystalline thin films, with remarkably higher deposition rates, can be developed.

Furthermore, the introduction of  $\text{SiH}_2\text{Cl}_2$  correlates with the higher generation rate of dust precursors and is accompanied by an increase in the electron temperature presumably due to the loss of the low-energy electrons via the electron attachment (leading to an increase of the negative ion density) to the high-affinity chlorinated species. Likewise, small additions of dichlorosilane appear to be instrumental in the improvement of the overall film quality. Physically, termination of active bonds on the surface becomes more efficient once chlorine atoms become able to participate in this process alongside with hydrogen atoms. Hence, diffusion of film precursors such as  $\text{SiH}_3$  over the surface can be enhanced, which further results in the improved surface morphology and the film quality. Film precursors, binding and surface diffusion of various radicals, surface roughness evolution, and other aspects of hydrogenated amorphous silicon and other silicon-based films have been extensively discussed [125–127]. For further details of the effect of dust generation and electron attachment processes on the deposition rates of various silicon-based films, the reader can be referred to Ref. [124].

On the other hand,  $a\text{-Si:H}$  films deposited at the high deposition rates (which usually feature higher silane-related species  $\text{Si}_x\text{H}_y$  actively taking part in dust polymerization) often suffer from the pronounced photo-induced degradation. It has been reported that contribution of the  $\text{Si}_x\text{H}_y$  species is intimately related to the electron temperature in the discharge [128]. It was also demonstrated that the photostability of  $a\text{-Si:H}$  films can be drastically improved when the contribution of the  $\text{Si}_x\text{H}_y$  species to the film growth is low [128]. Therefore, reduction of the electron temperature in the plasma during the film growth is a key issue to improve the photoinduced degradation properties in the high-rate grown amorphous silicon films. Extensive theoretical efforts were made to link the electron temperature to the dust size and number density under conditions relevant to the experiments of Ref. [128]. The results of computation of the equilibrium electron temperature for the capacitively coupled plasmas of the RF hydrogen-diluted silane discharge [129] are displayed in Fig. 5. The computation parameters are: the gas pressure  $p_0 = 300$  mTorr, the neutral gas/substrate temperature

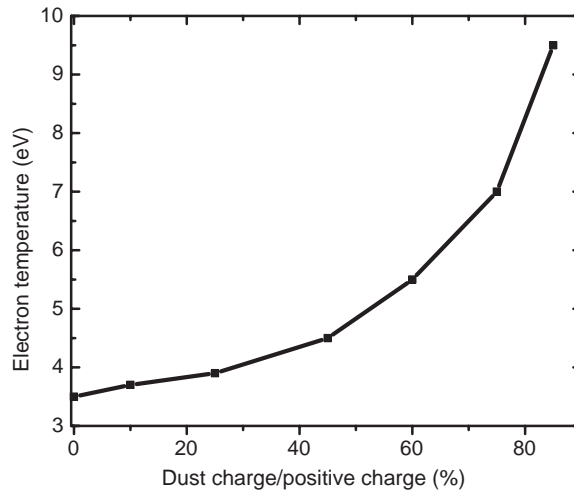


Fig. 5. Electron temperature versus dust charge proportion [129] for the representative parameters of the experiments of Ref. [128].

$T_n = 150^\circ\text{C}$ , the electrode radius and spacing of  $R = 13$  cm and  $L = 1.7$  cm (parallel plate geometry), respectively; the total number density of the positive ions  $\Sigma n_i = 10^{10} \text{ cm}^{-3}$ ; the dust number density  $n_d = 10^7 - 1.1 \times 10^8 \text{ cm}^{-3}$  and the dust radius  $a = 50$  nm. The equilibrium nanoparticle charge has been obtained from the balance of the microscopic electron and total ion currents onto the dust particles and in this particular example ranged from 76 to 83 electron charges. From Fig. 5 one can clearly see that an increase in the charge proportion on dust particles  $\xi_d = n_d Z_d / \Sigma n_i$  results in the remarkable rise of  $T_e$ , in this particular example from 3.5 eV to almost 9.5 eV. This is consistent with the results of modeling of the effect of fine particles on an RF discharge plasma [130–132]. The increase in the electron temperature is a consequence of the self-consistent response of the plasma that aims to minimize the electron/ion loss to the particles by enhancing the ionization process. More modeling results on the Si+H<sub>2</sub> dust-containing discharges can be found in [133]. In particular, it has been shown that the dust influences the electric field distribution through its charge and the plasma density through recombination of the positive ions and electrons at the grains' surfaces. Furthermore, the presence of dust enhances the deposition rate of the amorphous silicon because of the rise of the average electron temperature [133].

Another interesting aspect of nanoparticles in silane-based plasmas is that 30–50 nm-sized nanocrystals (identified by HR TEM) can be grown in the dual-frequency PECVD process of silicon oxides [134]. It was further noted that silicon-based crystalline nano-grains are usually formed inside the silicon-rich oxides.

Apparently, the controversy on whether the fine particles are favorable or deleterious for fabrication of the hydrogenated amorphous silicon films is definitely not over and a number of fascinating results is expected in the near future. For example, high-quality *a*-Si:H films can be grown under either cluster suppressing [85] or powder-generating [117] regimes. Nevertheless, it is certainly clear that fine powder particles do play an important role in thin film fabrication processes in silane-based (and other chemically active) discharges. On one hand, near the threshold of the powder generating

( $\gamma$ ) regime, dust particles originate and directly contribute to the high-rate film growth. On the other hand, higher silanes  $\text{Si}_x\text{H}_y$  have been evidenced to compromise the photostability properties of  $\alpha$ -Si:H films.

Particulate formation also elevates the electron temperature, which in turn affects the rates of the negative ion formation, the latter (e.g.  $\text{SiH}_3^-$ ) being precursors for dust polymerization in reactive plasma (see Section 2.1). Thus, the complex plasma system becomes dynamically and self-consistently coupled and further self-organizes into the states with higher electron temperatures that certainly affect the powder growth conditions. Therefore, chemically active plasmas do offer a great variety of options for thin film deposition. Specifically, one can deposit the films by predominantly using the atomic/radical units, which is usually the case in the regimes inhibiting significant dust growth. Alternatively, it appears possible to tailor the film deposition process in the dust-generating and high-deposition-rate regime.

### 3.5. High-rate cluster and particulate deposition on nanostructured surfaces: a new paradigm in thin film fabrication

Here, we discuss a new paradigm in the assembly of various nanostructured films that invokes a concept of the high-rate nano-cluster/particle deposition. In particular, the so-called charged cluster model (CCM) was recently developed [135] to explain various observations in the diamond chemical vapor deposition (CVD) process, where charged diamond clusters were suspended in the gas phase in the process of the diamond-like film deposition. According to the charged cluster model, a large number of the commercially available thin films were actually cluster-assembled ones even though they have been believed to be grown by the atomic unit. The idea was developed theoretically by examining the thermodynamic driving forces for the charge-induced nucleation of the (negatively charged) carbon-atom cluster. It was shown that the short-range ion-induced dipole interaction and the electrostatic effects were mainly responsible for the unusual gas-phase nucleation. The theoretical analysis [135] is quite generic and can thus be applied to any process (e.g. in the ionized gas phase) that involves the charge-induced nucleation (see Sections 2.1 and 2.2).

Evidence of the nanometer-sized charged carbon clusters in the gas phase of the diamond chemical vapor hot-filament deposition process is given in Ref. [136]. Similar processes are also common in the field of combustion and flame, where the charged carbon clusters are produced in the gas phase and are regarded as major precursors of the graphitic soot. Confirmation of the existence of charged carbon clusters in the gas phase certainly favors the hypothesis that CVD diamond is grown by the nano-cluster rather than atomic/molecular unit.

Molecular dynamics (MD) simulation studies were undertaken to examine the possibility of thin film growth by nano-sized clusters as building units. It was shown in the study [137] of deposition of various-sized (yet in the nanometer range) Au clusters on the Au(001) surface that the epitaxial recrystallization of the clusters on the substrate surface is the best for the 300-atom clusters. The epitaxial recrystallization behavior of small and large clusters used in the simulation suggests the possibility of thin film growth by a cluster unit as suggested by the CCM.

Therefore, according to the new, cluster-unit deposition paradigm of the thin film growth, the success of epitaxial growth of the actual production line in the microelectronics industry critically depends on the cluster size. A supporting evidence for the CCM in the diamond CVD process is that less stable diamond phase frequently grows with simultaneous etching of more stable

graphite, which would violate the second law of thermodynamics if the deposition unit were an atom [137]. This seemingly paradoxical phenomenon could be explained successfully by assuming that the gas-phase nucleation of the diamond clusters is followed by their subsequent deposition to form diamond-based films [138]. Efficient nucleation processes of silicon nanowires [9] in reactive silane/hydrogen/hydrochlorine atmospheres were also explained on a thermodynamically sound basis by the cluster-unit deposition and the atomic-unit etching.

The CCM theory has two basic assumptions [9,135], related to the spontaneous formation of charged clusters in the gas phase and their role as building units of various thin films. The charge of nano-clusters has two major implications on the gas–cluster–film system. First, the charged clusters maintain the nanometer size due to remarkably suppressed Brownian coagulation, which frequently leads to skeletal or fractal-shaped microparticle formation. Secondly, the charge enhances the diffusivity of the atoms in the clusters and induces a selective landing of charged clusters on the nanostructured surface, which can further result in the efficient self-assembly packing. The cluster size would be a decisive factor for the grain size control of thin films, which is a completely new paradigm of thin film growth and microstructure evolution [8]. It is thus quite probable that the carbon nanotube-like structures (discussed in Section 3.3) might also evolve as a result of growth by charged carbon cluster units [9].

In the growth of silicon nanowires in the  $\text{SiH}_4 + \text{HCl} + \text{H}_2$  gas mixtures [9], a highly anisotropic nanostructure growth was attributed to the electric charge of the gas-phase grown nano-clusters. Indeed, if the clusters were not electrically charged, they would be subjects to fast Brownian coagulation in the gas phase, leading to the porous fractal and skeletal structures. Thus, the highly anisotropic growth of nanowires is not expected from neutral clusters. Furthermore, it is quite common that the clusters land relatively easily on the conductive surfaces but have difficulty in landing on the insulating surfaces, which results in the selective deposition. The key to this puzzle is the electrostatic interaction between the charged clusters and the silicon nanostructures being grown. Indeed, the two conducting spherical particles carrying charges of the same sign interact with the interaction force [9,139]

$$F = \frac{q_1 q_2}{d_s^2} - \frac{q_1^2 r_2 d_s}{(d_s^2 - r_2^2)^2} - \frac{q_2^2 r_1 d_s}{(d_s^2 - r_1^2)^2} + \dots, \quad (3.1)$$

where  $r_j$  and  $q_j$  are the radii and the electric charges of the spheres, and  $d_s$  is the distance between their centers. From the above equation, one can conclude that if the size difference between the two conducting charged particles is small, they are repulsive. However, if the size difference is large, both particles can start to attract. Elongated particles of the cylindrical shape or nanowires typically have a small dimension in the radial direction but larger sizes in the axial direction. Therefore, small clusters might be subject to the electrostatic attraction from the nanostructure in the axial direction and at the same time be repelled from the structure radially. Thus, if a negatively charged conducting particle approaches axially to the nanowire/nanotip, the electrons in the nanostructure will move along the axial direction away from the approaching (negatively charged) particle. However, if the same particle approaches in the radial direction, electrons in the nanowire/nanotip cannot move a long distance away from the approaching particle because of the limited size the radial direction. It is also likely that once an elongated shape is initiated, a highly anisotropic growth will further accelerate to promote a pronounced growth of silicon nanowires. It is remarkable that an increase



in gas pressure can result in an enhanced gas-phase precipitation, which normally increases the cluster size. According to (3.1) the selectivity of the charged cluster deposition is weaker for larger clusters.

Several authors have also studied size distributions of clusters/nanoparticles suspended in the gas phase of various CVD (including PECVD) reactors by differential mobility analyser (DMA) and a particle number counter techniques [47,140]. Remarkably, in the process of CVD of silica films using tetraethylorthosilicate (TEOS) as a precursor, the films did not grow under conditions where clusters were not detected in the gas phase [140]. Note that various nanostructured materials can be prepared by the low-energy deposition of gas-phase preformed clusters. The composition of the clusters can be various, e.g. noble metal clusters, transition metal-based clusters, silicon, carbon-based clusters, etc. [141]. Complex compounds can also nucleate in the gas phase. For instance, AlN nanocrystals can be grown in the gas phase of the  $\text{AlCl}_3 + \text{NH}_3 + \text{N}_2$  CVD system via a homogeneous nucleation similar to that in silane-based discharges (see Section 2.1). It was also evidenced that AlN thin films can also be grown through the intermediate stage of the gas-phase powder formation [142]. Meanwhile, study of the square-wave modulated plasma discharges confirmed that silicon-based nanocrystals (powder precursors) can be advertently tailored in the gas phase of silane-based plasmas at the room temperatures. This result further encouraged investigation of the plasma/film parameters near the onset of fine powder generation [143,144]. The ultimate aim of research in this direction is to deposit nano-structured silicon-based films under discharge conditions favoring the fine powder generation. In this case the silicon clusters, nanoparticles, and crystallites are formed in the plasma and contribute to the actual film deposition process.

It is also interesting that the plasma-grown nanoparticles can be intentionally moved to or from the substrate, e.g. by using the thermophoretic force (see Section 4.3). It has recently been revealed that the plasma-grown nanocrystallites and/or clusters play a pivotal role in the deposition of the *pm*-Si:H (polymorphous silicon) films [143,144]. Therefore, tailoring the size and the number density of the nano-sized Si-based particles in the plasma opens up a new horizon of the dust-involving processes in the nanoelectronic technologies including the passivation, surface modification and coating of fine particles followed by their integration into devices as valuable functional elements [144]. Thermal low-temperature plasmas can also be used to produce hypersonic flows of ultrafine gas-phase nucleated micro-/nano-sized particles, which can be supersonically sprayed onto a temperature-controlled substrate to produce nanostructured materials with different properties [145].

Various nanostructured films can be tailored by using the cluster-unit deposition schemes. For example, for cluster-assembled carbon it appears possible to control the film morphology and the structure at nano- and mesoscales. Recently, the cluster beam deposition of carbon clusters onto Ag(100) and Si(100) surfaces has been reported [146]. The choice of Ag and Si as substrates is motivated by the idea of comparing the deposition of carbon nanoclusters on metal surfaces for which a high mobility of the clusters is expected as opposed to the deposition on substrates where the interaction is very strong [146]. Another interesting example is the deposition of size-selected clusters, which represents a new route to the fabrication of various nanometer-scale surface architectures, e.g. nanopores. A systematic experimental study, complemented with molecular dynamics simulations, of the implantation of size-selected  $\text{Au}_7$ ,  $\text{Ag}_7$ , and  $\text{Si}_7$  clusters into a model graphite substrate has recently been performed [146]. It is remarkable that interaction of the nanoclusters with the surfaces being processed shows a very strong size-dependent character. In particular, the Co nanoclusters can undergo a full contact epitaxy on landing or burrow into the Cu surface [147].

In any case, nanoclusters larger than a few nanometers in radius show a different, as compared to subnanometer-sized clusters, behaviour due to the higher structural integrity [147].

To conclude this section, we remark that the CVD growth of various nanostructures involves a large number of physical and chemical phenomena occurring at various length scales that sometimes differ by a few orders of magnitude. For example, the global particle/power balance, the distributions of particle number densities and temperatures, usually develop over the length scales comparable to the reactor dimensions. On the other hand, the elementary gas-phase reactions or the atomic/cluster interactions with the surface involve processes at the atomic/molecular length scales. Hence, modeling of cluster unit-based synthesis of advanced materials would require a multiscale approach [148].

### 3.6. Particle size as a key factor in nano-scale technologies

In this section, we discuss several examples showing that a particle size can indeed be a critical factor in several important applications. This size-dependent feature is the most impressive when the particle's size is in the nanometre range.

In the first example we address nano-sized particles for various optical applications. It is commonly known nowadays that spectacular changes happen when nano-crystals of various materials shrink in size [149]. When the crystal's size becomes smaller than the wavelength of the visible light, the coherence of the light scattered by the material's surface changes, which results in changes of the color. For instance, metals lose their metallic luster and change color usually to a yellow-brown hue. Usually white crystals of semiconductors ZnO and TiO<sub>2</sub> become increasingly colorless as the crystals shrink in size to below 15 nm [149].

Another important effect is due to an increasing role of surface effects that begin to perturb the periodicity of the “infinite” lattice of a regular crystal. These changes are known collectively as quantum size effects and typically occur in the 1–10 nm range. In the case of metals, their thermal and optical properties are determined by the electron mean free path, which typically ranges from 5 to 50 nm for most metals. If the crystal becomes comparable in size, the electrons are then scattered off the surface, which apparently increases the resistivity of the nano-particles. Furthermore, if the grains become small enough, the conduction and valence bands then break into discrete levels. For semiconductors, the bandgap widens when the crystal's size diminishes. Hence, pronounced molecular properties can emerge thus favoring the changes in the crystal color and the luminescence [149].

Thus, nanocrystals of almost any material feature various unique physical and optical properties primarily controlled by the nanocrystal size and shape. For example [149], gold metal can dramatically change color with the nanoparticle size. We emphasize here that gold nanoparticles with different size can be regarded as building units for the assembly of bulk gold material. Specifically, it is a common knowledge that bulk gold is normally yellow. Smaller gold particles, 30–500 nm in size, appear blue to purple and red in color. This is largely attributed to geometric light scattering effects that can be described by the Mie theory (we note that the Mie scattering theory is a sound background for the detection of fine particles, see Section 4.7 for details). The subsequent changes of color from the reddish-blue to orange and even colorless happen when the particle's size shrinks from 30 to 1 nm and are definitely attributed to strong quantum size effects.

This opens up a totally new principle for fabricating bulk films using building blocks of different size and architecture (see also Section 3.5). For example, one can control the size and spacing between the building blocks, thus changing the interaction between them. Hence, one could assemble

an object with tailored optical (and other) properties anywhere in between those of a nanoparticle and those of a bulk material. We note that modification of the optical absorption properties are presumably due to changes in the surface absorption band with grain's size.

It is also remarkable that the surface plasmon frequency of nanocrystals changes drastically with the particle shape (e.g. rod-like or ellipsoidal/spherical) due to the changes in the restoring force on conduction electrons that are extremely sensitive to the particle's curvature [149]. For example, the polarizability of a rod-like gold particle is

$$\alpha_{x,y,z} = \frac{4abc(\varepsilon_{\text{Au}} - \varepsilon_m)}{3\varepsilon_m + 3L_{x,y,z}(\varepsilon_{\text{Au}} - \varepsilon_m)},$$

where  $a, b$ , and  $c$  ( $a > b = c$ ) refer to the geometrical sizes of the rod,  $\varepsilon_{\text{Au}}$  and  $\varepsilon_m$  are the dielectric constants of the gold and optical medium, respectively, and  $L_{x,y,z}$  is the depolarization factor for the respective axis. It is notable that metal nanoparticles are interesting from the application point of view because of the high electrical capacitance and because the color of the nanoparticle colloid is affected by the stored electric charge on the particles. For the nanoparticles/clusters of an arbitrary shape one should use a general definition of the polarizability tensor

$$\alpha_{ij} = \frac{\partial \zeta_i}{\partial E_j},$$

where  $\zeta_i$  and  $E_j$  are the Cartesian components of the dipole moment and the applied electric field, respectively [150]. For example, the polarizability of two-dimensional gold clusters with an arbitrary size and shape in the normal direction can be estimated using the density functional method and the fitting formulas [150].

Thus, special attention should be paid to charge confinement and quantum size effects in metal nanoparticles and nanoclusters. In particular, by changing the overall size of a metal nano-cluster, one can control the electron storage and redistribution of the electron population between the inner and outer populations [151]. For example, the storage or release of electrons is allowed within  $\pm 2e$  for the cluster consisting of 169 Al atoms. Furthermore, the contribution of the atoms located at the outer part of the cluster in the overall cluster charging is the most important. It is also remarkable that using the first-principle semi-empirical molecular orbital calculations one can estimate the effective capacitance of a 3.8 nm metal cluster of the order of 0.15 aF [151]. Other examples of calculations of the electron energy levels and the electronic properties of nano-sized objects are given in Refs. [152–155].

In this range, the electronic levels, the bonding states, and other important characteristics of the solid state critically depend on the size of building blocks. The latter can be numerous, e.g. atomic, molecular, large polymerized molecules, atomic clusters, and nanoparticles (NPs). Since the plasma-grown solid grains are of our primary interest here, we will focus on the nanoparticle-assembled films. One of the viable examples is the layer by layer assembly of multilayered optical coatings made of nanoparticles such as doped and undoped CdSe, core-shell and naked CdSe, CdTe, PbS, TiO<sub>2</sub>, ZrO<sub>2</sub>, Au, SiO<sub>2</sub>, MoO<sub>2</sub>, Fe<sub>3</sub>O<sub>4</sub> and several others [156]. For multilayers made of NPs, the nanoparticle size and layer sequence are particularly important because their optical, electronic, and magnetic properties strongly depend on the interparticle connections and therefore, their nanometer-scale organization. In particular, magnetic phenomena of the ordered layers

of nanoparticles can be substantially modified by insulating particle coatings (coating of nanoparticles in low-temperature plasmas will be discussed in Section 3.7).

It is worth to pinpoint that one can even fabricate stratified/graded microstructures by using the nanoparticles of the same chemical composition and different size. Indeed, stratified assemblies of nanoparticles can be made from only one parent material by organizing NPs by size [156]. Such organization of the layers is particularly interesting for semiconductor quantum dots displaying strong dependence of the bandgap on the nanoparticle size. Since the absolute energy of both conduction and valence bands of semiconductors is affected by the confinement of the excitonic wave function, a film with a gradual change in particle diameter should display a similarly gradual evolution of the valence- and conduction-band energies.

Such assemblies are the examples of graded semiconductor films, known for exceptional capabilities as photodetectors, bipolar transistors, waveguides, and other photonic and electronic devices. PECVD methods are commonly used to fabricate such layers. However, a relatively high process cost can be an obstacle for immediate industrial applications. In particular, using layer-by-layer assembly of CdSe nanoparticles of different size, one can fabricate a graded “nano-rainbow”, in which the inner layers are made of smaller, 2–3 nm NPs with the luminescence maximum in the green (495–505 nm) and yellow (530–545 nm) wavelength ranges and larger (4–6 nm) NPs in the orange (570–585 nm) and red (605–620 nm) sides of the assembly [156]. In that way, one can engineer the polarizability, the refractive index, and other parameters at the nanometer scale so that the overall interaction of an electromagnetic wave with the film can be made very much different from many conventional optically uniform materials.

Nanocrystal quantum dots (QDs) are yet another interesting and important size-sensitive object for nano-electronic applications. QDs in the strong-confinement regime have the emission wavelength that is a pronounced function of the size, adding the advantage of continuous spectral tunability over a wide energy range simply by changing the size of dots [157]. In particular, QDs are very promising for the development of a new type of lasing elements often commonly called as quantum dot lasers. The obvious advantage of such a technology is that nanocrystal QDs can be prepared as close-packed films or incorporated with high densities into glasses or polymers. Thus, they are compatible with existing fiber-optic technologies and are useful as building blocks for bottom-up assembly of various optical devices, including optical amplifiers and lasers [157].

It is also remarkable that colloidal particles in the plasma are very much similar to colloidal nanoparticles chemically synthesized in a solution [158]. Since the chemical synthesis of QDs from nanoparticle colloids offers greater control over their chemical composition, shape, and size (as compared with surface growth methods), one can expect a similar flexibility for the plasma-based methods using complex plasma colloids [158]. In addition, colloidal NPs can be doped by another element, which can introduce extra carriers and provide an impurity center that can interact with the quantum-confined electron–hole pairs. However, the apparent modern challenge in this direction is to introduce the impurity in the core (i.e. not at the surface or interface) of the particle without compromising the quality of nanocrystals (e.g. high crystallinity, well-controlled size and monodispersity). It is thus apparently challenging to explore the applicability of the plasma-based methods for doping semiconductor QDs.

Finally, it appears that the main challenge of the current nanoscience is the creation of new materials through the manipulation of size-dependent effects in nanocrystals and their assembly into macroscopic objects [149]. In this regard, recent reports on the synthesis of Si-based nanoparticles

with selective size, composition and structure using low-temperature RF plasmas (see relevant discussion in Section 3.4) sound optimistic. In particular, depending on the discharge conditions, various ultrafine nano-particles based on the Si-C-N system were synthesized in the plasma of  $\text{SiH}_4 + \text{CH}_4 + \text{NH}_3 + \text{Ar}$  gas mixtures [122]. Moreover, under conditions of fast particle development, highly monodisperse SiCN powders were generated. It is notable that the above plasmas were also able to generate (before the onset of the particle coagulation) non-agglomerated amorphous clusters smaller than 10 nm in size [122]. We thus believe that plasma-based methods do have future in producing the nanometer-sized building blocks for the applications that require selective size and architecture of the building blocks for various nano-scale assemblies.

### 3.7. *Other industrial applications of nano- and micron-sized particles*

Apart from the common deleterious aspect discussed in Section 3.1, nano- and micron-sized particles have recently found a number of challenging applications in the material engineering, optoelectronic, optical, petrochemical, automotive, mineral and several other industries. For example, ultra-fine particles can be efficiently incorporated into polymeric/ceramic materials to synthesize a number of advanced nano-structured materials for the applications as water repellent, protective, fire resistant, functional and other coatings.

Furthermore, fine powders of  $\sim 10$  nm-sized particles have been widely used as catalysts for inorganic manufacturing, ultra-fine UV-absorbing additives for sunscreens and other outdoor applications. Other applications include textiles, wear-resistant ceramics, inks, pigments, toners, cosmetics, advanced nanostructured and bioactive materials, environmental remediation and pollution control, waste management, as well as various colloidal suspensions for mining, metallurgical, chemical, pharmaceutical industries, and food processing.

Meanwhile, nanoparticles have recently emerged as valuable elements of several technologies aiming to tailor the materials properties at nanoscales and manufacture novel nanoparticle-assembled materials with unique optical, thermal, catalytic, mechanical, structural and other properties and featuring nano-scale surface morphologies and architectures [159]. The rapidly emerging applications of nanoparticles include nano-patterned and nanocomposite films, nano-crystalline powders and consolidated structures, sophisticated nanoparticle assemblies that represent new forms of supramolecular crystalline matter. Further potential applications include but are not limited to nano-scale inorganic synthesis, dispersions and suspensions with the controlled fluid dynamics, and nano-sized single/few-electron data storage units.

It is noteworthy that PECVD methods have recently been instrumental in the fabrication of various nanostructures wherein the gas-phase grown nanoparticles play a pivotal role. A few years ago, it was discovered that generation, confinement and processing of solid grains in a plasma can be potentially beneficial for a number of applications [69]. Above all, completely new areas of research have recently been initiated. For example, embedding of nanometre-sized particles grown in silane discharges into an amorphous silicon matrix, can substantially improve the performance of silicon solar cells (see Section 3.4 for details). Similarly, one can develop substantially new classes of particle-seeded composite materials [160]. In addition, fine particles, advertently injected into the plasma, can be trapped and subsequently coated to enhance their surface properties (e.g., for catalytic applications). Plasmas can also be used to oxidize (and thus eliminate) contaminant particles in



biogas. In this way, it is also possible to electrically charge up nanometre sized soot particles in Diesel engine exhausts.

We emphasize that an entirely new class of materials can be synthesized in particulate form by using the plasma-based technology. Hence, the recently exploded interest of a number of major industries to the dusty plasma technologies is quite understandable. This interest is supported by constantly increasing research and development efforts. Thus, it becomes possible to tentatively categorize the applied dusty plasmas research into the directions of coating, surface activation, etching, modification, and separation of clustered grains in the plasma environment [74].

Powders produced using plasma technology possess a number of interesting and potentially useful properties, e.g. very small sizes, uniform size distribution; and chemical activity. Size, structure, and composition can be tailored for the specific application [160]. Specifically, unique objects, like coated or layered grains with the desired surface structure, color, and/or fluorescent properties can be created via the plasma processing. Normally, particle coating is a complex, multi-step process, involving various reactive chemistries and/or support by external devices. A sophisticated approach for the coating of eternally injected particles was proposed by [161], where an argon RF plasma was employed to charge and confine the particles. Simultaneously, a metal coating has been prepared by means of a separate DC magnetron sputtering source. This approach uses the unique ability of the complex plasma systems for the electrostatic trapping, control of the particle residence time and position.

A common arrangement of an RF plasma reactor for particle coating uses a built-in magnetron sputtering system. Particles can be dispersed externally, e.g. via a manipulator arm. The head of a magnetron electrode is usually positioned opposite the RF powered electrode and releases the sputtered metal particles. To obtain a stable electrostatic trapping in the plasma glow, a metal ring is sometimes placed on the RF electrode. This arrangement affects the plasma sheath and enables a reliable radial confinement of the particle cloud. Laser light scattering is frequently used to localize the particles in the potential trap and obtain the required spatial distributions in the cloud. To avoid any significant plasma disturbance by the magnetron sputter source, a metal grid can be placed between the magnetron and the RF plasma. In such a way, one can also trap in an almost motionless position and further etch even a single particle [162]. In addition, deposition of thin amorphous carbon (a-C:H) films onto SiO<sub>2</sub> grains ( $\sim 1\ \mu\text{m}$ ) has recently been reported [163]. A noticeable increase in the laser scattering during the process of the particle coating by a-C:H films signalled an additional generation of small dust particles. After the examination of the collected particles by the scanning electron microscopy (SEM), a rather small amount of large coated SiO<sub>2</sub> grains and a large amount of small and monodisperse carbon dust particles ( $\sim 100\ \text{nm}$ ) were observed.

As an alternative to the sputter-coating process, one can certainly use several metallorganic gas precursors. For instance, a metallorganic precursor ATI has been used to deposit an alumina layer on fluorescent (e.g. barium magnesium aluminate particles common as an active coating material in fluorescent lamps) particles to improve their stability and adhesive properties. Coating of ZnO particles (the most important constituent of sunscreens) with SiO<sub>x</sub> films by injecting ZnO grains into TEOS/Ar/O<sub>2</sub> plasma is yet another viable example of the plasma processing of ultrafine powders.

Fundamental research related to industrial treatment of dust grains aims to reveal the underlying surface physics and chemistry of particulate processing [160]. More specifically, the nature of plasma–particle interactions in chemically active plasmas is yet to be uncovered. In this regard, particle



temperature and surface heat exchange are of the major interest for the modern applied dusty plasma research.

Recently, it has been demonstrated that complex plasma systems can be successfully used not only for etching but also for PECVD on small particles. This technique can be used for coating both nano- and micron-sized grains, and is particularly suited for highly uniform ultrathin film deposition [164]. The size distribution and the uniformity of deposition have been studied as a function of the deposition time and particle size. The results are interpreted qualitatively via a surface deposition model, which assumed the linear film growth rate

$$da/dt = 2\tau k_{\text{diss}} m_r n_e [M_0] / [\sigma_t (\tau_{\text{res}} k_{\text{diss}} n_e + 1)] ,$$

where  $\sigma_t = \rho[(2\pi m_r/T_n)^{1/2} + A_{\text{tot}}\tau_{\text{res}}/V_R]$ ,  $V_R$  is the plasma volume in the reactor in  $\text{m}^3$ ,  $A_{\text{tot}}$  is the total surface area available for deposition,  $k_{\text{diss}}$  is the dissociation rate constant ( $\text{m}^3/\text{s}$ ),  $n_e$  and  $[M_0]$  are the electron density and the concentration of the hydrocarbon (isopropanol in the deposition experiments [164]) at the inlet of the reactor, respectively. Here,  $T_n$  is the temperature of neutrals (K),  $m_r$  is the mass of the radical (kg),  $\tau_{\text{res}} = V_R/J_{\text{flow}}$  is the residence time of the reactive radical in the plasma reactor,  $J_{\text{flow}}$  is the flow rate of the gas inlet, and  $\rho$  is the material density of the film ( $\text{kg}/\text{m}^3$ ). We note that the linear growth model is valid as long as the variations in the total surface area available for the film deposition due to the particle growth, are negligible. In the cases, when the combined surface area of the growing particles is comparable with the surface areas of the walls and electrodes, the variation of  $A_{\text{tot}}$  with the particle size should be accounted for.

We now discuss yet another interesting application is the plasma-based synthesis of carbon nanoparticles. Specifically, nano-sized plasma-grown crystallites do play an important role in the synthesis of ultrananocrystalline diamond films, which possess many unique and fascinating properties, such as extremely high hardness, sound velocity and thermal conductivity different from any other forms of diamond [165]. A common approach to synthesize nanocrystalline carbon films is a PECVD in hydrogen-diluted hydrocarbon gas precursors. It appears that diamond nano-films can be grown in a 2.45 MHz microwave PECVD system, using diamond nano-particles seeded over a heated substrate (including silicon, silicon nitride, silicon carbide, silicon oxide, aluminum oxide, titanium, molybdenum, and tungsten at temperatures ranging from 400°C to 800°C) in contact with the plasma [165]. Ultrananocrystalline state of diamond features a highly dense nanocrystalline structure with a crystallite size distribution that peaks at 3–5 nm. Amazingly, the nanocrystalline diamond can also be synthesized in the atmospheres of carbon-rich red giant stars by a mechanism similar to the laboratory microwave PECVD synthesis [165].

Nanostructuring of carbon-based films, presumably via the plasma-grown nanoparticle incorporation, results in a substantial improvement of the field-emission properties due to electric field enhancement created by highly non-uniform electronic properties over nanometer scales [166]. Diamond field emitter cathode tips with a radius of curvature of less than 5 nm have recently been fabricated and show a significant improvement in the emission characteristics [167]. Furthermore, the self-aligned gate diamond emitter diodes and triodes are being developed using the silicon-based microelectromechanical system (MEMS) processing technology to achieve totally monolithic diamond field emitter devices on silicon wafers [167].

Plasma-modified nanoparticles also have various challenging biomedical applications. In particular, calcium-phosphate-based [e.g., hydroxyapatite (HA)] nano-particulate material produced in plasma-spray [168] or sputtering [169,170] RF plasma deposition systems was used to develop

functional biocompatible coatings for enhanced intimate bone ingrowth and rapid fixation for orthopaedic applications. The observed particulate sizes ranged from 10 nm to 4  $\mu\text{m}$  [171]. A general trend of diminishing the particle size and increasing the particle density with RF power is consistent with the experiments on particulate growth in other plasma reactors (see Section 2.1) and further supports the role of plasma grown/modified ultra-fine particulate powders in the deposition of nanocomposite biocompatible materials.

From another application point of view, calcium phosphate nano-clusters have recently been proposed as reagents to control pathological calcification and calcium flows in tissues and biological fluids exposed to or containing high concentrations of calcium [171]. Furthermore, poly(butylcyanoacrylate) coated nanoparticles can be instrumental for the development of drug delivery systems for the treatment of disseminated and aggressive brain tumors [172]. Plasma-based synthesis of nanoparticles is quite similar to other gas-phase processes, common from other physico-chemical fields of research. The nanoparticles, smaller than 100 nm, have many properties, which differ them from the corresponding bulk materials, and make them attractive for many new electronic, optical or magnetic applications. The applications include quantum dots, luminescent materials, gas sensors, resistors and varistors, conducting and capacitive films, high-temperature superconductors, and thermoelectrical, optical, and magnetic materials [173].

We emphasize that present and potential applications of the plasma-treated fine particles are numerous: treatment of soot and aerosols for environmental protection [174]; powder particle synthesis in high-pressure and low-pressure plasmas; lighting technology; enhancement of adhesive, mechanical and protective properties of powder particles for sintering processes in the metallurgy fragmentation of powder mixtures in order to sort them [75]; improvement of thin film hardness by incorporation of nanocrystallites in hard coatings [175]; coating of lubricant particles [176]; application of tailored powder particles for chemical catalysis; functionalization of fine particles for pharmaceutical and medical applications; production of color pigments for paints; improvement of anti-corrosion properties of fluorescent particles; tailoring of surface properties of toner particles [161], and several others. Furthermore, using plasma-grown nanoparticles, it is possible to produce composite coatings, where the properties of various materials are combined. An example is the deposition of wear-resistant self-lubricated coatings [74]. The idea of such coatings is based on the incorporation of small grains of lubricant (e.g.  $\text{MoS}_2$  particles) into a hard matrix (e.g.  $\text{TiN}$ ). When the surface is exposed to friction and wear, small amounts of lubricant are released to form a thin protective film over the surface. Such hybrid coatings are efficiently lubricated and at the same time are environmentally clean.

Manufacturing of hydrophobic/hydrophilic coatings in acetylene-nitrogen and fluoroalkylorthosilicate (FAS)-based reactive gas chemistries is yet another industrial example where an intensive plasma polymerization is accompanied by a pronounced nano- and micro-powder formation [41,177]. In particular, C–N hydrophilic coatings of aluminum rolls surfaces are utilized by the refrigerating and airconditioning industries [41]. Moreover, water repellency has recently been required for many types of substrate (e.g. glass, plastics, fibers, ceramics and metals) in various industrial fields (biomedical, automotive, mining, various consumer goods and appliances, etc.). It has recently been shown that ultra-high water-repellency can be achieved by using FAS (and similar)-based PECVD in microwave discharges at total pressures over 40 Pa [177]. In this case the surface becomes rough due to the growth (presumably, plasma-based) of fine particles. Physically, the surface roughness is intrinsically linked to the wetting angle; the latter should be in the range of  $140\text{--}180^\circ$  to warrant the industrial applicability as a water-repellent coating. The ongoing work includes the means of control

of the surface morphology of the deposited films, which appears to be the most important to obtain highly-transparent ultra water-repellent films [177].

At the end of this section we remark that from the point of view of mass production, high-pressure technologies do have advantages over low-pressure ones, the latter requiring sophisticated vacuum equipment. Furthermore, the plasma route for nanoparticle production in bulk quantities would certainly pose a number of technological and cost efficiency problems. Nevertheless, low-pressure plasma-based techniques offer a better deal of process control and precision, without damage or thermal overload and are promising for the production of small amounts of nanoparticles with the specific properties tailored for the required industrial applications.

#### 4. Levitation and dynamics of fine particles

In this section, we give a few examples of dynamic processes in complex plasma systems. Since most of the laboratory plasmas have natural boundaries such as chamber walls, internal electrodes, substrate holders, etc., a large number of experiments with the plasma–particle systems involves investigation of various dynamic processes near the boundaries. The plasma–boundary transition area includes sheath and pre-sheath regions where dust grains can levitate due to a dynamic balance of several forces acting on a particle. Such forces include but not limited to the force of gravity, electrostatic force, ion and neutral drag forces, etc. If the boundary is located below a dust cloud, one should expect a relatively strong action of the gravity force on large and thus heavy grains. Such an arrangement is quite common for parallel-plate RF and DC plasma reactors, other RF and microwave discharges with external substrate holders, etc. The electrostatic charge on the dust grains is also one of the most important parameters that significantly affects their dynamics in the plasma–boundary transition areas. Since plasma parameters vary dramatically in the sheath/pre-sheath regions, so does the equilibrium electric charge on a particle. The latter in turn dynamically affects the force balance while the particle moves towards the wall.

Another key feature of the plasma–wall transition areas is that the levitation and dynamics of dust grains is strongly affected by the established ion flows directed towards the walls. The interaction of the particle with the flows can give rise to a number of plasma collective phenomena discussed in detail in Section 6. The key focus of this section is on the basic charging mechanisms of nano- and micron-sized particles (Sections 4.1 and 4.2) and major forces acting on the fine particles in the plasma (Section 4.3). The analysis of forces on the particles is crucial for investigation of their dynamic behavior in the near-electrode areas (sheaths/pre-sheaths) of argon (Section 4.4), silane (Section 4.5.1) and fluorocarbon (Section 4.5.2) low-temperature plasmas. The study of the force balance is also instrumental in probing various plasma–surface interactions (Section 4.6). Section 4 ends with a brief review of the most common methods of detection, diagnostics and characterization of fine charged particles.

##### 4.1. Charging of dust particles

Here, we discuss the most established approach to the charging of colloidal particles in the plasma. The knowledge of the charge is of fundamental importance and also is in the foundation of the character of self-organized structures observed in a complex plasma such as Coulomb crystals, liquids,

clusters, etc., as well as phase transitions between them [178–183]. These structures have recently attracted cross-disciplinary attention because of the similarities with processes in condensed matter physics, statistical physics, biophysics, etc. [7].

Most dusty plasma's charging theories are based on the theories of the electrostatic probes in a plasma [184]. These theories predict the electron and ion currents to the probe. The currents are termed “orbit-limited” when the condition  $a \ll \lambda_{Di} \ll \lambda_{mfp}$  applies, where  $a$  is the particle radius,  $\lambda_{Di}$  is the ion Debye length, and  $\lambda_{mfp}$  is a collisional mean free path between neutral gas atoms and either electrons or ions [44]. In this case, the currents are calculated by assuming that the electrons and ions are collected if their collisionless orbits intersect the probe's surface. The Orbit Motion Limited (OML) approach has two major assumptions, specifically [10].

(i) independently of the structure of the electrostatic potential in the plasma near the dust particle, any plasma particle which initially is far from the dust particle, can reach the surface of the dust particle, and if it is allowed by the conservation laws, will attach to the dust particle;

(ii) for spherical dust particles, the limiting impact parameter of a plasma particle (when the plasma particle is absorbed by the dust particle) corresponds to a tangential trajectory to the dust particle.

An obvious advantage of this model is that the cross sections of the plasma particle attachment to the dust can be found using the energy and momentum conservation laws only, independently of the complexity and nonlinearity of the plasma potential close to the dust particle [10].

For the collection of Maxwellian electrons and ions characterized by the temperatures  $T_e$  and  $T_i$ , the orbit-limited currents for an isolated spherical particle are given by [3]

$$I_e = I_{0e} \exp(e\phi_s/T_e), \quad \phi_s < 0, \quad (4.1)$$

$$I_e = I_{0e}(1 + e\phi_s/T_e), \quad \phi_s > 0, \quad (4.2)$$

$$I_i = I_{0i} \exp(-Z_i e\phi_s/T_i), \quad \phi_s > 0, \quad (4.3)$$

$$I_i = I_{0i}(1 - Z_i e\phi_s/T_i), \quad \phi_s < 0, \quad (4.4)$$

where  $\phi_s$  is the surface potential of the particle relative to the local plasma potential and  $Z_i$  is the electronic charge of the ions. The coefficients  $I_{0e}$  and  $I_{0i}$  represent the current collected at  $\phi_s = 0$ , and are given by

$$I_{0\alpha} = n_\alpha q_\alpha (T_\alpha/m_\alpha)^{1/2} \pi a^2 f_\alpha(w, V_{T\alpha}),$$

where  $n_\alpha$  is the number density of the plasma species  $\alpha$ . Here,  $f_\alpha(w, V_{T\alpha})$  is a complicated function of the thermal velocity  $V_{T\alpha} = (T_\alpha/m_\alpha)^{1/2}$  and the drift velocity between the plasma and the particles. Simple expressions are available in the cases of small and large drift velocities:

$$I_{0\alpha} = 4\pi a^2 n_\alpha q_\alpha (T_\alpha/2\pi m_\alpha)^{1/2},$$

which is valid for  $w/V_{T\alpha} \ll 1$  and

$$I_\alpha = \pi a^2 n_\alpha q_\alpha w (1 - 2q_\alpha \phi_s/m_\alpha w^2)$$

in the case when  $w/V_{T\alpha} \gg 1$ . The dust charge  $Q$  is related to the particle's surface potential  $\phi_s$  by  $Q = C\phi_s$ , where  $C$  is the capacitance of the particle in the plasma. For a spherical particle with  $a \ll \lambda_{Di}$ , the capacitance is simply  $C = a$ .

The standard “continuous charging model” of dust charging in the plasma assumes that the grain charge varies due to collection of electron and ion currents from the adjacent plasma

$$\frac{dQ}{dt} = \Sigma I_\alpha . \quad (4.5)$$

To find the equilibrium particle charge, one can set  $dQ/dt = 0$  in Eq. (4.5) and, by solving the equation  $\Sigma I_\alpha = 0$ , obtain the equilibrium particle surface potential  $\phi_{s0}$  and the particle charge  $Q_0$ . Generally speaking, since the electrons have higher thermal velocities and higher mobility than the ions, the electric charge and floating surface potential of the particle are negative. Note that  $\phi_s$  is independent on the particle size, whereas the charge in this model is directly proportional to the particle’s radius,  $Q \propto a$ .

The solution for the equilibrium dust charge critically depends on whether the charging for an individual particle (or a rarefied dust cloud) or for a dense ensemble of particles is considered. Specifically, this is reflected in the quasineutrality condition (the negative ions are neglected for simplicity here)

$$n_i = n_e(1 + P_e) ,$$

where  $P_e = n_d |Z_d|/n_e$  [185] reflects the ratio of the charge density carried by the dust particles to the electron number density. Here,  $Z_d$ ,  $n_d$ , and  $n_e$  are the dust charge (in units of the electron charge), and number density of dust particles and electrons, respectively. If  $P_e \ll 1$ , we deal with the individual grain charging case, otherwise the effects of dense particle clouds should be taken into account. Indeed, when  $P_e > 1$ , the charge and the floating potential can be noticeably diminished as compared to the values obtained in the case when  $P_e \ll 1$ . The effect of the dust charge proportion  $P_e$  on  $Z_d$  and  $\phi_s$  can be analyzed using the steady state equation for the microscopic grain currents  $\Sigma I_{\alpha 0} = 0$ , which can be rewritten into a convenient non-dimensional form for the electropositive plasma with the single ion species [10]

$$\exp(-\mathcal{Z}) = \frac{(1 + P_e)(\tau + \mathcal{Z})}{\sqrt{\tau\mu}} , \quad (4.6)$$

where  $\mathcal{Z} = |Z_d| e^2/aT_e$ ,  $\tau = T_i/T_e$ , and  $\mu = m_i/m_e$ . Here,  $T_e$ ,  $T_i$ ,  $m_e$ , and  $m_i$  are the electron and ion temperatures and masses, respectively. The simplest illustrative solution of (4.6) for a hydrogen plasma with  $T_e = T_i$  and  $P_e \ll 1$  yields  $\mathcal{Z} = 2.5$ . In an RF discharge, the dust density is often high enough to yield  $P_e \gg 1$ . For example, for the representative parameters of the experiments of Boufendi *et al.* described in Section 2.1 ( $n_i \sim 5 \times 10^9 \text{ cm}^{-3}$ ,  $n_d \sim 10^8 \text{ cm}^{-3}$ ,  $T_e \sim 2 \text{ eV}$ ), the parameter  $P_e$  appears to be approximately 3.2. Hence, from (4.6) one can deduce that the particle charge is approximately 60% smaller than the charge of an individual dust particle under the same conditions [44].

Physically, the grains in the dense powder clouds have larger, as compared to the case of individual particles, capacitance. Each of the grains can be regarded as a tiny capacitor with an inner conducting spherical core and a near-grain plasma sheath as an outer capacitor shell. The closer dust packing results in a smaller interparticle spacing, which can become comparable to  $\lambda_{Di}$ . In this case the near-grain sheaths shrink, which increases the effective capacitance of the grain-sheath structure. An increase of the capacitance can also be regarded as an increase in the dust size  $a$  entering (4.5) and the effective area of collection of the plasma particles. Hence, each grain in a powder cloud would

be capable to collect more plasma electrons than any individual particle of the same size. However, the number of electrons in the plasma is controlled by the established creation–loss species balance in the discharge and the average number of electrons available per each grain is smaller than it would be in the case of an individual grain, which does result in a substantial decline of the average dust charge as well as the grain surface potential. Furthermore, an increase of the relative charge density of fine particles  $P_e$  enhances the charge imbalance between the electrons and ions in and elevates the overall electrostatic potential of the cloud [186].

The charge reduction phenomenon in the ensembles of dust particles has a remarkable effect on the formation of correlated and coupled complex plasma systems. As it will be detailed in the following sections, the efficiency of dust coupling is proportional to  $Z_d^2/d$ , where  $d$  is the interparticle spacing. Hence, the reduction of the average grain electrostatic charge in the ensemble can be interpreted as a natural reaction of the system to impede the formation of the coupled state. For this reason, very dense (up to  $n_d \sim 10^{12} \text{ cm}^{-3}$ ) clouds of nano-sized particles (generated in the plasma processing experiments discussed in Section 2) carrying only a few electron charges most often remain weakly coupled. However, in situations when the interparticle spacing becomes small enough, the coupling effects discussed in the following sections prevail provided that the dust charge exceeds a certain value derived from Ikezi's criterion [187]. Most recently, it has been shown [188] that the dust grains, when packed closely (intergrain spacing is less than the Debye length), shield each other via charge reduction. In other words, dust charge reduction is a consequence of the mutual screening of grain charges [188].

The simplest dust charging model discussed above has been extended into more complicated cases of charging in multiple-species plasmas (by including negative ions, streaming effects, etc., see e.g. [189,190]), various effects of electron emission (photoelectron, secondary electron, field emission, etc.), size-dependent quantum effects, charge fluctuations above the equilibrium value, dust polarization phenomena, geometrical/shape effects, effects of magnetic field, and several others. Some of the above situations will be briefly discussed below.

Even though the dust particles are usually charged negatively (as in the previous examples), in some cases they can have a positive electric charge. Such a situation can develop, e.g. when electrons are emitted from the particle due to electron emission that originates because of the electron impact, UV exposure, thermoionic emission, and field emission. The electron emission constitutes a positive current with respect to the particle, and if it is large enough, it can cause the particle to be positively charged. It is remarkable that even if the particle is not always positive, the charge on it might sometimes fluctuate to a positive level.

The secondary emission yield  $\delta$  depends on both the impact energy and particle material. The yield is generally much larger for the electron impact than for the ion impact. However, the secondary electron emission due to the ion impact can be important for ion energies above several keV, which can be the case in the plasma immersion ion implantation and ion extraction experiments. Note that the secondary emission from small particles can be significantly enhanced above the value of bulk materials. This was shown by Chow et al. [191], whose theory also included relevant geometric effects. Scattered electrons escape more easily from a small particle than from a semi-infinite slab of material, so  $\delta$  is also enhanced. The expressions for the secondary electron currents caused by impinging electron currents are normally complex functions of the impact energy, maximum-yield energy, temperatures of the plasma and emitted (secondary) electrons, surface potential of the grain, and are presented for the case of Maxwellian electron energy distribution functions in Ref. [44].



Submicron and nano-sized particles also feature a pronounced field emission due to strong electrostatic fields near curved (e.g. sharp) surfaces. The critical fields for the ion (for positively charged particles) and electron (for negatively charged dusts) emission vary depending on the material and are typically in the range  $10^6$ – $10^8$  V/cm. This mechanism has recently been of a great importance due to the fabrication of carbon-based electron field emitting structures in chemically active complex plasmas.

Photoelectron emission is yet another factor that affects the dust charge. It is caused by intensive UV-fluxes that can release photoelectrons and thus cause positive grain charging currents. Such strong UV fluxes can originate e.g. in low-temperature plasmas of gas mixtures containing highly-radiant gases with high excitation and UV emitting capacity. In  $\text{SiH}_4 + \text{Ar}$  gas mixtures (see Section 2) of many plasma processing tools, UV-radiation from excited argon atoms has shown to be a factor affecting the coagulation (via the equilibrium electrostatic charge) of nanometer-sized particles [16]. If the flux of the emitted photoelectrons is strong enough, the grain can charge positively.

The electron emission depends on the material properties of the particle (its photoemission efficiency). It also depends on the particle's surface potential, because a positively charged particle can recapture a fraction of its photoelectrons. Taking this into account, the photoemission current is given by [2]

$$I_v = 4\pi a^2 \Upsilon_v \gamma_{\text{ph}}, \quad \phi_s \leq 0,$$

$$I_v = (4\pi a^2 \Upsilon_v \gamma_{\text{ph}}) \exp(-e\phi_s/T_p), \quad \phi_s > 0,$$

where  $\Upsilon_v$  is the UV flux and  $\gamma_{\text{ph}}$  is the photoemission efficiency (typically,  $\gamma_{\text{ph}} \approx 1$  for metals and  $\gamma_{\text{ph}} \approx 0.1$  for dielectrics). The above expressions assume an isotropic source of UV radiation and Maxwellian distribution of the photoelectrons with temperature  $T_p$ . Further discussion of the effect of UV on dust charging and collective phenomena in strongly irradiated plasmas can be found elsewhere [192,193].

Note that in thermal plasmas irradiated by intense lasers, the electron current can be emitted thermionically, which results in the positive dust charge [194]. We also note that in very low-density plasmas of various space environments a photoelectric charging mechanism can be a dominant one. For example, the photoelectric charging measurements were performed on isolated grains and grains near a photoemissive surface in vacuum [195]. Isolated grains reach a positive-equilibrium floating potential, dependent upon the work function of the particle, which causes the emitted electrons to be returned. Fine particles near a photoemitting surface can reach a negative floating potential, which reaches the equilibrium when the sum of the emitted and collected currents is zero. The particles tested are 90–106  $\mu\text{m}$  in diameter and are composed of Zn, Cu, graphite, and glass.

Charging of dust grains in the plasma was investigated experimentally in Ref. [196]. The experiment utilized as the basic plasma source, a  $Q$ -machine in which a fully ionized, magnetized potassium plasma column of  $\sim 4$  cm diameter and  $\sim 80$  cm length is produced by surface ionization of potassium atoms from an atomic beam oven on a hot ( $\sim 2500$ ) tantalum plate. The basic constituents of the ambient plasma are  $K^+$  ions and electrons with approximately equal temperatures  $T_e \approx T_i \approx 0.2$  eV and densities in the range of  $10^5$ – $10^{10}$   $\text{cm}^{-3}$ . To dispense the hydrated aluminum silicate (kaolin) dust particles into the plasma, the plasma column was surrounded over its portion by a rotating dust dispenser. The grains had a size distribution in the range of 1–15  $\mu\text{m}$  with an average grain size of 5  $\mu\text{m}$ . The dust number density was measured via estimating the dust flux

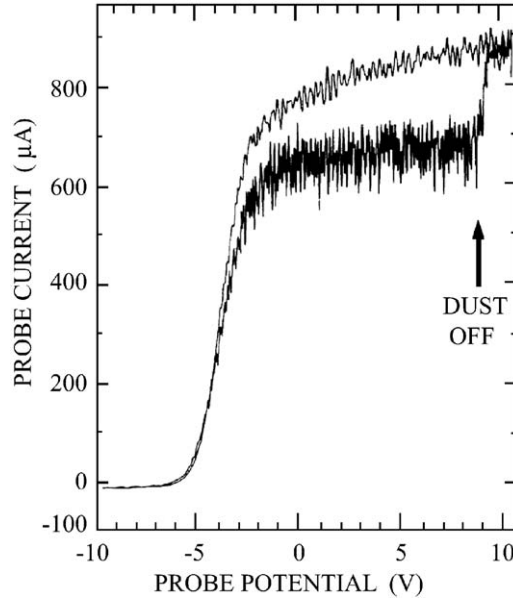


Fig. 6. Langmuir probe characteristics obtained for the same conditions, except for the absence (upper plot) or presence (lower plot) of dust. When the dust dispenser is turned off (dust off arrow on a diagram), the lower plot reproduces the upper one. Reprinted from Ref. [196].

from the dispenser to the collector and via measuring the spatial decay of the ion density within the dust cloud, and was approximately  $\sim 5\text{--}6 \times 10^4 \text{ cm}^{-3}$ .

The main diagnostic tool of the plasma was a Langmuir probe, which is a 5 mm in diameter tantalum disk. The Langmuir probe enabled one to determine how the negative charge in the plasma is divided between free electrons and negatively charged dust grains. Fig. 6 shows the Langmuir probe characteristics obtained under identical conditions except for the absence (upper curve) or presence (lower curve) of dust, with the electron portion of the characteristic shown as a positive current. When the dust is present, the electron saturation current  $I_e$  to a positively biased probe is smaller than the current  $I_{e0}$  measured without dust. This is due to the fact that the plasma electrons, which attach to dust grains of extremely low mobility are not collected by the probe. The ratio  $\eta_{ei} = (I_e/I_{e0})/(I_i/I_{i0})$  is then a measure of the fraction of negative charge present as the free electrons in the dusty plasma  $\eta_{ei} = n_e/n_i$ , where  $I_i$  and  $I_{i0}$  are the ion saturation currents with and without dust, respectively. Careful checks were made to ensure that the probe functions properly by the return of the electron saturation current to the “no-dust” level when the dust inlet is abruptly turned off. The plasma density was estimated from the electron saturation current. The dust charge was then computed from the overall charge neutrality condition.

The experimental procedure, details of which can be found in Ref. [196], then involved the measurement of  $\eta_{ei}$  as a function of the electron number density  $n_{e0}$ , keeping the dust size and density as well as electron/ion temperatures fixed. Variation of  $n_{e0}$  resulted in remarkable changes in the ratio between the intergrain spacing  $d \sim n_d^{-1/3}$  and the electron Debye length  $\lambda_{De}$ , which, in turn, affected the dust grain charge values due to the “close packing effect”. Specifically, for the

parameters of the experiment [196], the measured value  $Z_d$  approaches to the charge of the isolated grain of  $\approx 3000$  when the ratio  $d/\lambda_{De} \sim 5$  and decreases to  $Z_d \approx 30$  when  $d/\lambda_{De} \sim 0.5$ . Thus, the reduction of the dust charge in a dense dust cloud compared to an isolated dust grain has been confirmed experimentally. Further details can be found in Ref. [196].

For nanometer-sized particles, which are often merely macromolecules or atomic/molecular clusters, one has to consider the specific cross-sections for the electron/ion capture. Therefore, one cannot a priori predict the charge of an arbitrary nanometer particle, and one can also expect noticeable charge fluctuations [197]. The latter continuous fluctuations arise from the stochastic nature of the charging process (e.g. stochastic nature of encounters between particles in the plasma) and the discrete nature of the electric charge [198].

The charging equation (4.5) was obtained by assuming the continuity of the charging process and the equal electric charge on the same size grains. This is apparently not the case for nano-sized particles that typically carry a positive or negative charge of a few to few tens of electric charges. The charge fluctuations can be quantified by the probability  $f_q$  of the grain to carry the electric charge  $qe$  and accounting for stepwise changes of the grain charge in the positive and negative directions upon collisions with the plasma electrons and ions. In the model of monodisperse cloud of identical non-interacting cloud, the discrete population balance equation is [198]

$$\frac{\partial f_q}{\partial q} = J(q+1 \rightarrow q) + J(q-1 \rightarrow q), \quad (4.7)$$

where  $J(q+1 \rightarrow q) = I_{e,q+1}f_{q+1} - I_{i,q}f_q$  and  $J(q-1 \rightarrow q) = I_{i,q-1}f_{q-1} - I_{e,q}f_q$  are the net flows of particles from the charging state  $q+1$  to  $q$  and from  $q-1$  to  $q$ , respectively. The solutions for each of the charging states  $q$  are found recursively by successive iterations by noting that in the equilibrium  $J(q+1 \rightarrow q) = J(q-1 \rightarrow q) = 0$  and enforcing the appropriate normalization conditions. It is notable that the charging states of larger nanoparticles with relatively slower changes of  $f_q$  with charge can be treated as a quasicontinuous function  $f(q)$ . In this case (4.7) can be reduced to the Fokker–Planck equation:

$$\frac{\partial f(q)}{\partial q} = -\frac{\partial (I_i - I_e)f(q)}{\partial q} + \frac{\partial^2 (I_i + I_e)f(q)}{\partial q^2}, \quad (4.8)$$

where the second term on the rhs of (4.8) is the source of fluctuations around the equilibrium value  $q_0$  obtained from the equality of electron and ion currents. The term proportional to the current imbalance  $I_i - I_e$  is responsible for the restoring force, which tends to bring the charge to the equilibrium. Further assuming that in the vicinity of  $q_0$  the electron and ion currents vary slowly with charge, one can arrive to the following Gaussian charge distribution

$$f(q) = \frac{1}{\sqrt{2\pi\sigma_q^2}} \exp \left[ -\frac{(q - q_0)^2}{2\sigma_q^2} \right], \quad (4.9)$$

where the physical details of the charging process are incorporated into the mean ( $q_0$ ) and the variance ( $\sigma_q$ ) of the distribution function.

It is remarkable that the ratio  $\sigma_q/q_0$  scales with the grain size as  $1/\sqrt{a}$  [198]. Thus, the relative magnitude of charge fluctuations is smaller for larger particles. Furthermore, for the particles larger

than 100 nm, the assumption of the invariable mean charge is usually valid. On the other hand, treatment of the charging of nanoparticles smaller than 10–20 nm will most likely require the consistent discrete population balance approach with the charging equation (4.7). In this case, when the variance  $\sigma_q$  is comparable with  $q_0$ , the fluctuations can reverse the sign of the grain charge [197,198]. An example of the use of this technique in the modeling of silane plasma discharges contaminated by the plasma-grown nanoparticles is given in [199].

Another effect that complicates description of the charging of nanometre-sized particles is an instantaneous charge separation on the nanoparticle surface under the action of external electrostatic fields such as the fields of the charged plasma species. Thus, the finite polarizability of the grains gives rise to induced (image) forces. The latter forces are always attractive and contribute to the enhancement of the nanoparticle collision cross-sections with the electrons and ions [198].

Moreover, highly polarizable conductive nanoclusters and nanoparticles are strongly affected by the long-range image forces as a result of their interaction with the low-energy plasma electrons. The resulting electron–nanoparticle interaction potential  $V_{\text{pol}} = -\alpha_{\text{dip}}e^2/2r_{\text{en}}^4$ , which is proportional to the nanoparticle dipole polarizability  $\alpha_{\text{dip}}$  and inversely proportional to the distance between the electron and nanoparticle  $r_{\text{en}}$  thus contributes to the larger electron capture cross sections and has recently been invoked in the explanation of the enhanced electron attachment to C<sub>60</sub> fullerenes [200]. The resulting size-dependent electron capture cross-section is  $\sigma_e(\mathcal{E}) = \pi a^2 + (2\pi^2\alpha_{\text{dip}}e^2/\mathcal{E})^{1/2}$  and represents a sum of the nanoparticle hard-sphere area and the Langevin cross-section. This result has been experimentally verified via precise measurements of the absolute cross-sections for the capture of low-energy electrons by the large Na<sub>9000</sub> nanoclusters ( $a \sim 4$  nm) [200]. Furthermore, the image forces modify the charge and variance of a 1 nm particle by 30% [198]. However, this effect is reduced to  $\sim 15\%$  for  $\sim 10$  nm particles. Naturally, the enhanced electron capture by highly polarizable nanoparticles results in the collection of larger amounts of negative charge and hence to the shift of the charge distribution to more negative values.

In some circumstances, a precise quantification of the electronic levels in individual nanoparticles/nanoclusters may be in order. For example, the results on the electronic properties of silicon nanocrystals (nc-Si) grown on Si(100) are presented in Ref. [201], where the charging and confinement energies of single hemispherical quantum dots were deduced from  $I(V)$  curves recorded using scanning tunnelling microscopy. The inclusion of the electronic structure into the charging theories of the dust grains in the plasma is a challenging task for the coming years.

Nevertheless, simpler semiclassical considerations have been recently used to estimate the capacitance and polarizability of nanospheres and nanocylinders in a Thomas–Fermi approximation [202–204]. In this case the nanoparticle electronic level structure is dense enough to warrant a semiclassical treatment but not so dense that the contribution of the finite density of states is negligible. The corresponding Thomas–Fermi capacitance  $C_{\text{TF}}$  is a complex function of the ratio  $a/l_s$ , where  $l_s$  is the charge screening distance that depends on the density of states per unit volume at the Fermi level. It is notable that  $C_{\text{TF}} < C_0$ , where  $C_0 = a$  is the classical nanoparticle self-capacitance. The addition of surface localized (bound) charge states drives the actual nanoparticle capacitance towards the classical limit [202]. These results are relevant to metallic and semiconductor nanoparticles and various carbon-based nanostructures.

Interaction of nano-sized particles with the high-energy plasma electrons can be even more complicated due to the tunnelling effects, when electrons can pass through the grain. However, the tunnelling currents are non-negligible for the electron energies  $\mathcal{E} > 10^4 \sqrt{a(\mu\text{m})}$  eV [186].

The shape of the particle is yet another important factor affecting the charging process. This has been clearly demonstrated by modeling and experiments on the dust levitation (the physics of this process will be discussed below in Sections 4.3–4.5) in a plasma sheath. One of the most recent experiments was performed in a Gaseous Electronics Conference (GEC) reference plasma reactor without an upper grounded electrode and a ring on a driven electrode to create a shallow electrostatic well for the levitating powder [205]. The two kinds of nylon microrods of the diameters 7.5 and 15  $\mu\text{m}$  and the typical lengths of 0.3 mm, with some as long as 0.8 mm. The microrods were levitated in a collisional sheath of the RF plasma. The rods below a critical length settled vertically, parallel to the electric field, while the longer rods floated horizontally. In the case of the levitation of 7.5  $\mu\text{m}$  thick microrods in a 52 Pa discharge in krypton with the characteristic electron temperature of 2.2 eV and the electron number density of  $\sim 3 \times 10^9 \text{ cm}^{-3}$ , the critical orientation length appears to be 0.37 mm. The typical intergrain distance was varied in the experiments but remained within the range of 0.3–1.0 mm. The details of the plasma sheath and rod-like particle charging models that find a reasonable agreement with the experiment, can be found in Ref. [205].

Recently, a theoretical model adequately describing the charging of rod-like particles in gas discharge plasmas of the experiments [205] has been developed [206]. The equilibrium charge has been calculated for the elongated particles orientated differently with respect to the established ion fluxes in the near-electrode areas. In the calculations, it was assumed that the charge redistribution over the particle surface requires much shorter time scales compared with the charging time scales due to the plasma particle absorption. In this case the surface potential can be assumed constant and the problem was solved through the calculation of the total ion flux onto the particle surface [206].

Despite a remarkable progress in the studies of the dust charging mechanisms in the past decade, there are still many unsolved problems. For example, there is very little known about the charging of dust grains in magnetized plasmas. In particular, this is due to the overwhelming complexity to self-consistently incorporate the effects of finite Debye lengths, collisions, and magnetic field-affected particle trajectories near the grain surface [207]. However, the simplest expressions for the electron and ion currents (4.1)–(4.4) are fairly accurate in the limit of weak magnetic fields when  $\rho_L \gg a$ , where  $\rho_L = v_{Te}/\omega_{ce}$  is the electron Larmor radius, and  $\omega_{ce}$  is the electron cyclotron frequency [208].

Another apparent challenge in the development of the adequate models of dust charging in non-stationary plasmas. An example of the so-called dust “decharging” (neutralization) phenomenon in the discharge afterglow (after switching the discharge power off) is given in [209].

The examples given in this section certainly do not cover the overwhelming variety of the charging scenarios and mechanisms of nano- and micron-sized particles in low-temperature plasmas. Further discussions on the recent progress in the physics of dust charging can be found in [210].

#### 4.2. Particle charge as a function of the grain size

Since complex plasmas are open systems, parameters of the macroscopic particle component such as particle charge appear as a function of not only their “internal” characteristics (size, shape, material, etc.), but also as a function of “external”, with respect to that component, plasma conditions (e.g. plasma density and temperature). From Section 4.1 we recall that the charge can be reasonably predicted by the widely adopted OML model, where the dust grain is considered as a spherical probe and the charging is due to the plasma currents onto the grain surface [3,44]. The currents are calculated by assuming that the electrons and ions are collected when their (mostly collisionless)

orbits intersect the probe surface. Usually, the electrons are assumed to be Boltzmann distributed, and the ions are “shifted Maxwellian”, taking into account their possible drift velocity in the external field [45]. We also recall that in the simplest approximation of small ( $a \ll \lambda_{Di}$ ) spherical particles their charge is  $Q = a\varphi_s$  [3,44]. If  $\varphi_s = \text{const}$ , one can expect that the particle charge is directly proportional to its radius.

It is a common experimental practice to levitate the dust particle structures in the sheath region of RF discharge plasmas. Sophisticated experimental methods have been developed [213–218] to elucidate the charge on a dust grain. Most of these reported experimental data demonstrate nonlinear dependency of the particle charge on its size. Here, we discuss the experiments dedicated to clarify the dependence of the dust charge as a function of its size in an RF discharge plasma [219]. The experiments are complemented by modeling the charge behavior of a dust particle in the sheath region. Among the possible contributions to the particle charging, the effects of superthermal electrons (STE) are singled out. We note that the presence of STE can indeed cause the observed nonlinear behavior of the charge on the size of a levitating particle.

The experiments were carried out in a capacitively coupled RF discharge in argon at the University of Sydney. The experimental setup is described in detail in Refs. [219–221]. The typical plasma parameters of the experiments [219] are: the plasma density  $n_e \sim 2\text{--}8 \times 10^8 \text{ cm}^{-3}$  and the electron temperature  $T_e \sim 1\text{--}1.5 \text{ eV}$ . The particles used in the experiments were spherical of different material: melamine formaldehyde ( $\rho = 1.5 \text{ g/cm}^3$ , radius  $a = 1.45, 2.12, 2.83, 3.05, 3.52 \text{ }\mu\text{m}$ ), carbon ( $\rho = 2.1 \text{ g/cm}^3$ ,  $a = 1.05 \text{ }\mu\text{m}$ ), corundum ( $\text{Al}_2\text{O}_3$ ,  $\rho = 4.05 \text{ g/cm}^3$ ,  $a = 2.45 \text{ }\mu\text{m}$ ), and glass balloons ( $\rho_{\text{eff}} = 0.8 \text{ g/cm}^3$ ,  $a = 5 \text{ }\mu\text{m}$ ). The charges on the particles were measured by two techniques successfully used previously, namely, by the vertical equilibrium technique [221,222] and by the vertical resonance technique [222,223]. The results of these methods are in a good agreement. Some other techniques for the dust charge measurement are reviewed in Section 4.7.

Circles in Fig. 7 represent the experimental dependence of the charge on the levitating melamine formaldehyde particle on the size for the input power of 60 W and the pressure of 18.3 Pa (Fig. 7a) and of 12.1 Pa (Fig. 7b). The obtained dependencies are strongly nonlinear and have the exponentials 1.85 (Fig. 7a) and 1.66 (Fig. 7b). This result is in agreement with the data (the exponentials are within the range from 1.7 to 2.5) reported elsewhere [216,218].

In general, the particle charge can be written as  $Q = F(a)\varphi_s$ , where the function  $F(a)$  is not necessarily linear. On the other hand, the surface potential reflects the plasma parameters “probed” by the particle at the point of levitation. Indeed, from the current balance equation, the potential appears as  $\varphi_s = f^\varphi(n_e/n_i, T_e, v_i)$ . The plasma parameters at the point of levitation are the functions of the particle size, i.e.  $n_e/n_i = f^n(h_{\text{lev}})$ ,  $T_e = f^T(h_{\text{lev}})$ , and  $v_i = f^v(h_{\text{lev}})$ , where, in turn, the levitation height  $h_{\text{lev}} = f^h(a)$ . Thus the surface potential is  $\varphi_s = f^\varphi[f^n(f^h(a)), f^T(f^h(a)), f^v(f^h(a))]$  and the particle charge appears as a complex function of its size via the size dependence of the levitation height and the height dependence of the plasma parameters.

To elucidate the contribution of different functions ( $f_n^\varphi$ ,  $f_T^\varphi$ , and  $f_v^\varphi$ ) into the charge dependence on the radius of a levitating particle, the charge was also calculated [219] on the basis of the self-consistent hydrodynamic model of the dust levitation and equilibrium in the collisional plasma sheath taking into account the ionization processes. For more details of the model, see Ref. [224], where a one-dimensional (1D) discharge configuration is considered for typical experimental parameters. All variables of interest are calculated self-consistently in the sheath as functions of the distance  $z$  from the electrode and given plasma parameters in the bulk, namely, the sheath potential  $\varphi(z)$ , the



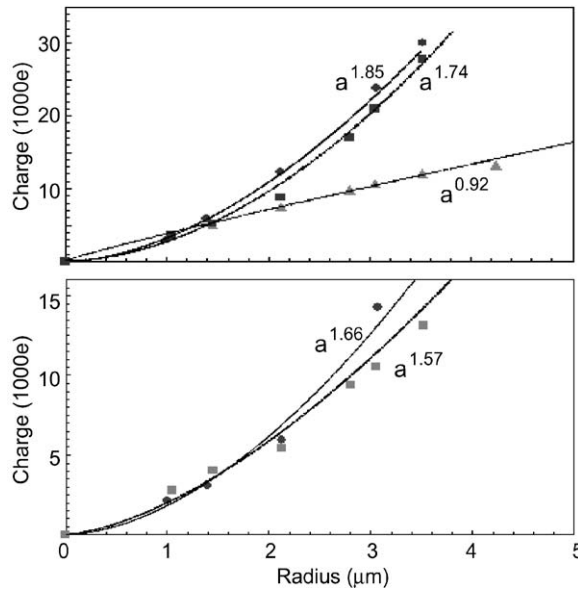


Fig. 7. Dependence of the charge of the levitating particle on the size. Circles represent the experimental results, rectangles—the results of theoretical modeling with STE, and triangles—the theoretical modeling without STE [219].

electric field  $\mathbf{E}(z) = \hat{\mathbf{z}}E(z) = -d\phi(z)/dz$ , the ion flow velocity  $\mathbf{v}_i(z) = \hat{\mathbf{z}}v_i(z)$  and density  $n_i(z)$ , and the main electron density  $n_e(z)$ , which is supposed to be Boltzmann distributed. The temperature of the main electron population is assumed uniform in the entire region of interest. The fraction of STE, with the ratio of the STE density to the ion density at the electrode as a boundary condition, is determined by the secondary emission yield and is taken as  $n_{eh}(0)/n_i(0) = 0.045$  [225,226]. Furthermore, the model space distribution is taken in the form close to the step function in space, namely,  $n_{eh} = (n_0/2)(\tanh[(z - z_0)/z_1] + 1)$ , where the shift of the step is  $z_0 \sim z_{sh}$  where  $z_{sh}$  is the sheath and pre-sheath width, and the width of the step  $z_1 \sim \lambda_{De}$ .

The ion dynamics is governed by the continuity and momentum equations. The continuity equation for the ions takes into account plasma production; the main mechanism of ionization is assumed to be electron impact ionization with the additional contribution of STE so that the effective plasma ionization source is proportional to the neutral gas, and contains “standard” contribution of plasma Boltzmann electrons with exponential of the inverse of the electron temperature [48,224], and the additional STE contribution depending on the STE density and the STE temperature. Solution of the equation for the balance of forces together with the charging equation gives the dependence of the charge of the grain, levitating in the sheath electric field, as a function of its size, see rectangles in Fig. 7. Note a strongly nonlinear dependence for the experimental and simulation curves, with the exponentials to be sufficiently close (1.85 and 1.66 for the experiment, and 1.74 and 1.57 for the simulation). As an example of the contribution of STE, the triangles on Fig. 7a show the simulated charges of the levitating particles in the absence of hot electrons.

This effect demonstrates the nonlinear dependence of the levitating particles on the grain size when bigger and therefore heavier particles levitate deeper into the sheath (and closer to the electrode)

where the fraction of energetic electrons is higher because of the secondary emission from the electrode. On the other hand, in the absence of STE, the closer the particle to the electrode is, the more pronounced is the deficit of thermal electrons because of the electrode's electric field. Indeed, by fitting the data without STE we see that the actual power index is 0.92, i.e. the slope of the dependence is decreasing. The analysis of this simulations demonstrates that out of various contributions to the dependence of  $Q$  on the particle's size one can single out the effect of  $f_T^\phi$ . It is common to assume that the main electron temperature is not changing in the sheath region. Therefore the change of  $f_T^\phi = f_{Te}^\phi + f_{STE}^\phi$  is due to the increased number of STE closer to the electrode and the observed nonlinear dependencies are due to the different levitation heights of the particles with different sizes (and masses).

Recently, it was demonstrated [227] that even a small proportion of STE is able to significantly influence the properties of the sheath. In the experiment [227], the presence of STE was attributed to the features of the filament discharge. In the sheath of an RF discharge plasma, despite vast number of experiments, possible presence of STE was not discussed yet. One of the possible reasons for that is that the standard models [48,228] for the capacitively-coupled RF discharge plasma usually do not take into account the role of the secondary emission electrons since most of the electron current through the sheath is the capacitive displacement current. However, the ion-induced secondary electron emission from DC biased plasma electrodes is a well known phenomenon required to sustain a DC discharge [229]. Although for normal RF biases ( $\sim 10$ – $15$  V) the yield coefficient is relatively small, less than 0.05 [225,226], the influence of superthermal electrons on the sheath properties and especially on the charging of macroscopic particles is profound even in this case. The simulations discussed above indeed show that the sheath size and other characteristics such as plasma density distributions are strongly affected by STE. This, together with the effect of STE on the particle charge, leads to the significant change of the levitation heights.

The strong dependence of the surface potential on the levitating particle's size reflects the dependence of the surface potential on the levitation distance from the electrode. This opens an opportunity to employ the particles as microscopic probes for determination of the electron distribution function; this goal, however, needs more elaborated model for the sheath region. We stress here that the observed character of the charge (or the surface potential) vs size dependence can provide the information on the presence of energetic electrons in the sheath. Indeed, in the absence of STE, the surface potential shows a distinctively different behavior. Note also that the maximum possible levitation radius decreases in the absence of STE.

#### 4.3. Forces acting on the grains in the plasma

Here, we review the major forces acting on dust particles in the complex ionized gas systems. First, we discuss the original results of Ref. [45], where the transport of dust particles in glow-discharge plasmas was studied. The first apparent force that significantly affects the dust particle's transport is due to the gravity. It has the form  $F_g = m_d g$ , where  $m_d$  is the dust mass and  $g$  is the gravitational acceleration. The second, electrostatic, force  $F_E = QE$  is exerted by the electric field  $E$ . It is notable that the ion velocity that enters the expression for the microscopic ion current on the grain is a local function of the electric field (and can be related to  $E$  via the ion mobility). Hence, the electric charge of the particle also indirectly depends on the local value of  $E$ .

The third force  $F_{\text{fr}}$  results from collisions with neutral gas atoms/molecules and is therefore proportional to the working gas pressure in the chamber. Interactions between the neutrals and the dust particles are assumed to be hard sphere, elastic collisions. Using the relevant momentum cross-sections, the average momentum transferred per neutral is given by the average relative neutral velocity multiplied by the reduced mass (which is close to the neutral's mass  $m_n$ , since  $m_d \gg m_n$ ) and the cross-sectional area. Thus, the neutral drag force can be approximated by

$$F_{\text{fr}} = n_n v_R^2 m_n \sigma_{n-d} , \quad (4.10)$$

where  $n_n$  is the density of neutrals,  $v_R$  is the relative particle–neutral velocity, and  $\sigma_{n-d}$  is the cross-section for the dust particle–neutral interaction, which can approximately be taken as  $\pi a^2$ . When the grain is drifting, this force is in the direction opposite to the motion. Alternatively, when there is a net flows of neutral gas molecules, there is a momentum transfer to the particles in the direction of these flows.

The ion drag force  $F_{\text{dr}}$  is caused by the momentum transfer from the positive ion current driven by the electric field. This force consists of two components: the collection force  $F_{\text{dr}}^c$  and the orbit force  $F_{\text{dr}}^o$ . The collection force represents the momentum transfer from all ions that are collected by the particle. Each ion that impacts the grain transfers its original momentum  $m_i v_i$ . Hence, this component is given by

$$F_{\text{dr}}^c = n_i v_s m_i v_i \pi b_c^2 , \quad (4.11)$$

where  $n_i$  and  $m_i$  are the ion density and mass, respectively,  $v_s = (v_i^2 + v_{Ti}^2)^{1/2}$  is the mean ion speed that includes the directional (in the electric field)  $v_i$  and the thermal  $v_{Ti} = (8T_i/\pi m_i)^{1/2}$  components. The collection impact parameter is given by

$$b_c = a \left[ 1 - \frac{2e(\varphi_p - \varphi_s)}{m_i v_s^2} \right] ,$$

where  $\varphi_p - \varphi_s$  is the difference between the local plasma ( $\varphi_p$ ) and the particle surface ( $\varphi_s$ ) potentials. The above expression is based on the orbit motion limited probe theory. The orbit force is given by

$$F_{\text{dr}}^o = 4\pi n_i v_s m_i v_i b_{\pi/2}^2 A , \quad (4.12)$$

where  $b_{\pi/2}$  is the impact parameter with the asymptotic orbit angle of  $\pi/2$  and

$$A = \frac{1}{2} \ln \left( \frac{\lambda_{Di}^2 + b_{\pi/2}^2}{b_c^2 + b_{\pi/2}^2} \right)$$

is the Coulomb logarithm integrated over the interval from  $b_c$  to  $\lambda_{Di}$ . The contribution from the orbit force is negligible when the collection impact parameter is greater than or equal to the ion Debye length.

However, recent experiments (see e.g. [209,211]) suggested that the above classical expression underestimates the actual ion drag force. For this reason, the problem of estimating this force was revisited [212]. It has been revealed that the standard calculation of the ion–dust elastic scattering (orbital component) cross-section often fails in dusty plasmas due to larger than the Debye length range of the ion–grain interactions. Indeed, the conventional expression of [45] uses the Debye length as a cut-off in the impact parameter.

These forces acting on the dust particles critically depend on the ion velocity, particle size and specific position within the discharge. In particular, each of the forces has a different power-law dependency on the particle radius suggesting that the dominant force changes as the particle grows. The electrostatic force  $F_E$  is proportional to the particle radius since the charge depends linearly on the radius. The momentum transfer forces  $F_{fr}$  and  $F_{dr}$ , are proportional to the particle's surface area and hence the radius squared. Finally, the gravity force  $F_g$  is proportional to the particle's mass, which is proportional to  $a^3$ .

In the example given in Ref. [45] it is clearly demonstrated that the forces on the particles are very sensitive to the location within the argon discharge with neutral gas pressure of 100 mTorr, plasma density of  $10^{10} \text{ cm}^{-3}$ ,  $T_e = 2 \text{ eV}$ ,  $T_i = 0.05 \text{ eV}$ . For 100 nm particles with the densities twice the density of the water, the ion drag force moves the particle towards the wall/electrode until it senses the electric field of approximately 14 V/cm in the sheath. At this point the electrostatic and ion drag forces balance each other. For a 1  $\mu\text{m}$  particle, this point occurs for an electric field of approximately 35 V/cm. Finally, the 10  $\mu\text{m}$  particles are pulled towards the lower wall surface by the gravity force until the electric field of 82.6 V/cm is reached. In the low-density plasmas, the ion drag force is not a dominant force for the particles of this size [45].

Many recent experimental observations suggest that several complex plasma structures can be supported by the thermophoretic force  $F_T$ . The latter originates due to the temperature gradient of the neutral gas  $\nabla T_n$  from the electrode towards the bulk plasma. This force can lift the fine particles from the near-electrode area back to the central part of the discharge. The thermophoretic force opened up several new opportunities for the observation of the microparticles at a kinetic level in the plasma bulk and facilitate the investigation of complex plasma structures such as dusty plasma voids. The force  $F_T$  acting on a spherical particle in a monoatomic gas at a low pressure is given by

$$F_T = -3.33(a^2/\sigma_{at})\nabla T_n ,$$

where it was assumed that the mean free path is much larger than the particle radius. Here,  $\sigma_{at}$  is the gas kinetic cross-section for the atomic scattering. Further details about the thermophoretic force in a complex plasma and its implications for the chemically active discharges can be found in Ref. [230,76].

Note that some complex temperature effects can result in additional forces acting on the dust particles. For instance, the supersonic ion flows yield inhomogeneous temperature distributions on the grain surface. In this case the interaction of the grain with the neutral gas results in a force similar to photophoresis, although the latter is provided by a plasma recombination on the grain surface [231].

It should be noted that experimental investigation of the forces acting on dust particles is a very complex matter. Recently, an experiment has been performed to characterize the forces that act upon the fine particles in the void region of a complex plasma [232]. A dust void in an RF-generated complex plasma was produced in a laboratory experiment with an externally applied temperature gradient (for more on dust voids see Section 5.2). Laser flashing techniques were used to identify the dust and to obtain two-dimensional maps of the particle velocities. From these measurements, 2D maps of the acceleration and force acting on the grains in the void have been obtained [232].

Most recently, a series of elegant experiments on the qualitative determination of the ion drag, thermophoretic, and electrostatic forces have been reported [211]. The principle of these investigations is to study the free falling particles where the force of gravity is balanced in the vertical direction by

the neutral gas friction at a constant particle velocity, whereas all other forces act in the horizontal direction. In this way, it appeared possible to decouple the effects of the forces in two mutually perpendicular directions. Moreover, the regimes featuring weaker ion drag force have been identified. This case is important to prevent the frequently observed formation of dust voids (discussed in detail in Section 5.2) in microgravity experiments.

#### *4.4. Dynamics and levitation of fine particles in the plasma sheath: modeling and simulation*

It is well known that the charge of dust particles, being one of the most important characteristics for the trapping and interaction of dust grains, appears as a result of various processes in the surrounding plasma, mainly (under typical laboratory conditions) due to the electron and ion currents onto the grain surfaces (see Section 4.1). Thus the first step in any research on the properties of dust in a plasma is the adequate description of the surrounding plasma. Here, we note that, in general, there are two situations of interest: (i) the dust particles do not affect significantly the properties of the plasma they are embedded in (this usually corresponds to low number densities of the dust component, i.e., to a lower number of dust particles), and (ii) the dust component is relatively dense, thus changing significantly the field and density distributions of the surrounding plasma. Note that the second case corresponds to such interesting self-organized dust–plasma structures as voids and clouds in the dust–plasma sheaths [233–236].

Here, following the original work [224], we are mainly concerned with a plasma with a rarefied dust component, i.e., assuming that dust charges and electric fields do not change the plasma parameters significantly. We therefore consider the case of essentially isolated dust grains (the intergrain distance exceeds the plasma Debye length), with a low total number of dust particles. Thus the first step is the modeling of those plasma regions where the dust particles are trapped, i.e. the sheath and pre-sheath regions of the discharge.

Due to relatively high neutral gas pressures (often more than 50 mTorr for typical dust–plasma experiments), the laboratory plasma is strongly influenced by the effects of ion–neutral collisions. Thus the simplest mathematical approach relevant for collisionless plasmas [237–239] is not fully appropriate in this case. On the other hand, the correct description of collisional effects involves the speed of the ion flow and therefore naturally depends on the properties of the region (sheath or pre-sheath) we are interested in. While in the sheath region, where the speed of the ion flow is expected to exceed the ion sound velocity, a simple approximation [240] describing ion–neutral collisions can be used, in the total pre-sheath/sheath region more sophisticated approaches are necessary [241]. Thus an advanced model of momentum transfer between the ion and neutral species, which describes the ion–neutral collisions on the basis of kinetic theory, without semi-empirical approximations [242] was employed [224].

Another important issue is the rate of ionization. It was demonstrated experimentally (see, e.g., [233,235]) that an increase of the ionization rate leads to an increased size of the dust-free void region, moving the equilibrium position of the dust cloud closer to the electrodes. It is thus reasonable to expect that even in the case of dust in a plasma, with a negligible influence of the dust on the plasma and sheath parameters, the equilibrium positions of the grains are affected by the ionization process, which is included in the basic set of equations.

Note that various numerical models of dust levitation in the low-temperature plasma discharge sheath region have been developed, see, e.g., [236,243–247]. Some of the models deal with the

collisionless [246,247] or collisional [236] fluid cases without ionization, the kinetic (i.e., coupled Poisson–Vlasov equations) case [245] without collisions in the vicinity of a dust grain, as well as with particle-in-cell simulations [244] of a uniform, steady state DC plasma where plasma particle losses are assumed to be exactly balanced by a constant ionization source, or a hybrid model [243] combining Monte Carlo with fluid simulations, with the latter ignoring the equations of motion of the plasma particles.

Possible vertical motions of the dust can lead to the disruption of the equilibrium position of the grains. Note that most of the earlier analytical models considering vertical lattice vibrations [248,249] as well as numerical models studying phase transitions [250] in the dust–plasma system, dealt with dust grains of a constant charge. It was also demonstrated [247], that the dependence of the dust particle charge on the sheath parameters has an important effect on the oscillations and equilibrium of dust grains in the vertical plane, leading to a disruption of the equilibrium position of the particle and a corresponding transition to a different vertical arrangement (here, the simplest model of a collisionless plasma sheath, with supersonic velocities of the ion flow, was used [247]). On the other hand, the whole range of possible velocities of the ion flow was studied [224]. Furthermore, the sheath problem was treated self-consistently, which allows one to study possible dust trapping in a collisional plasma with an ionization source, as well as the disruption of the equilibrium. The latter can occur at various positions corresponding to not only supersonic, but also subsonic ion flow velocities at the position of the dust grain.

The charge  $Q$  of the particles (depending on the plasma parameters, in particular, on the local electric sheath potential and the velocity of the ion flow) was found in a standard way from the condition of zero total plasma current onto the grain surface. Numerical solutions [224] for the charge of a dust particle, as a function of the particle position  $z$ , are presented in Fig. 8, for the example of a dust grain of radius  $a = 4 \mu\text{m}$ .

The characteristic values of the charge at various positions, as well as the position for the maximum possible charge, are summarized in Table 4.1. The vertical and horizontal lines indicate the position of the maximum charge, and the charge where the Mach number of the ion flow becomes unity, i.e.  $v_i = v_s$  (Figs. 8a–c). An extra line in Fig. 8a indicate that in general there are two positions for a charge of less than the maximum charge.

Note that the higher is the input power (i.e. the higher  $T_e$  and  $v_{\text{ion}}$ ), the stronger are the ion fluxes, and, correspondingly, the lower is the size of the negative charge on a grain placed very close to the electrode. The dust charge can even become positive; in the case  $v_{\text{ion}} = 0.1\omega_{pi}$ , the dust charge becomes positive near the electrode, with the result that no (equilibrium) levitation is possible. The maximum possible size of the charge is larger for a higher level of ionization rate; the position of the maximum charge size becomes closer to the electrode as the ionization rate increases. We note also that the negative gradient of the equilibrium charge (i.e.,  $dQ(z)/dz < 0$ ) can lead to an instability of dust particles with respect to their vertical oscillations due to delayed charging [251].

For a particle levitating in the sheath field, the force acting on the grain includes the sheath electrostatic force, the ion drag force, and the gravity force:

$$F(z) = Q(z)E(z) - F_{\text{dr}}(z) - m_d g, \quad (4.13)$$

where the ion drag force  $F_{\text{dr}}(z) = F_{\text{dr}}^c(z) + F_{\text{dr}}^o(z)$  includes two components discussed in Section 4.3 namely, the collection force  $F_{\text{dr}}^c(z)$  and the orbit force  $F_{\text{dr}}^o(z)$ . Note that the force (4.13) includes the



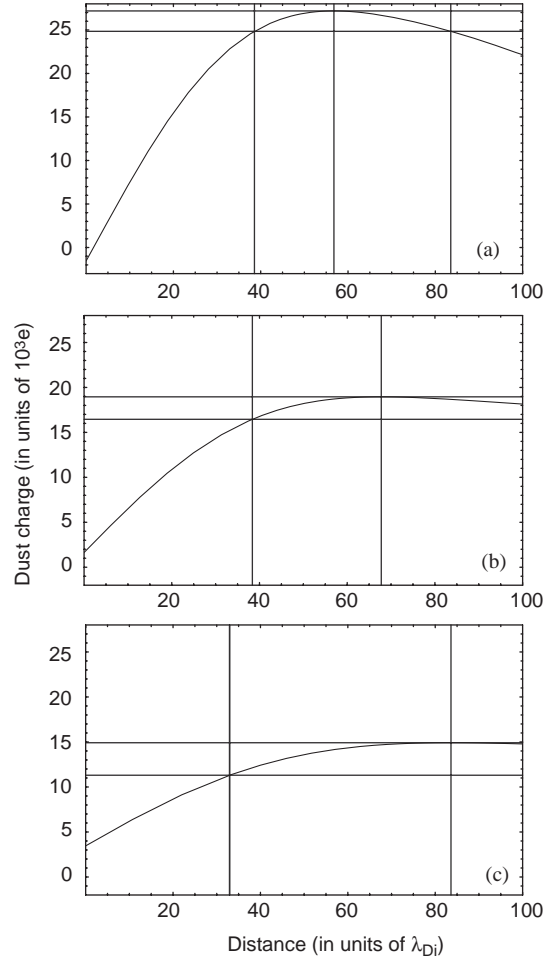


Fig. 8. Dependence of the charge  $\bar{q} = -(Q/e) \times 10^{-3}$  of the dust grain, of radius  $a = 4 \mu\text{m}$ , on the grain position  $h = z/\lambda_{Di}$ . Here, (a)  $v_{\text{ion}}/\omega_{pi} = 0.1$ , (b)  $v_{\text{ion}}/\omega_{pi} = 0.01$ , and (c)  $v_{\text{ion}}/\omega_{pi} = 0.001$ . The characteristic values of the charge at various positions, as well as the position for the maximum possible charge, are summarized in Table 4.1. The vertical and horizontal lines indicate the position of maximum charge, and the charge where  $v_i = v_s$  [224].

$z$ -dependence of the grain charge  $Q$ , since we assume an instantaneous transfer of charge onto and off the dust grain at any grain position in the sheath. The balance of forces in the vertical direction is

$$Q(z)E(z) = m_d g + F_{\text{dr}}(z) . \quad (4.14)$$

Solution of this equation together with the charging equation gives the dependence of the charge of the grain, levitating in the sheath electric field, as a function of its size. For the levitating dust particle, there is therefore a one-to-one correspondence of its size to the equilibrium position of levitation in the sheath, as shown in Fig. 9.

Table 4.1

The characteristic numbers for the dust charge calculation (Fig. 8) [224]

| Ionization<br>frequency<br>$\nu_{\text{ion}}/\omega_{pi}$ | Charge at<br>electrode<br>$q_0$ ( $10^3 e$ ) | Maximum<br>charge<br>$q_{\text{max}}$ ( $10^3 e$ ) | Position<br>of $q_{\text{max}}$<br>$z_{qm}$ (in $\lambda_{Di}$ ) | Charge at<br>$v_i = v_s$<br>$q_{vs}$ ( $10^3 e$ ) | Charge at<br>$v_i = v_{Ti}$<br>$q_{vT}$ ( $10^3 e$ ) |
|---|--|--|--|---|--|
| 0.1   | (–)  | 27.19  | 56.77  | 24.84   | 20.11  |
| 0.01  | 1.64   | 18.96  | 67.77  | 16.46   | 14.72  |
| 0.001   | 3.46   | 14.91  | 83.60  | 11.31   | 12.14  |

Here, the lines corresponding to various sizes of dust grains are plotted: as an example,  $a = 4 \mu\text{m}$ , as well as the maximum possible sizes, and the sizes corresponding to a grain levitating at the position where the Mach number of the ion flow is unity (i.e., at  $v_i = v_s$ ), as summarized in Table 4.2. Note that there are no equilibrium solutions for  $a > a_{\text{max}}$ , the latter being a function of the ionization rate (see Table 4.2). The absence of an equilibrium means that the particles with such sizes will fall down onto the electrode.

From Fig. 9 and Table 4.2, one can conclude that the greater is the ionization rate, the closer is the equilibrium position of a levitating dust grain to the electrode. This fact agrees well with the experimental observations [233,235] showing that the size of a dust void is directly proportional to the ionization rate. The void corresponds to a dust-free region where the electron impact ionization rate is relatively high, producing an outward electric field and ion flow, thus dragging the dust particles outwards. In the case discussed here, a higher ionization rate again gives a stronger ion flow, dragging the dust grain closer to the electrode. Note that if there are two positions for a grain of a given radius (e.g.,  $4 \mu\text{m}$  in Fig. 9), the one with a negative derivative  $da(z)/dz$  is stable, while the one with a positive derivative is unstable (see also the next section). We also note that the maximum possible radius for the grain levitation increases with the increase of the ionization rate, and its position also shifts closer to the electrode. Finally, we see that the smaller is the ionization rate, the smaller is the maximum possible size  $a_{\text{max}}$  of a grain capable of levitating, and therefore the greater is the proportion of dust (if there is a dispersion of grain sizes) levitating in the region of subsonic ion flow velocities, i.e., in the pre-sheath region.

It is instructive to find the total “potential energy”, relative to the electrode position, of a single dust particle of given size at the position  $z$  in the sheath electric field:

$$U_{\text{tot}}(z) = - \int_0^z dz' [Q(z')E(z') - F_{\text{dr}}(z') - m_d g] . \quad (4.15)$$

Note that the total energy in this case contains not only the electrostatic energy  $Q(z)\phi(z)$ , but also the terms associated with  $dQ/d\phi$  which represent, because of the openness of the system, the work of external forces which change the dust charge. The dependence of the total potential energy on the distance from the electrode is shown in Fig. 10.

It can be seen that the potential has a maximum and a minimum, corresponding to the two equilibrium positions found above. The minimum (the stable equilibrium) disappears if  $a > a_{\text{max}}$  (curve (1) in Fig. 10). Other effects, such as an electron temperature increasing towards the electrode, may serve to increase the negative charge on a grain, and so preserve an equilibrium. The critical (maximum possible for levitation) radius appears also in Fig. 9; for the decreasing ionization rate,

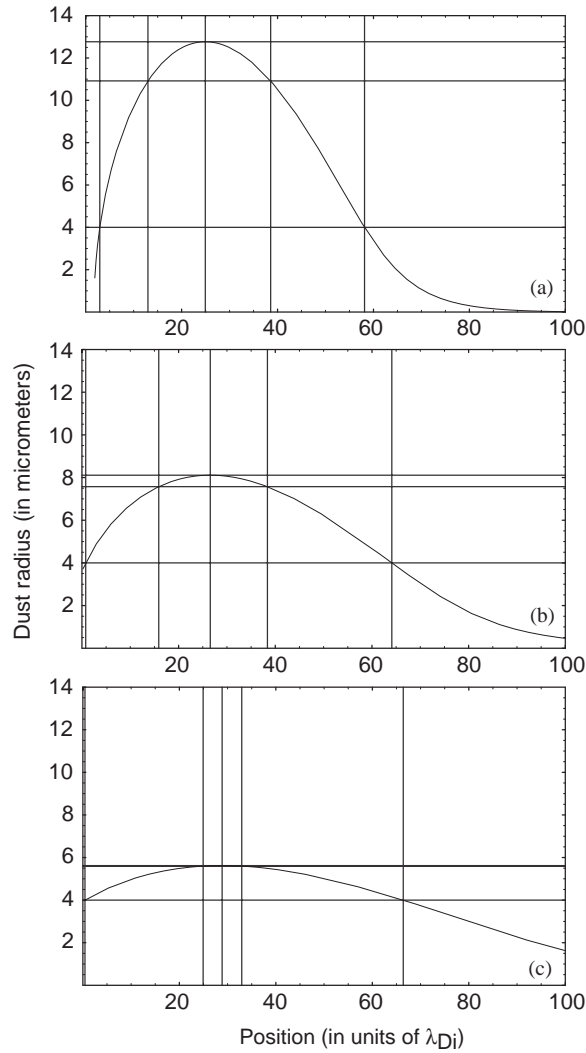


Fig. 9. Dependence of the size of the dust grain (in  $\mu m$ ), levitating in the sheath electric field, on its position  $h = z/\lambda_{Di}$ . Here, (a)  $v_{ion}/\omega_{pi} = 0.1$ , (b)  $v_{ion}/\omega_{pi} = 0.01$ , and (c)  $v_{ion}/\omega_{pi} = 0.001$ . The lines correspond to various sizes of dust grains: as an example,  $a = 4 \mu m$ , as well as the maximum possible sizes, and the sizes corresponding to a grain levitating at the position where the Mach number of the ion flow is unity (i.e., at  $v_i = v_s$ ), as summarized in Table 4.2. Reprinted from Ref. [224].

$a_{max}$  also decreases (see Table 4.2). For  $a > a_{max}$ , the minimum of the potential energy curve disappears thus indicating that there is no equilibrium position for such grain sizes.

Thus, for a collisional plasma with an ionization source, for a grain size  $a$  less than the critical radius  $a_{max}$ , there is a stable equilibrium position close to (or in) the presheath; for sufficiently high input powers (within a certain range of grain sizes, see Fig. 9), there can also be an unstable equilibrium position deeper inside the sheath. For  $a$  greater than the critical radius  $a_{max}$ , there is no

Table 4.2

The characteristic numbers for the dust grain radius and the position of dust levitation (Fig. 9); reprinted from Ref. [224]

| Ionization<br>frequency<br>$\nu_{\text{ion}}/\omega_{pi}$ | Maximum<br>grain radius<br>$a_{\text{max}}$ ( $\mu\text{m}$ ) | Position of<br>grain $a_{\text{max}}$<br>$z_{\text{am}}$ (in $\lambda_{Di}$ ) | Radius of the<br>grain ( $v_i = v_s$ )<br>$a_{vs}$ ( $\mu\text{m}$ ) | Positions<br>of a 4 $\mu\text{m}$ grain<br>(in $\lambda_{Di}$ ) | Unstable<br>position<br>$a_{vs}$ (in $\lambda_{Di}$ ) |
|---|---|---|--|---|---|
| 0.1   | 12.77   | 24.93   | 10.92  | 58.14(2.93)   | 12.97   |
| 0.01  | 8.11  | 26.55   | 7.57   | 64.11(0.78)   | 15.89   |
| 0.001   | 5.62  | 28.87   | 5.60   | 66.41(0.43)   | 24.93   |

equilibrium position. Note that possible vertical oscillations about the stable equilibrium may develop high amplitudes, thus leading to a fall of the oscillating grain onto the electrode when the potential barrier (see Fig. 10) is overcome.

Here, we would like to note the discussion [224] of how the change of the ionization power can affect dust size distributions in an experiment. Suppose that we start with a low ionization power and then *increase* it in the process of the experiment. Since the maximum possible size of particles capable to levitate in this case is only *increasing*, no change of dust size distribution occurs, with dust levitating closer to the electrode as the input power increases. However, if in the next experiment the ionization power is *decreased*, the possible size of particles capable to levitate is also *decreasing*, with the heaviest grains (whose size and, correspondingly, mass does not satisfy the condition for levitation) falling down to the electrode. Thus the dust size (and mass) distribution can be changed in this way, leaving only smaller particles levitating. Note also that another experimental possibility to force bigger particles (whose sizes are close to the critical one) to fall down to the electrode is to apply a low frequency modulated voltage (with the frequency close to the resonant frequency of vertical vibrations of the dust grains around the equilibrium position [247,249]) to the lower electrode thus forcing particles to oscillate. When their amplitude (and therefore the energy of oscillations) becomes large enough to overcome the potential barrier, cf. Fig. 10, they fall down and therefore are removed from the sheath region.

It was assumed in [224] that the dust density is small enough not to influence significantly the plasma parameters (such as the electric field, etc.). The performed study has also demonstrated some qualitative features of dust trapping and equilibrium for those experiments (e.g. on void formation [233,235]), where the dust density is higher. One can therefore qualitatively conclude that the effects of single particle trapping and equilibrium are important also for the levitation of dust distributions. For dust clouds, there are several physical effects important for the particle trapping and equilibrium, among which are: the change of the plasma electric field, density, etc. distributions due to the charged dust cloud [234,236], and the change (decrease) of the charge of a dust particle due to the presence of neighbouring grains in the cloud [252,253]. The quantitative answer to the question of the differences between the dense dust cloud and the isolated dust particle trapping can be done only after the corresponding theory for the dust distributions is developed.

Another issue is the influence of the ion flow effects on the stability and equilibrium of dust grains. For an adequate description of the effects of the ion wake [254], see Section 6 below, a treatment taking into account the plasma ion kinetics is necessary. It is physically clear that for

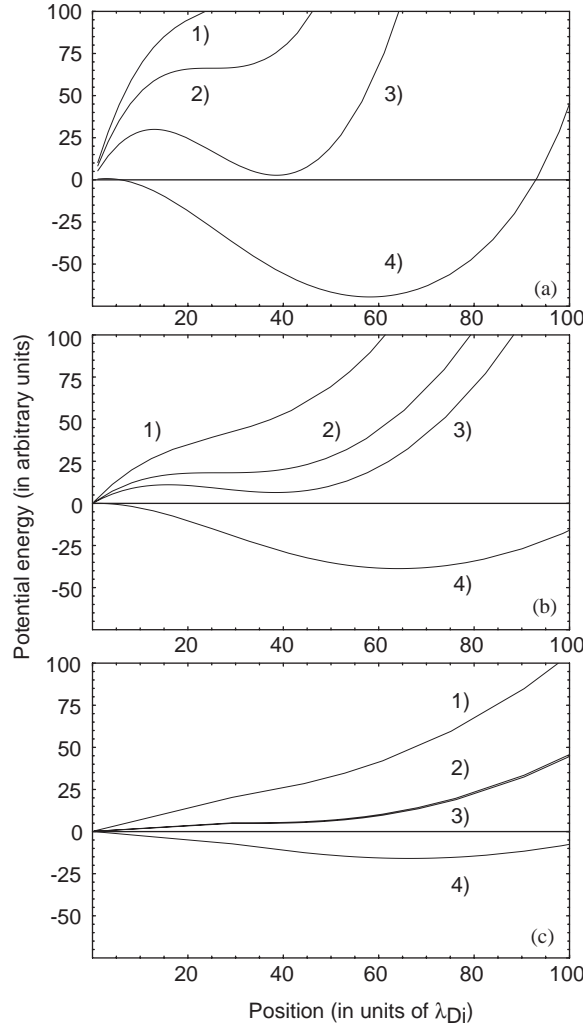


Fig. 10. The total interaction energy  $U_{\text{tot}}$  as a function of the distance  $h = z/\lambda_{Di}$  from the electrode for the different sizes of a dust particle and the different ionization rates: (a)  $v_{\text{ion}}/\omega_{pi} = 0.1$ , (b)  $v_{\text{ion}}/\omega_{pi} = 0.01$ , and (c)  $v_{\text{ion}}/\omega_{pi} = 0.001$ . The curves correspond to: (1)  $a = a_{\text{max}} + 1 \mu\text{m}$ ; (2)  $a = a_{\text{max}}$ ; (3)  $a = a_{\text{vs}}$  and (4)  $a = 4 \mu\text{m}$ . See also Fig. 9 and Table 4.2. Reprinted from Ref. [224].

a monolayer dust distribution (in the plane of the electrode) the ion wake effects are not important. On the other hand, for a highly collisional plasma the wake effects are not strong if the ion–neutral mean free path is of the order of the plasma Debye length, when the ion focussing is destabilized by frequent ion–neutral collisions. Similarly, for sufficiently dense dust distributions the plasma ion kinetics can be effective only for a layer near the dust cloud-void boundary, of the order of the ion–dust (or the ion–neutral, whichever is smaller) mean free path.

#### 4.5. Dynamics of fine particles in chemically active plasmas

Dynamics of fine particles in near-electrode areas of discharge plasmas is relevant to the attempts to increase the deposition rates in a number of microfabrication processes. In this section we discuss the forces acting on and the dynamic/trapping phenomena involving submicron-sized particles in silane and fluorocarbon plasmas. The mechanisms of origin and growth of such particles in chemically active plasma environments have been discussed in detail in Section 2.1.

##### 4.5.1. Dynamics of fine particles in silane plasmas

The aim of Ref. [258] was to study experimentally how the gas flow conditions and temperature gradient govern the trapping and fallout of the particles in RF parallel-plate discharges between parallel plates and to understand this behaviour by means of a simplified theoretical modeling. The experiments were conducted in a parallel-plate 13.56 MHz capacitively coupled plasma reactor with externally heatable electrodes. The plasma discharges were sustained in silane at 20 Pa with 15–80 W RF powers. To view the dust particles in the discharge, the scattered light of a He–Ne laser was collected by a video camera. With the help of a complicated mirror system, the fine particles were visualized in various regions of the reactor. It was found that the motion and trapping of the particles is strongly affected by the gas flow conditions and the temperature gradient in the discharge.

To understand the dynamics of submicron-sized particles in the plasma, the following simplified set of equations was used

$$m_d dv_x/dt = -6\pi a \eta_{\text{eff}} v_x, \quad (4.16)$$

$$m_d dv_y/dt = -6\pi a \eta_{\text{eff}} v_y, \quad (4.17)$$

$$m_d dv_z/dt = -m_d g - \kappa_T \nabla_z T_g - 6\pi a \eta_{\text{eff}} (v_z - v_f) + F_E(z), \quad (4.18)$$

where the four terms in the r.h.s. of Eq. (4.18) correspond to the gravity, thermophoretic, neutral friction, and electrostatic forces, respectively. Here,  $a$ ,  $v$  and  $m_d$  are the radius, velocity and mass of dust particles, respectively. Furthermore,  $v_f$  is the velocity of the gas flow,  $\eta_{\text{eff}}$  and  $T(z)$  are the dynamic effective viscosity and the temperature of silane gas, and  $\kappa_T$  is the thermophoretic coefficient. In the case of a constant flow velocity in the axial direction and the constant thermophoretic force, Eqs. (4.16)–(4.18) can be decoupled. Outside the sheath, where the effect of the electric force can be neglected, the analytical solution of Eq. (4.18) can be presented as

$$v_z = v_s [1 - \exp(-t/\tau_a)] + v_{0z} \exp(-t/\tau_a),$$

where  $\tau_a = m_d/6\pi a \eta_{\text{eff}}$ ,  $v_{0z}$  is the axial component of the initial velocity, and

$$v_s = v_f - g\tau_a - \frac{\kappa_T}{6\pi a \eta_{\text{eff}}} \nabla_z T$$

is the asymptotic grain velocity at  $t \rightarrow \infty$ . The corresponding solutions of Eqs. (4.16) and (4.17) can be written in the exponential form.

The validity of the friction force is verified by monitoring the sinks of the particles after switching the discharge off when the electric force disappears. In Ref. [258], the particle positions and velocities as a function of time have been calculated for the grain radii of 150 and 100 nm. When



the discharge was on, the light particles were trapped at the sheath boundary. When the temperature gradient was applied (heating the lower electrode), the lighter particles were driven upwards by the thermophoretic force and were trapped at the sheath edge. Finally, the downward-directed gas flow (feeding gas through the upper electrode) of 30 cm/s can strongly impede the trapping of particles at the lower sheath boundary, as was confirmed by the experimental observations. The electrode heating, together with the adjustable gas flow, can result in a complete de-trapping of the fine particles in the inter-electrode region. Further details can be found in Ref. [258]. Therefore, the proper control of the thermophoretic and drag forces can contribute to the solution of the particle contamination problem in the design of industrial PECVD reactors.

#### 4.5.2. Levitation of submicron-sized particles in fluorocarbon plasmas

It has recently been revealed that inductively coupled (IC) and surface wave sustained (SWS) plasmas generated in the  $C_4F_8 + Ar$  gas mixtures have an outstanding potential for ultra-fine and highly selective etching of large-area silicon wafers [36,259]. Physically, it appears possible to achieve high dissociation rates of the feedstock gas and the high densities ( $\sim 10^{13} \text{ cm}^{-3}$  and higher) of neutral radicals at the low ( $\sim 20 \text{ mTorr}$ ) pressures.

An interesting peculiarity of fluorocarbon plasmas is that fluorine atoms and other fluorocarbon radicals relatively easily become negatively charged, in particular, due to the electron attachment. Recent data on the laser photo-detachment measurements in high-density  $C_4F_8 + Ar$  plasmas suggest that under certain conditions the negative ions can constitute a substantial proportion among other discharge species [260]. The negative ions modify the power and particle transport, the potential distribution in the discharge, as well as directly participate in the etching process. Furthermore, as was shown in Section 2.1, the fluorocarbon plasmas are prone of plasma polymerized nanoparticles that can also carry a substantial proportion of negative electric charge. Thus, the problem of the nanoparticle dynamics and trapping in fluorocarbon plasmas is of a vital interest for a number of advanced plasma etching technologies.

Using a simple model adopted in Ref. [190], we consider here a one-dimensional near-electrode region of the width  $x_{ps}$ , with an electrode placed at  $x=0$ , and plasma occupying the region  $x > 0$ . In the plasma bulk  $x > x_{ps}$ , all plasma parameters are uniformly distributed. The plasma composition is taken from the etching experiments in the mixtures of octafluorocyclobutane ( $c-C_4F_8$ ) and argon and includes the electrons, and the positive  $Ar^+$ ,  $CF^+$ ,  $CF_2^+$ , and  $CF_3^+$ , as well as negative  $F^-$  ions. The charging, the forces acting on, and the trapping of an individual single particle are considered. In the plasma bulk, the overall charge neutrality is assumed.

The specific plasma parameters and proportions of positive ions have been taken as typical values from the experiments on  $SiO_2$  wafer etching in 2.45 GHz SWS and 13.56 MHz IC plasmas at low pressures [36]. In particular, in 90% Ar and 10%  $C_4F_8$  gas mixture at 20 mTorr, the proportion of argon ions varies from 55% in the surface-wave plasmas sustained with  $\sim 400 \text{ W}$  to about 90% in the ICP ( $\sim 1.5 \text{ kW}$ ) [36]. Both plasmas feature dominant  $CF^+$ ,  $CF_2^+$ , and  $CF_3^+$  fluorocarbon ion radicals in a wide range of the RF input powers. The proportion of the negative ions in electronegative  $C_4F_8 + Ar$  discharges varies within 15% and 45% from the total number density of negative charge in some of the etching experiments in fluorocarbon-based plasmas [260].

Because of the overwhelming complexity of the gas-phase reactions and the large number of elementary processes in the fluorocarbon plasmas with negative ions, a realistic choice of the near-wall

potential  $\phi(x)$  was made [190]. The density profiles within the sheath/pre-sheath were computed according to the following Poisson's equation

$$\frac{d^2\phi(x)}{dx^2} = 4\pi e[n_e(x) + n_{F^-}(x) - n_{Ar^+}(x) - n_{CF^+}(x) - n_{CF_2^+}(x) - n_{CF_3^+}(x)] , \quad (4.19)$$

where it was assumed that the electrons and negative ions are “Boltzmann-distributed”,

$$n_e(x) = n_0(1 - \alpha_{F^-}) \exp[e\phi(x)/T_e] , \quad (4.20)$$

$$n_{F^-}(x) = n_0\alpha_{F^-} \exp[e\phi(x)/T_{F^-}] , \quad (4.21)$$

and  $e$  is the electron charge,  $T_e$  and  $T_{F^-}$  are the temperatures of electrons and negative fluorine ions. Here,

$$n_0 = n_e(x_{ps}) + n_{F^-}(x_{ps}) = n_{Ar^+}(x_{ps}) + n_{CF^+}(x_{ps}) + n_{CF_2^+}(x_{ps}) + n_{CF_3^+}(x_{ps})$$

is the combined number density of negative or positive plasma species in the plasma bulk ( $x = x_{ps}$ ), and  $\alpha_{F^-} = n_{F^-}(x_{ps})/n_0$ .

We now turn to the discussion of the ion motion in the RF-driven sheath. It is assumed that  $T_{RF} \ll \tau_{sh}$ , where  $\tau_{sh}$  is the ion sheath traverse time, and  $T_{RF}$  is the RF period. In this case, the ions respond to the time-averaged (over the time scales  $\tau_{sh} \sim t \gg T_{RF}$ ) electric field. The positive ion fluid velocities  $v_{(j)f}$  satisfy the following momentum equation:

$$v_{(j)f} \frac{dv_{(j)f}}{dx} + v_{(j)n}v_{(j)f} = -\frac{e}{m_{(j)}} \frac{d\phi(z)}{dx} , \quad (4.22)$$

where  $v_{(j)n} = n_n\sigma_{(j)n}v_{(j)}$  is the rate of the ion–neutral collisions,  $\sigma_{(j)n}$  is the cross-section for the resonance charge exchange in argon,  $n_n$  is the density of neutrals,  $v_{(j)} = [v_{(j)f}^2 + 8T_{(j)}/\pi m_{(j)}]^{1/2}$ , and  $m_{(j)}$  and  $T_{(j)}$  are the ion mass and temperature, respectively. The profiles of the non-dimensional number densities of the charged particles, spatial coordinate-dependent charges and the major forces acting on them have been computed for the following main plasma/dust parameters: the electron temperature of 2 eV, the dust size of 300 nm and 2  $\mu$ m, the particle mass density  $\rho = 1.5$  g/cm<sup>3</sup>, the plasma bulk density  $n_0 = 4 \times 10^{11}$  cm<sup>-3</sup>, the ion and neutral temperatures of 0.067 and 0.026 eV, respectively, and various positive/negative ion proportions.

From the computed distributions of the charged species in the near-electrode area one can conclude that the number density of negative ions dramatically decreases towards  $x \sim 0.6x_{ps}$ , and is negligible in the areas closer to the electrode. Furthermore, the computation suggests that all ion velocities  $v_{(j)}$ , being equal to the ion thermal velocity  $v_{T(j)} = \sqrt{8T_{(j)}/\pi m_{(j)}}$  in the plasma bulk, become equal to the ion-acoustic velocity  $v_{S(j)} = \sqrt{T_e/m_{(j)}}$  within the area  $0.2 < x/x_{ps} < 0.3$ . Thus, it sounds reasonable to tentatively term the area  $0.6 < x/x_{ps} < 1$  as the electronegative region, or the pre-sheath with the negative ions (Region I),  $x_s < x/x_{ps} < 0.6$  as the electropositive region, or the pre-sheath without negative ions (Region II), and  $0 < x/x_{ps} < x_s$  as the sheath itself (Region III). In this case, the uncertainty in the sheath edge location  $x_s$  falls within the limits  $0.2x_{ps} < x_s < 0.3x_{ps}$ . The exact location of the sheath edge can be obtained by applying the Bohm sheath criterion for a multi-component plasma [261]. In Region I, the positive ions are accelerated towards the electrode, and the negative ions contribute to the sheath structure. In Region II, the positive ions are further

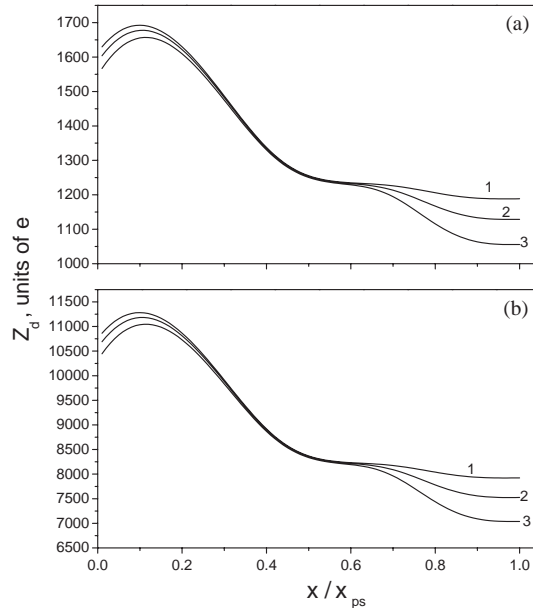


Fig. 11. Profiles of the equilibrium charge on 300 nm (a) and 2  $\mu\text{m}$  particles in the near-electrode region for  $\alpha_{\text{Ar}^+} = 0.65$  and other parameters given in Table 1 of Ref. [190]. Curves 1–3 correspond to  $\alpha_{\text{F}^-} = 0.15, 0.3$ , and  $0.45$ , respectively [190].

accelerated, whereas the effect of the negative ions on the sheath structure is already negligible. In the near-wall Region III, the electron and ion densities diminish, the latter remains higher sustaining the electrostatic field in the sheath. This approximate model thus reflects basic features of the plasma sheaths in electronegative gases [261].

The value of the average particulate charge is determined by the dynamic charging equation

$$\frac{dQ}{dt} = \Sigma_{(j^-)} I_{(j^-)}(Q, x) + \Sigma_{(j^+)} I_{(j^+)}(Q, x) , \quad (4.23)$$

where  $Q = -|Z_d|e$  is a negative dust charge, and  $\Sigma_{[j^{(+,-)}]} I_{[j^{(+,-)}]}(Q, x)$  are the combined microscopic currents of the positive and negative plasma species [189]. The microscopic currents onto the dust grain were computed using the Orbit Motion Limited approximation discussed above in Section 4.1. The equilibrium state of the dust charge ( $Q_0 = \text{const}$ ) was calculated by invoking the stationary balance of the positive and negative plasma currents on the grain. The results for the spatial profiles of the equilibrium particulate charge are presented in Fig. 4.12 for 300 nm and 2  $\mu\text{m}$  particles, respectively. Fig. 11 reveals that the particulate charge has a tendency to grow in the near-wall region, and starts to decline after reaching maximum at  $x \sim 0.12x_{ps}$ .

Likewise, the dependence  $Z_{d0}(x)$  features a distinctive minimum in the electronegative region, which reflects the dust charge depletion caused by the negative ions. If the proportion of the negative ions is low (curve 1), the dust charge is almost independent on the local position within  $0.5x_{ps} < x$ . In the region  $0.12x_{ps} < x < 0.5x_{ps}$  the charge rises, which is a consequence of the increased electron/ion currents onto the grain. Physically, the diminishing of the potential lowers the potential barrier for the plasma electrons, which can easier be collected by the particulates. Meanwhile, the strong electron/ion

density depletion within the sheath results in the weakening microscopic fluxes on the dust grains, and hence, of  $|Z_d|$ . It is notable that the particulate charge is lower when the number density of the negative fluorine atoms in the electronegative region is higher (Fig. 11). Above all, a variation of  $\delta_{F^-}$  (essentially in Region I) affects the particulate charge in the sheath (Region III). Physically, the negative ions affect the formation of the ion flows originating in the electronegative region, and hence, the grain currents within the sheath.

Knowledge of the ion velocity and the dust charge distributions allows one to compute the total force acting on the fine particles

$$F_{\text{tot}}(x) = -F_g + |F_E(x)| + F_{\text{dr}}^{(j^-)}(x) - F_{\text{dr}}^{(j^+)}(x) ,$$

which includes the gravity force  $F_g$ , the electrostatic force  $F_E$ , and the drag forces due to positive  $F_{\text{dr}}^{(j^+)}$  and the negative  $F_{\text{dr}}^{(j^-)}$  ions. The numerical results of Ref. [190] demonstrate that nearly in the whole electronegative and electropositive pre-sheaths the particles are pushed by the positive ion drag force towards the electrode without any serious counteraction by other forces. In the electronegative region  $F_{\text{dr}}^{(j^+)}(x)$  increases, reaches maximum in Region II at  $x \sim 0.5x_{ps}$  and declines towards the electrode thereafter. It is worth noting that the flex point in the ion drag force corresponds to the area of the significant depletion of the positive ion number density. One can further infer that the resulting force on the particulates  $F_{\text{tot}}$  is directed towards the wall in the entire region  $x_{\text{tr}} < x$  and reverses at  $x \sim x_{\text{tr}}$ , where  $x_{\text{tr}} \sim 0.25x_{ps}$  for 300 nm particles, and  $x_{\text{tr}} \sim 0.18x_{ps}$  for 2  $\mu\text{m}$  particles. Furthermore, the gravity force makes a noticeable contribution only in the plasma bulk.

The electrostatic force, negligible in the plasma bulk, becomes comparable with the positive ion drag force at positions  $x < 0.35x_{ps}$ . Inside the sheath (Region III) the force on a particle is essentially electrostatic and pushes it outwards. Indeed, the electric field becomes strong (in our example it is  $\sim 200$  V/cm in the electrode proximity), while the ion drag force diminishes further. At the equilibrium (particle levitation/trapping position)  $x = x_{\text{eq}}$  the electrostatic and negative ion drag forces balance the positive ion drag force and the gravity force

$$|F_E(x_{\text{eq}})| + F_{\text{dr}}^{(j^-)}(x_{\text{eq}}) = F_{\text{dr}}^{(j^+)}(x_{\text{eq}}) + F_g .$$

As evidenced by the numerical results, the equilibrium position of the larger (2  $\mu\text{m}$ ) particle appears to be closer to the electrode ( $x_{\text{eq}} \sim 0.18x_{ps}$ ), which is consistent with the experimental results on the dust void formation [233]. One can thus presume that the effect of the positive ion drag force is stronger for larger particles. It is worthwhile to mention that in the near-electrode areas of low-density ( $\sim 10^9 \text{ cm}^{-3}$ ) hot cathode discharges the effect of the ion drag force on micron size dust grains is negligible [262]. We emphasize that due to the negative dust potential, the collection impact parameter, and hence the microscopic grain current of the negative fluorine atoms, appear to be small. Hence, the major effect of the negative ions on the equilibrium particulate charge is associated with the electron density depletion in the electronegative Region I. Indeed, in the plasma bulk/electronegative pre-sheath,  $Z_d$  is 10–30% lower than in the absence of fluorine ions (Fig. 11). Likewise, the negative ions are not expected to affect the particulate trapping in the Region III. However, as Fig. 11 suggests, the dust charge within the sheath depends on the fluorine ion number density in the plasma bulk. Physically, this can be regarded as an example of the action of the ‘pre-history’ effects associated with the formation and acceleration of ion flows in the electronegative pre-sheath region.

Meanwhile, it becomes apparent that in high-density fluorocarbon plasmas the negative ion drag force is weak, so is the gravity. Furthermore, the orbit component dominates in the positive ion drag force. The gravity effects for both 0.3 and 2  $\mu\text{m}$  particles appear to be important in the plasma bulk only. Within the region  $x < 0.9$ , the competition between the positive ion drag and electrostatic forces controls the particulate dynamics. The ion drag force peaks at  $x \sim 0.45x_{ps}$ , which reflects the dynamic balance between the counteracting effects of the positive ion acceleration towards the electrode and depletion of their number density in Regions II and III. Finally, we note that the sheath/pre-sheath structure, the ion fluxes, and hence, the particulate charging and trapping processes, are very sensitive to the temperatures of the electrons, the positive and negative ions, as well to the electron energy distribution functions, which often appears to be non-Maxwellian in numerous etching experiments.

#### 4.6. *Fine particles as probes for plasma–surface interactions*

It is important to mention that interaction between the plasma and injected micro-disperse powder particles can also be used as a diagnostic tool for the characterization of electric fields in the plasma sheath (particles as micro-probes) [216,263], energy fluxes in the plasma and towards surfaces (particles as micro-calorimeters) [264], and plasma–wall interactions (particles as micro-substrates) [162,263]. Here, we discuss how fine particles can be used as micro-probes for the diagnostics of the electric field in front of the electrodes and substrates, as well as for observation of the energy fluxes between the plasma and the surface [263]. The experiments on probing the electric field by using micron-sized particles were conducted in an asymmetric capacitively coupled 13.56 MHz plasma source, where the plasma glow was located between the planar RF electrode and a spherically shaped grounded plasma chamber. A copper ring was placed on the electrode to confine the injected iron powder particles ( $\sim 1 \mu\text{m}$ ) in a potential trap.

The injected dust grains were charged and confined near the sheath edge where they were observed by the laser light scattering techniques. A video camera and a CCD camera coupled with a photo-electrical filter were used to determine the location of the confined particles and the sheath width in front of the powered electrode. A movable Langmuir probe was employed to monitor the internal plasma parameters. The distribution of the confined iron particles was inferred through the analysis of the forces acting on the dust particles. Under the prevailing experimental conditions, the balance between the electrostatic and gravity forces controlled the particulate dynamics. On the other hand, the distribution of the injected powder is an indicator of the sheath structure and the potential distribution. The sheath thickness was cross-referenced by direct Langmuir probe measurements of the plasma density profiles, CCD sheath photometry at two wavelengths, as well as video imaging of the confined dust particles [263]. The results from different techniques were found to be in a reasonable agreement.

Since in the laboratory dusty plasma experiments, not only conducting but also dielectric (or dielectric-coated) particles are usually used, the basic charging model of Section 4.1 should be generalized to adopt the case of insulating surfaces and account for the adsorption/desorption, surface recombination and diffusion of incoming charge carriers. In the simplified model, the stationary case was determined by the balance between the number densities of the adsorbed charge carriers and those that desorb or recombine. In this case, the balance equations of the adsorbed particles can be

written as [263]

$$\frac{d\sigma_{ed}}{dt} = (1 - \Theta_e)S_e j_e - \frac{\sigma_{ed}}{\tau_{Re}} - \alpha_R \sigma_{ed} \sigma_{id} , \quad (4.24)$$

$$\frac{d\sigma_{id}}{dt} = (1 - \Theta_i)S_i j_i - \frac{\sigma_{id}}{\tau_{Ri}} - \alpha_R \sigma_{ed} \sigma_{id} , \quad (4.25)$$

where  $\sigma_{(ed,id)}$  are the electron/ion number density on the particle,  $j_{(e,i)}$  are the current densities towards the particle (given by the OML theory, see Section 4.1),  $S_{(e,i)}$  are the sticking probabilities,  $\tau_{(Re,Ri)}(T_p)$  are the residence times of the adsorbed particles,  $\Theta_{(e,i)}$  are the fractions of surface coverage,  $\alpha_R$  is the recombination coefficient, and  $T_p$  is the particle's temperature. The net negative charge on the particle's surface is

$$\sigma_p = \sigma_{ed} - \sigma_{id} = Q/A_p ,$$

where  $Q$  and  $A_p$  are the charge and surface area of the powder particle. For the conditions of experiment in Ref. [263], the representative value of the dust charge on 1  $\mu\text{m}$  particles was of the order of 7000 electron charges. Using this value and the force balance (with dominant contributions from the electrostatic and gravity forces), and visualizing the particle equilibrium position  $z = z_0$ , one can infer the electrical field strength of approximately 350 V/m, which is a typical value for the plasma pre-sheaths. Alternatively, this method can be useful to determine the equilibrium charge carrier density if the field distribution in the sheath region is known.

In addition, the use of micro-particles as thermal probes in argon plasmas has been successfully demonstrated. The equilibrium temperature of the particles, which is controlled by the energy fluxes from the plasma, has been estimated to be of the order of 100–200°C by the temperature-dependent fluorescence of laser dye mixed with the fine powder [263]. In argon plasmas, the particle heating by the charge carrier recombination was identified as a dominant energetic contribution, while the losses were mostly due to radiation and conduction. The energy flux towards the particles was estimated to be approximately 0.1 J/(cm<sup>2</sup> s). For further details, see Ref. [263].

Test dust grains have also been successfully used to locate the sheath edge [221]. The sheath edge location measurements were based on finding the equilibrium position of fine (< 500 nm) dust particles levitated above the powered electrode of 20–100 mTorr, 15 MHz RF parallel-plate discharge in argon. On the other hand, the Langmuir probe diagnostic and the optical emission from the discharge (transition from a dark sheath to bright plasma regions) were used to estimate the sheath width, which was further used in the calculations of the equilibrium charge residing on the dust particles.

#### 4.7. Detection and characterization of dust particles

In this section, our focus is on conventional experimental techniques of detection and characterization of fine particles. The current challenges in the diagnostics of nano-sized particles have been discussed in Section 2.4. Numerous experimental procedures have been proposed by several authors to determine the grain charge  $Q$ . For example, they were: the driven particle oscillations about the equilibrium position by superposition of an external low-frequency voltage [214]; the laser-induced photodetachment of charge and subsequent detection by microwave interferometry methods or probes [265,266]; the formation of Mach cones behind moving dust particles [267].



Below, we discuss some of the methods that are most suitable for RF discharge plasmas. As suggested in Ref. [214], the charge can be derived from the response of a simple ordered system (chain, monolayer, etc.) of dust particles on a periodic disturbance. In another method [215], the charge can be inferred from the trajectories of the particles in binary collisions. As proposed in Ref. [267], the Mach cones can be excited in a 2D crystal behind a fast dust grain, and the charge can be derived from the analysis of these excitations. However, we note that the critical condition for the application of the above methods is a low neutral gas pressure (of the order of  $p_0 = 10^{-2}$ – $10^{-1}$  Torr) [217].

In Ref. [217] a method of the charge measurement of the particles levitating in the striations of a DC glow discharge, is proposed. The light beam from an  $\text{Ar}^+$  laser with the power density of the order of  $10^3 \text{ W/cm}^3$  was focused onto a single melamine formaldehyde particle ( $1.87$ – $13.57 \mu\text{m}$  in radius  $a$ ) levitated in striations of a DC discharge sustained in a glass discharge tube (diameter  $36 \text{ mm}$ , interelectrode distance of  $40 \text{ cm}$ ) with a DC current of  $0.4$ – $3 \text{ mA}$ . Under the effect of the laser light, the particle moves  $1.5$ – $3 \text{ mm}$  out of the structure, then leaves the beam and returns back into the structure. The charge on the particle is deduced from the analysis of trajectories of the particles moving back to the structure under the action of the electrostatic and neutral drag forces. The motion of a micron-sized particle can then be described by the harmonic oscillator equation

$$d^2r/dt^2 + 2\beta_d(dr/dt) + \omega_d^2 r = 0 ,$$

where  $\omega_d = (2.4/R)(\epsilon_{\text{loc}}/2em_d)^{1/2}$  is the eigenfrequency of the particle motion in the radial field of the discharge, and  $\beta_d$  is a damping factor arising from the neutral drag. Here,  $R$  is the tube radius and  $\epsilon_{\text{loc}}$  is the local value of the electron energy. The aperiodic motion of dust particles is determined from the frame-by-frame analysis of the 25 frame-per-second video recording. In the point of the maximal velocity  $v_m$  the radial electric force is balanced by the neutral drag, which yields the approximate value of the dust charge

$$Q = \frac{32\sqrt{\pi}}{3\epsilon_{\text{loc}}} p_0 a^2 \frac{v_m}{v_{Tn}} \left( \frac{R}{2.4} \right)^2 \frac{e}{r_m} ,$$

where  $r_m$  is the radial position, at which the velocity maximum occurs, and  $v_{Tn}$  is the thermal velocity of the gas atoms.

However, one should be extremely cautious in measuring the dependence of the grain charge on its size. For example, the size dependence of the dust charge in DC glow discharge plasmas reported quite nonlinear due to the increase of the grain surface potential with the size. However, the results of Ref. [217] in fact exhibit not the dependence of the dust particle's surface potential on the particle size but rather the response of the surface potential to the changing plasma parameters along the plasma striations [268].

The charge on fine particles can also be measured by studying the afterglow diffusion, as described in Ref. [269]. The particles can also be suspended in the diffused region of a low-pressure plasma discharge [270]. In this case, the dust can be trapped due to the balance of the neutral drag and the electrostatic forces, which yields a quite accurate estimate for the particle charge.

It is worth noting that measurements of the electric charge on the dust grains are inseparably associated with the fine particle detection methods, which, at different stages of particle growth, include the mass spectrometry [271], the photo-detachment [265], the infrared absorption [272], the microwave cavity measurements [266], the Mie laser scattering [71] as well as other techniques. After

the particles have been collected on a solid surface (substrate), a number of conventional solid-state characterization methods [SEM, TEM, FTIR, Raman spectroscopy, X-ray photoelectron spectroscopy (XPS), X-ray diffractometry (XRD), etc.] can be used (see e.g. Ref. [273] and references therein).

The laser light scattering (LLS) diagnostic methods can be subdivided [5] into spatially resolved detection of the dust from its Mie scattering using a broad area beam and CCD video cameras, angular variation of the scattered light intensity from a small focal volume, and scattering depolarization using a polarized laser (or white light) beam. One should always keep in mind that the Mie scattering formalism allows one to infer the particle size and the number density unambiguously when the complex refractive index is known, the dust particles are spherical, and the size distribution is monodisperse. However, the ex situ examination of the dust by the SEM can be used to verify the latter two assumptions making the analysis unambiguous. We note that the concentration of the particles can also be obtained in situ by examining the fluctuations of the scattered optical signal. The ratio of the fluctuations to the total signal scales as  $n_d^{-1/2}$ , where  $n_d$  is the number of fine particles in the scattering volume. This method works fine for the number densities of the particles exceeding  $\sim 10^7 \text{ cm}^{-3}$ . Unfortunately, the Rayleigh scattering ( $\sim a^6/\lambda^4$ , where  $\lambda$  is the laser wavelength) law imposes strict limitations on the accuracy of the LLS technique in the small grain size limit. For example, using the blue (488 nm) line of the  $\text{Ar}^+$  laser, the scattered intensity becomes observable after  $\sim 2 \text{ s}$  into the discharge run [14]. At this time, the average particle size in silane discharges (see Section 2.1) can reach approximately 20 nm. On the other hand, the particle detection limit for the 647 nm  $\text{Kr}^+$  laser is about 60 nm. Thus, as has already been mentioned in Section 2.4, this method falls short in detecting the nanometer-sized grains.

To end this section, we note that the dynamics of dust particles (one of the key problems of this review) can also be studied using the Doppler velocimetry. The relevant two-dimensional analysis of monodisperse  $10.2 \mu\text{m}$  polystyrene latex spherical particles trapped in argon plasmas using this method was reported in Ref. [274].

## 5. Self-organized structures and phase transitions in complex plasma systems

Complex plasma is a system where self-organization occurs in many ways. One of the most striking examples of self-organization of micrometer-sized colloidal particles in a low-temperature gas-discharge plasma was a discovery of colloidal dust-plasma crystals by a number of research groups around the world [178,179,223,275–277]. Under certain conditions, the particles were found to form regular arrays exhibiting various lattice-like structures [7]. In most of the laboratory experiments, the gravity pulls the relatively heavy particles down in the sheath until the gravitational force (as well as other forces acting in the same direction, e.g., the ion drag force) is balanced by the sheath electric field force. Thus structures levitate in the highly inhomogeneous sheath region; obviously because of the clear distinction between the horizontal (parallel to the electrode) and vertical directions (where the plasma is non-uniform and the ions are flowing towards the electrode), the system structures in a quasi-two-dimensional manner, with often clear two-dimensional features, e.g., the hexagonal-type lattice cells [7].

While the vertical arrangements are mostly determined by the forces acting in that direction, such as the gravity force, the sheath electrostatic force, the ion drag force, as well as the plasma collective effects such as the ion wake formation [254–257] (see Section 6), the horizontal patterns

appear mostly as a result of the particle interaction potentials. In the simplest approximation, these potentials can be modeled as those of Debye–Hückel or Yukawa type, i.e. they involve the standard Coulomb interaction potential screened by the surrounding plasma. However, the openness of the dust–plasma system implying plasma flows to the particles, leads to more complex features of the interaction potential [278]: it was theoretically demonstrated that the so-called shadow forces of Lesage type [279] can lead to the change of the simple screened Coulomb potential and even to particle attractions at some distances. Thus future experiments and/or ab initio computer simulations can further elucidate these unusual and intriguing complex phenomena.

Other unusual structures of particles in a plasma are the self-organized clouds and voids. The clouds of dust particles appearing in the sheath region change the sheath properties in a self-similar way leading therefore to formation of the so-called dust–plasma sheath [236]. Dust voids or regions of the absence of dust often appear in initially homogeneous dust–plasma systems, as numerous experiments demonstrate [233,235,280,281,290–294]. The feature that unifies this sort of structures is that they are also intimately related to the open character of a complex plasma, namely, they are created and supported not only by interactions of charged particles but also by processes in the surrounding plasma. One of the most important features of these structures is the sharp boundaries between the regions occupied by the particles and the dust voids. Obviously, such distinctive inhomogeneities can be created and supported by external sources of energy; in the case of voids this is the ionization source. Below, we review the physics of these structures in more details.

### 5.1. *Dust–plasma sheath—a self-organized structure*

In the presence of the particles in the near-wall region, there are two physically different possibilities: (1) when the dust influence is relatively weak (typical for rarified dust component), the sheath electric field is mostly determined by the plasma–wall boundary conditions, and (2) when the dust strongly influences all the parameters in the sheath thus creating a specific structure in the near-wall region. Here we focus on the latter possibility [236].

The formulation of the problem is not trivial since the main parameter, viz. the electric field in the sheath, depends not only on the boundary conditions, but also on the distribution of the particles which therefore must be found simultaneously with the electric field distribution. Paradoxically, the new physics introduced by the dust can make the problem somewhat simpler to describe mathematically. One of the most important effects is that the grains absorb plasma particles (which recombine on the grain surfaces) thus creating a sink for the plasma species. This makes the dust–plasma sheath highly dissipative. If the plasma particle mean-free path is shorter than the width of the dust layer, the cloud constitutes a dispersed virtual wall, in addition to the real wall bounding the plasma. Thus the Bohm criterion [237] is changed in the presence of dust, and the dust–plasma sheath appears as an open dissipative system where the plasma fluxes are created consistently by the dust structure and the wall. Simple estimates show [10] that the width of the dust–plasma sheath can significantly exceed the width of the plasma sheath, however, the self-organization restricts its size.

In the absence of dust, there are two regions in the near-wall plasma [237]: the plasma sheath itself where the main drop of the electric field potential occurs, and the pre-sheath region where the drop of the potential is rather small and where the ionization and the ion acceleration take place. In the presence of dust, the main drop of the electric field potential is in the dust layer. Here, the simplest model is discussed where the ionization is only in the pre-sheath, and there are three

different layers: the plasma boundary layer (containing no impurities, but the ionization is absent), the dust cloud, and the wall–plasma layer (containing no dust; this layer does not always exist) [236]. What is important physically is that the dust layer can have sharp boundaries. The drop of the electric field potential is small both in the wall–plasma and plasma layers.

The next problem is to determine the domain in the parameter space where the equilibrium state is possible. Indeed, the dust–plasma sheath can support only specific Mach numbers of the ions flowing toward the dust cloud and the wall, thus creating the ranges of allowed ion flow velocities; moreover, the self-organized dust sheath can contain only a certain number of dust particles per unit surface of the sheath. These results are important for dust–plasma experiments, especially for those on dust–crystal formation. The electrons are assumed to be Boltzmann distributed  $n_e = n_0 \exp(e\varphi/T_e)$ , where  $n_0$  is the unperturbed electron density in the region where quasineutrality holds (i.e., in the pre-sheath), and  $\varphi$  is the electric field potential (which is practically zero in the pre-sheath). Then the electric field distribution should be found, with the total electrostatic field  $E$  including the fields created by the grains as well as the field due to the charged wall. The forces acting on the particles are the electric field force  $-Z_d e E$ , where  $Z_d$  is the dimensionless dust charge, and the ion drag force. For simplicity, other forces such as the gravity thermophoretic forces, etc., are ignored, and the electron and ion temperatures are assumed to be constant in the sheath region.

The equations to solve are those for the ion force balance, the stationary ion continuity equation, and the balance equation for the electron and ion charging currents onto the grain surface. These equations are complemented by Poisson's equation to determine  $P = n_d Z_d / n_i$ . In the case of a subthermal ion flow, the jump of  $P$  at the boundary of the sheath is small, and the set of model equations, using the quasineutrality condition, is converted to a set of three equations for the changes of the ion density and flow as well as for the change of the dust charge. This case is in fact not much interesting for applications since according to the Bohm criterion the ion flow is expected to be at least superthermal. Below, we consider only the latter limit which covers both the subsonic and supersonic cases.

The dust–plasma sheath can have sharp boundaries; solutions outside those boundaries must be found without dust. These solutions, which are matched at the boundaries with the solutions inside the dust cloud, also depend on the boundary conditions at the walls. Thus the result inside the dust cloud is a function of the plasma–wall boundary conditions as well. There are several alternatives, in particular: (1) the boundary conditions on the wall can be satisfied inside the dust sheath; in this case the dust cloud exists everywhere up to the wall and the grains cannot levitate inside the discharge, (2) the boundary conditions can be satisfied outside the dust sheath, e.g. for the specific values of such parameters as the ion flow velocity  $v_0$  far from the sheath; in this case the dust levitation is possible.

In the presence of one wall only, the dust–plasma boundary conditions are different for the side of the dust cloud bordering the quasi-neutral plasma bulk and for the side oriented to the wall. However, the presence of the wall influences the conditions at the opposite boundary by affecting the ion flow. In the plasma bulk, the same equations can be used but with  $P = 0$ . In the way similar to that used for the plasma sheath problem [237,248,249], the ion continuity, the balance of forces equations, and the adiabaticity assumption for the electrons in the plasma bulk are invoked to find the first integral of Poisson's equation and to obtain the electric field.

The set of the boundary conditions was solved numerically [236] to determine the parameter ranges allowed by the boundary conditions. These ranges correspond to the equilibrium states of the dust

Table 5.1

Two first regions of the allowed Mach numbers for the ion flow (all values between  $M_{\min}$  and  $M_{\max}$  are allowed). The results are given for argon plasma [236]

| Temperature ratio<br>$\tau = T_i/T_e$ | Grain size<br>$a/\lambda_{Di}$ | First zone<br>$M_{\min,1}$ | First zone<br>$M_{\max,1}$ | Second zone<br>$M_{\min,2}$ | Second zone<br>$M_{\max,2}$ |
|---------------------------------------|--------------------------------|----------------------------|----------------------------|-----------------------------|-----------------------------|
| 0.001                                 | 0.5                            | 0.708                      | 1.094                      | 1.742                       | 2.550                       |
| 0.01                                  | 0.5                            | 0.710                      | 1.096                      | 1.743                       | 2.297                       |
| 0.001                                 | 0.1                            | 0.709                      | 1.104                      | 1.746                       | 3.363                       |
| 0.01                                  | 0.1                            | 0.712                      | 1.106                      | 1.748                       | 3.342                       |

sheath. The numerics were performed for  $1 > (T_i/T_e) > 0.001$ ,  $0.01 < M < 10$ , where  $M$  is the Mach number of the ion flow, and  $0.001 < (a/\lambda_{Di}) < 0.5$  for various gases (hydrogen, argon, and krypton). It was found that the ranges of the plasma parameters corresponding to the equilibrium states do exist; Table 5.1 gives a summary of the first two allowed zones for the initial Mach number in argon plasmas with various values of  $\tau = T_i/T_e$  and  $a$ . It can be seen that the allowed values of the Mach number change from 0.7 to 3, i.e. the sheath can be either subsonic or supersonic, in contrast to the Bohm criterion in the absence of dust. This is not a surprise since the charged dust layer strongly affects the electric field distribution in the sheath. Important experimental consequences are that by changing the system control parameters, one can easily obtain or exclude the equilibrium dust–plasma sheath (the latter can be desirable in applications to fusion plasmas where high-power loading can lead to significant dust contamination from the walls). The obtained equilibrium ranges look like the quantization zones. Mention that the model relations describe the balance of the electrostatic pressure, the thermal pressure of electrons and ions, and the ram pressure of electrons. In fact, they describe the electrostatic confinement of electrons, ions, and dust in the sheath similar to the widely known magnetic confinement, where the magnetic pressure is balanced by the thermal pressure of the plasma.

In Ref. [236], the set of equations for the quasi-neutral sheath was solved first, followed by the solution of more accurate equations without the quasineutrality assumption. The calculations were done for the Mach numbers near the lower and the upper limits of the allowed range, as well as sometimes in the middle of the range. The temperature ratio has been changed in a wide range to understand its influence on the structure of the dust–plasma sheath. The calculations started at the dust–plasma boundary of the sheath followed by solution of the nonlinear model equations in the region occupied by dust. Then the solution was found in the region between the dust cloud and the wall (if the levitation criterion is satisfied). The solutions at the first boundary were used to obtain the drop of the potential in the region. The total thickness of the plasma–dust sheath was calculated as a sum of three regions: the plasma layer between the pre-sheath and the dust cloud, the dust cloud, and the region between the dust layer and the wall.

Fig. 12 gives the result (without the quasineutrality assumption) for the dust layer in argon where the boundary with the plasma is in the left and the boundary with the wall–sheath layer is in the right. The upper solid line gives the ion density as a solution of the wall–boundary conditions; since it does not intersect the lower solid line (representing the ion density in the sheath), the levitation is possible. The thickness of the dust layer is  $\Delta x_d = 8.20a^2/\lambda_{Di}$ . Note the sharp peak of the dust

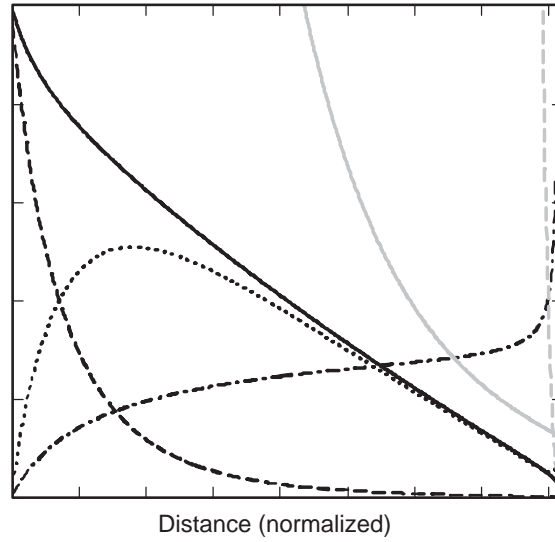


Fig. 12. The dust layer in argon plasma: the normalized ion density  $n/n_0$  (solid curves; the upper line gives the ion density as a solution of the wall-boundary condition, the lower solid line gives the actual distribution), the normalized electron density  $n_e/n_0$  (dotted curve), the normalized dust density  $n_d a T_e / n_0 e^2$  (dash-dotted curve), and the parameter  $P = n_d Z_d / n_0$  (the dashed curve). The initial Mach number is  $M_0 = 1.743$  corresponding to the second allowed range (see Table 5.1). Other parameters are:  $T_i = 0.001 T_e$ ,  $a = 0.5 \lambda_{Di}$ . Reprinted from Ref. [236].

density near the wall. The total number of dust particles per unit area is  $N_d = 1.96$ , the drop of the potential is  $\Delta\varphi_d = -5.878 T_e / e$ . The calculation gives also the values of the parameters at the near-wall boundary of the dust layer:  $n_{dw} = 0.015 n_0$ ,  $n_{e,dw} = 0.003 n_0$ , and  $M_{dw} = 2.720$ . The results for the thickness and the drop of the potential in the plasma-wall layer, as well as the final Mach number at the wall are  $\Delta x_w = 0.28 a^2 / \lambda_{Di}$ ,  $\Delta\varphi_w = -0.004 T_e / e$ , and  $M_w = 3.396$ , respectively. The thickness of the plasma layer between the pre-sheath and the dust layer is  $\Delta x_{ps} = 0.11 a^2 / \lambda_{Di}$ , and the potential drop is  $\Delta\varphi_{ps} = -0.104 T_e / e$ . The total width of the plasma-dust sheath in this case is  $\Delta x_{pd} = 8.59 a^2 / \lambda_{Di}$ , with the total potential drop  $\Delta\varphi_{pd} = -5.986 T_e / e$ .

Fig. 13 gives the result for argon plasma when the initial Mach number is the lowest allowed in the first range. The solid line gives the ion density distribution, other lines are the same as in Fig. 12. The thickness of the dust layer is  $\Delta x_d = 30.0 a^2 / \lambda_{Di}$ . Note the completely different (shock-like) structure of the dust density distribution as compared with Fig. 12. The total number of dust particles per unit area is  $N_d = 0.61$ , the drop of the dimensionless potential is  $\Delta\varphi_d = -3.481 T_e / e$ . The parameters at the near-wall boundary of the dust layer are:  $n_{dw} = 0.011 n_0$ ,  $n_{e,dw} = 0.009 n_0$ , and  $M_{dw} = 2.381$ . The thickness and drop of the potential in the plasma-wall layer, as well as the final Mach number at the wall are  $\Delta x_w = 0.69 a^2 / \lambda_{Di}$ ,  $\Delta\varphi_w = -0.007 T_e / e$ , and  $M_w = 3.593$ , respectively.

Solution of the equations for the near-wall layer gives its thickness at the point where the ion density curve reaches the value corresponding to the ion density at the wall. The results for the total thickness, total drop of the potential, and the final Mach number at the wall are  $\Delta x_w = 8.481 a^2 / \lambda_{Di}$ ,  $\Delta\varphi_w = -5.882 T_e / e$ , and  $M_w = 3.396$ , respectively. The final problem is to find the solution back in the pre-sheath to find the thickness of the plasma layer between the pre-sheath and the dust layer,



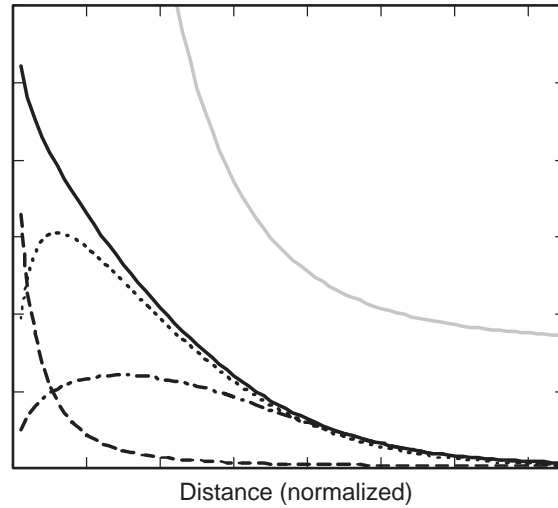


Fig. 13. The same as Fig. 12, but for  $M_0 = 0.708$  corresponding to the sub-sonic ion flow in the first allowed range (see Table 5.1) [236].

and the potential drop. The thickness of the plasma layer between the pre-sheath and the dust layer is  $\Delta x_{ps} = 0.108a^2/\lambda_{Di}$ , with the potential drop in it  $\Delta\phi_{ps} = -0.104T_e/e$ . The total width of the plasma–dust sheath is  $\Delta x_{pd} = 8.589a^2/\lambda_{Di}$ , with the potential drop in it  $\Delta\phi_{pd} = -5.986T_e/e$ .

Thus the most important general properties of the plasma–dust sheaths as appearing from the extensive numerics are the following: (1) The plasma–dust sheath is a self-organized structure determined by the limited set of external parameters such as the initial Mach number of the ion flow, the size of the dust grains, and the electron to ion temperature ratio; (2) The plasma–dust sheath can exist only within the certain ranges of the Mach numbers; the plasma–dust boundaries are sharp in the limit of the cold grains (the zero dust temperature); (3) The size of the plasma–dust sheath is much larger than the usual sheath size when  $a^2/\lambda_{Di} \gg \lambda_{De} \equiv (T_e/4\pi n_0 e^2)^{1/2}$ ; (4) For the sufficiently high Mach numbers, the grains cannot levitate; the size of the particles influence the sheath structure in such a way that the smaller the size of the grain is, the less probable is the levitation. Also, when the mass of the plasma ion is smaller, the range of parameters corresponding to the absence of the dust levitation is wider.

The possibility to find the solution is related to the new (comparing with usual plasma–wall problem in a dust-free plasma) physics involved, which is particularly because of the high dissipation introduced in the system by the dust grains. The solutions describe the electrostatic equilibrium so that the electrostatic confinement appears due to the balance of the electrostatic force with the pressure force including the ram pressure of the flowing ions. The balance of the electrostatic pressure, the thermal pressure of the electrons and ions, and the ram pressure of the flowing ions in the dust–plasma sheath is similar to the well known magnetic confinement balance, where the magnetic pressure force is compensated by the plasma thermal pressure force. It is important, however, that this electrostatic confinement is not imposed externally and is created by the plasma–dust sheath itself in a self-similar way, which can be considered as a new phenomenon of self-confinement.

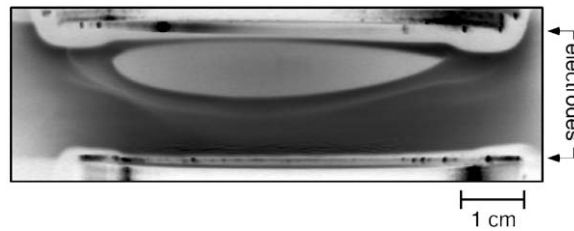


Fig. 14. Image of the dust void [233] in a carbon sputtering plasma. A dusty plasma is between the two electrodes. Darker grays correspond to higher particle number densities. Note the sharp boundary between the void and the surrounding dust cloud. Reprinted from Ref. [233].

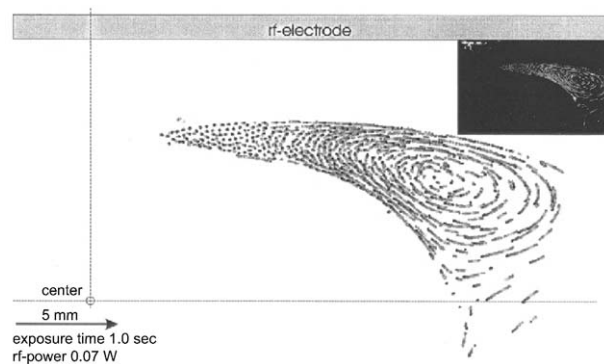


Fig. 15. Cross-sectional view of the spheroidal dust void structure in the microgravity experiment [235].

## 5.2. Dust voids in plasmas

Dusty plasmas in a gas discharge often feature a stable dust void, i.e., a region free of dust. This occurs under conditions relevant to both plasma processing discharges and plasma crystal experiments. The void was originally discovered in several experiments [233,235,280,281]. In particular, it was found [280] that as particles in a sputtering plasma grew in diameter, an instability developed in two stages. First was the sudden onset of a “filamentary mode” of  $\sim 100$  Hz in which the ionization rate and dust number density were both modulated. Then this mode developed into the second stage, a void. The void was a stable centimeter-size region completely free of dust. It was observed [233] that the void has a sharp boundary with the surrounding dusty plasma, as shown in Fig. 14. The electron density and ionization rate were enhanced in the void, compared to the surrounding dust cloud. Similar voids [281] were also found in a silane deposition plasma. Using much larger particles to form a strongly-coupled dusty plasma in a microgravity, a centimeter-size void (Fig. 15) was observed [235]. For some operating conditions the voids exhibit a 1–1.5 Hz relaxation oscillation, termed the “heartbeat”, in which the void shrank drastically and then expanded to its original size. All the experiments described above were carried out in gas discharges that were sustained by the electron-impact ionization, and all featured a void with a sharp boundary.

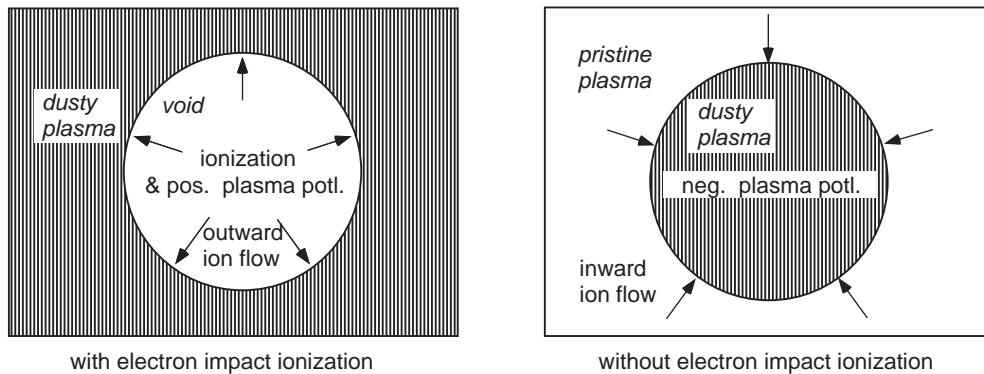


Fig. 16. Sketch of a void (left) and its converse (right). In the presence of the electron-impact ionization, a positive space potential develops, creating an outward ambipolar electric field that drives ions outward, applying an outward ion drag force, which can maintain a void. In the absence of the electron impact ionization, for example in a space plasma where plasma is generated far away, the dust cloud forms with its boundary sustained by an inward ion drag force driven by an inward electric field. Reprinted from Ref. [234].

Two mechanisms are required to explain the voids: a force balance on a dust particle and maintenance of a sharp boundary. The balance of the electrostatic and ion drag forces [233] involves the electron depletion and the electron-impact ionization. The electron depletion, i.e. the reduction of the electron number density in the dust cloud, is due to absorption on the particles. This can reduce the electron-impact ionization rate within the cloud. In a void, the comparatively higher ionization rate leads to an electric field that is directed outward from the void's center. This yields an outward ion flow, which exerts an outward ion drag force on the dust particles, as sketched in Fig. 16. In equilibrium, there is a balance of forces on a dust particle: an inward electrostatic force and an outward ion drag force. The second mechanism required to explain the voids is the maintenance of a sharp boundary. Sharp boundaries are a common feature of dusty plasmas, not only those with voids, but many others as well. In etching plasmas, dome and ring-shaped dust clouds are formed above electrodes, and these clouds have sharp edges [71]. Planetary rings [10] and the noctilucent clouds in the lower ionosphere [282] also have sharp boundaries. The elaborated theory of dust voids [234,283] including the ionization and plasma fluxes, was able to explain the sharp boundaries.

In experiments [233] the void arises from a uniform dust cloud as a result of an instability. This instability develops as follows. Suppose that in a uniform dust cloud in a gas discharge, there is a spontaneous fluctuation in the dust number density. In the region of reduced dust density, there is less electron depletion by the dust. This leads to a higher electron density there, and hence to a higher ionization rate. This high ionization spot develops a positive space charge with respect to the surrounding medium. The resulting force balance involves two forces acting on the negatively-charged particles: the inward electrostatic force and the outward ion drag force, Fig. 16. For a small particle size, the inward force will dominate and fill the spot again with the dust, and the fluctuation will disappear. This is the initial stable situation. However, if the particle size exceeds a critical size, the outward ion drag force exceeds the electrostatic force. The region of the reduced dust density will then expel more dust particles, and the fluctuation will grow. This is an instability that yields the 'filamentary mode'. The threshold for the instability is determined by the particle size and the

electric field strength. The particle size is an independent parameter, whereas the electric field is determined self-consistently by the electron and ion transport mechanisms and Poisson's equation. This initial stage of the linear growth of the instability has also been modeled [284].<sup>1</sup> Then the mode becomes nonlinear and the instability saturates. The final nonlinear state can be a stable void.

### 5.2.1. Collisionless dust voids

Here, we review how a stable equilibrium of the voids is modeled in the collisionless case [234]. The actual mechanism that led to the formation of the void, whether by an instability as described above or by some other process, is not considered here. Because the equilibrium develops through nonlinear effects, we use a nonlinear treatment of the relevant fluid equations. The only collisions taken into account are the dust–electron and dust–ion collisions inside the dust region. This model was used [234] to predict the conditions for the void's existence, its size, and its sharp boundary with the surrounding plasma.

The void's existence requires a local source of ionization of a background gas. This means that the problem is mostly applicable to gas discharges, where the ionization is due to electron impact, although photo-ionization and other sources of ionization could have a similar effect. In the absence of the local ionization, the converse of a void appears, as sketched in Fig. 16. The latter problem is applicable for example to astrophysical dust clouds [10]. The electron depletion within the dust cloud causes the cloud to acquire a negative space charge, which attracts ions. The developed ion flow causes the void to develop. The one-dimensional model is based on the set of fluid equations, Poisson's equation, and the charging equation for dust. We assume that the problem is symmetric around  $x = 0$ , which is the system's center. The electric potential and the ion flow velocity are zero at the center. If the void appears, its center is at  $x = 0$ . Thus, two regions are modeled: the void with  $|x| < x_v$  and the surrounding dusty plasma with  $|x| > x_v$ , where  $x_v$  indicates the void boundary.

Three main forces act on the dust: the electrostatic, the ion drag, and the neutral gas drag forces. The latter force is proportional to the dust particle velocity, which is zero in the stationary state, but we retain it here to include the possible slow motions of the void. For the ion drag force, it is assumed that (for the considered here collisionless case) the ion velocity in the dust region is superthermal. At the center, the electric field  $E = 0$ , so that the potential is parabolic for small  $x$ . This is the first boundary condition to be satisfied. Another boundary condition is applied at the void's edge,  $x = x_v$ .

In the region occupied by the dust, the dust charge is taken into account in Poisson's equation. The charge is found from the charging equation, which depends on the electron and ion parameters. The number density is obtained using the equations of motion and continuity for dust. An exact analytic solution of the Poisson's equation in the dust region is possible because of the electrostatic force balance for dust particles. Under the assumption of the steady-state conditions the dust inertia can be neglected and the force balance on a dust particle is

$$F_E + F_{dr} + F_{fr} = 0, \quad (5.1)$$

<sup>1</sup> Note here that the linear theory cannot answer the question what is the final nonlinear stage, is there a void or another nonlinear structure such as that observed at the filamentation stage. Only fully nonlinear treatment can answer this question.

where the Coulomb, ion drag, and neutral drag forces are, respectively:

$$F_E = -Z_d e E ,$$

$$F_{dr} = m_i u_i v ,$$

$$F_{fr} = 3n_n a^2 v_{Tn} m_n v_d .$$

Here  $v$  is the collision frequency for the momentum transfer between the ions and dust. The electric field includes the field of the dust particles. The particle charge  $z$  or the “floating potential” is determined in the steady state by the balance of the electron and ion currents collected by the particle [3,44]. The dust continuity equation is trivial when the dust is stationary. On the other hand, for a void with moving dust, for example when the void is expanding or contracting in size, the dust continuity equation must be included in the model.

For the case of a void that is expanding or contracting with time, the boundary’s motion should be taken into account. Assume that  $x=x_v(t)$  describes the boundary motion, where  $x_v(t)$  is the boundary’s position at time  $t$ . The dust density near the boundary can be written as  $n_d(x, t) = n_d(x - x_v(t))$ . It is then obtained from the dust continuity equation that

$$\frac{\partial n_d}{\partial x} \left( -\frac{dx_v(t)}{dt} + v_d \right) + n_d \frac{\partial v_d}{\partial x} = 0 ,$$

where  $n_d$  and  $v_d$  are functions of  $x$  and  $t$ . The dust velocity at the boundary equals the boundary velocity  $dx_v(t)/dt$ , and

$$\left. \frac{\partial v_d}{\partial x} \right|_{x \rightarrow x_v(t)} \rightarrow 0 . \quad (5.2)$$

Note that a slow motion is assumed, i.e. the electrostatic equilibrium is maintained. In this case, the boundary’s motion, but not the dust motion inside the dust cloud, can be investigated.

Numerous experiments have shown that the dust-void boundary is a sharp, discontinuous interface [233,235,280,281,290–294]. As was theoretically demonstrated in Ref. [234], in the steady state this is because the force balance acting on dust particles requires a jump in the dust number density at the boundary, provided that the dust kinetic temperature is zero. First, we must recognize that at the boundary between the dust cloud and the void, the ion and electron parameters, and the electric field, are all continuous. The electric field  $E$  is continuous because the particle cloud is a diffuse body that can sustain no surface charge on its boundary. The ion and electron densities and the ion velocity are therefore also continuous. Moreover, the dust charge is also continuous, since it is determined by the ion and electron parameters. Second, the dust force balance equation can be generalized to include a nonzero dust pressure,  $n_d T_d$ . The dust kinetic temperature  $T_d$  describes a dust particle’s random motion (and should not be confused with the particle’s surface temperature, which can be different). In dimensionless units the dust pressure is the product of the dust number density and the dust dimensionless temperature  $\tau_d = T_d e^2 / a T_e^2 = T_d z / T_e Z_d$ . If  $\tau_d$  is small, then the dust number density is discontinuous. This means that the parameter  $P = n_d Z_d / n_i$  is also discontinuous. Under these conditions, it is valid to use the simplified force balance for a stationary void. The jump in  $P$  is positive,  $\Delta P = P_v > 0$ , since  $Z_d > 0$  (the negatively charged dust). This criterion is necessary to determine whether a void can exist. The explanation presented above applies to a stationary void.

It is also applicable to a void with a moving boundary, provided that the motion is sufficiently slow so that the force balance is maintained at all times.

Consider now what would happen if one started with a void that had a smooth profile, rather than a sharp edge. As the ions flow from the void into the dust cloud, they are gradually absorbed by the dust. The ion flux will therefore diminish with depth in the dust cloud. Thus, the ion drag force will act more weakly on the second dust layer than on the first, and for subsequent layers it will decrease continuously. In other words, the ion drag pressure is most severe on the first dust particles that encounter the ion flow from the void. This pushes the first layer back toward the others, compressing the dust so that a sharp edge is developed. Note that there are several effects that can smoothen the sharp profile, in particular, the dust particle temperature, the particle size dispersion, and the dust particle inertia.

Numerical results valid inside a void in a dusty argon plasma are presented in Fig. 17. These show the structure of the potential  $\psi(x)$ , the ion velocity  $M(x)$  and the electric field  $E(x)$  in the void. The void's edge is marked in these profiles; its location was found from the boundary conditions. The ions flow from the void center toward the edge. They accelerate toward the void boundary. The ions attain a speed almost exactly equal to the ion acoustic speed, i.e., a Mach number of unity, when they reach the boundary. This condition is analogous to the Bohm criterion for a collisionless sheath. The ions are subsonic in the void and sonic as they enter the dust cloud.

The potential in Fig. 17(a) varies smoothly, with a nearly parabolic dependence on  $x$  in most of the void region. There are small oscillations superimposed on the otherwise smooth monotonic shape of the potential profile. These oscillations are also apparent in the ion velocity in Fig. 17(b), but they are most prominent in the electric field, Fig. 17(c). These spatial oscillations reveal the presence of a stationary ionization striation; they are suppressed when the ion-neutral collisions are included in the model. Near the void edge, the potential and the electric field vary rapidly with  $x$ . This occurs beyond the point where the oscillatory regime dies out.

By including a moving boundary between the void and dust cloud, but keeping the void center stationary at  $x = 0$ , the void that can expand or contract with time can be modeled. The motion should be slow enough so that the equilibrium force balance on dust particles is maintained. Under these conditions it is still possible to find the velocity of the void's edge, because the force balance includes the dust-neutral drag force, which depends on the dust velocity. Results are shown in Fig. 18. The parameters assumed here are a relatively large dust size  $a = 0.1$  and a low ionization rate  $1/x_{0i} = 0.09$ . The phase diagram shown in Fig. 18(a) is a plot of velocity vs. position of the void edge  $x_v$ . It reveals a single stable equilibrium void size, where the velocity of the void edge  $dx_v/dt$  is zero. Smaller voids will grow, because their edge will have a positive velocity. Larger voids will shrink, with an edge moving with a negative velocity. This 'stationary point' of the phase diagram was found for all the parameters tested. It indicates a single stable equilibrium for a given particle size and ionization rate. This is a noteworthy result that we compare to experimental results below.

Contracting voids with a size larger than a maximum one cannot exist. Near the maximum size, the velocity of the void's edge is always directed inwards, i.e., the void is contracting. The maximum possible void size in all investigated cases was larger than the size of a stationary void. The dust charge in Fig. 18(b) has a maximum for a void size slightly larger than the stationary void size. The charge decreases rapidly for the voids that are large and shrinking, i.e., near the maximum void size.



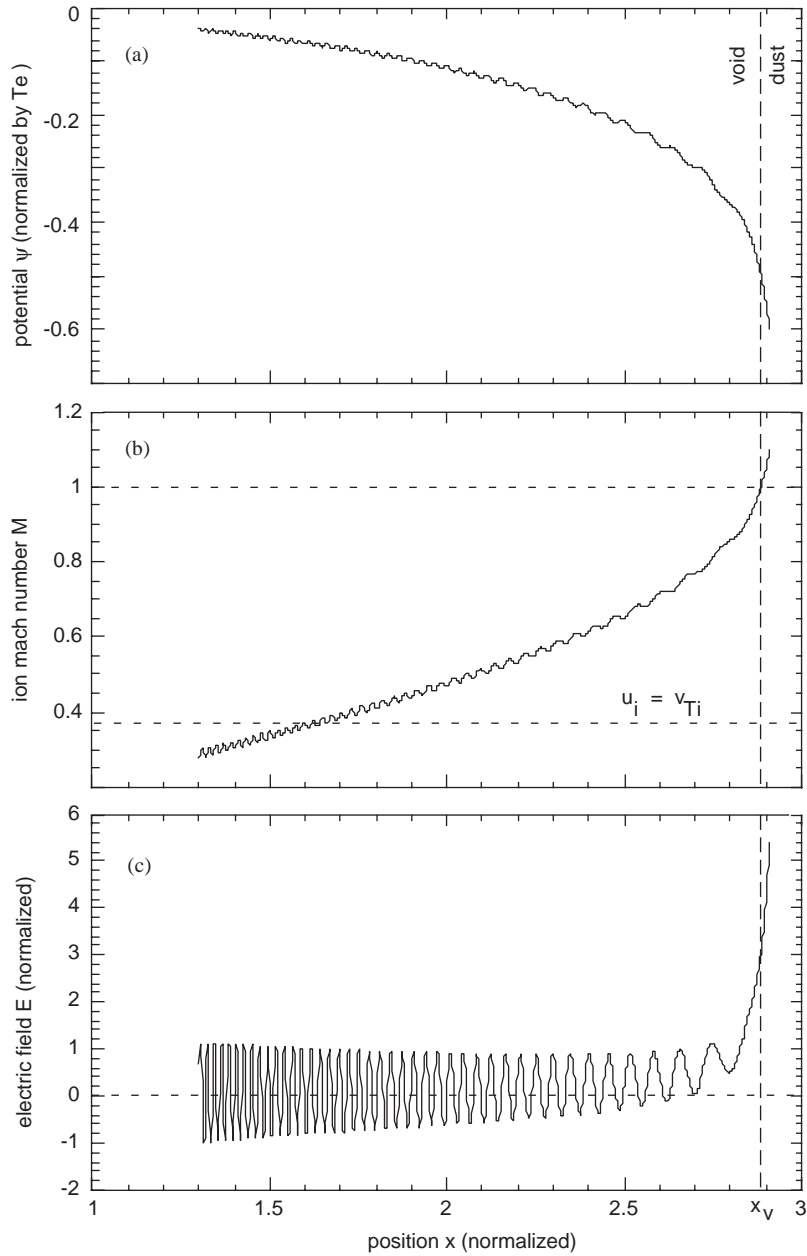


Fig. 17. Solutions in the void region showing the spatial profiles of: (a) normalized electrostatic potential  $\psi$ , (b) normalized electric field  $E$ , and (c) the Mach number of the ion flow. Note that the ion Mach number is almost exactly unity at the void edge. The ion thermal velocity indicated by a dashed line in (b) has a Mach number of 0.376. Reprinted from Ref. [234].

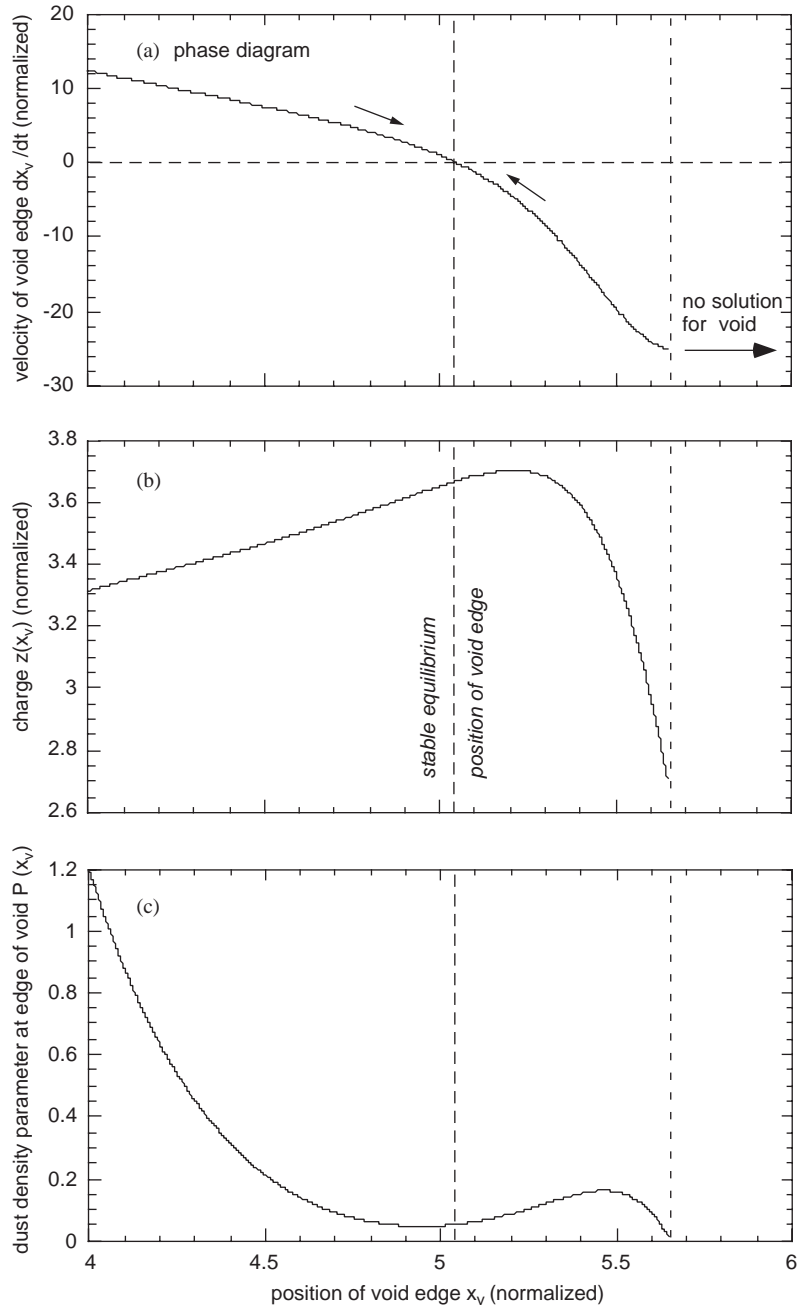


Fig. 18. Solutions for an expanding or contracting void, showing the spatial profiles of: (a) the normalized velocity of the void edge  $dx_v/dt$ , (b) the normalized dust charge  $z$  at the void edge; (c) the jump of the dust number density parameter  $P$  at the void edge. The phase diagram (a) shows a stationary point. Larger voids contract and smaller voids expand. There is a maximum size for a contracting void; it occurs where the dust density jump becomes zero. Reprinted from Ref. [234].

Under some operating conditions voids exhibit a 1.5 Hz relaxation oscillation [235]. This mode was termed the “heartbeat” because the particles underwent a throbbing motion like a muscle in a heart. The void repeatedly collapsed to a no-void condition and then reversed to the original size. In the simulations, when a void is expanding or contracting with time, it always approaches the equilibrium stationary size. If the ionization rate in the void varies in time in some self-consistent manner with the void size and other plasma parameters, it is possible for the void size to oscillate in a repetitive cycle as observed in the microgravity experiment [235].

### 5.2.2. Voids in collision-dominated plasmas

According to the experiments [233,235,280,281,290–294], dust voids usually appear from a uniform dust cloud as a result of an instability associated with increased local ionization in spontaneously appearing depletions of the dust number density. In many of the existing experimental observations, e.g. [233,235,280,281], the size of the void is comparable or even larger than the ion mean free path in the ion–neutral collisions. Thus the theory of a collision-dominated dust void was developed [283]. If the ion–neutral collisions are sufficiently effective in the void region, they substantially lower the ion flow velocity which can then become of the order of the ion thermal velocity [224]. The dust drag and dust capture coefficients [45,224] should take into account the fact that the ion flow velocity can be of the order of the ion thermal velocity. Thus the corresponding generalization of the dust drag and capture rates should be taken into account.

Following the original work [283], we introduce here the dimensionless quantities relevant to the high ion–neutral collision rates. The ion density  $n_i$  and the electron density  $n_e$ , are normalized to the ion density in the void’s center, i.e.  $n = n_i/n_{i0}$  and  $n_e = n_e/n_{i0}$ . The electrostatic potential is  $\phi = e\varphi/T_e$ , and the dimensionless electric field  $E$  and the distance  $x$  are normalized as  $E = Ee\lambda_{Di}^2/aT_e$  and  $x = xa/\lambda_{Di}^2$ . For the collision-dominated case, a new characteristic length related to the ion–neutral mean free path appears. Since all the lengths are normalized to the same distance  $\lambda_{Di}^2/a$ , the dimensionless electric field is measured in units of the field in which an electron receives the energy  $T_e$  on the distance equal to the ions mean free paths in their collisions with the dust particles. The velocity  $v_i$  of the ion flow is normalized as  $u = v_i/\sqrt{2}v_{Ti}$ .

The number density of the plasma neutrals is usually much higher than the ion number density (i.e., the plasma has a low degree of ionization) and the change in the neutral distribution due to the ion–neutral collisions can be neglected. The ion–neutral collisional friction decelerates the ion flow and for the low ion flux velocities the friction force is proportional to the ion velocity. Thus for the case when only the electric field and the friction with neutrals are important, the total dimensionless force acting on the plasma ions is given by

$$F = -\frac{2u}{x_n} + E. \quad (5.3)$$

Here,  $x_n/2$  is the ion mobility in the dimensionless units introduced above,  $u = (x_n/2)E$  for  $F = 0$ . The values for the ion mobility are well known from the experimental data in a low temperature plasma [285–287]. The experimental data show that with the increase of the electric field  $E$  the mobility starts to depend on  $E$  and for large field  $u \propto \sqrt{E}$ . Therefore the expression for the friction force (leading to the mentioned changed in the dependence of the mobility on the electric field in the

presence of the electric and friction forces only) can be written as

$$F_u = -\frac{u}{x_n} (2 + \alpha_u u) . \quad (5.4)$$

The balance of the electric and friction forces then leads to

$$u = \frac{1}{\alpha_u} \left( \sqrt{1 + x_n \alpha_u E} - 1 \right) , \quad (5.5)$$

which provides both the limits ( $x_n \alpha_u E \ll 1$  and  $x_n \alpha_u E \gg 1$ ) with the known dependence of the mobility on the electric field. If a void is in the intermediate regime where the ion–neutral collisions (although being important) do not dominate the ion ram pressure forces, the calculations should take into account the friction, the ram pressure, and the electric field forces. In this case expression (5.5) is violated and the ion balance equation appears as an additional equation.

In the collision-dominated case, it is necessary to know the dependence of forces acting on the dust particles (such as the ion drag and the ion capture force) on the ion flow velocity when the latter is close to the ion thermal velocity. These coefficients can be calculated in the standard way [45] (since the cross-sections are well known) and they are presented in Appendix of Ref. [283] for an arbitrary value of the ratio of ion flow velocity to the ion thermal velocity. The electron drift velocity in the void region cannot be larger than the ion flow velocity, i.e. it is much less than the electron thermal velocity, and thus the electron friction with neutrals is much less than the electric and the electron pressure force. According to the known dependence of the ionization rate for the electron impact ionization, the ionization rate is proportional to the electron density. The length  $x_i$  is, in the units used, the distance on which the ionization makes the dimensionless electron density to become unity. The size of the void can be found as a simultaneous solution of two boundary conditions: the continuity of the electric field and the dust charges at the edge of the void. The electric field at the void side is calculated numerically by solving the set of equations inside the void region. The electric field at the dust side can be calculated once the dust charges at the void surface are known.

There are two dimensionless parameters of the system describing the void, namely,  $D$ , which is the ratio of the void size to the electron Debye length, and  $x_i$ , which is the ratio of the ionization length to the ion–neutral collisions mean free path. Note that the parameter  $x_i$  does not depend on the neutral gas pressure and depends only on the ionization power while the parameter  $D$  is proportional to the neutral gas pressure. In numerical solution in the void region one can use either equations for the quasi-neutral void which depend only on one parameter,  $x_i$ , or for a void smaller or of the order of the electron Debye length, the set of equations depending on both  $D$  and  $x_i$ .

In addition to the solution of the equations in the void region it is necessary to satisfy the boundary conditions at the void edge which additionally depend on  $x_n$ , i.e. the ratio of the ion–neutral mean free path to the ion–dust collision mean free path times the parameter  $P$ . The value of  $P$  at the boundary of the void determines the discontinuity of the dust density. The boundary conditions give two values: the dust charge at the void boundary and the size of the void. The electron and ion densities at the void surface and the value of the ion flow velocity are found straightforwardly. There could be two possibilities for which the void does not exist: the absence of the solution for the boundary conditions and the negative value of the parameter  $P$  at the surface of the void.

The calculations in Ref. [283] were started in the center of the void  $x=0$ . The void was assumed to be planar and symmetric, and the one-dimensional nonlinear equations were solved at  $x > 0$ . At the center of the void,  $x=0$ , the electric field is zero,  $E=0$ , and the dimensionless ion density is  $n=1$ . For the quasi-neutral voids  $n_e=n$  and the dimensionless electron density is also equal to 1. For the non-quasi-neutral voids the proper asymptotics in the center of the void was used:  $\Phi \rightarrow x/x_i$ ,  $E \rightarrow 2x/x_i$  for  $x \rightarrow 0$  which implies that  $n_e \rightarrow 1 - 2D^2/x_i$ . Since  $n_e > 0$  in the center, the non quasi-neutral void can exist only for  $x_i > 2D^2$ . This condition is taken into account for numerical solution of the non-quasi-neutral dust voids.

For fixed  $D$  and  $x_i$  for non-quasi-neutral voids or for fixed  $x_i$  for quasi-neutral voids the void exists if  $x_n$  exceeds some critical value. In some cases the void exists within the certain range between  $x_{n,\min}$  and  $x_{n,\max}$ , while for other conditions the void can exist in several ranges of the parameter  $x_n$ . The boundary conditions depend also on  $\tau = T_i/T_e$  and  $a_d = a/\lambda_{Di}$ . The calculations were performed for the parameter range most interesting for the existing experiments:  $0.02 < \tau < 0.1$  and  $a_d = 0.1$ . In principle, the boundary conditions can restrict the range of these parameters as well (for a void to exist). Thus an increase of  $\tau$  can lower the threshold for  $x_n$  as can be seen from the results given below. The results are presented for the parameter  $x_n$  exceeding the threshold for the smallest value of  $\tau$  used. In this case the results can be presented in a compact form as surface plots. All calculations are performed for argon plasma.

In the case of a quasi-neutral void the calculations were done for  $x_i$  equal to 1/5, 1 and 5. The first case corresponds to the high ionization rate and the third case corresponds to the low ionization rate (the high and low ionization power, respectively). Fig. 19 shows the results for the allowed range of the void sizes for the first case. Fig. 19a shows the size of the void  $x_v$  as a function of  $x_n$  and  $\tau$  in the range  $x_n > x_{n,\min}$  and  $0.02 < \tau < 0.1$ , Fig. 19b shows the dust charges  $z_v$  at the surface of the void in the same range, Fig. 19c shows the boundary jump  $P_v$  of the parameter  $P$ , and Fig. 19d shows the ion flow velocity  $u_v$  at the void boundary. The calculations were done until  $x_n = 10$  (note that the latter value does not violate the boundary conditions).

Note that the void size can significantly exceed the ion neutral mean free path. An increase of the mean free path leads to the increasing size of the void proportionally to the mean free path. Indeed, the size of the void is approximately equal to the ion-neutral collision mean free path divided by  $\tau$ . The voids larger than this size do not exist since the ion drag force will not increase with the size of the void (the ions accelerated in the void will be stopped by the ion-neutral collisions). This behavior is found for all calculations performed for the quasi-neutral voids. The critical value of  $x_n$  for which the void starts to form is shown in Fig. 19 as the minimum value of the  $x$  axis. The minimum value  $x_{n,\min}$  increases gradually with  $x_i$  (with the decrease of the ionization power). This minimum value also decreases with the increase of the temperature ratio  $\tau$ . The jump of the parameter  $P$  at the void boundary,  $P_v$ , is the highest when the void size is close to the  $x_{n,\min}$ . The ion flow velocity at the surface of the void is of the order of the ion thermal velocity, the minimum value being about 0.2 and the maximum value less than 2. With the increase of the ionization length  $x_i$  the velocity of the ion flow increases. As soon as the size of the void becomes comparable to the electron Debye length the condition of the plasma quasi-neutrality is violated. The two series of numerical calculations were performed: one for  $D=0.5$ ,  $x_i=1$  which corresponds to the initial electron density  $n_e=0.5$  and another for  $D=3$ ,  $x_i=40$ , which corresponds to the initial electron density  $n_e=0.45$ . The case of  $D=0.5$  corresponds to the marginal violation of plasma quasi-neutrality,

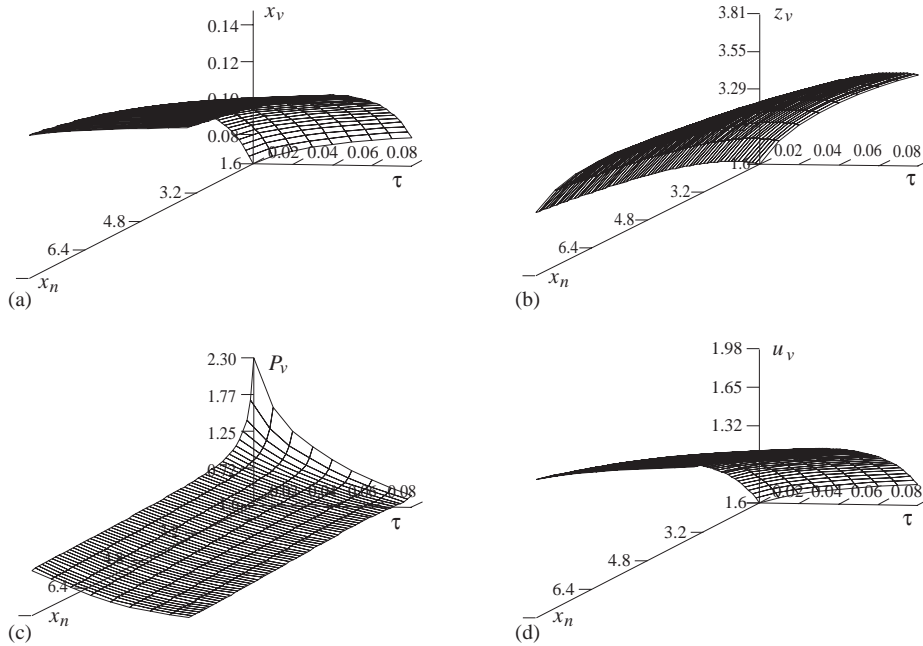


Fig. 19. Dependence of the collisional void parameters on  $x_n$  and  $\tau$  in the range  $x_{n,\min} < x_n < 10$  and  $0.02 < \tau < 0.1$ : (a) the surface plot for the dimensionless void size  $x_v$ ; (b) the surface plot for the dimensionless dust charge at the void boundary  $z_v$ ; (c) the surface plot for the dust density parameter jump  $P_v$  at the void boundary; and (d) the surface plot for the dimensionless ion velocity at the void boundary  $u_v$ . The results are obtained for quasi-neutral voids when  $x_i = 1/10$ . The value of  $x_{n,\min}$ , where the void size is close to zero, is 1.6 for  $\tau = 0.02$ , for larger  $\tau$  the minimum  $x_n$  decreases. Figure shows that the size of the void at lowest  $x_n$  increases with  $\tau$ . Reprinted from Ref. [283].

while the case  $D = 3$  corresponds to the substantial violation of the quasi-neutrality. Some results are shown in Fig. 20.

The new phenomenon created by the absence of the quasi-neutrality is the presence of two zones of possible values of  $x_n$  for a void to exist. The second zone not shown in Figs. 20 is for the relatively narrow range  $1.1 < x_n < 1.2$ . For the second set of numerical calculations for a large violation of the quasi-neutrality, with  $D = 3$  and  $x_i = 40$ , it was revealed that the two zones of possible values of  $x_n$  determine the conditions for a void to exist. One of the zone is for the narrow range of  $x_n$ , namely,  $4.7 < x_n < 5.06$ . Another zone appears at rather low values of  $x_n$ , namely  $0.69 < x_n < 3.4$ . For this zone, the value of the ion flow velocity at the surface of the void becomes very large when the parameter  $x_n$  is approaching the largest possible values in the zone.

The calculated size of the void is of the order of the mean free path (with respect to the ion-neutral collisions) divided by the ion/electron temperature ratio, i.e.,  $x_n/\tau$ , this corresponds to the void sizes observed in the experiments [233,235,281]. Also, an increase of the size of the void with an increase of the ionization power is observed, in accordance with the experimental results. We note that a “collisionless” void [234] can be sustained by the ion drag force when the ions have a velocity greater than the ion thermal speed,  $u \gg 1$ . In the collisional case, see Fig. 20, it appears that  $u \leq 1$  almost everywhere in the void. That means that the ion drag force is basically in the regime



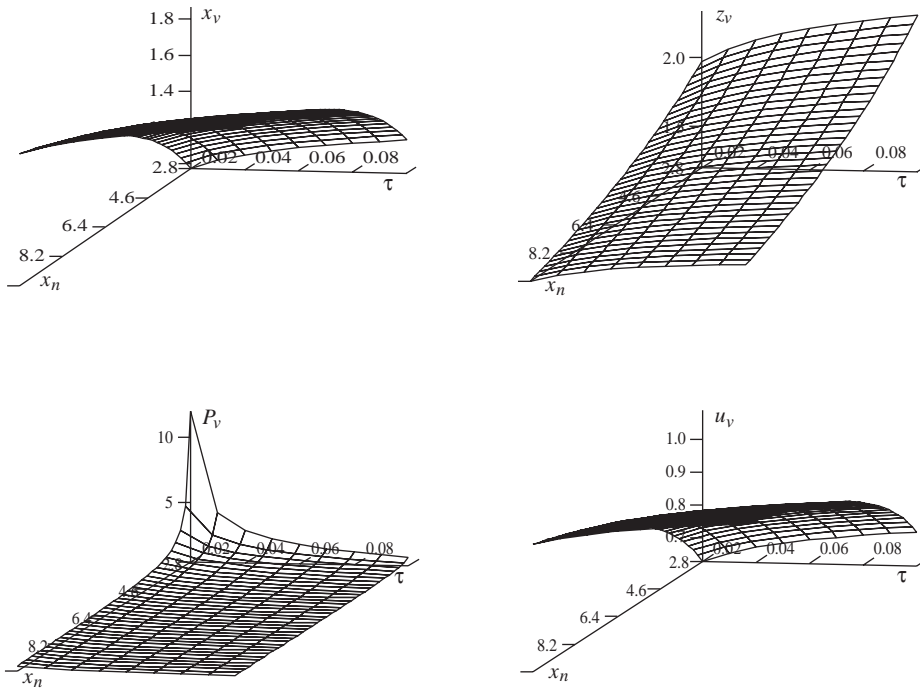


Fig. 20. The parameters of not quasi-neutral void for  $x_i = 1, D = 0.5; x_{n,\min} = 2.8$  [283].

where the force increases with  $u$ , which is different from the collisionless case considered above [234]. In particular, in the collisional case, the electric field and the ion drag force both increase with the ion speed. However, the faster increase of the electric field  $E$  can lead to the force balance, especially for  $u \sim 1$  when the further increase (with the distance off the center of the void) of the ion drag force actually stops. On the other hand, the charge of a dust particle also enters the force balance equation, and also is a function of the distance. The result is a complex interplay of a number of functions of the distance from the center of the void (the electric field, dust charge, speed of the ion flow, etc.), see Fig. 20.

In calculations [234,283], the (possible) influence of the thermophoretic force associated with temperature gradients [292] was neglected. The gradient of the neutral temperature in the void region is produced by the flowing ions colliding with the neutrals. The flow velocity of the ions increases towards the boundary of the void.

We finally note that the presented theory does not provide the initial transition stages of the void formation but rather demonstrates the existence of stationary solutions in the case of bordering void–dust regions. Instabilities leading to the void formation should be studied separately [288–290].

### 5.3. Dynamics and diffusion of particles in strongly coupled complex plasmas

Here, we review the dynamics and diffusion of dust particles [295] in strongly coupled dust–plasma systems. Electrostatic interactions between highly charged grains is very strong thus often making the

complex plasma a highly non-ideal system. The combined effect of interactions of the grains between themselves as well as with the ambient plasma leads to formation of various structures which can be strongly correlated (like clusters and crystals composed of dust particles), with complex behavior exhibiting various oscillations, regular and chaotic motions, etc. [179,235,223,277,235,220].

The simplest model for the three-dimensional (3D) electrostatic interaction of grains in a complex plasma takes into account the plasma screening and therefore the interaction potential is of the Yukawa (Debye) type

$$\phi_D = \frac{eZ_d}{d} \exp\left(-\frac{d}{\lambda_D}\right), \quad (5.6)$$

where  $d$  is the interparticle distance. The non-ideality of the system of charged particles is usually characterized by the factor  $\Gamma = (eZ_d)^2 n_d^{1/3} / T_d$  which is the ratio of the Coulomb potential energy of the interaction between two neighboring particles to the kinetic energy of their thermal motion (here,  $n_d$  is the number density of the colloidal dust particles, and the temperature  $T_d$  of their thermal motion is in energy units). Numerical simulations demonstrate, that for  $\Gamma > 1$  in a Coulomb system of particles the short-range order appears, with the critical value of the parameter  $\Gamma = \Gamma_m$  on the melting line to be approximately equal to 106 [296–299]. For complex plasmas, the assumption of plasma screening (5.6) leads to larger values of  $\Gamma_m$  on the melting line since in this case the normalized parameter  $\Gamma^* = \Gamma(1 + \kappa + \kappa^2/2)^{1/2} \exp(-\kappa)$ , where  $\kappa = \lambda_D n_d^{1/3}$ , is constant  $\Gamma_m^* = \Gamma_m(1 + \kappa + \kappa^2/2)^{1/2} \exp(-\kappa) \approx 106$  for all  $\kappa < 7$  [300].

Diffusion of dust grains is one of the most important processes for mass transfer in a complex plasma; it determines the energy losses (dissipation) as well as the system's dynamic characteristics, formation of structures, and phase transitions, see, e.g., Refs. [301,302]. We note that for various complex systems such as colloidal suspensions [301], complex quasi-2D plasmas [303], sandpile models [304], turbulent flows [305], etc., the diffusion exhibits anomalous character associated with nontrivial topology of the phase space of the system and spatio-temporal correlations [306]. The main manifestation of the anomalous diffusion is in the nonlinear time dependence of the mean square displacement, in contrast to the linear character for the normal diffusion process [306]. Complex plasmas provide a natural example of a system of strongly interacting particles with often anomalous character of the grain diffusion.

The hydrodynamic approach makes it possible to describe the macroparticle's diffusion in a complex plasma only for the case when the short-range order interactions dominate. On the other hand, when the particle interactions are stronger than in (ideal) gases, the relevant kinetic equation is difficult to derive. Essentially, the theory of diffusion in molecular liquids developed in two directions, one of which is based on general ideas of statistical physics while another one utilizes the analogies between the liquid and solid states and gives for the diffusion of molecules the relation [307]:

$$D_M = \frac{d^2}{6\tau_0} \exp\left(-\frac{W}{T}\right), \quad (5.7)$$

where  $d$  is the average distance between the molecules,  $\tau_0$  is the characteristic time, defining the frequency  $\nu_0$  of flights (“jumps”) of the particles from one stable position to another, and  $W$  is the energy threshold for the particle flights. The exponential character of the temperature dependence for the self-diffusion of macroparticles was obtained for dissipative Yukawa systems [308]. Note that the experimental verification of this result in a complex plasma is difficult since in the laboratory

change of any parameter of a plasma–dust systems inevitably leads to the self-consistent change of other parameters determining the grain dynamics. To solve the problem, a proper determination of basic functional dependencies under certain approximations for the self-diffusion rates of grains in Yukawa system is necessary; this has been the subject of extensive studies [302,307–312]. The correct expression for the diffusion rate in dissipative systems of macroparticles interacting via Yukawa potential (5.7) is important not only from the point of view of determining the dynamical characteristics of a complex plasma, but also for the analysis of various kinetic processes in molecular biology, medicine, polymer chemistry, etc. [307–312]. Various approximations are mostly based on either virial expansions of the thermodynamic functions, e.g., the effective viscosity in the Einstein expression  $D_0 = \eta T$  [310–312], or on the analogies with the critical phenomena in gases [302,309]. Thus, for some conditions the rate  $D$  can be expressed as a sum of the first terms in an expansion like  $D_0(1 + \zeta_0)$  or as a power function like  $\zeta_1 + \zeta_2(T/T_c - 1)^\psi$ , where  $T_0$  is the temperature at the melting point, and the parameters  $\zeta_0$ ,  $\zeta_1$ ,  $\zeta_2$ , and  $\psi$  can be determined for particular values of the complex plasma parameters from experimental or numerical simulation data.

Now, we present the results of the study [295] of the diffusion processes of Yukawa-type interacting particles in a dissipative system (complex plasma) with the parameters close to those in the experiments on laboratory weakly ionized gas-discharge plasmas. To model the motion of dust grains in a weakly ionized plasma, the Brownian dynamics method is invoked which is based on the solution of ordinary differential equations with the stochastic Langevin force  $F_{br}$ , taking into account random collisions with the plasma neutrals:

$$m_d \frac{d^2 \mathbf{l}_k}{dt^2} = \sum_j F_{\text{int}}(l) \Big|_{l=|\mathbf{l}_k - \mathbf{l}_j|} \frac{\mathbf{l}_k - \mathbf{l}_j}{|\mathbf{l}_k - \mathbf{l}_j|} - m_d \nu_{\text{fr}} \frac{d\mathbf{l}_k}{dt} + \mathbf{F}_{br} , \quad (5.8)$$

where  $m_d$  is the mass of the dust particle, and the force  $F_{\text{int}}(l) = -eZ_d \partial \phi_D / \partial l$  accounts for the pairwise particle interaction in the system. The characteristic friction frequency can be written as  $\nu_{\text{fr}}[\text{s}] \cong C_v p_0[\text{Torr}] / (\rho[\text{g/cm}^3] \cdot a[\mu\text{m}])$  [313], where  $a$  is the particle radius (in  $\mu\text{m}$ ),  $\rho$  is the particle density (in  $\text{g/cm}^3$ ),  $p_0$  is the neutral gas pressure (in Torr), and  $C_v$  is a dimensionless parameter, defined by the nature of the neutral gas, e.g., for argon  $C_v \cong 840$ , and for neon  $C_v \cong 600$ . The equilibrium charge of a dust particle (in the approximation of charging by plasma currents) is  $Z_d \approx C_z a[\mu\text{m}] T_e[\text{eV}]$  [44], where  $C_z \cong 2000$  for the majority of experiments in noble gases. Three-dimensional equations of motion (5.8) are solved with the periodic boundary conditions. The full number of particles in the modeled system is  $N_p = 125 \times 27$ , and the number of independent particles is 125. The cutoff of the interaction potential is imposed at distances equal or more than  $4d$ , where  $d = n_d^{-1/3}$  is the average interparticle distance. The time step is  $\Delta t = \min(1/\nu_{\text{fr}}, 1/\omega^*)/20$ , where  $\omega^* = eZ_d(n_d/m_d)^{1/2}(1 + \kappa + \kappa^2/2)^{1/2} \exp(-\kappa/2)$  is the normalized dust frequency. The total simulation time is  $2000/\nu_{\text{fr}}$  for  $\nu_{\text{fr}} < \omega^*$ , and  $2000\nu_{\text{fr}}/(\omega^*)^2$  for  $\nu_{\text{fr}} > \omega^*$  being in the range from  $2 \times 10^5 \Delta t$  to  $2 \times 10^6 \Delta t$  depending on the parameters of the system. More details of the numerical method can be found in Ref. [308].

The self-diffusion coefficient of the dust particles can be considered as the parameter determining the dynamic behavior of the complex plasma system. It is defined by

$$D = \langle (\mathbf{l}(t) - \mathbf{l}(0))^2 \rangle_N / 6t , \quad (5.9)$$

where  $\mathbf{l}(t)$  is the displacement of an isolated particle, and  $\langle \dots \rangle$  stands for the ensemble ( $N$ ) and time ( $t$ ) average, respectively. The self-diffusion rate (5.9) of the particles in a complex plasma

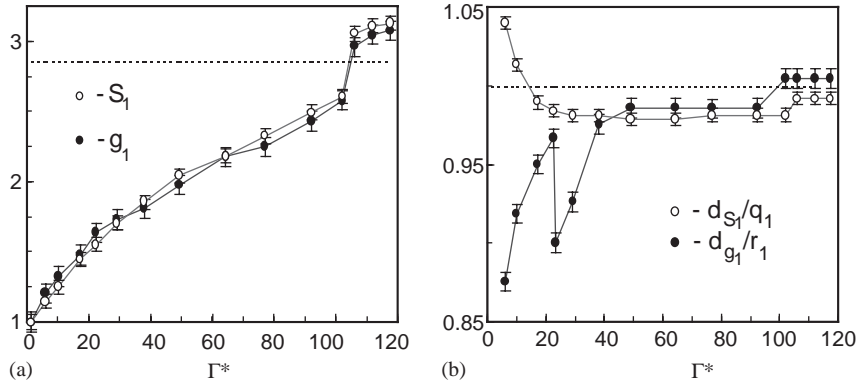


Fig. 21. Dependence of the first maxima of the structure factor  $S_1$  and pair correlation function  $g_1$ , (a), as well as their positions  $d_{S_1}/q_1$  and  $d_{g_1}/r_1$ , (b), on the parameter  $\Gamma^*$ . The ranges of the deviations of the computed functions are plotted for various runs when  $\xi = (0.166 - 1.5)$  and  $\kappa = (2.4, 4.8)$ . Reprinted from Ref. [295].

is calculated for various pressures of the neutral gas ( $v_{fr}$ ), the characteristic dust frequencies  $\omega^*$ , the dust temperatures  $T_d$ , and the Debye screening lengths  $\lambda_D$  ( $\kappa = 2.4$  and  $\kappa = 4.8$ ). Note that the particular choice of the plasma screening length is limited by the condition  $L \gg \lambda_D$  necessary for the correct modeling of the dynamics of Yukawa systems [314]; in simulations [295] that was  $L \cong 5 \times n_d^{-1/3} > 12 - 24\lambda_D$ . The ratio between the interparticle interaction and dissipation in the system is defined by the parameter  $\xi = \omega^*/v_{fr}$ , i.e.

$$\xi = eZ(n_d/m_d)^{1/2}(1 + \kappa + \kappa^2/2)^{1/2} \exp(-\kappa/2)/v_{fr}, \quad (5.10)$$

The particular numbers for this parameter can be chosen utilizing data of gas-discharge plasma experiments [178,179,220,223,235,277]; for the typical experimental parameters ( $\rho \cong 4 \text{ g/cm}^3$ ,  $T_e \cong 1.5 \text{ eV}$ ,  $C_v \cong 700$ ,  $\kappa \cong 2$ ), one can obtain from (5.10)  $\xi \approx 10^{-3}(n_d[\text{cm}^{-3}]/r[\mu\text{m}])^{1/2}(p_0[\text{Torr}])^{-1}$ , and for the particles of the radius  $a = 2.5$  micrometer when their number density  $n_d$  is changed from  $10^3$  to  $10^5 \text{ cm}^{-3}$  and the neutral gas pressure  $p_0$  is changed from 1 Torr to 0.01 Torr, one obtains the range of values  $\xi = 0.02 - 4.2$ . Accordingly, in [295] was chosen  $\xi = 0.055, 0.166, 0.5, 1.5, 4.5$ .

To analyze particle's ordering in the modeled system, the pair correlation function  $g(r)$  and structure factor  $S(q)$  can be used. The dependencies (on the factor  $\Gamma^*$ ) of the first two maxima of these functions ( $g_1$ ,  $S_1$ ) as well as their positions ( $r = d_{g_1}$ ,  $q = d_{S_1}$ ) are presented in Figs. 21(a) and 21(b), respectively. The analysis of these simulations demonstrates that the normalized factor  $\Gamma^*$  fully determines the particle correlations (formation of the long-range order as well as the short-range ordering in the complex dust-plasma system) and can be considered as the parameter responsible for the ordering in the dissipative Yukawa system. The ratio of the diffusion coefficient  $D$  of the charged colloidal particles to the diffusion coefficient  $D_0 = T_d/v_{fr}m_d$  of the non-interacting (Brownian) particles is presented in Fig. 22(a) for different values of the parameters  $\kappa$  and  $\xi$ . For the range from  $\Gamma_c^* \cong 102$  to  $\Gamma_m^* \cong 106$  we have abrupt changes of  $g_1$  and  $S_1$ , see Fig. 21(a), as well as of the ratio  $D/D_0$  (cf. Fig. 22(a),  $D \rightarrow 0$  for  $\Gamma^* \rightarrow 106$ ). With increasing  $\Gamma^* \rightarrow \Gamma_m^*$ , the body-center cubic (bcc) crystal structure has been formed. The positions of the first maxima of the functions  $g$  and  $S$  for the crystal lattice also correspond to the bcc-type lattice ( $d_{g_1} \cong r_1 = (3\sqrt{3}/4n_d)^{1/3}$ ,

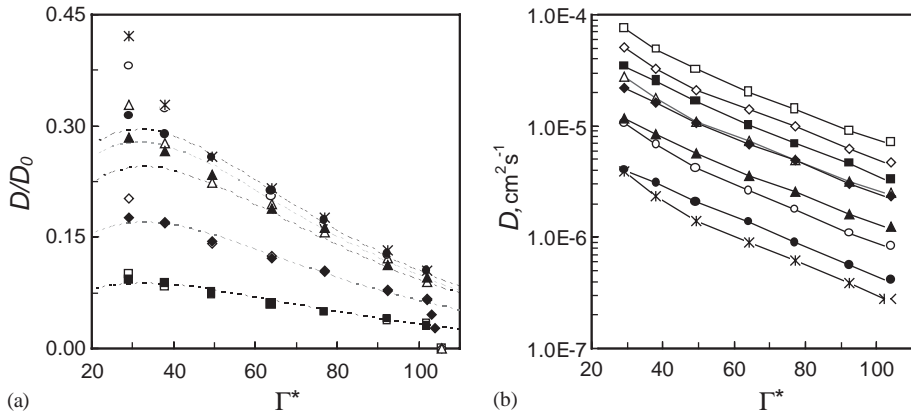


Fig. 22. Dependence of the ratio  $D/D_0$  (a) and the diffusion coefficient  $D$  (b) on  $\Gamma^*$  for different  $\kappa$  (filled symbols correspond to  $\kappa = 2.4$ ; others—to  $\kappa = 4.8$ ) and  $\xi$ :  $\times$ 's correspond to  $\xi = 0.055$ ; circles—to  $\xi = 0.166$ ; triangles—to  $\xi = 0.5$ ; diamonds—to  $\xi = 1.5$ ; and boxes—to  $\xi = 4.5$  [295].

Table 5.2

The best fit of the calculated parameters  $c_1$  with the precision  $\pm 4\%$  for the considered values of  $\xi$  and  $\kappa$  [295]

| $\xi$                    | 0.055 | 0.166 | 0.5  | 1.5  | 4.5  |
|--------------------------|-------|-------|------|------|------|
| $c_1$ ( $\kappa = 2.4$ ) | 3.12  | 3.13  | 2.92 | 2.89 | 2.93 |
| $c_1$ ( $\kappa = 4.8$ ) | —     | 3.13  | 2.96 | 2.96 | 3.05 |

$d_{S1} \cong q1 = 2\pi(\sqrt{2}n_d)^{1/3}$ , see Fig. 22(b) as well as [315]. Thus, the dynamics of the dissipative Yukawa system is determined by two fundamental parameters  $\Gamma^*$  and  $\xi$ . The first parameter can be considered as that responsible for the order in the system (and for the order/disorder transition) for its values from  $\Gamma^* < 1$  up to the melting point, and the second one is responsible for the scaling of the system's dynamics, i.e., can be considered as a scaling factor for the strongly coupled dissipative liquid-type system with  $\Gamma_c^* > \Gamma^* > 50$ .

The diffusion coefficient  $D$  of the particles in strongly non-ideal Yukawa systems exhibits exponential dependence on the parameter  $\Gamma^*$ , namely,  $D \sim \exp(-c_1 \Gamma^*/\Gamma_c^*)$ . To illustrate that, Fig. 22(b) presents the functional dependence of the diffusion rate  $D$  on the factor  $\Gamma^*$  in the logarithmic scale. It is easy to see that the dependence  $D(\Gamma^*)$  for  $\Gamma^*$  within the range of 50 to 102 is almost linear. Moreover, different curves corresponding to the different values of  $\xi$  and  $\kappa$  have almost similar inclination (i.e.,  $c_1 \cong \text{const}$ ). The best fit of the calculated dependencies  $D(\Gamma^*)$  gives  $c_1 \cong 3$  with the precision  $\pm 4\%$  for all considered  $\xi$  and  $\kappa$ , see Table 5.2. Fig. 23 shows the character of particle diffusion in the modeled system and presents the difference between the ensemble average  $\Delta_N = \sqrt{\langle \mathbf{l}(t) - \mathbf{l}(0) \rangle_N^2 / d^2}$  and its time average  $\Delta_N^t = \sqrt{\langle \langle \mathbf{l}(t) - \mathbf{l}(0) \rangle_N^2 \rangle_t / d^2}$  near the crystallization line.

The time-average diffusion rate  $D$  of the interacting particles can be determined by the proper choice of the characteristic time  $\tau_0$  in relation (5.7). It is assumed that the characteristic frequency

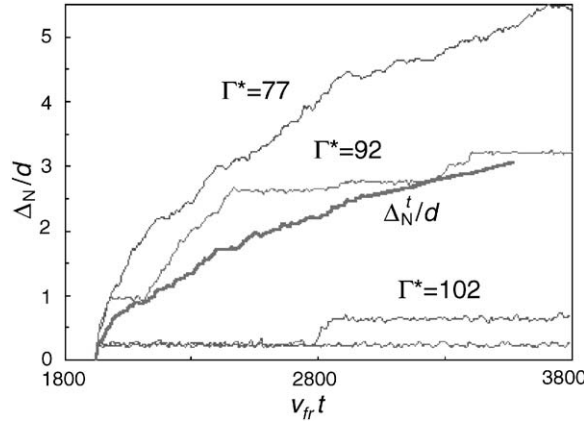


Fig. 23. Dependence of the normalized mean square displacement  $\Delta_N/d$  on the normalized time  $\nu_{fr}t$  for the system of macro-particles with  $\xi = 0.5$  and  $\kappa = 0.4$ . The bold line corresponds to the time averaged normalized displacement  $\Delta_N^t/d$  for  $\Gamma^* = 92$  [295].

$\nu_0$  of the transitions between the neighboring quasistable states is related to random collisions between the colloidal macroparticles with the characteristic frequency  $\omega \cong c_2\omega^*$ , where  $c_2 = const$ , as well as to collisions with the molecules of the ambient neutral gas with the characteristic frequency  $\nu_{fr}$ . Also,  $\tau_0 \approx 2/\nu_0$  can be written as  $\tau_0 = 2(\omega + \nu_{fr})/\omega^2$ , since the frequency  $\nu_0$  tends to  $\omega$  for  $\xi \ll 1$ , and  $\nu_0$  tends to  $\omega^2/\nu_{fr}$  in the case  $\xi \gg 1$  [316]. The unknown constant  $c_2$  can be found by the best fit to the numerical results; the procedure of the minimization of the mean square deviation between the relation (5.7) and the numerical data within the range of  $\Gamma^*$  from 50 to 102 gave  $c_2 \cong 1/\sqrt{\pi}$ . Thus taking into account the values of the coefficients obtained for expression (5.7) as well as equality  $(\omega^*d)^2 = (T_d\Gamma^*)/m_d$ , the diffusion coefficient is

$$D \cong \frac{T_d\Gamma^*}{12\pi m_d (\nu_{fr} + \omega^*/\sqrt{\pi})} \exp\left(-3\frac{\Gamma^*}{\Gamma_c^*}\right). \quad (5.11)$$

The error of the approximation of the numerical results by expression (5.11) does not exceed 2.5% for  $\Gamma^*$  within the range 50 to 102; with  $\Gamma^*$  decreasing down to 40, the error increases up to 7–13%, and for  $\Gamma^* = 30$  the error is 25–30%. The dependence of the ratio  $D/D_0$ , where  $D$  is determined by Eq. 22), on the value of  $\Gamma^*$  is given on Fig. 22(a) for various  $\xi$ .

The characteristic collision frequency between the dust particles in a liquid state  $\omega_l = \omega^*/\sqrt{\pi}$  can be obtained if to consider the interparticle force in the dust–plasma system  $F = (eZ_d)^2 \exp(-l/\lambda_D)(1 + l/\lambda_D)/l^2$ , taking into account that the electric fields of all particles except the nearest ones are fully compensated [300]. Then the frequency  $\omega_l$  determined by the first derivative  $dF/dl$  at the point  $l=d$  is given by  $\omega_l^2 = 4n_d(eZ_d)^2 \exp(-\kappa)(1 + \kappa + \kappa^2/2)/4\pi m_d$ . It is interesting to note that oscillations of particles with the frequencies close to  $\omega_l = \omega^*/\sqrt{\pi}$  can be observed for particle motions in the system even for relatively high viscosity when  $\xi=0.5$ . The detailed investigation of these oscillations is beyond the scope of this review, however, we note that this type of regular motion disappears with decreasing  $\Gamma^*$ .



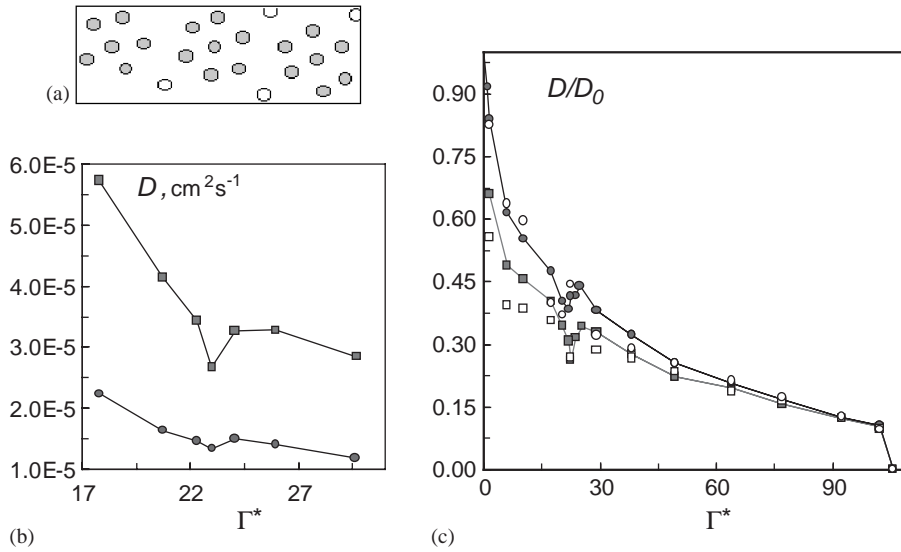


Fig. 24. Condensation of the colloidal clusters (a), and dependence on  $\Gamma^*$  of the diffusion coefficient  $D$  (b) and the ratio  $D/D_0$  (c) for various  $\zeta$ : circles correspond to  $\zeta = 0.166$ , and boxes—to  $\zeta = 0.5$ , filled circles and boxes are for  $\kappa = 2.4$ , others—for  $\kappa = 4.8$  [295].

Finally, note the effect of the particle condensation (growing dust clusters), Fig. 24(a), which was observed in numerical simulations [295], for the parameter  $\Gamma^*$  approximately equal to 23.5. The formation of groups of correlated particles is also reflected in the displacement of the position of the first maximum of the pair correlation function, see Fig. 21(b), as well as in the rapid change of the diffusion rate, Figs. 24(b) and (c). It can be suggested that this phenomenon is the second-order phase transition of the system from the strongly correlated liquid state to the non-ideal gas state. However, the attraction forces were not explicitly introduced into the set of equations (5.8), and the diffusion coefficient has not exhibited the tendency to disappear at the critical point  $\Gamma_g^* \approx 23.5$  [317]. The observed effect can be also related to the symmetry properties of the particle interaction potential; then the value of  $\Gamma_g^* \approx 23.5$  should define such conditions when the system properties related to the particles' identity are developed. Indeed, the mean free path of a particle in the liquid phase  $l_{p-p} = (6Dt_0)^{1/2}$  is assumed to be equal to the Wigner–Seitz radius  $a_{\text{WS}} = (4\pi n_d/3)^{-1/3}$ , then for the critical parameter  $\Gamma^*$  the value  $\sim 26$  can be obtained, which, within the considered accuracy of Eq. (5.11) in the range  $\Gamma^* < 30$ , coincides with  $\Gamma_g^*$ . We remind that for  $\Gamma^* < 40$ , the considered system cannot be modeled by simple relations obtained under the assumptions of the theory of “jumps”, and the scaling parameter  $\zeta$  given by (5.10) cannot be used for the analysis of the particle dynamics.

Note that the mean free path of the particle–particle collisions  $l_{p-p}$  is independent on the particle–neutral collisions in this approach. We can also estimate it from other considerations. For example, if to assume the mean free path as  $l_{p-p} = (8T_d/\pi\omega^2 m_d)^{1/2}$  equal to the Wigner–Seitz radius  $a_{\text{WS}} = (4\pi n_d/3)^{-1/3}$  then for the critical parameter at the point of the gas-liquid transition, we obtain  $\Gamma_{g-l}^* \approx 21$  for the Maxwellian particle velocity distribution. On the other hand, if to assume the particle velocity as the quadratic mean  $(3T_d/m_d)^{1/2}$ , we find  $\Gamma_{g-l}^* \approx 26$ , similar to the above

estimate on the basis of the diffusion coefficient. This condition can be analogous to the condition of finding one particle in the sphere with the radius  $l_{p-p}$  and can serve as a criterion of the transition of the system to the strongly non-ideal state.

Thus at present it is hardly possible to say definitely whether the observed effect is the (second order) phase transition or not. Nevertheless, it is obvious that at the point  $\Gamma^* \approx 23.5$  the simulated system qualitatively changes its dynamic characteristics. We note that the investigated transition is the transition from one non-ideal gas-like state to another non-ideal liquid-like state; it can be perhaps also related to the “flow and floe” state [7].

#### 5.4. Criteria of phase transitions in the dust-plasma crystals

The particle coupling in the dust-plasma crystals is usually characterized by the parameter  $\Gamma = (eZ_d)^2/dT_d$ . It is also well known that phase transitions in Yukawa systems are determined by two dimensionless parameters:  $\Gamma$  and  $\kappa = d/\lambda_D$ . The extensive numerical studies [296–300,318–320] demonstrate that in a Coulomb system of particles the short-range order appears for  $\Gamma \gg 1$ , with the critical value  $\Gamma_m \approx 106$  on the melting line [296–299] (for complex plasmas, the assumption of plasma screening (5.6) leads to larger  $\Gamma_m$ ). The studies [300,308] suggest that the condition of the constant (normalized) non-ideality parameter  $\Gamma^* = (1 + \kappa + \kappa^2/2) \exp(-\kappa)\Gamma$  (namely,  $\Gamma_m^* \cong 106$ ) can be used as the melting criterion for the body-center cubic (*bcc*) lattice. However, the functional dependence relating  $\Gamma$  and  $\kappa$  with the critical value  $\Gamma_m = f(\Gamma, \kappa)$  is presently unknown for the transitions of face-center cubic (*fcc*) lattice into the liquid as well as for the transitions between the *bcc* and *fcc* structures. Some authors suggest various linear approximations of numerical data for different parts of the phase diagram [318,320]; these approximations usually appear as a result of the best mathematical fit, though sometimes being not fully justified physically. Here, we review the criteria of phase transitions in Yukawa system by employing simulation data [299,318,320] obtained for systems without dissipation, as well as on the basis of simulations [183] of a three-dimensional dissipative Yukawa system, with parameters close to those in the experiments on laboratory weakly ionized gas-discharge plasmas.

There are various phenomenological criteria for phase transitions in Yukawa system used for a complex plasma. The most popular is the Lindemann criterion stating that the melting occurs when the ratio of the root-mean-square displacement  $\Delta_0$  of a particle from its equilibrium position to the average interparticle distance  $d$  achieves 0.15. Since in numerical simulations the displacement  $\Delta = \sqrt{2}\Delta_0$  of a particle from the center of mass is usually computed, the ratio  $\delta_c = \Delta/d$  on the melting line should be expected about  $\sim 0.21$  (for the majority of real solids  $\Delta/d \sim 0.2$ – $0.25$  at the melting point). However, various numerical simulations give for the Lindemann parameter the range from 0.16–0.19 for *fcc* lattices to 0.18–0.2 for *bcc* structures. These numbers, less than 0.21, may be related to the insufficient number of particles  $N_p$  in the modeled systems; we note that  $\Delta/d \rightarrow 0.2$  with the increase of  $N_p$  for the melting of the both types of lattices [320]. Another popular criterion, proposed by Hansen [321], defines the value of the first maximum  $S_1$  of the structure factor in the liquid state to be less than 2.85. These numbers can also vary (from 2.5 to 3.2) for different simulations and strongly depend on the definition of the structure factor in the systems with a finite number of particles.

A condition, analogous to the Lindemann criterion, can be obtained [183] with the assumption that the average volume of thermal fluctuations  $V_{\text{tf}} \sim (\alpha_\pi \Delta)^3$  for *bcc* lattice should not exceed

Table 5.3

The ratio  $\delta_c$  of the most probable displacement  $\Delta$  to the mean interparticle distance  $d$ , the factors of the coupling parameter  $\Gamma = (eZ_d)^2 n_d^{1/3} / T_d = C_p (K_n \exp(-\kappa))^{-1}$  on the lines of various phase transitions, as well as the coefficient  $C_w$  for the approximation  $\omega_c^2 = C_w n_d (eZ_d)^2 \exp(-\kappa)$  of the characteristic oscillation frequencies in *bcc* and *fcc* lattices; here,  $\alpha_\pi = (4\pi/3)^{1/3}$ ,  $\kappa = d/\lambda_D$ ; reprinted from Ref. [183]

| Phase transition                    | $\delta_c = \Delta/d$   | $C_p$  | $K_n$   | $C_w$  |
|-------------------------------------|---|--|---|--|
| <i>bcc</i> $\rightarrow$ liquid     | $\frac{(1-\pi\sqrt{2}/8)^{1/3}}{2\alpha_\pi}$<br>$\sim 0.211$                                   | $3\pi/(2\delta_c^2)$<br>$\sim 106$           | $\left(1 + \kappa + \frac{\kappa^2}{2}\right)$  | $\frac{4}{\pi} \left(1 + \kappa + \frac{\kappa^2}{2}\right)$ |
| <i>bcc</i> $\rightarrow$ <i>fcc</i> | $\frac{(1-\pi\sqrt{2}/6)^{1/3}}{\sqrt{2}\alpha_\pi} \left(1 - \frac{\alpha_\pi}{\kappa}\right)$ | $3\pi/(2 \times 0.27^2)$<br>$\sim 64$        | $\left(1 + \kappa + \frac{\kappa^2}{2}\right) \left(1 - \frac{\alpha_\pi}{\kappa}\right)^2$ |  |
| <i>fcc</i> $\rightarrow$ <i>bcc</i> | $\sim 0.27 \left(1 - \frac{\alpha_\pi}{\kappa}\right)$  | $3/(0.27^2 \alpha_\pi^3)$<br>$\sim 9.8$      | $\kappa \left(1 - \frac{\alpha_\pi}{\kappa}\right)^3$                                       | $2\alpha_\pi^3 (\kappa - \alpha_\pi)$                        |
| <i>fcc</i> $\rightarrow$ liquid     | $\frac{(1-\pi\sqrt{2}/6)^{1/3}}{2\alpha_\pi}$<br>$\sim 0.198$                                   | $3/(\alpha_\pi^3 \delta_c^2)$<br>$\sim 18.5$ | $\kappa - \alpha_\pi$   |  |

$\left(1 - \pi\sqrt{2}/8\right) V_d \approx 0.32V_d$ , where  $\alpha_\pi = (4\pi/3)^{1/3}$ ,  $V_d = n_d^{-1} \equiv (\alpha_\pi a_{W-S})^3$ , and  $a_{W-S} = (4\pi n_d/3)^{-1/3}$  is the Wigner–Seitz radius. For a stable *fcc* structure to exist, we have  $V_{\text{tf}} < \left(1 - \pi\sqrt{2}/6\right) V_d \approx 0.26V_d$  [312]. Accounting for the possibility of counter displacements of particles,  $V_{\text{tf}} \cong (2\alpha_\pi \Delta)^3$  (the factor 2), we find that the value of the ratio  $\Delta/d$  must either exceed 0.211 ( $\Delta_0/d \geq 0.15$ ) to melt *bcc* structure or 0.198 ( $\Delta_0/d \geq 0.14$ ) to melt *fcc* lattice. The criterion for the transition between the *bcc* and *fcc* structures can then be obtained with the assumption that for the change of the *bcc* symmetry of the lattice, the interparticle distances should exceed  $\lambda_D$  (the grain interaction is in this case similar to that of “hard spheres” when formation of *fcc* structures is possible [322]). Thus, we have the following expression for the line of transition between the *bcc* and *fcc* structures:

$$2 \left(1 - \pi\sqrt{2}/6\right)^{-1/3} \Delta_0 \approx a_{W-S} - \lambda_D, \quad (5.12)$$

where  $(a_{W-S} - \lambda_D)$  determines the effective size of the region where a displacement of one particle does not significantly influence other particles of the crystal lattice. This assumption is supported by numerical simulations [299] where the *fcc* structure was not formed when  $a_{W-S} < \lambda$  even for  $\Gamma \rightarrow \infty$ . For the present simulation, the values of  $\delta_c$  and  $\Delta_0/d$  for various phase transitions are presented in Table 5.3 and Fig. 25; the range of  $\kappa$  between 5.8 and 6.8 defines the region with the triple (*bcc*-*fcc*-liquid) phase transition.

New empirical rules can be formulated to determine the normalized coupling parameter  $\Gamma_n = K_n \exp(-\kappa) \Gamma$  as a value close to a constant  $C_p$  at the line of different phase transitions (including the melting of cubic lattices and the transition between the *bcc* and *fcc* structures). The normalized coefficient  $K_n$  and constant  $C_p$  can be obtained from the relationship for the harmonic oscillator

$$\Delta_0^2 = 3T_d/m_d \omega_c^2, \quad (5.13)$$

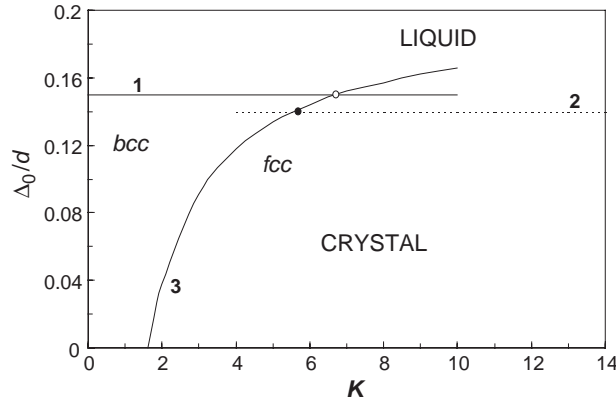


Fig. 25. Dependence of  $\Delta_0/d$  on  $\kappa$  for various phase transitions: 1— $bcc \rightarrow$  liquid, 2— $fcc \rightarrow$  liquid; 3— $bcc \leftrightarrow fcc$ ; filled circle— $\kappa = 5.8$ ; circle— $\kappa = 6.8$  [183].

where  $m_d$  is the particle mass and  $\omega_c$  is the characteristic frequency of the particle vibrations in the lattice. Approximation (5.13) takes place when  $T_d \gg \Theta_D$  ( $\Theta_D$  is the Debye temperature) and the displacement  $\Delta_0$  can be characterized by the frequency  $\omega_c$  not depending on the temperature. To determine this frequency, the most frequently used are the quasi-harmonic [318] and/or the Einstein approximations [297,318] based on the calculations of the oscillation frequency of a particle about its equilibrium position when all other particles are fixed. For both cases, there is no analytical form for  $\omega_c$ , and the results are usually additionally adjusted by the linear, quadratic, and/or cubical fits of the numerical results for various (sufficiently short) parts of the phase diagrams [297,318].

It has also been demonstrated [295,298,299] that the characteristic frequencies of particle oscillations in complex dust fluids and  $bcc$  lattices are proportional to the dust–lattice wave frequencies. Thus the frequency  $\omega_c = \omega_{bcc}$  for the  $bcc$  lattice can be obtained from the expression  $F = (eZ_d)^2 \exp(-l/\lambda_D)(1 + l/\lambda_D)/l^2$  for the intergrain force assuming that the electric fields of all particles except the nearest ones are fully compensated [300]: it is determined by the probability  $8/4\pi$  of the intergrain collisions and by derivative  $dF/dl$  at  $l = d$ , and is given by  $\omega_{bcc} = eZ_d(4n_d/\pi m_d)^{1/2}(1 + \kappa + \kappa^2/2)^{1/2} \exp(-\kappa/2)$ . Substituting this expression into Eq. (5.13) gives  $\Gamma_n = \Gamma^*$  and  $C_p \cong 3\pi/(2\delta_c^2) \approx 106$  in accordance with [300,308] (here,  $\delta_c \equiv \sqrt{2}\Delta_0/d = (1 - \pi\sqrt{2}/8)^{1/3}/2\alpha_\pi \approx 0.211$  at the melting line of the  $bcc$ -structure, see Table 5.3).

On the other hand, the assumption that for the  $fcc$  structure  $\omega_c = \omega_{fcc} \propto dF/dl$  leads to  $\Gamma^* = const$  on the crystallization line for lattices of both types thus contradicting the results of numerical simulations, see Fig. 26. Suitable approximation  $\omega_{fcc}^2 \approx 2\alpha_\pi^3 n_d (eZ_d)^2 \exp(-\kappa)(\kappa - \alpha_\pi)/m_d$  can be obtained for a homogeneous system with the gradient  $dF_\Sigma/dl$  of the sum  $F_\Sigma$  of the electrical forces estimated as  $dF_\Sigma/dl \propto n_d (eZ_d)^2 \exp(-\kappa)(\kappa - \alpha_\pi)$ . Thus, assuming that  $\delta_c = (1 - \pi\sqrt{2}/6)^{1/3}/2\alpha_\pi$  on the melting line of the  $fcc$  lattice, we find from Eq. (5.13)  $\Gamma_n = \Gamma(\kappa - \alpha_\pi) \exp(-\kappa)$ ,  $C_p \cong 3/(\alpha_\pi^3 \delta_c^2) \approx 18.5$  (see Table 5.3), and

$$\Gamma_m^* \approx 18.5(1 + \kappa + \kappa^2/2)/(\kappa - \alpha_\pi). \quad (5.14)$$

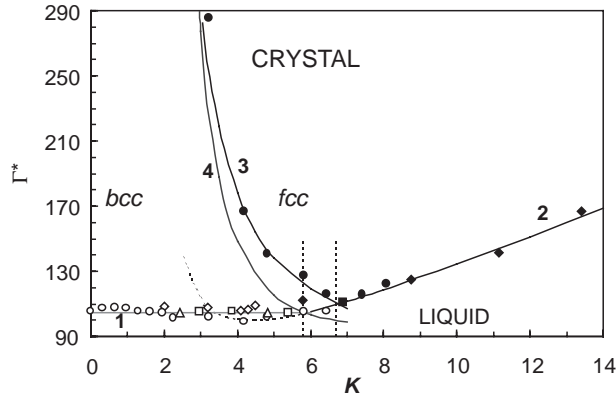


Fig. 26. Dependence of  $\Gamma^*$  on  $\kappa$  for various phase transitions: circles—data of [308]; diamonds—[297]; squares—[296]; triangles—[312]; and jump of  $S_1$  for various  $\xi$  (filled symbols correspond to formation of  $fcc$  lattice); 1— $\Gamma^* = 106$  ( $bcc \rightarrow$  liquid), 2— $fcc \rightarrow$  liquid; 3— $bcc \rightarrow fcc$ ; 4— $fcc \rightarrow bcc$  [183].

The use of the modified parameter  $\Gamma_m^*$  (5.14) allows one to illustrate the behavior of the melting curves for the transitions  $fcc$ -lattice–liquid and  $bcc$ -lattice–liquid, Fig. 26. The difference between condition (5.14) and results of Ref. [299,320] of modeling the  $fcc$ -lattice–liquid phase transition does not exceed 2% for  $\kappa > 6.8$ .

The normalized coupling parameter  $\Gamma_n$  (see Table 5.3) and the modified parameter  $\Gamma^*$  at the line of transition from the  $bcc$  structure to the  $fcc$  structure can be obtained from Eqs. (5.12)–(5.13) with  $\omega_c = \omega_{bcc}$ . We have

$$\Gamma^* \approx 64\kappa^2(\kappa - \alpha_\pi)^{-2}. \quad (5.15)$$

Suitability of condition (5.15) as a criterion for the  $bcc$ – $fcc$ -transition was checked using data of Ref. [299]. The deviation of the calculated values of  $\Gamma^*$  for the  $bcc$ – $fcc$  transition from Eq. (5.15) is within  $\pm 2\%$ , as illustrated in Fig. 26 (curve 3). Taking into account that the possibility of the reverse transition from the  $fcc$  to  $bcc$  structure is defined by the frequency  $\omega_{fcc}$ , as a criterion for this transition one can use

$$\Gamma^* \approx 9.8\kappa^2(\kappa - \alpha_\pi)^{-3}(1 + \kappa + \kappa^2/2). \quad (5.16)$$

Note that condition (5.16) depends on the approximation of the frequency  $\omega_{fcc}$  and therefore can be incorrect for small  $\kappa \rightarrow \alpha_\pi$ . However, calculations on the basis of (5.15)–(5.16) (curves 3 and 4 in Fig. 26) fully determine the region of the triple phase transition ( $\kappa = 5.8$ – $6.8$ ) and agree well with the results obtained for  $\Delta_0/d$  (see Fig. 25). We note that the difference in the positions of curves described by Eqs. (5.15)–(5.16) makes it possible to explain the discrepancy of the numerical results on the position of the triple point of in Refs. [299,320].

Since the determination of the coupling parameters on the lines of phase transitions is based on Eq. (5.13), their values are independent on the viscosity of the background gas. To examine this assumption, the arrangements of grains have been calculated in a complex plasma for various neutral gas pressures, dust charges and temperatures, and the plasma screening lengths ( $\kappa = 2.4$  and  $4.8$ ). The simulation has been performed by the Brownian dynamics method with the stochastic Langevin force taking into account the particle friction with the plasma neutrals. To analyze the particle dynamics,

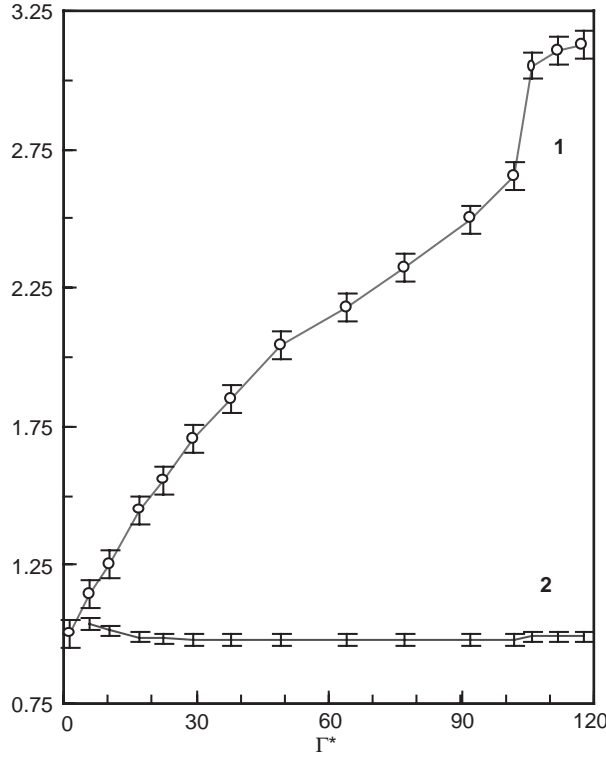


Fig. 27. Dependence on  $\Gamma^*$  of the first maximum of the structure factor  $S_1$  (curve 1) and its position  $d_{S1}/q_1$  (curve 2). The ranges of the deviations of the computed functions are plotted for various values of  $\xi$  [183].

three-dimensional equations of motion under the periodic boundary conditions were solved, and the number of independent particles  $N_p = 125$ ; more details are in Ref. [183].

The ratio between the particle interaction and dissipation in the system is defined by the parameter  $\xi = \omega_{bcc}/\nu_{fr}$ . Then for typical experimental conditions ( $\rho \cong 4 \text{ g/cm}^3$ ,  $T_e \cong 1.5 \text{ eV}$ ,  $C_v \cong 700$ ,  $\kappa \cong 2$ ),  $\xi \approx 10^{-3}(4n_d[\text{cm}^{-3}]/\pi a[\mu\text{m}])^{1/2}(p_0[\text{Torr}])^{-1}$ . If the particle radius is  $a = 2 \mu\text{m}$ , the number density  $n_d$  is from  $10^3$  to  $10^5 \text{ cm}^{-3}$ , and the neutral gas pressure  $p_0$  is from 1 to 0.01 Torr, the range is  $\xi = 0.04\text{--}6.9$ .

To analyze the ordering of particles in the modeled system, the structure factor  $S(q)$  is used. The dependencies of the first maxima of  $S_1$  for  $S(q)$  as well as the ratios of their positions  $q = d_{S1}$  to the position  $q_1 = 2\pi(\sqrt{2}n_d)^{1/3}$  of  $S_1$  for the crystal *bcc* structure versus  $\Gamma^*$  are presented in Fig. 27 for different  $\xi = 0.08, 0.26, 0.79, 2.37, 7.1$ . The analysis of these simulations demonstrates that the normalized coupling parameter  $\Gamma^*$  fully determines the particle correlations (formation of the long-range order as well as the short-range ordering) and can be considered as the parameter responsible for the ordering in the dissipative Yukawa system when it changes from  $\Gamma^* \sim 1$  up to the crystallization point. For  $\kappa < 5.8$ , the *bcc* lattice is formed with the increase of  $\Gamma^* \rightarrow \Gamma_m^*$ ; the abrupt changes of  $S_1$  from 2.65 to 3.1 is observed in the range from  $\Gamma_c^* \cong 102$  to  $\Gamma_m^* \cong 106$  (Fig. 27). We stress that  $\Gamma_{cm}^* \cong 104(\pm 2\%)$  is practically independent on the viscosity of the neutral



gas, that is why this criterion is in agreement with results of numerical simulations without dissipation [299,318,320] (see Fig. 26). Deviations of these results from  $\Gamma_{cm}^*$  are within  $\pm 5\%$  and can be related to the differences in the details of the numerical methods used, as well as by the particular choice of the value  $\Gamma$  either at the melting line or at the crystallization point of the system. We note that the obtained  $\Gamma_{cm}^*$  agrees well with the theoretical result [298], where for the coupling parameter on the line of the phase transition in a Coulomb system the number  $105(\pm 3\%)$  was obtained, also agreeing with the result of the calculations of the liquid-crystal (crystallization) [297] as well as the crystal-liquid (melting) phase transitions [296]. The obtained results (including the criteria for the phase transitions) are independent on the viscosity of the surrounding gas and can be applied for the analysis of the particle dynamics in binary colloidal systems of various types where the Yukawa-type potentials are used extensively, for example, in solutions of viruses or for studies of diffusion-controlled processes in the physics of polymers.

## 6. Collective plasma phenomena in the dust–plasma interactions: the ion wake

In a series of pioneering experiments [178,179,223,275,323], the formation of microscopic Coulomb crystals of solid particles has been demonstrated. Associated with the Coulomb crystallization in strongly coupled complex plasmas, there have also been indications of the formation of pairs of particulates with relatively small separations [179], as well as of the presence of the enhanced low-frequency fluctuations [323]. In a typical experiment, the dust levitates in the sheath region [237] where the balance between the gravitational and electrostatic forces is established (see, e.g., [178,179]), with often observed aligning of the dust particles in the direction of the flow [7].

The fundamental question of importance for the understanding of the processes involving formation and evolution of various self-organized structures such as dust–plasma crystals [7] and other formations like dust clouds, dust voids, etc. [233–235,283,324] in a complex plasma, is the interaction of dust grains with other grains and the surrounding plasma. Since in a typical laboratory discharge the particles are negatively charged and usually levitate in the sheath or pre-sheath region under the balance of gravitational, electrostatic (due to the sheath electric field) and plasma (such as the ion drag) forces, these interactions involve collective processes associated with the specifics of the plasma sheath.

In the sheath region, the ion flow to the electrode is established thus naturally providing a distinctive direction, with the plasma properties different in the direction parallel or perpendicular to the flow. The ion flow, providing a direct dragging influence (and supporting, in particular, the formation of dust voids, see Section 5), is also responsible for the generation of associated collective plasma processes. The latter strongly influence the formation of the plasma–dust crystals. A theory taking into account these features and suggesting that in the case of supersonic velocities of the flow the ion wake field is formed behind the levitating dust grain was proposed [254–256]<sup>2</sup> and later developed

---

<sup>2</sup> Note that similar attractive forces appear between moving dust particles [341] involving the collective interactions via the low-frequency electrostatic perturbations. The effect is analogous to the Cooper pairing [342] of electrons in superconductors, and has been also studied for the two-component electron–ion plasmas [343] in which the possibility of electron attraction has been demonstrated.

in a number of studies [324–328]. It was demonstrated that the plasma wake can strongly modify the interactions of dust grains between themselves and with the plasma; in particular, supporting a Cooper-pairing-like attraction of the grains of the same sign of the charge [254,257]. The theory proved to be very successful in explaining the observed experimental phenomena (e.g., dust particle vertical alignments), and was confirmed in specifically designed dedicated experiments [329] (see also experiments on pairing of two dust particles [386,387]).

The complete problem of the plasma dynamics around a macroscopic body in the presence of plasma flows is highly nonlinear and therefore its numerical analysis is of a major importance. Various numerical methods can be employed to solve the problem. Among them, direct integration of the equations of motions of the plasma particles represents a numerical experiment with significance approaching experiments in the laboratory. The particle-in-cell (PIC) simulations [330] clearly demonstrated the formation of the wake potential with the potential wells attracting the lower dust grains. Recent *ab initio* three dimensional molecular dynamics (MD) studies [331–333] also show the region of the strong ion focusing behind the grain for the case of a single grain as well as two grains aligned parallel and perpendicular to the ion flow. According to the majority of the experiments, the most studied (theoretically, numerically, and experimentally) cases correspond to spherical dust grains. However, recent experiments [205,334,335] prompted the interest to rod-like grains and the theoretical study [336,337] predicted the wake formation as generated by the ion flow in the cases of particles with dipole moments and elongated (rod-like) particles.

### 6.1. Plasma and levitated dust in the collisionless sheath region

The physics of the sheath region of two-component plasmas has been qualitatively understood for many years [237]. It was demonstrated that strong electric fields, plasma density gradients, and ion flows are established in the sheath. According to the Bohm criterion, the average velocity of the plasma ion flow in the sheath region must exceed the ion sound speed. The effects of dust grains in the collisionless plasma–wall region were also investigated [338–340]. In particular, it was found that, similar to the Bohm criterion for two-component plasmas, the ions entering the sheath region must have a velocity exceeding the critical one (the latter depends on the dust concentration and is not less than the ion sound velocity) [340].

The standard model of the dust-free sheath [237] considers the Boltzmann distributed electrons and the ballistic (cold) ions. Here, following [247], we assume the discharge pressure to be low enough that ion collisions with neutrals and other species can be neglected and ignore the influence of the dust grains on the field distribution in the sheath region. The ion continuity equation gives the ion density  $n_i$  in terms of the density  $n_0$  and velocity  $v_0$  of the ion flow in the plasma bulk, i.e. far away from the electrode,

$$n_i(z) = n_0 \left[ 1 - \frac{2e\phi(z)}{m_i v_0^2} \right]^{-1/2},$$

where  $\phi(z)$  is the sheath potential. The collisionless sheath structure depends on the ballistic ions within the sheath with the distribution function  $f_i \propto \delta(\mathbf{v}_\perp) \delta(v_z - v_i(z))$ , where  $v_i(z)$  is the ion streaming velocity at the distance  $z$  from the electrode. The ion velocity determined from the energy

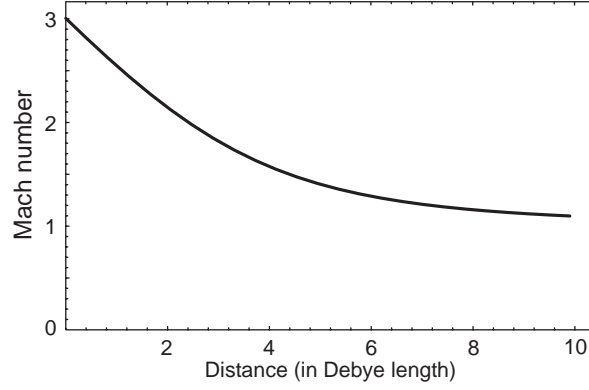


Fig. 28. Dependence of the Mach number of the ion flow  $M(z) \equiv v_i(z)/v_s$  on the distance  $h = z/\lambda_D$  from the electrode. Here we have  $M_0 = v_0/v_s = 1$ ,  $\lambda_D = 3 \times 10^{-2}$  cm,  $T_e = 1$  eV, and  $m_i/m_e = 40 \times 10^3$ . Reprinted from Ref. [247].

balance equation is thus given by

$$v_i(z) = v_0 \left[ 1 - \frac{2e\phi(z)}{m_i v_0^2} \right]^{1/2}.$$

The sheath potential is found from Poisson's equation [237]

$$\frac{d^2\phi(z)}{dz^2} = 4\pi en_0 \left[ \exp\left(\frac{e\phi(z)}{T_e}\right) - \left(1 - \frac{2e\phi(z)}{m_i v_0^2}\right)^{-1/2} \right], \quad (6.1)$$

where the total charge contributed by the dust grains is neglected (i.e., assuming the dust number density to be small), in contrast to Ref. [340], where the space charge of the dust grains is included, but the mutual interaction of the grains is neglected. Note that the case of a higher pressure, with a sheath structured by ions drifting through the background neutrals, was considered above in Section 4.4.

Eq. (6.1) can be integrated once to give (applying the boundary conditions  $E(z=\infty)=\phi(z=\infty)=0$ )

$$\left(\frac{d\phi(z)}{dz}\right)^2 = 8\pi n_0 T_e \left[ \exp\left(\frac{e\phi(z)}{T_e}\right) - 1 + \frac{v_0^2}{v_s^2} \left( \left(1 - \frac{2e\phi(z)}{T_e} \frac{v_s^2}{v_0^2}\right)^{1/2} - 1 \right) \right], \quad (6.2)$$

where  $v_s^2 = T_e/m_i$  is the squared ion-sound speed. Assuming the electrode has a potential of  $-4$  V, typical of dust plasma experiments in the collisionless regime, Eq. (6.2) can be numerically integrated to give the dependence of the potential, and thence of the sheath electric field, on the distance from the electrode. Dependence of the Mach number  $M(z) \equiv v_i(z)/v_s$  of the ion flow on the distance from the electrode is presented in Fig. 28.

Linearizing Eq. (6.2) with respect to small potential and field variations, one can find

$$\delta E \approx \frac{4\pi n_0 T_e}{E_0} \left[ \exp\left(\frac{e\phi_0}{T_e}\right) - \left(1 - \frac{2e\phi_0}{T_e} \frac{v_s^2}{v_0^2}\right)^{-1/2} \right] \frac{e\delta\phi}{T_e},$$

where the electric field  $E_0$  is at  $z = 0$ . Now, if to assume that the sheath electric field near the position of the dust grains can be linearly approximated, one obtains

$$\delta E \approx -4\pi n_0 e \left[ \exp\left(\frac{e\phi_0}{T_e}\right) - \left(1 - \frac{2e\phi_0}{T_e} \frac{v_s^2}{v_0^2}\right)^{-1/2} \right] \delta z .$$

Thus the effective width of the potential well trapping dust particles can be written as

$$\gamma_w = 4\pi e |Q| n_0 \left[ \exp\left(\frac{e\phi_0}{T_e}\right) - \left(1 - \frac{2e\phi_0}{T_e} \frac{v_s^2}{v_0^2}\right)^{-1/2} \right] . \quad (6.3)$$

The charge  $Q$  of the dust particles (which is dependent on the sheath parameters, in particular, on the local electric sheath potential) is found from the standard condition of a zero total plasma current onto the grain surface  $I(Q) = I_e(Q) + I_i(Q) = 0$ . For the collective processes investigated on the time scale of the characteristic frequencies of the order of a few times  $10 \text{ s}^{-1}$ , which are much lower than the charging frequency [12] (that can be of the order of  $10^5 \text{ s}^{-1}$ ), the (re)charging of dust grains is practically instantaneous, and their charging dynamics can be ignored. The electrons are Boltzmann distributed, and the possible changes of the electron temperature in the plasma sheath are neglected. The inter-grain distance is assumed not less than the Debye length, so that the ion trajectory is affected by only a single grain. Thus the charge of a dust particle in the sheath region is determined by

$$\sqrt{2\pi} \left[ 1 - \frac{2eQ(z)}{am_i v_0^2 (1 - 2e\phi(z)/m_i v_0^2)} \right] = \frac{v_s}{v_0} \sqrt{\frac{m_i}{m_e}} \exp \left[ \frac{e}{T_e} (\phi(z) + Q(z)/a) \right] . \quad (6.4)$$

Note that from (6.4) follows that if the electrode potential is sufficiently negative, and a dust grain is very close to the electrode, its charge can become zero and, possibly, positive (a result obtained also in Ref. [340]); for real conditions this only means that the particle cannot levitate at this distance and falls down on the electrode.

For a particle levitating in the sheath field, the sheath electrostatic force on the grain is given by  $F_E = Q(z)E(z)$ , this includes the  $z$ -dependence of the grain charge  $Q$ , since the instantaneous transfer of charge onto and off the dust grain at any grain position in the sheath is assumed, such that Eq. (6.4) is always satisfied. The balance of forces in the vertical direction also includes the gravitational force  $F_g = m_d g$ , so that for the equilibrium of the grain,

$$Q(z)E(z) = m_d g .$$

Solution of this equation together with the charging equation (6.4) gives the dependence of the charge of the grain, levitating in the sheath electric field, as a function of its size, an example is shown in Fig. 29. For the levitating dust particle, there is a one-to-one correspondence of its size to its equilibrium position of levitation in the sheath, as shown in Fig. 30. Note that the equilibrium solutions for positions closer than  $z_{\min} = 1.64\lambda_D$ , where the grain has a critical size  $a = a_{\text{cr}}$ , are unstable with respect to vertical oscillations, see Section 8.1.

## 6.2. Supersonic wake behind a charged spherical particle levitating in the sheath

Here, we present a possibility [254,255] of the charged particle attraction in dust plasma systems with the finite ion flows. The important feature of the present investigation is that we consider the

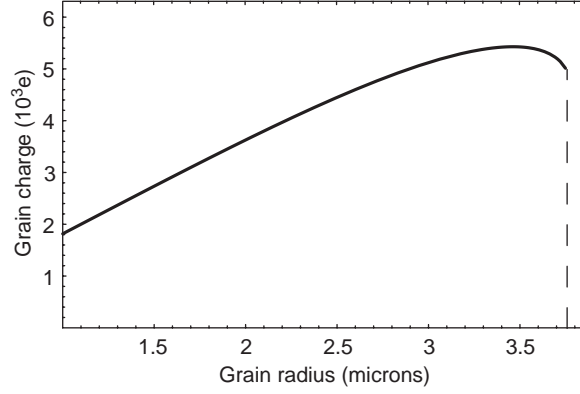


Fig. 29. Dependence of the charge  $q = -(Q/e) \times 10^{-3}$  of the dust grain, levitating in the sheath electric field, on its size. Here,  $M_0 = 1$ ,  $\lambda_D = 3 \times 10^{-2}$  cm,  $T_e = 1$  eV,  $m_i/m_e = 40 \times 10^3$ ,  $\rho = 1$  g/cm<sup>3</sup>, and  $a_{\max} = 0.375 \times 10^{-3}$  cm [247].

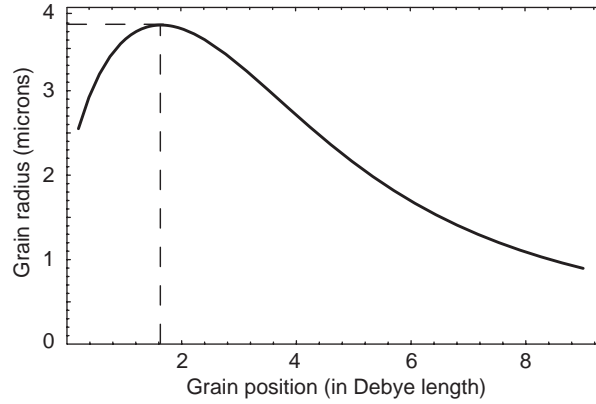


Fig. 30. Dependence of the position  $h = z/\lambda_{D0}$  of the dust grain, levitating in the sheath electric field, on its size. The sheath plasma parameters are the same as in Fig. 29; the position, corresponding to  $a_{\text{cr}}$ , is  $z_{\min} = 1.64\lambda_{D0}$  [247].

situation close to laboratory experiments, namely, static dust particles which can interact through the ion low-frequency oscillations in the ion flow, which velocity  $v_0$  exceeds the ion-acoustic velocity  $v_s$ . Physically, the generation of the wake acoustic fields in this case is the same as the generation of the electromagnetic fields for the charge at rest placed in a medium moving faster than light.

The electrostatic potential around the isolated test dust particle can be written as

$$\Phi(\mathbf{x}, t) = \int \frac{Q}{2\pi^2 k^2} \frac{\delta(\omega - \mathbf{k} \cdot \mathbf{v}_d)}{\varepsilon(\mathbf{k}, \omega)} \exp(i\mathbf{k} \cdot \mathbf{x} - i\omega t) d\mathbf{k} d\omega, \quad (6.5)$$

where  $Q$  and  $\mathbf{v}_d$  ( $|\mathbf{v}_d| \equiv v_d \ll v_{Ti}$ ) are the charge and velocity of the test dust particle, respectively. The dielectric response function of the plasma in the presence of a finite ion flow with the speed  $v_0$  ( $v_{Ti} \ll v_0 \ll v_{Te}$ , where  $v_{Ti,e} = (T_{i,e}/m_{i,e})^{1/2}$  is the electron (ion) thermal velocity,  $T_i \ll T_e$ ) is calculated

under the condition

$$kv_{Ti} \ll |\omega - k_z v_0| \ll kv_{Te} , \quad (6.6)$$

where the  $z$ -axis is directed along the ion flow.

We note that two different cases appear. The first one corresponds to the situation when the influence of the dust on dielectric properties of the plasma can be neglected; the polarization of plasma is determined by the contribution of electrons and ions. The second case corresponds to the sufficiently high dust density. For the latter situation, the dust particle is considered at rest, i.e.  $|\omega = \mathbf{k} \cdot \mathbf{v}_d| \ll kv_{Td}$ , where  $v_{Td} = (T_d/m_d)^{1/2}$  is the dust thermal velocity. The plasma dielectric response is given by

$$\varepsilon(\mathbf{k}, \omega) = 1 + \frac{1}{k^2 \lambda_D^2} - \frac{\omega_{pi}^2}{(\omega - k_z v_0)^2} , \quad (6.7)$$

where  $\lambda_D = \lambda_{De} \equiv (T_e/4\pi n_e e^2)^{1/2}$  is the plasma Debye length for the first case (of an isolated test particle),  $\lambda_D^{-2} = \lambda_{De}^{-2} + \lambda_{Dd}^{-2}$  for the second situation (when condition (6.6) takes place),  $\lambda_{Dd} = (T_d/4\pi n_d Q_d^2)^{1/2}$  is the dust Debye radius,  $Q_d$  is the charge of the other dust particles. The negative contribution due to the ion flow is the most important for the present consideration. From Eq. (6.7), we can also see that the relative contribution of the plasma electrons is of less importance.

The inverse of function (6.7) can be written as

$$\frac{1}{\varepsilon(\mathbf{k}, \omega)} = \frac{k^2 \lambda_D^2}{1 + k^2 \lambda_D^2} \left[ 1 + \frac{\omega_s^2}{(\omega - k_z v_0)^2 - \omega_s^2} \right] , \quad (6.8)$$

where  $\omega_s = kv_s/(1 + k^2 \lambda_D^2)^{1/2}$  is the frequency of the oscillations in the ion flow, and  $v_s = \lambda_D \omega_{pi}$  is the ion sound velocity. Substituting Eq. (6.8) into (6.5), the total electrostatic potential can be represented as the sum of the two potentials

$$\Phi(\mathbf{x}, t) = \Phi_D(\mathbf{x}, t) + \Phi_W(\mathbf{x}, t) , \quad (6.9)$$

where

$$\Phi_D = \frac{Q}{r} \exp(-r/\lambda_D) \quad (6.10)$$

is the usual static Debye screening potential, and the additional potential involving, in particular, the collective effects (the ion wake) caused by the oscillations in the ion flow is given by

$$\Phi_W = \int \frac{Q}{2\pi^2 k^2} \frac{k^2 \lambda_D^2 \omega_s^2 \exp(i\mathbf{k} \cdot \mathbf{x} - i\omega t)}{(1 + k^2 \lambda_D^2)[(\omega - k_z v_0)^2 - \omega_s^2]} \delta(\omega - \mathbf{k} \cdot \mathbf{v}_d) d\mathbf{k} d\omega . \quad (6.11)$$

From Eq. (6.11), it follows that the potential changes its sign due to the overscreening depending upon whether  $\omega - k_z v_0$  is larger or smaller than  $\omega_s$ . In the case when  $\omega - k_z v_0$  is close to this frequency, strong resonant interaction between the oscillations in the ion flow and the test particulate appears. The important point is that even for the static test charge, the potential “behind” it oscillates as a wake field, if the speed of the ion flow exceeds the ion-acoustic velocity. Therefore the formation of the quasi-lattice structures can be possible since the periodic regions of attractive and repulsive forces between the particulates of the same charge appear.



Furthermore, Eq. (6.11) is integrated over frequencies assuming  $\mathbf{k} \cdot \mathbf{v}_d \approx 0$ . Integration over angles can be proceeded using an expansion in spherical harmonics [343]. Assuming that  $k_\perp^2 \lambda_D^2 \ll (M^2 - 1)$  as well as  $k_\perp \lambda_D \ll 1$ , where  $M = v_0/v_s$  is the Mach number of the flow, one can obtain

$$\Phi_W(z, \rho) \approx \frac{2Q\lambda_D^2}{\sqrt{M^2 - 1}} \int_0^1 J_0(k_\perp \rho) \frac{k_\perp^2}{1 - M^{-2}} \sin(k_\perp z / \sqrt{M^2 - 1}) dk_\perp, \quad (6.12)$$

where  $z$  and  $\rho$  are the cylindrical coordinates of the field point, and  $J_0$  is the Bessel function.

The main contribution to the integral (6.12) is for  $k_\perp \lambda_D \sim 1$ . Then at distances  $\rho > \lambda_D$  and  $|z| > \lambda_D \sqrt{M^2 - 1}$  the approximate expression for the wake potential is given by

$$\Phi_W(\rho, z) \simeq \frac{Q}{1 - M^{-2}} \sqrt{\frac{\lambda_D}{2\pi\rho}} \times \left[ \frac{\cos[(\pi/4) + (z_-/\lambda_D \sqrt{M^2 - 1})]}{z_-} + \frac{\cos[(\pi/4) - (z_+/\lambda_D \sqrt{M^2 - 1})]}{z_+} \right], \quad (6.13)$$

where  $z_\pm \equiv |z| \pm \rho \sqrt{M^2 - 1} > 0$  (note that the oscillating potential exists only in the wake of the test particle, i.e., for  $z < 0$  and  $|z| > \rho \sqrt{M^2 - 1}$ ). Obviously, this function oscillates for changing  $\rho$  or  $z$ . Because the oscillating potential (6.13) is proportional to the same test dust particle charge  $Q$  as the static Debye potential (6.10), and contains no screening exponential, there are regions in space corresponding to the change of the effective potential sign and, hence, to the most probable positions of the particulates (note that these regions are not only on the line  $\rho = 0$ ). For small distances in the perpendicular direction,  $k_\perp \rho \ll 1$ , and for  $|z| > \lambda_D \sqrt{M^2 - 1}$ , the main contribution to the stationary wake potential is given by [254]

$$\Phi_W(\rho = 0, z) \approx \frac{2Q}{|z|} \frac{\cos(|z|/L_s)}{1 - M^{-2}}, \quad (6.14)$$

where  $L_s = \lambda_D \sqrt{M^2 - 1}$  is the effective length. Thus the wake potential is attractive for  $\cos(|z|/L_s) < 0$ . Note that this result cannot be found from (6.13) because of the different asymptotics used. The effective periodic spacing in the plane perpendicular to the flow is of the order of the Debye length; note that this can be seen not only from the approximate expression (6.13), but also from a more exact formula. Numerical integration [256] gives the wake potential distributions as shown in Fig. 31.

Thus the collective interaction of a static test dust particulate with the low-frequency perturbations in the ion flow can provide the attractive wake potential. The mechanism is similar to that responsible for the Cooper pairing. We note that the physics of the Cooper-pairing effect is that the test electron polarizes the medium by attracting positive ions. The excess positive ions, in turn, attract the second electron. If this attractive interaction is strong enough to overcome the repulsive screened Coulomb interaction, the effective attraction between two electrons can be realized, resulting in the superconductivity phenomenon. For example, the model [344] leads to an expression similar to Eq. (6.8) where the first term is due to the screened Coulomb repulsion, whereas the second term corresponds to the attraction forces. For the effective attraction, the speed of moving charged particles (in the frame where the background medium is at rest) should exceed the sound velocity. However,

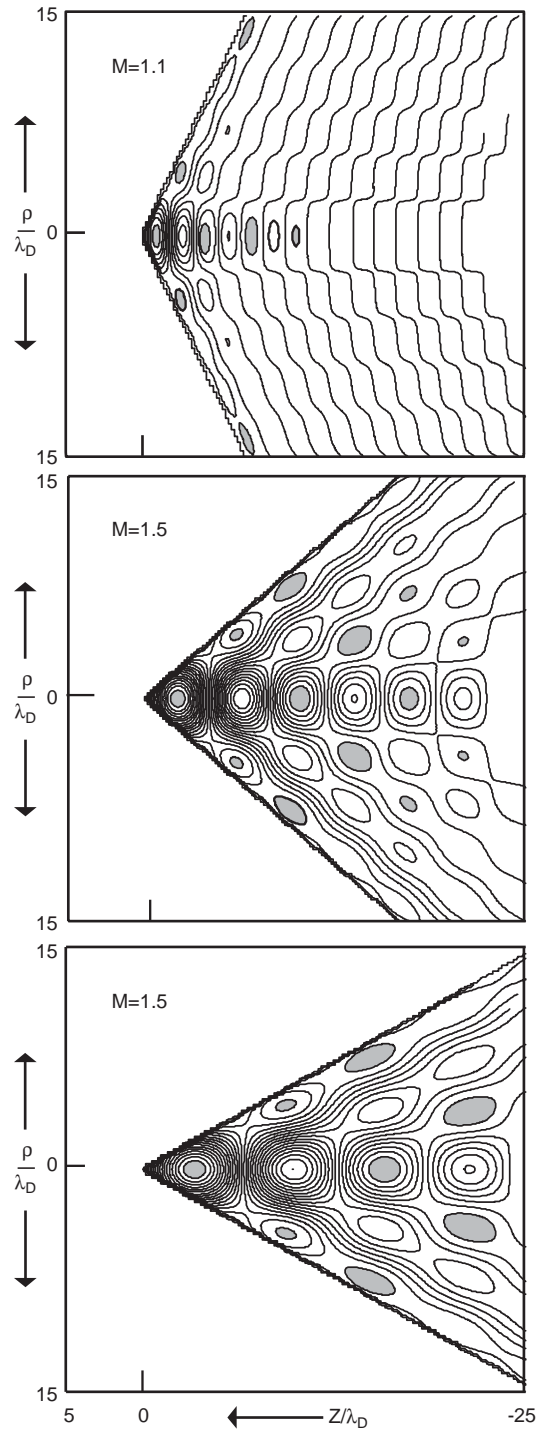


Fig. 31. The wake potential and the potential minima in  $(\rho, z)$  plane for various Mach numbers. The potential minima are shaded [256].

the mechanism is the most effective when the particles' speed is quite close to the latter (in this case the resonant interaction with phonons is maximum). In the situation with the static charged dust particulates, the moving ions of the flow create the polarization necessary for the resulting attraction. In order for the latter to be effective it is required that one has continuous ion flow with the velocity exceeding the ion sound speed. As we already noted above in Section 6.1, this condition can be observed in the sheath region of low-temperature laboratory plasmas. The test particles can attract to each other forming the quasi-lattice structures with the characteristic period of the order of  $\lambda_D \sqrt{M^2 - 1}$ .

We note that, in principle, any charged particles can have similar attractive potentials under certain conditions. However, the speed of plasma electrons is usually too high (this corresponds to the condition  $v_{Te} \gg v_s$ ) for the effective attraction to be realized. On the other hand, the ion velocity is too small in the absence of the flow. For the model considered here (with the ions moving as a flow), we have to compare  $v_0$  with the characteristic velocity of collective perturbations in such kind of plasma. Note that for ion-acoustic waves in the flow the (relative) speed of the ions is too small (which corresponds to the reference frame moving with  $v_0$ ). Therefore we can conclude that the interaction of the static dust particulate with the ion oscillations in the flow provides the most effective contribution for the situation considered. For quantitative comparison with the results of particular experiments, other factors should be taken into account. In particular, the potential of ensemble (in contrast to the isolated test particle) of dust particulates might be calculated. This can be done by either adding the contributions of the isolated particulates (if their density is not high), or introducing their distribution function (when dust collective effects become important). Furthermore, contribution of other forces acting on the dust, as well as such factors as an inhomogeneity of the ion flow should be considered to obtain more detailed picture.

### 6.3. Wakes behind dipoles and non-spherical particles

The theory of the wake potential proved to be successful for explanation of the formation of vertical arrangements and alignment of grains in the dust-plasma crystals [254–256]. The wake potential was experimentally confirmed to be responsible for the attraction of vertically aligned adjacent dust grains in a plasma crystal [329]. The theory presented above is based on a test dust particle which is characterized by a point charge. However, the recent observation of the formation of plasma crystals of finite size dust grains [205,334,335] as well as the theoretical predictions [337] prompted the interest to the formation of the wake potential for these more complicated cases of less symmetric particles, e.g., particles with the dipole moments and the elongated (rod-like) particles. Here, we present the results of the theoretical predictions of the plasma wake calculated for a spherical particle with a dipole moment [336] and for a rod-like particle [337].

#### 6.3.1. Wakes behind dipoles

The appearance of a large dipole moment for a dielectric dust grain in a supersonic flow has been studied in the context of the charging process on the surface of the dust grain, but using an unscreened Coulomb potential neglecting the plasma (and therefore wake) effects [345]. Here, we point out the effect of a dipole moment on the formation of the wake potential behind a dust grain in the presence of a flowing plasma. We do not attempt the difficult self-consistent calculation of the dust charge and dipole moment in an array of grains with wake potentials here. We instead

consider the wake potential produced by a single dust grain which is characterized by a given charge  $Q$  and a dipole moment  $\mathbf{p}$ . For simplicity, we do not consider the process of the dust charging, thereby assuming that the test dust grain has a given (constant) charge and a dipole moment, for example, those calculated, without the wake potential effect, for a grain in various gases in Ref. [345]. Furthermore, the dust grain is assumed to be placed in the ion flow in a collisionless plasma, which supports the plasma collective modes. The approach [336] of treating the charge and dipole moment as parameters is necessary to form a basis for later self-consistent calculations which can avoid unphysical assumptions such as the neglect of the wake fields.

The potential of the distributed test charge in a plasma without an ion flow can be written, retaining the monopole and dipole contributions, as

$$\phi = \frac{q}{r} \exp\left(-\frac{r}{\lambda_D}\right) + \frac{\mathbf{p} \cdot \mathbf{e}_r}{r^2} \left(1 + \frac{r}{\lambda_D}\right) \exp\left(-\frac{r}{\lambda_D}\right),$$

where  $\mathbf{p}$  is the dipole moment of a test charge  $q$ ,  $\mathbf{e}_r$  is a unit vector in the direction  $\mathbf{r}$ ,  $r = |\mathbf{r}|$ , and  $\lambda_D$  is the plasma Debye length.

As has been shown previously, the first term should be modified in a plasma with an ion flow in a way to produce a wake potential behind a point test charge. Oscillations of the potential occur due to the excitation of an ion-acoustic wave standing in the flow downstream of the dust grain. Here, we show how the dipole moment will modify the wake potential behind a test dust grain in an ion flow. Let the dust grain be made up of distributed point charges  $q_j$ , so the charge density is

$$\rho(\mathbf{r}, t) = \sum_j q_j \delta(\mathbf{r} - \mathbf{r}_j - \mathbf{v}_j t) = \frac{1}{V} \sum_j \sum_{\mathbf{k}} q_j \exp[i\mathbf{k} \cdot (\mathbf{r} - \mathbf{r}_j - \mathbf{v}_j t)], \quad (6.15)$$

where  $V$  is the volume of the system, and  $\mathbf{r}_j$  and  $\mathbf{v}_j$  are the location and the velocity of the distributed dust charges, respectively. We assume a small displacement  $\Delta\mathbf{r}_j$  about the point  $\mathbf{r}_0$  for each distributed charge, or  $\mathbf{r}_j = \mathbf{r}_0 + \Delta\mathbf{r}_j$  and set  $\mathbf{v}_j = \mathbf{v}$ . Expanding  $\exp(-i\mathbf{k} \cdot \Delta\mathbf{r}) \approx 1 - i\mathbf{k} \cdot \Delta\mathbf{r}$ , one obtains from (6.15)

$$\rho(\mathbf{r}, t) = \frac{1}{V} \sum_{\mathbf{k}} Q \exp[i\mathbf{k} \cdot (\mathbf{r} - \mathbf{r}_0 - \mathbf{v}t)] - \frac{1}{V} \sum_{\mathbf{k}} i\mathbf{k} \cdot \mathbf{p} \exp[i\mathbf{k} \cdot (\mathbf{r} - \mathbf{r}_0 - \mathbf{v}t)],$$

where  $Q = \sum_j q_j$  and  $\mathbf{p} = \sum_j \Delta\mathbf{r}_j q_j$ . The potential of such a grain is given by

$$\phi(\mathbf{k}, \omega) = \frac{4\pi}{Vk^2} \frac{i}{\omega - \mathbf{k} \cdot \mathbf{v}} \frac{\exp(-i\mathbf{k} \cdot \mathbf{r}_0)}{\varepsilon(\mathbf{k}, \omega)} (Q - i\mathbf{k} \cdot \mathbf{p}). \quad (6.16)$$

Note that the dipole correction appears in such a way as to effectively modify the charge  $Q$  in Eq. (6.16). The poles in Eq. (6.16) are from  $\omega - \mathbf{k} \cdot \mathbf{v} = 0$  and  $\varepsilon(\mathbf{k}, \omega) = 0$ .

The contribution to the dipole potential term, due to the electron dielectric function, can be written, in the limit  $V \rightarrow \infty$ , as

$$\phi_{I0}^p(\mathbf{r}, t) = 4\pi \int \frac{d^3k}{(2\pi)^3} \frac{\lambda_D^2}{1 + k^2 \lambda_D^2} (-i\mathbf{k} \cdot \mathbf{p}) \exp[i\mathbf{k} \cdot (\mathbf{r} - \mathbf{r}_0 - \mathbf{v}t)], \quad (6.17)$$

where the subscript  $I0$  indicates the contribution from the pole given by  $\omega - \mathbf{k} \cdot \mathbf{v} = 0$ , just with the electron contribution to the dielectric permittivity. Eq. (6.17) may be evaluated for the spherical

symmetry assuming  $\mathbf{r}_0 = \mathbf{v} = 0$  (i.e., for a stationary grain at the origin of the reference frame) and  $d^3k = 2\pi k^2 \sin \Theta d\Theta dk$  as

$$\phi_{I0}^P(\mathbf{r}, t) = \frac{\mathbf{p} \cdot \mathbf{e}_r}{r^2} \left(1 + \frac{r}{\lambda_D}\right) \exp\left(-\frac{r}{\lambda_D}\right). \quad (6.18)$$

On the other hand, for the cylindrical symmetry, assuming  $\mathbf{r}_0 = \mathbf{e}_z z_0$ ,  $\mathbf{v} = \mathbf{e}_z v$ , and  $d^3k = k_\perp dk_\perp dk_z d\Theta$ , the potential is

$$\phi_{I0}^P(\rho, z, t) = \frac{p}{\rho \lambda_D} \frac{z - z_0 - vt}{|z - z_0 - vt|} \exp\left(-\frac{|z - z_0 - vt|}{\lambda_D}\right), \quad (6.19)$$

where  $p$  is the  $z$ -component of  $\mathbf{p}$ , and the cylindrical coordinates  $(\rho, z)$  are used. For an ion flow induced dipole moment,  $\mathbf{p}$  is in the reverse direction to the ion flow ( $p > 0$ ). As was done previously, all the pole contributions should be taken into account. The potential given by Eq. (6.19) is cancelled in the downstream direction by the part of the potential produced by the ion contribution. Thus the total potential in the range  $z_0 + v_0 t < z < z_0 + vt$  and  $|z - z_0 - vt| > \rho(M^2 - 1)^{1/2}$  can be written as

$$\begin{aligned} \phi(\rho, z, t) = & \frac{2M^2}{(M^2 - 1)^{3/2}} \int_0^{1/\lambda_D} dk_\perp (k_\perp \lambda_D)^2 J_0(k_\perp \rho) \left[ Q \sin\left(\frac{k_\perp (z - z_0 - vt)}{\sqrt{M^2 - 1}}\right) \right. \\ & \left. - \frac{k_\perp p}{\sqrt{M^2 - 1}} \cos\left(\frac{k_\perp (z - z_0 - vt)}{\sqrt{M^2 - 1}}\right) \right], \end{aligned} \quad (6.20)$$

where  $J_0$  is the zeroth-order Bessel function of the first kind. The near-field approximation,  $k_\perp \rho < 1$ , is given by, for  $|z - z_0 - vt| > \lambda_D$ ,

$$\begin{aligned} \phi(z, t) = & \frac{2/(1 - M^{-2})}{|z - z_0 - vt|} \left[ \left( Q - \frac{p}{|z - z_0 - vt|} \right) \cos\left(\frac{z - z_0 - vt}{\lambda_D \sqrt{M^2 - 1}}\right) \right. \\ & \left. - \frac{p}{\lambda_D \sqrt{M^2 - 1}} \sin\left(\frac{|z - z_0 - vt|}{\lambda_D \sqrt{M^2 - 1}}\right) \right], \end{aligned} \quad (6.21)$$

and for  $|z - z_0 - vt| < \lambda_D$  by

$$\phi(z, t) = \frac{1}{M^2(1 - M^{-2})\lambda_D^2} \left[ Q(z - z_0 - vt) - \frac{p}{2} \right].$$

Eq. (6.21) indicates that the dipole moment plays a major role in forming a wake potential if the magnitude of the dipole moment  $p$  approaches the order of  $|Q|\lambda_D\sqrt{M^2 - 1}$ . Around  $z - z_0 - vt = -(p/2)\lambda_D(M^2 - 1)^{1/2}$ , the dipole moment modifies the potential structure in a way to distort the oscillatory character. An analysis of the dipole moment of a dust grain of the radius  $a$  placed in a supersonic plasma flow showed that the magnitude of the induced dipole moment  $p_{FI}$  could be significant, with  $p_{FI} \sim a|Q|/2$ , due to the assymmetric ion flow producing a strongly nonuniform charge distribution on the surface [345]. Thus the condition for the dipole moment to play a dominant role in forming the wake potential is  $a \sim \lambda_D$ . The dipole moment  $\mathbf{p}_E$  induced by the sheath electric field (in the same direction as the ion flow, i.e.  $\mathbf{p}_E \cdot \mathbf{e}_r < 0$  or  $p_E < 0$ ) can be only neglected in comparison with the dipole moment caused by the ion flow for a grain size  $< 40 \mu\text{m}$  [345].

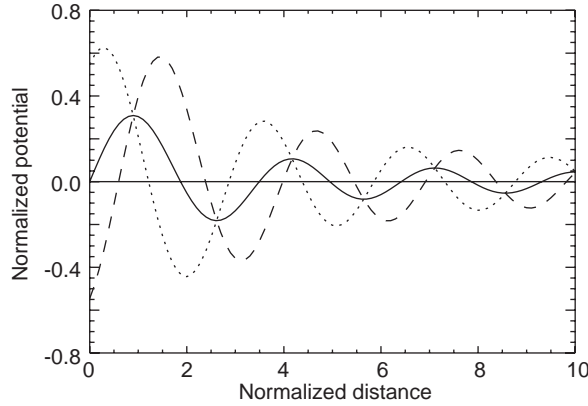


Fig. 32. Wake potential  $\phi$ , normalized by  $2M^2|Q|/(M^2 - 1)^{3/2}\lambda_D$ , at  $\rho = 0$ , against distance downstream of the grain, normalized by  $\lambda_D$ .  $M = 1.1$  and  $p = 0$  (solid curve),  $p = |Q|\lambda_D$  (dashed curve) and  $p = -|Q|\lambda_D$  (dotted curve) [336].

Note that the moment  $\mathbf{p}_E$  is nonzero also for a conducting grain, in contrast to the case of the dipole moment induced by the plasma flow.

Fig. 32 shows the normalized wake potential for a negatively charged grain at  $\rho = 0$ , plotted against the normalized distance downstream of the grain  $|z - z_0 - vt|/\lambda_D$ , for  $M = 1.1$ , and for  $p/|Q|\lambda_D = 0$  (no dipole moment), as well as for (extreme) cases  $p_{FI}/|Q|\lambda_D = 1$  (ion flow induced dipole moment) and  $p_E/|Q|\lambda_D = -1$  (electric field induced dipole moment). The downstream potential maxima, where other dust grains can reside in the stable equilibrium, are stronger and more distant from the original grain if the ion flow induced dipole moment is included, as is expected for this orientation of the moment, whereas the maxima are stronger and closer to the grain for the electric field induced dipole moment. These characteristics of the oppositely directed dipole moments may provide a way for experimental observations to distinguish between the mechanisms of creation of the dipole moment in the grains.

Thus a charged dust grain with a dipole moment creates an oscillatory wake potential behind the grain, analogously to the monopole case. When the size of the dust grain becomes comparable to the Debye length, the dipole moment plays an essential role in the structure of the wake potential. The structure is found to depend on the directionality of the dipole moment. The potential of a dust grain is given by Eq. (6.21) behind the particle in the presence of a supersonic ion flow when the ion acoustic wave (standing in the dust grain reference frame) is generated within the Mach cone. If the wake potential contributes to the alignment of grains in a dust crystal, the separation of the grains in the ion flow direction will be larger due to the ion flow induced dipole moment. Finally, we note that the wake potential will in turn modify the process of dust charging (and inducing the dust dipole moment), making the fully self-consistent problem of dust charging and screening as well as the dust–dust interaction in the presence of an ion flow highly nonlinear.

### 6.3.2. Wakes behind elongated particles (rods)

Recent observations of the formation of plasma crystals composed of elongated particles [334,335] as well as experiments [205] with the cylindrical particles levitating in the sheath of an RF plasma prompted the study [337] of the formation of the wake potential in the case of a rod-like charged



particle. Here, we do not discuss the effect of the charging of such type a particle [206] therefore just assuming that there is a given distribution of charges on the rod. We note that, in general, an inhomogeneous linear charge density distribution along the rod leads to the appearance of a dipole moment of a particle. The effect of the dipole moment on the wake formation of a point-like particle was just reviewed above in the preceding section. However, the finite size of the rod affects the character of the wake, in particular, providing the additional rotational degree of freedom related to the rotational inclination of the rod.

Here, we would like to note, that this additional (rotational) degree of freedom will lead to new effects in experiments with cylindrical particles. Indeed, in the crystal lattices composed of spherical particles, vibration modes associated with the longitudinal [346] of the transverse [248] (with respect to the propagation of the wave) motions of grains can be excited. The “liquid crystal” lattices composed of rods will have new rotational modes associated with their rotational motions, similar to those in liquid crystals [391,392]. Excitation and interactions of all these modes introduce new phase transitions and affect those existing in lattices composed of spherical grains. As was pointed out recently [347], the wake can affect the interaction of the horizontal (longitudinal) and vertical (transverse) modes for spherical grains. Thus similar (or more complex) effects will exist for cylindrical particles, affecting their interaction and involving also the rotational modes. All this makes the theory [337] presented here to be a necessary first step to understand the formation of “liquid crystal” lattices levitating in the sheath region where strong ion flows are established.

Consider a finite size (in one direction) particle of the length  $l_d$  is immersed in an ion flow of the speed  $v_0$ . The angle between the direction of the flow and the rod is  $\Theta_0$ . The reference frame is chosen with the  $x$ -axis along the rod, and the ion flow is in the  $xz$ -plane, i.e.  $\mathbf{v}_0 = (v_0 \cos \Theta_0, 0, -v_0 \sin \Theta_0)$ . The  $y$  and  $z$  sizes of the particle are zero. The angle  $\Theta_0 = \pi/2$  corresponds to the ion flow in the negative  $z$ -direction, perpendicular to the rod, and the angle  $\Theta_0 = 0$  corresponds to the ion flow in  $x$ -direction, parallel to the rod; note that in the experiments [205] both possibilities were observed. The three-dimensional charge density of such a particle is given by

$$\rho_d = \rho_l \delta(y) \delta(z) ,$$

where  $\rho_l$  is the linear density of the charge distribution on the rod. Below, we specify the following linear charge distributions:

- (a) charges distributed uniformly along the rod,  $\rho_l = (Q_0/l_d)\theta(x)\theta(l_d - x)$ ;
- (b) charges distributed non-uniformly along the rod,  $\rho_l = (2Q_0x/l_d^2)\theta(x)\theta(l_d - x)$ ;
- (c) charges located at the ends of the rod,  $\rho_l = Q_1\delta(x) + (Q_0 - Q_1)\delta(x - l_d)$ .

The total charge on the rod is  $Q_0$  for all cases. Note that cases (b) and (c) correspond to the nonzero dipole moment of the rod:  $P_0 = Q_0 l_d / 6$  for the case (b), and  $P_0 = (Q_0 - 2Q_1) l_d$  for the case (c) (we assume  $Q_1 \neq Q_0/2$ ). For the Fourier-transforms of the (stationary) particle charge density we have  $\rho_d(\mathbf{k}, \omega) = 2\pi \rho_d(\mathbf{k}) \delta(\omega)$ , where:

- (a)  $\rho_d(\mathbf{k}) = iQ_0[\exp(-ik_x d) - 1]/k_x d$ ;
- (b)  $\rho_d(\mathbf{k}) = 2Q_0[(1 + ik_x d) \exp(-ik_x d) - 1]/k_x^2 d^2$ ;
- (c)  $\rho_d(\mathbf{k}) = Q_1 + (Q_0 - Q_1) \exp(-ik_x d)$ .

For the static rod in the presence of the ion flow, the electrostatic potential is given by

$$\Phi(\mathbf{r}) = \text{Re} \int \frac{d\mathbf{k}}{2\pi^2 \mathbf{k}^2} \frac{\rho_d(\mathbf{k}) \exp(i\mathbf{k} \cdot \mathbf{r})}{\varepsilon(\mathbf{k}, -k_x v_0 \cos \Theta_0 + k_z v_0 \sin \Theta_0)} .$$

Separating the static Debye and the oscillating wake potentials,  $\Phi(\mathbf{r}) = \Phi_D(\mathbf{r}) + \Phi_W(\mathbf{r})$  [254–256], the wake potential  $\Phi_W(\mathbf{r})$  can be written as

$$\Phi_W(\mathbf{r}) = \text{Re} \int \frac{d\mathbf{k}}{2\pi^2 \mathbf{k}^2} \frac{\rho_d(\mathbf{k}) \mathbf{k}^2 \lambda_D^2}{1 + \mathbf{k}^2 \lambda_D^2} \frac{\omega_{\mathbf{k}}^2 \exp(i\mathbf{k} \cdot \mathbf{r})}{(-k_x v_0 \cos \Theta_0 + k_z v_0 \sin \Theta_0 + i0)^2 - \omega_{\mathbf{k}}^2} . \quad (6.22)$$

Here,  $\omega_{\mathbf{k}} = |\mathbf{k}| v_s / (1 + \mathbf{k}^2 \lambda_D^2)^{1/2}$  is the characteristic frequency of the oscillations in the flow. Potential (6.22) describes the strong resonant interaction between the oscillations in the ion flow and the test rod when  $|k_x v_0 \cos \Theta_0 - k_z v_0 \sin \Theta_0|$  is close to the eigenfrequency  $\omega_{\mathbf{k}}$  of the ion oscillations in the flow. Eq. (6.22) can be integrated over  $k'_x$  by the standard way (see above as well as [254–256]). Taking into account only those poles corresponding to the ion-acoustic wake (other poles contribute to the Debye screening potential) and integrating over the angles in the plane perpendicular to the direction of the ion flow, the main contribution to the integral for  $M \gg 1$  is for  $k_{\perp} \lambda_D \sim 1$  if  $d < \lambda_D$ . Then for the distances  $r_{\perp} = |\mathbf{r}_{\perp}| > \lambda_D$  and  $|(x - \tau) \cos \Theta_0 - z \sin \Theta_0| > L_s$ , the approximate expression for the wake potential is given by

$$\begin{aligned} & \Phi_W(x \cos \Theta_0 - z \sin \Theta_0, \mathbf{r}_{\perp}) \\ & \simeq \frac{Q_0}{1 - M^{-2}} \int_0^{l_d} \frac{d\tau}{l_d} A_d(\tau) \left[ \frac{\lambda_D / 2\pi}{\sqrt{y^2 + ((x - \tau) \sin \Theta_0 + z \cos \Theta_0)^2}} \right]^{1/2} \\ & \times \left[ \frac{\cos[(\pi/4) + (x_-(\tau)/L_s)]}{x_-(\tau)} + \frac{\cos[(\pi/4) - (x_+(\tau)/L_s)]}{x_+(\tau)} \right] , \end{aligned} \quad (6.23)$$

where  $x_{\pm}(\tau) = |(x - \tau) \cos \Theta_0 - z \sin \Theta_0| \pm \sqrt{M^2 - 1} \sqrt{y^2 + ((x - \tau) \sin \Theta_0 + z \cos \Theta_0)^2} > 0$  (we remind that the oscillating potential exists only in the wake cone of the test rod, i.e., for positive  $x_{\pm}(\tau)$ ).

For small distances in the perpendicular direction,  $r_{\perp} \ll \lambda_D$ , and for the Mach number not near unity,  $|(x - \tau) \cos \Theta_0 - z \sin \Theta_0| > L_s$ , assuming  $k_{\perp}^2 \ll (M^2 - 1)$  as well as  $k_{\perp} \ll 1$ , one obtains

$$\begin{aligned} & \Phi_W(x \cos \Theta_0 - z \sin \Theta_0, \mathbf{r}_{\perp}) \\ & \simeq \frac{2Q_0}{L_s} \int_0^{l_d} \frac{d\tau}{l_d} A_d(\tau) \int_0^1 \frac{k_{\perp}^2 dk_{\perp}}{1 - M^{-2}} J_0 \left( k_{\perp} \sqrt{y^2 + ((x - \tau) \sin \Theta_0 + z \cos \Theta_0)^2} / \lambda_D \right) \\ & \times \sin [k_1((x - \tau) \cos \Theta_0 - z \sin \Theta_0) / \lambda_D] . \end{aligned} \quad (6.24)$$

The main contribution to the stationary wake potential for  $l_d \sin \Theta_0 < \lambda_D$  is now given by

$$\begin{aligned} \Phi_W(x \cos \Theta_0 - z \sin \Theta_0, r_\perp = 0) \\ \approx \frac{2Q_0}{1 - M^{-2}} \int_0^{l_d} \frac{d\tau}{l_d} A_d(\tau) \frac{\cos [(x - \tau) \cos \Theta_0 - z \sin \Theta_0]/L_s]}{|(x - \tau) \cos \Theta_0 - z \sin \Theta_0|}. \end{aligned} \quad (6.25)$$

Note that in the case  $M \gg 1$  and smaller distances  $|(x - \tau) \cos \Theta_0 - z \sin \Theta_0| < L_s$  (which can be realized for  $l_d < L_s$ ), Eq. (6.24) gives the near-particle field ( $M \gg 1$  asymptotics)  $\Phi \sim Q_0(x - (l_d/2))M^2/L_s^2 \sim Q_0(x - (l_d/2))/\lambda_D^2 M^2$  for the case (a), and  $\Phi \sim Q_0((x/2) - (l_d/3))M^2/L_s^2 \sim Q_0((x/2) - (l_d/3))/\lambda_D^2 M^2$  for the case (b). Furthermore, the upper limit for integration in Eq. (6.24), when  $M \approx 1$ , is  $1 - M^{-2}$ , that for  $|(x - l_d/2) \cos \Theta_0 - z \sin \Theta_0| > L_s$  gives  $\Phi \sim \int_0^{l_d} (d\tau/l_d) A_d(\tau) [Q_0/((x - \tau) \cos \Theta_0 - z \sin \Theta_0)] \cos(((x - \tau) \cos \Theta_0 - z \sin \Theta_0)/\lambda_D M)$  and the scaling for the maximum potential (that can be estimated from  $|(x - l_d/2) \cos \Theta_0 - z \sin \Theta_0| \sim L_s$ ) as  $\Phi_{\max} \sim \text{Const}/\sqrt{M^2 - 1}$ .

For the case (c), one can obtain from Eq. (6.23)

$$\begin{aligned} \Phi_W^{(c)}(x \cos \Theta_0 - z \sin \Theta_0, \mathbf{r}_\perp) \\ \simeq \frac{Q_1}{1 - M^{-2}} \left[ \frac{\lambda_D/2\pi}{\sqrt{y^2 + (x \sin \Theta_0 + z \cos \Theta_0)^2}} \right]^{1/2} \\ \times \left[ \frac{\cos[(\pi/4) + (x_-(0)/L_s)]}{x_-(0)} + \frac{\cos[(\pi/4) - (x_+(0)/L_s)]}{x_+(0)} \right] \\ + \frac{Q_0 - Q_1}{1 - M^{-2}} \left[ \frac{\lambda_D/2\pi}{\sqrt{y^2 + ((x - l_d) \sin \Theta_0 + z \cos \Theta_0)^2}} \right]^{1/2} \\ \times \left[ \frac{\cos[(\pi/4) + (x_-(l_d)/L_s)]}{x_-(l_d)} + \frac{\cos[(\pi/4) - (x_+(l_d)/L_s)]}{x_+(l_d)} \right]. \end{aligned} \quad (6.26)$$

Eq. (6.25) in this case gives

$$\begin{aligned} \Phi_W(x \cos \Theta_0 - z \sin \Theta_0, r_\perp = 0) \\ \approx \frac{2Q_1}{1 - M^{-2}} \frac{\cos [(x \cos \Theta_0 - z \sin \Theta_0)/L_s]}{|x \cos \Theta_0 - z \sin \Theta_0|} \\ + \frac{2(Q_0 - Q_1)}{1 - M^{-2}} \frac{\cos [(x - l_d) \cos \Theta_0 - z \sin \Theta_0]/L_s]}{|(x - l_d) \cos \Theta_0 - z \sin \Theta_0|}. \end{aligned} \quad (6.27)$$

For the charge distributions (a) and (b), approximate expressions for the potential can be presented for the most important special cases  $\Theta_0 = \pi$  and  $\Theta_0 = -\pi/2$ , i.e. when the rod is oriented along the

flow and perpendicular to the ion flow, respectively. Note that these cases are of the most interest since current experiments demonstrate that  $\Theta_0 = \pi$  and  $\Theta_0 = -\pi/2$  correspond to the observed stable equilibrium positions of rods, e.g., see [205]. For  $\Theta_0 = \pi$ , the wake potential is

$$\Phi_W(x, r_\perp = 0) \approx \frac{2Q_0}{1 - M^{-2}} \int_0^{l_d} \frac{d\tau}{l_d} A_d(\tau) \frac{\cos[(x - \tau)/L_s]}{|(x - \tau)|}.$$

For  $\Theta = -\pi/2$  if  $l_d \ll \lambda_{De}$ , a simple expression is obtained

$$\Phi_W(z, r_\perp = 0) \approx \frac{2Q_0}{1 - M^{-2}} \frac{\cos[z/L_s]}{|z|}.$$

Note that this expression coincides in this limit with the wake field potential generated by a point charge.

The obtained approximate analytical expressions cannot describe the character of the wake potential for the interesting cases when the rod length is of the order of (or exceeds) the plasma Debye length. Thus here we present results of numerical integration for the rod lengths  $l_{d1} = \lambda_{De}/6 = 50 \mu\text{m}$ ,  $l_{d2} = \lambda_{De} = 300 \mu\text{m}$ , and  $l_{d3} = 2\lambda_{De} = 600 \mu\text{m}$  [337]. The first case  $l_d = l_{d1}$  is interesting for the comparison since the wake character in this case is practically close to that of a point charge.

The dependence of the wake field on the orientation of the rod with respect to the direction of the ion flow is the most pronounced for the flow velocities close to the speed of sound ( $M \sim 1$ ), when the first maximum of the generated wake is close to the rod. We note that in general, the larger are the ion velocities, the stronger are the ballistic effects in the ion focusing; this is because fewer ions participate in the wave-particle resonance, and the Mach cone is narrower. For  $M = 1.1$ , we present in Fig. 33 the result for the case (a) (the surface plots for other cases look similar) and three orientations of the relatively long rod,  $\Theta_0 = \pi, 5\pi/4, 3\pi/2$  (other parameters are:  $\lambda_{De} = 300 \mu\text{m}$ ,  $T_e = 1 \text{ eV}$ ,  $M = 1.1$ ,  $Q_0 = 5000e$ , and  $Q_1 = Q_0/3 = 5000e/3$ ). From these plots, we clearly see the wave character of the wake potential. Note that the more is the angle between the rod and the direction of the flow, the closer is the first maximum of the wake potential to the rod. This type of behavior is more pronounced for longer rods with the big charge separation. Physically, it is clear that the shorter is the rod length, the closer is the character of the wake potential to that of a point charge.

Thus we note that the basic feature of the wake in the case of the supersonic velocities of the ion flow, namely, its oscillating character, first reported for spherical particles, takes also place for the rods. The longer are the rods, the more is the difference in the characteristics of the wake potential as functions of the rod lengths and/or charge distribution along the rod. Regarding the formation of the wake potentials of rod-like particles, the plasma electron Debye length is the most important characteristic scale: for rods much shorter than the Debye length, the wake potential is almost the same as for the point particles; on the other hand, for rod lengths comparable or exceeding the Debye length, the characteristics of the wake potential develop the dependence on the orientation of the rod with respect to the ion flow as well as on the character of the charge distribution along the rod. The actual difference, e.g., for the location of the potential first minimum in the case of long (of the order of or exceeding the plasma electron Debye length) rods with a large charge separation can be of the order of the electron Debye lengths, i.e., of the order of a half of a millimeter for the typical discharge parameters which is an easily detectable effect in the laboratory. These results are important for the present and future experiments involving cylindrical particles. Furthermore,

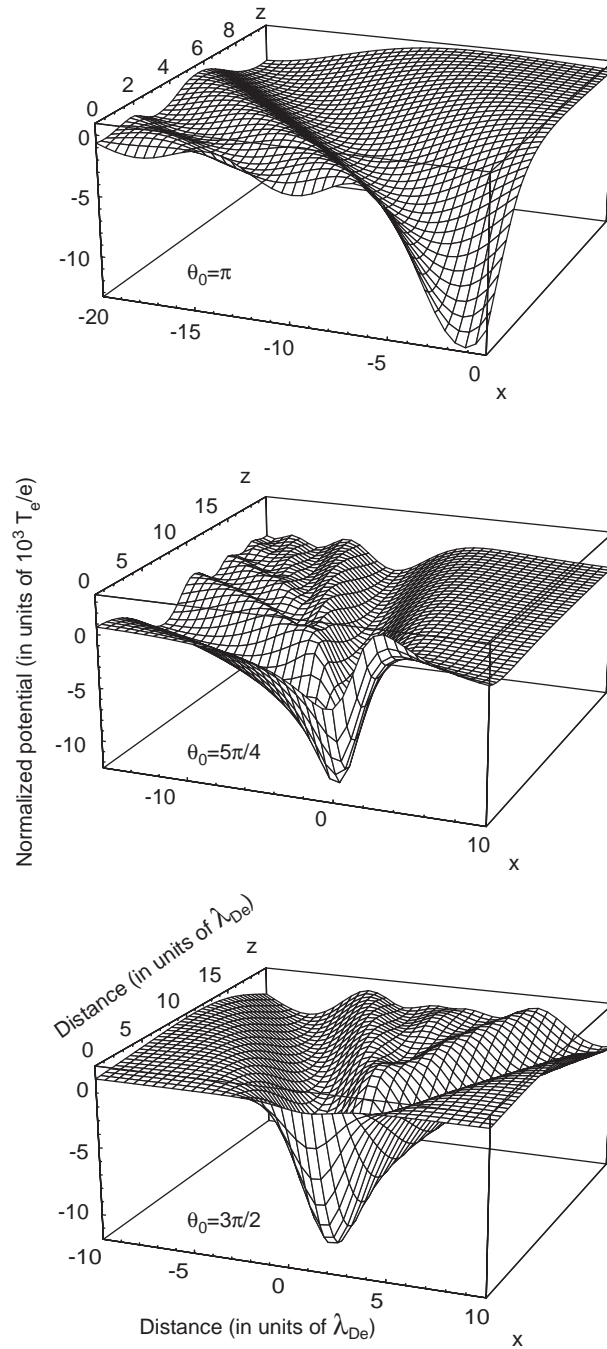


Fig. 33. The surface plot of the wake potentials for the case (a) and three different angles between the rod and the direction of the ion flow. Other parameters are:  $\lambda_{De} = 300 \mu\text{m}$ ,  $T_e = 1 \text{ eV}$ ,  $M = 1.1$ ,  $Q_0 = 5000e$ . Reprinted from Ref. [337].

oscillations of rods as well as specific lattice modes propagating in the “liquid plasma” crystals, will be affected by the wake. Indeed, for the rotationally oscillating (in the plane parallel to the ion flow, i.e. in the vertical plane in the experiment) rods the motion of the wake potential minimum will take place thus strongly influencing the location of the downstream particles as well as the vertical arrangements and the vibration modes in the downstream chains.

#### 6.4. Dust Cooper pairing: Hamiltonian description

The Hamiltonian formalism is one of the most favored in physics since it is very useful in statistical and interaction analyses as well as in numerical simulations [250,351]. The knowledge of the system’s Hamiltonian is essential for the description of propagation and interaction of modes and especially for calculation of the free energy to study phase transitions and critical phenomena. Although the dust–plasma systems (e.g., two- and three-dimensional structures as well as phase transitions observed [7,348–350]) are thermodynamically open, the Hamiltonian description can provide useful insights, especially for the cases when the energy exchange with the external sources/sinks is insignificant.

Here, following [257] we derive the semi-classical Hamiltonian which describes the interaction with external fields, screened Coulomb potential, and the effective interaction of the particulates by exchanging virtual phonons. The study of the effective interaction is motivated by the finding of an oscillating stationary wake behind a static test particle [254–256] in the sheath region [352]. The interaction of the particles in the wake field appears to be similar to the Cooper pairing of electrons in superconductors [342]. Furthermore, we demonstrate how the oscillations of the grains, viz. longitudinal [346] and transverse [248] lattice modes, can be obtained within the framework of the present formalism. The excitation of the vibrational modes can be responsible for phase transitions in the system.

Consider an ensemble of charged test particles, with the coordinate  $\mathbf{x}_j$  and the momentum  $\mathbf{p}_j$ , in a background plasma and interacting with longitudinal collective plasma fields. The kinetic energy of the test particles is given by the particle Hamiltonian  $\sum_j p_j^2/2m_j$ . The interaction of test particles with the longitudinal electric fields  $\mathbf{E}(\mathbf{x}, t)$  can be conveniently expressed in terms of the longitudinal vector potential  $\mathbf{A}$  by replacing  $\mathbf{p}_j$  by  $\mathbf{p}_j - (Z_j e/c)\mathbf{A}(\mathbf{x}_j)$  in the Hamiltonian. The test particles interact not only with the longitudinal electric fields, but also through forces derivable from the external potential  $V_{\text{ext}}$  such as the sheath potential. The Hamiltonian for our system is thus given by [353]

$$H = \sum_j \frac{1}{2m_j} \left[ \mathbf{p}_j - \frac{Z_j e}{c} \mathbf{A}(\mathbf{x}_j, t) \right]^2 + \int d\mathbf{x} \frac{\mathbf{E}^2}{8\pi} + V_{\text{ext}} , \quad (6.29)$$

where the summation is over the test particles with masses  $m_j$ , momenta  $\mathbf{p}_j$ , and charges  $Z_j e$ ,  $\mathbf{A}(\mathbf{x}, t)$  is the longitudinal vector potential (in the assumed gauge the scalar potential  $\phi$  is zero), and  $\mathbf{E}(\mathbf{x}, t)$  is the longitudinal electric field. If to introduce

$$\mathbf{A}(\mathbf{x}, t) = \sum_{\mathbf{k}} \left[ \frac{4\pi c^2}{V|\mathbf{k}|^2} \right]^{1/2} q_{\mathbf{k}}(t) \mathbf{k} e^{i\mathbf{k} \cdot \mathbf{x}} ,$$

where  $V$  is the volume of the system, Hamiltonian (6.29) can then be written as

$$H = H_{\mathbf{p}} + H_f + H_I^{(1)} + H_I^{(2)} + V_{\text{ext}} , \quad (6.30)$$



where the kinetic energy of the particles is

$$H_p = \sum_j \frac{1}{2m_j} \mathbf{p}_j^2,$$

the energy of the electric field is

$$H_f = \int d\mathbf{x} \frac{\mathbf{E}^2}{8\pi} = -\frac{1}{2} \sum_{\mathbf{k}} \wp_{\mathbf{k}} \wp_{-\mathbf{k}},$$

and the interaction terms are given by

$$H_I^{(1)} = -\sum_j \sum_{\mathbf{k}} \frac{Z_j e}{m_j} \left[ \frac{4\pi}{V|\mathbf{k}|^2} \right]^{1/2} \mathbf{k} \cdot \left( \mathbf{p}_j - \frac{\hbar \mathbf{k}}{2} \right) q_{\mathbf{k}} e^{i\mathbf{k} \cdot \mathbf{x}_j}$$

and

$$H_I^{(2)} = \sum_j \sum_{\mathbf{k}} \sum_{\mathbf{k}'} \frac{2\pi Z_j^2 e^2 \mathbf{k} \cdot \mathbf{k}'}{m_j V |\mathbf{k}| |\mathbf{k}'|} q_{\mathbf{k}} q_{\mathbf{k}'} e^{i(\mathbf{k}+\mathbf{k}') \cdot \mathbf{x}_j}.$$

Here,  $\dot{q}_{\mathbf{k}}(t) \equiv dq_{\mathbf{k}}(t)/dt = -\wp_{-\mathbf{k}}$ .

The short-range Coulomb static interaction term can be explicitly obtained from (6.30) by applying a unitary transformation

$$U = \exp \left[ -\frac{1}{\hbar} \sum_j \sum_{|\mathbf{k}| > \lambda_D^{-1}} \left( \frac{4\pi Z_j^2 e^2}{V|\mathbf{k}|^2 \varepsilon(\mathbf{k}, 0)} \right)^{1/2} q_{\mathbf{k}} e^{i\mathbf{k} \cdot \mathbf{x}_j} \right],$$

where the summation over  $\mathbf{k}$  is restricted for  $|\mathbf{k}| > \lambda_D^{-1}$ , and  $\varepsilon(\mathbf{k}, 0) = 1 + |\mathbf{k}|^{-2} \lambda_D^{-2}$  is the static plasma form factor. Thus the Hamiltonian transforms to

$$H \rightarrow U^{-1} H U = H_p + H_f + H_I^{(1)} + H_I^{(2)} + V_{\text{ext}} + \frac{1}{2} \sum_{|\mathbf{k}| > \lambda_D^{-1}} \sum_{i \neq j} \frac{4\pi e^2 Z_i Z_j e^{i\mathbf{k} \cdot (\mathbf{x}_i - \mathbf{x}_j)}}{V|\mathbf{k}|^2 \varepsilon(\mathbf{k}, 0)}.$$

The terms including the factor  $(1/[\varepsilon(\mathbf{k}, 0)]^{1/2})$  for  $|\mathbf{k}| > \lambda_D^{-1}$  are neglected since the Debye screening makes the plasma wave propagation impossible in the wavenumber range  $|\mathbf{k}| > \lambda_D^{-1}$  (the effects of dynamic screening will be included below). Such a procedure of the transformation introduces the wave number domain appropriate for the interactions in consideration, and it is similar to that invoked in Ref. [353].

The Hamiltonian appropriate to a set of harmonic oscillators which represent the collective field of the plasma wave can be written as

$$H_{\text{osc}} = H_f + H_I^{(2)} = \frac{1}{2} \sum_{\mathbf{k}} \left( \wp_{\mathbf{k}} \wp_{\mathbf{k}}^* + \sum_j \omega_{pj}^2 q_{\mathbf{k}} q_{\mathbf{k}}^* \right),$$

where  $\mathbf{k} = -\mathbf{k}'$  for  $H_I^{(2)}$ . Here,  $\wp_{\mathbf{k}}^* = -\wp_{-\mathbf{k}}$  and  $q_{\mathbf{k}}^* = -q_{-\mathbf{k}}$  because of the reality condition for the electric field, and  $\omega_{pj} = (4\pi Z_j^2 e^2 / V m_j)^{1/2}$  is the frequency of the collective particle motion. Taking

into account the dynamic screening of the wave fields and setting

$$\wp_{\mathbf{k}} = i \sqrt{\frac{\hbar \omega_{\mathbf{k}}}{(\partial \omega \varepsilon / \partial \omega)_{\omega_{\mathbf{k}}}}} (a_{-\mathbf{k}} + a_{\mathbf{k}}^*), \quad q_{\mathbf{k}} = \sqrt{\frac{\hbar}{\omega_{\mathbf{k}}(\partial \omega \varepsilon / \partial \omega)_{\omega_{\mathbf{k}}}}} (a_{\mathbf{k}} - a_{-\mathbf{k}}^*),$$

it is obtained

$$\begin{aligned} H_I^{(1)} = & - \sum_j \sum_{\mathbf{k}} \frac{Z_j e}{m_j} \left[ \frac{4\pi \hbar}{V |\mathbf{k}|^2 \omega_{\mathbf{k}} (\partial \omega \varepsilon / \partial \omega)_{\omega_{\mathbf{k}}}} \right]^{1/2} \left[ \mathbf{k} \cdot \left( \mathbf{p}_j - \frac{\hbar \mathbf{k}}{2} \right) a_{\mathbf{k}}(t) e^{i\mathbf{k} \cdot \mathbf{x}_j} \right. \\ & \left. + e^{-i\mathbf{k} \cdot \mathbf{x}_j} a_{\mathbf{k}}^*(t) \mathbf{k} \cdot \left( \mathbf{p}_j - \frac{\hbar \mathbf{k}}{2} \right) \right] \end{aligned} \quad (6.31)$$

as well as

$$\begin{aligned} H_{\text{osc}} = & \sum_{\mathbf{k}} \frac{\hbar \omega_{\mathbf{k}}}{(\partial \omega \varepsilon / \partial \omega)_{\omega_{\mathbf{k}}}} (a_{\mathbf{k}}^* a_{\mathbf{k}} + a_{\mathbf{k}} a_{\mathbf{k}}^*) + \sum_{\mathbf{k}} \frac{\hbar}{2 \omega_{\mathbf{k}} (\partial \omega \varepsilon / \partial \omega)_{\omega_{\mathbf{k}}}} \left( \sum_j \omega_{pj}^2 - \omega_{\mathbf{k}}^2 \right) \\ & \times (a_{\mathbf{k}}^* a_{\mathbf{k}} + a_{\mathbf{k}} a_{\mathbf{k}}^* - a_{\mathbf{k}} a_{-\mathbf{k}} - a_{-\mathbf{k}}^* a_{\mathbf{k}}^*), \end{aligned} \quad (6.32)$$

where  $\varepsilon = \varepsilon(\mathbf{k}, \omega)$  is the linear plasma dielectric permittivity. The solution of the dispersion equation  $\varepsilon(\mathbf{k}, \omega) = 0$  gives the eigenfrequency of the plasma waves  $\omega = \omega_{\mathbf{k}}$ . Below, we assume that there is no plasma wave damping, and consider the positive wave eigenfrequencies,  $\omega_{\mathbf{k}} > 0$ .

Next, the canonical transforms  $\mathbf{x}_j = \exp(-iS/\hbar) \mathbf{X}_j \exp(iS/\hbar)$ ,  $\mathbf{p}_j = \exp(iS/\hbar) \mathbf{P}_j \exp(iS/\hbar), \dots$ , is applied, where

$$S = i \sum_j \sum_{\mathbf{k}} (\alpha_{j\mathbf{k}} A_{\mathbf{k}} e^{i\mathbf{k} \cdot \mathbf{X}_j} - e^{-i\mathbf{k} \cdot \mathbf{X}_j} A_{\mathbf{k}}^\dagger \alpha_{j\mathbf{k}})$$

and

$$\alpha_{j\mathbf{k}} = \frac{Z_j e}{m_j} \left[ \frac{4\pi \hbar}{V |\mathbf{k}|^2 \omega_{\mathbf{k}} (\partial \omega \varepsilon / \partial \omega)_{\omega_{\mathbf{k}}}} \right]^{1/2} \frac{\mathbf{k} \cdot (\mathbf{P}_j - \hbar \mathbf{k} / 2)}{\omega_{\mathbf{k}} - (\mathbf{k} \cdot \mathbf{P}_j / m_j) + (\hbar |\mathbf{k}|^2 / 2 m_j)}$$

to obtain the set of the new variables  $(\mathbf{X}_j, \mathbf{P}_j, A_{\mathbf{k}}, A_{\mathbf{k}}^\dagger, \mathcal{H})$  from  $(\mathbf{x}_j, \mathbf{p}_j, a_{\mathbf{k}}, a_{\mathbf{k}}^*, H)$ . The new canonically transformed interaction Hamiltonian includes the static Debye contribution  $\mathcal{H}_D$ , the external potential  $\mathcal{V}_{\text{ext}}$ , the term  $\mathcal{H}_I^{(1)}$  corresponding to  $H_I^{(1)}$ , and the interaction parts of  $\mathcal{H}_{\mathbf{P}}$  and  $\mathcal{H}_{\text{osc}}$  in the lowest order, i.e.,

$$\begin{aligned} \mathcal{H}_{\text{int}} = & \mathcal{H}_D + \mathcal{V}_{\text{ext}} + \mathcal{H}_I^{(1)} + \left( \mathcal{H}_{\mathbf{P}} - \sum_j \frac{\mathbf{P}_j^2}{2m_j} \right) \\ & + \left[ \mathcal{H}_{\text{osc}} - \sum_{\mathbf{k}} \frac{\hbar \omega_{\mathbf{k}}}{(\partial \omega \varepsilon / \partial \omega)_{\omega_{\mathbf{k}}}} (A_{\mathbf{k}}^\dagger A_{\mathbf{k}} + A_{\mathbf{k}} A_{\mathbf{k}}^\dagger) \right], \end{aligned} \quad (6.33)$$

where

$$\mathcal{H}_D = \frac{1}{2} \sum_{|\mathbf{k}| > \lambda_D^{-1}} \sum_{i \neq j} \frac{4\pi e^2 Z_i Z_j e^{i\mathbf{k} \cdot (\mathbf{X}_i - \mathbf{X}_j)}}{V |\mathbf{k}|^2 \varepsilon(\mathbf{k}, 0)}. \quad (6.34)$$

The last three terms in Eq. (6.33) can be combined and expressed as

$$\begin{aligned} \mathcal{V}^{\text{eff}} = & - \sum_{i \neq j} \sum_{\mathbf{k}} \frac{2\pi Z_i Z_j e^2}{V m_i m_j |\mathbf{k}|^2 \omega_{\mathbf{k}} (\partial \omega \varepsilon / \partial \omega)_{\omega_{\mathbf{k}}}} \times \left[ \mathbf{k} \cdot \left( \mathbf{P}_i - \frac{\hbar \mathbf{k}}{2} \right) \mathbf{k} \cdot \left( \mathbf{P}_j + \frac{\hbar \mathbf{k}}{2} \right) \right. \\ & \times \frac{e^{i\mathbf{k} \cdot (\mathbf{X}_i - \mathbf{X}_j)}}{\omega_{\mathbf{k}} - (\mathbf{k} \cdot \mathbf{P}_j / m_j) - (\hbar |\mathbf{k}|^2 / 2 m_j)} \\ & \left. + e^{-i\mathbf{k} \cdot (\mathbf{X}_i - \mathbf{X}_j)} \mathbf{k} \cdot \left( \mathbf{P}_j + \frac{\hbar \mathbf{k}}{2} \right) \frac{1}{\omega_{\mathbf{k}} - (\mathbf{k} \cdot \mathbf{P}_j / m_j) - (\hbar |\mathbf{k}|^2 / 2 m_j)} \mathbf{k} \cdot \left( \mathbf{P}_i - \frac{\hbar \mathbf{k}}{2} \right) \right]. \quad (6.35) \end{aligned}$$

Here, the effective interaction between particles through the exchange of virtual plasma waves or quasi-particles is described. Note that the dynamic collective effect of the background plasma is included through the dielectric function  $\varepsilon(\mathbf{k}, \omega)$ .

Consider a pair of dust particles interacting via the plasma ion-acoustic waves. Let a pair of dust grains have masses  $m_1, m_2$  and charges  $Q_1 = Z_1 e$ ,  $Q_2 = Z_2 e$ , and consider the quasiclassical limit  $\hbar \rightarrow 0$ . When the particles move in the same direction  $z$  with the velocities  $v_1$  and  $v_2$ , the effective potential energy derived from the interaction Hamiltonian is given by

$$\mathcal{V}_{12}^{\text{eff}} = - \frac{Q_1 Q_2 v_1 v_2}{(2\pi)^2} \int dk_Z d\mathbf{k}_{\perp} \frac{k_z^2 \lambda_D^2 \exp(i\mathbf{k} \cdot \mathbf{R})}{1 + |\mathbf{k}|^2 \lambda_D^2} \left[ \frac{1}{\omega_k^2 - (k_Z v_2)^2} + \frac{1}{\omega_k^2 - (k_Z v_1)^2} \right],$$

where the integration is limited to the range  $|\mathbf{k}| < \lambda_D^{-1}$ ,  $\mathbf{R} = \mathbf{X}_1 - \mathbf{X}_2$ , and  $k^2 = k_Z^2 + |\mathbf{k}_{\perp}|^2$ . We see that

$$\mathcal{V}_{12}^{\text{eff}} = 0$$

for  $v_1 = 0$  or  $v_2 = 0$  and

$$\begin{aligned} \mathcal{V}_{12}^{\text{eff}} = & Q_1 Q_2 \int \frac{dk_Z d\mathbf{k}_{\perp}}{2\pi^2} \frac{\lambda_D^2 \exp(i\mathbf{k} \cdot \mathbf{R})}{1 + k^2 \lambda_D^2} \left[ 1 + \frac{\omega_k^2}{k_Z^2 v_0^2 - \omega_k^2} \right. \\ & \left. + \frac{1}{2} \left( \frac{\delta v}{v_0} \right)^2 \left( 1 + \frac{\omega_k^2 (3k_z^2 v_0^2 - \omega_k^2)}{(\omega_k^2 - k_z^2 v_0^2)^2} \right) \right], \end{aligned}$$

for  $v_1 = v_0$ ,  $v_2 = v_0 \pm \delta v$  ( $|\delta v| \ll |v_0|$ ). In the limit of  $\delta v \rightarrow 0$ ,

$$\mathcal{V}_{12}^{\text{eff}} = Q_1 Q_2 \int \frac{dk_Z d\mathbf{k}_{\perp}}{2\pi^2} \frac{\lambda_D^2 \exp(i\mathbf{k} \cdot \mathbf{R})}{1 + k^2 \lambda_D^2} \left[ 1 + \frac{k^2 \lambda_D^{-2} M^{-2}}{(k_Z^2 + k_0^2)(k_Z^2 - k_1^2)} \right], \quad (6.36)$$

where  $k_{0,1}^2 = \pm((1 - M^{-2})\lambda_D^{-2} + |\mathbf{k}_{\perp}|^2)/2 + [|\mathbf{k}_{\perp}|^2 M^{-2} \lambda_D^{-2} + ((1 - M^{-2})\lambda_D^{-2} + |\mathbf{k}_{\perp}|^2)^2/4]^{1/2}$ . The vanishing effective potential was investigated in the context of the study of molecular-ion beams interacting with metals [354]. The effective potential, Eq. (6.36), is in agreement with the wake

potential derived for the screened electrostatic potential due to a test dust particle in the ion flow [256]. It is noteworthy that the effective potential vanishes when one dust grain is stationary while another dust grain is moving with respect to the ambient plasma. The exchange of phonons between a pair of dust grains is only possible when the grains are moving together (or alternatively they are stationary in the presence of plasma flow). Note that the addition of the first term in the square brackets in (6.36) and  $\mathcal{H}_D$ , given by Eq. (6.34), forms the complete Debye static interaction potential  $\mathcal{V}_D = \sum_{i \neq j} \mathcal{V}_{ij}^D/2$ , where

$$\mathcal{V}_{ij}^D = \sum_{\mathbf{k}} \frac{4\pi Q_i Q_j e^{i\mathbf{k} \cdot (\mathbf{X}_i - \mathbf{X}_j)}}{V |\mathbf{k}|^2 \varepsilon(\mathbf{k}, 0)}.$$

Here, the summation is within the whole range of possible values of  $\mathbf{k}$ . For  $M > 1$ , the contribution from the poles at  $\pm k_1$  in the  $k_Z$  plane gives the oscillatory wake potential.

Assuming a cylindrical symmetry  $\mathbf{k} \cdot \mathbf{R} = |\mathbf{k}_\perp| R_\perp \cos \phi + k_Z Z$  and integrating over  $k_Z$  in Eq. (6.36), the approximate expression for the oscillatory interaction potential energy at the distance  $R_\perp > \lambda_D$  and  $|Z| > \lambda_D \sqrt{M^2 - 1}$  is given by

$$\begin{aligned} \mathcal{V}_{12}^W(R_\perp, Z) \simeq \frac{2Q_1 Q_2}{1 - M^{-2}} \sqrt{\frac{\lambda_D}{2\pi R_\perp}} & \left[ \frac{\cos[(\pi/4) + (Z_-/\lambda_D \sqrt{M^2 - 1})]}{Z_-} \right. \\ & \left. + \frac{\cos[(\pi/4) - (Z_+/\lambda_D \sqrt{M^2 - 1})]}{Z_+} \right], \end{aligned} \quad (6.37)$$

where  $Z_\pm \equiv |Z| \pm R_\perp \sqrt{M^2 - 1} > 0$ . The oscillating potential exists only in the wake of the test particle, i.e., for  $Z < 0$  and  $|Z| > R_\perp \sqrt{M^2 - 1}$  [255,256]. On the other hand, for  $R_\perp < \lambda_D$  and  $|Z| > \lambda_D \sqrt{M^2 - 1}$ , we recover [254]

$$\mathcal{V}_{12}^W(R_\perp = 0, Z) \simeq \frac{2Q_1 Q_2}{|Z|} \frac{\cos(|Z|/\lambda_D \sqrt{M^2 - 1})}{1 - M^{-2}}. \quad (6.38)$$

The Debye static interaction potential can be expressed explicitly as

$$\mathcal{V}_{ij}^D = \frac{Q_i Q_j}{|\mathbf{X}_i - \mathbf{X}_j|} e^{-|\mathbf{X}_i - \mathbf{X}_j|/\lambda_D}.$$

The derived Hamiltonian describes the effective potential produced by a pair of moving dust grains due to their interaction with the external fields, the Debye screening potential, and the exchange of virtual phonons in the ion flow. It is shown that the wake potential will vanish if one of the pair dust particles is stationary with respect to the ambient plasma. The Hamiltonian can be also applied to oscillations in a coupled system of dust particles, and characteristic frequencies of both longitudinal and transverse modes can be therefore derived [257].

### 6.5. Subsonic plasma wakes

According to the Bohm criterion [355], the plasma ions, accelerated by the sheath electric field, can achieve supersonic velocities in the plasma sheath. Such ion flows can excite longitudinal plasma

oscillations in the sheath region, as known from numerical simulations and experimental observations [48,356]. The influence of the longitudinal random fields leads to the broadening of the ion distribution in the direction of the ion flow. In this case, the width of the ion distribution in the direction parallel to the ion flow (“downstream”) should be larger than that in the perpendicular direction. Thus the ion drifting distribution is highly anisotropic. Moreover, the downstream parallel ion distribution should be wider than the ion distribution in the opposite direction (“upstream”). This is due to the fact that the oscillations excited upstream act mostly on the downstream particles. It is noted also that the electric field of the sheath produces self-consistently an ion distribution downstream/upstream asymmetry in the widths [357]. Both arguments (the excited plasma turbulent fields and the influence of the electric field on the ion distribution) suggest that the ion distribution in the sheath should be asymmetric. This characteristic feature must be taken into account when considering the charging and shielding of dust particles.

So far there have been few experimental measurements of the ion distribution in the sheath. The most reliable is the recent investigation of the ion velocity distribution in the sheath by means of a laser induced fluorescence [358]. These experiments show that the general observed features of the ion distribution asymmetry agree qualitatively with the theoretical predictions [357] in which the effect of the excited plasma fields in the sheath was neglected. However, the measured absolute value of the width appears to be much larger than the theoretical result [357]. A plausible candidate to explain this anomalous width is the sheath turbulence. The turbulence also modifies the regular electric field in the sheath and therefore can affect the results of [357] in this way.

The important observation of the experiment [358] is that the observed width of the ion distribution perpendicular to the flow is at least one order of magnitude less than the upstream (or downstream) width. The ion flow can thus finally appear to be moderate as compared to the thermal ion velocity parallel to the flow. The ion thermal velocity in the direction perpendicular to the ion flow is almost the same as in the bulk plasma and is therefore small compared with the ion flow velocity. The collective field that can broaden the ion distribution, can be created mainly in the direction of the ion flow. For the moderate longitudinal ion flow the problem of shielding can be considered only numerically since the Landau damping of the fields of the dust particle moving through the ion plasma (in the frame of ions at rest) should be rather strong.

Here, we present the theory [324] of shielding and charging of dust in the plasma sheath using the ion distribution function with a marginal (subsonic) velocity which is of the order of the characteristic broadening of the ion distribution in the longitudinal direction. In this framework, the physics of shielding is strongly modified as compared to the case of superthermal (and especially supersonic) ion flows. The main mechanism in this case is closely related to the Landau damping of collective plasma perturbations excited by flowing ions. The case of the subsonic ion flow velocities is physically different from the wake excitation by a supersonic ion flow, considered above, as the wake field cannot be excited in this case. In the subsonic case, the stopping power of ions by the Landau mechanism changes the ion distribution around the dust particle and produces the ion bunching as well as the local excess of positive charges around the dust particle. The latter can create potential wells not only in the direction parallel to the ion flow but also in the direction which is almost perpendicular to it (note that the wake field has a similar behavior [255,256]).

The ion distribution function  $f_i$  is characterized here by three temperatures:  $T_i$  is the temperature perpendicular to the direction of the ion flow,  $T_1$  is the temperature which corresponds to the direction parallel to the ion flow (which we call the downstream direction) and  $T_2$  is the temperature in the

direction antiparallel to the ion flow (which we call the upstream direction). Thus the ion distribution function can be written as

$$f_{i(1,2)} = \frac{n_i}{(2\pi)^{3/2} v_{Ti}^2 v_T} \exp \left[ -\frac{v_\perp^2}{2v_{Ti}^2} - \frac{(v - v_0)^2}{2v_{(T1,T2)}^2} \right],$$

where  $v_0$  is the ion flow velocity,  $v$  corresponds to the ion velocity component along the flow direction and  $v_\perp$  corresponds to the velocity component perpendicular to the flow, the subscript 1 corresponds to the downstream part of the ion distribution where  $v > v_0$ , and the subscript 2 corresponds to the upstream part of the distribution function where  $v < v_0$ ;  $v_{Ti} \equiv \sqrt{T_i/m_i}$  is the thermal ion velocity characterizing the width of the ion distribution perpendicular to the flow,  $v_{T1}$  and  $v_{T2}$  (it is assumed  $T_i \ll T_2 < T_1$ ) are the ion downstream and upstream thermal velocities, characterizing the width of the distribution function downstream and upstream in the direction of the flow, respectively. Finally,  $v_T = (v_{T1} + v_{T2})/2$  is the averaged thermal velocity along the ion flow. The linear dielectric function for this distribution can be written in the form

$$\varepsilon = 1 + \frac{1}{k^2 \lambda_{Di}^2} + \frac{4\pi e^2}{k^2} \int \frac{1}{k(v_0 + v) + \mathbf{k}_\perp \cdot \mathbf{v}_\perp} \left[ \frac{kv}{v_{T1,T2}^2} - \frac{k(v_0 + v)}{v_{Ti}^2} \right] f_i^r d^3 v, \quad (6.39)$$

where  $k$  and  $v$  are the components of the wave vector and ion velocity along the direction of the flow respectively while  $\mathbf{k}_\perp$  and the  $\mathbf{v}_\perp$  are the components perpendicular to it. The  $f_i^r$  is the ion distribution in the frame of ions at rest, and, finally,  $\lambda_{Di} = v_{Ti}/\omega_{pi}$  is the ion Debye length determined by the transverse ion thermal velocity. In the ion frame (of ions at rest) the plasma is moving with the velocity  $-v_0$  and thus only the upstream part of the ion distribution can produce the strong Landau damping. Introduce also the Debye length for the “averaged” longitudinal temperature

$$\bar{\lambda}_D^2 \equiv \frac{[(\sqrt{T_1} + \sqrt{T_2})/2]^2}{4\pi n_i e^2}, \quad (6.40)$$

and the relative flow velocity

$$w_1 = \frac{v_0}{\sqrt{2}v_{T1}}, \quad w_2 = \frac{v_0}{\sqrt{2}v_{T2}} = \frac{w}{\sqrt{t_{21}}}, \quad (6.41)$$

where  $w = v_0/\sqrt{2}v_{T1}$  and  $t_{21} \equiv T_2/T_1$ . Other dimensionless parameters are  $\tau = T_i/T_e$ ,  $\tau_1 = T_i/T_1$ , and  $z = Z_d e^2 / a T_e$ .

The dielectric function for the screening at large angles to the ion flow is given by

$$\varepsilon = 1 + \frac{1}{k^2 \bar{\lambda}_D^2} \frac{1 + \sqrt{t_{21}}}{2\sqrt{\pi}} \int_0^\infty e^{-y^2} y dy \left( \frac{1}{y + w_1 - i0} + \frac{1}{\sqrt{t_{21}}(y - w_2 + i0)} \right). \quad (6.42)$$

Here,  $v_0$  is positive, i.e.  $w_1 > 0$ ,  $w_2 > 0$ , and the imaginary part of Eq. (6.42) can be expressed as usual in the analytical form. The dielectric permittivity can be rewritten as

$$\varepsilon = 1 + \frac{1}{k^2 \bar{\lambda}_D^2} W(w),$$



where

$$W(w) = W_R(w) - i \frac{k}{|k|} W_I(w) , \quad (6.43)$$

$$W_R(w) = \frac{1 + \sqrt{t_{21}}}{2\sqrt{\pi}} P \int_0^\infty e^{-y^2} y dy \left( \frac{1}{y+w} + \frac{1}{\sqrt{t_{21}}y-w} \right) \quad (6.44)$$

and

$$W_I(w) = \frac{\sqrt{\pi}}{2} \left( 1 + \frac{1}{\sqrt{t_{21}}} \right) \frac{w}{\sqrt{t_{21}}} e^{-w^2/t_{21}} . \quad (6.45)$$

The negative sign in the imaginary part of Eq. (6.43) shows that the plasma perturbations propagating along the direction of ion flow are amplified while the perturbations propagating against the direction of the flow are damped. Both damping and amplification are strong for the moderate flow ( $w$  of order of 1) and cannot be described as the wave excitation since the flow velocity is subsonic. This effect is the manifestation of the strong Landau damping (since the amplification is just the inverse Landau damping).

The potential of a particle normalized to its Coulomb potential is given by

$$\phi = \frac{r}{2\pi^2} \operatorname{Re} \int \frac{\exp(i\mathbf{k} \cdot \mathbf{r})}{k^2 \varepsilon} d^3 k . \quad (6.46)$$

The presence of  $k/|k|$  in the dielectric permittivity changes the screened potential in the upstream and downstream directions. The component of the wave vector along the  $\mathbf{r}$ -direction is  $k'$ . This component is equal to  $k$  for the downstream direction and  $-k$  in the upstream direction. This can be seen by introducing the spherical or cylindrical coordinates in the  $\mathbf{r}$ -space where the flow is directed along the positive  $z$ -axis for the downstream direction and the negative  $z$ -axis for the upstream direction. The potential  $\phi_+$  represents the downstream potential while the potential in the upstream direction is  $\phi_-$ . Introducing  $y = k_\perp r$ ,  $x = k' r$  ( $k'_\perp = k_\perp$ ) and  $r = r/\bar{\lambda}_D$ , one finds

$$\begin{aligned} \phi_\pm = & \frac{2}{\pi} \int_0^\infty dx \int_0^\infty \frac{J_0(y \sin \theta) y dy}{(y^2 + x^2 + r^2 W_R)^2 + (r^2 W_I)^2} \\ & \times [(y^2 + x^2 + r^2 W_R) \cos(x \cos \theta) \mp W_I r^2 \sin(x \cos \theta)] . \end{aligned} \quad (6.47)$$

This expression is useful to find the distribution of the potential perpendicular to the direction of the flow

$$\phi_\perp = \frac{2}{\pi} \int_0^\infty dx \int_0^\infty \frac{J_0(y) y dy}{(y^2 + x^2 + r^2 W_R)^2 + (r^2 W_I)^2} (y^2 + x^2 + r^2 W_R) . \quad (6.48)$$

Integrating over  $x$  is easily performed by converting the integration interval to  $[-\infty, +\infty]$  and determining residues in the complex  $x$ -plane. For the directions along the flow, it is more convenient to use the spherical coordinates and integrate over the angles of the wave vector

$$\phi_\pm = \frac{2}{\pi} \int_0^\infty \frac{\sin y(y^2 + r^2 W_R) y dy}{(y^2 + r^2 W_R)^2 + (r^2 W_I)^2} \mp \frac{4}{\pi} r^2 W_I \int_0^\infty \frac{\sin^2(y/2) y dy}{(y^2 + r^2 W_R)^2 + (r^2 W_I)^2} . \quad (6.49)$$

The first integral in Eq. (6.49) can be computed by the pole residue method in the complex plane while the second one should be calculated numerically. The first term of Eq. (6.49) reduces to unity in the case when one neglects the shielding and Landau damping and the second term is completely determined by the Landau damping. The condition of validity of Eqs. (6.47) and (6.48) is  $r_{\perp}/|z| \gg v_{Ti}/v_{T1,T2}$  which defines the corresponding solid angle. Thus the validity domain of Eq. (6.49) is outside the cone defined by this solid angle. The parameter  $P_e = (n_i - n_e)/n_e$  can be used to characterize the difference between the ion density  $n_i$  and the electron density  $n_e$ ; in the sheath  $P_e > 0$ .

In order to investigate the dust shielding, the real and imaginary parts of the dielectric function Eq. (6.39) have been calculated. The negative values of the dielectric function appear mostly in the range of the strong Landau damping. The appearance of the damping implies the existence of the collective stopping power for the incoming ions which allows an additional accumulation of the ion charges around the dust particle. The usual process of screening in the absence of the flow ends when the charge of the particle is totally compensated by the ambient plasma. The Landau damping provides corrections which are of the order of  $w$  for  $w \ll 1$ . For  $w$  of order unity, the stopping power related to the Landau damping is appreciable and the incoming ions from the flow can create a net positive polarization charge around the particle. This charge can be larger than the negative charge of the particle itself leading to the attraction of other negatively charged dust particles. The potential (normalized to the non-screened Coulomb potential) of the particle in the transverse direction is shown in Fig. 34. The normalized potential is presented as a function of the ratio of the distance from the dust particle to the Debye length  $\tilde{\lambda}_D$  defined by Eq. (6.40). One can see that the potential well indeed exists and increases with the increasing  $w$  and/or decreasing  $t_{21}$ .

Expressions for the potentials created by the dust particle close to the upstream and downstream directions but outside the narrow cone where the Debye shielding is present were also analyzed [324]. In principle, this cone narrows with decreasing  $v_{Ti}$ , and the expressions used are approximately valid for the almost upstream and downstream directions. The potential well increases with the flow velocity. The tendency for the upstream case is the opposite: with the increase of the ion flow velocity, the dust particle becomes more shielded and the potential well never appears. This has a simple explanation since the stopping power in the direction opposite to the ion flow is not sufficient to create significant ion space charges to change the sign of the shielding cloud. For comparison, the Debye shielding potentials for these cases are also plotted. Fig. 35 illustrates the fact that the smaller the angle between the direction of the flow and the direction of the screening, the deeper is the potential well and the larger is the distance between the dust particle and the position of the potential minimum.

To conclude this section, we first comment on the relation between the wake field potential wells and the Landau potential well. In the case of the large (supersonic) ion flow velocity, the dust particle velocity in the ion frame exceeds substantially all the ion thermal velocities (along and perpendicular to the direction of the flow). Then the Cherenkov condition for the excitation of the plasma modes by the particle is fulfilled (in the case such modes exist in the ion plasma at rest) and the emission of these modes as a wake is possible [254–256]. For the moderate subsonic longitudinal ion flows, the presence of the strong Landau damping is important since there are no excited wake fields. In the case of the strong Landau damping, the potential wells are mostly concentrated in the range of wave vectors belonging to the near zone where the electric field produced by the dust particle is of dissipative character (but not the wave field as in the case of the wake excitation). Creation of this

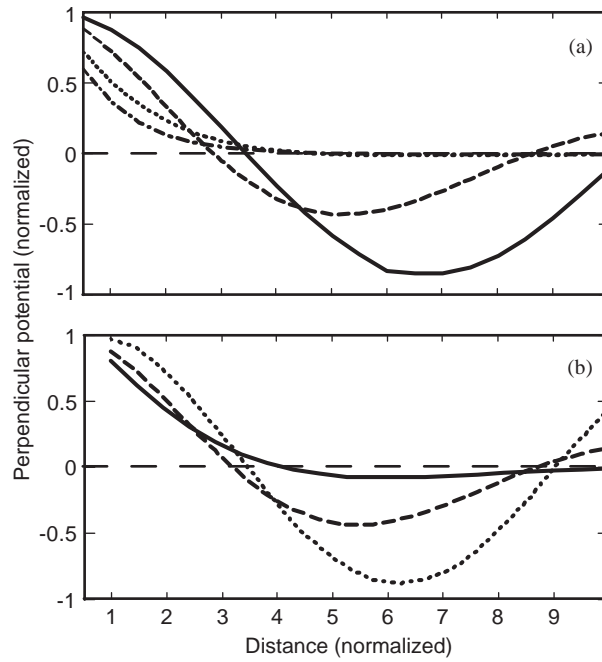


Fig. 34. (a) The potential well for  $t_{21} = 1/2$  and different values of  $w$ :  $w = 0$ —dash-dotted curve,  $w = 1/2$ —dotted curve,  $w = 1$ —dashed curve,  $w = 3/2$ —solid curve. (b) The potential well for  $w = 1$ : the solid curve corresponds to  $t_{21} = 1$ , the dashed curve corresponds to  $t_{21} = 1/2$ , and the dotted curve corresponds to  $t_{21} = 1/5$ . Reprinted from Ref. [324].

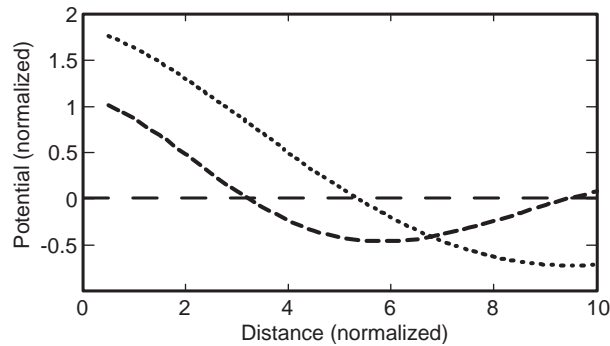


Fig. 35. Dependence of the dust potential (normalized to the Coulomb potential) on the angle with respect to the ion flow (such that  $\Theta = \pi/2$  corresponds to the downstream direction). The dashed curve is for  $\Theta = 3\pi/10$ , and the dotted curve is for  $\Theta = 2\pi/5$  [324].

field is independent of whether the wake field is created (since it is in the near zone) and is even independent on whether the ion plasma can have weakly damped modes.

The role of nonlinearities produced by the dust particles field is an important issue. Without detailed calculations, we present here the dimensional analysis [324] which can give the order of

magnitude of the distances where the plasma polarization charge can change and screen the dust charge independently of the sign of this polarization charge. Within the narrow angular interval with respect to the flow, the characteristic distance is of order  $\lambda_{Di}$  (note that for the isotropic ion distribution the only characteristic length is  $\lambda_{Di}$ ). Nonlinear effects are always strong close to the dust grain. Indeed, for the isotropic case the condition for the nonlinearity to be weak on the dust surface is

$$\frac{Z_d e^2}{a T_i} = \frac{T_e}{T_i} z \ll 1, \quad (6.50)$$

where  $z \equiv Z_d e^2 / a T_e$  is the dimensionless dust charge which is usually of order 2. Since in most of the sheath experiments the ratio  $T_e / T_i$  is high  $\approx 10^2$ , the inequality (6.50) can hardly be satisfied.

However, the linear approximation can correctly describe the shielding if the nonlinearities are at least weak within the shielding radius. The calculation of the ratio of the nonlinear charge density  $\rho_{\mathbf{k}}^N$  to the linear charge density  $\rho_{\mathbf{k}}^L = -Z_d e \delta(\omega + k v_0) / 2\pi^2$  of a dust particle in the ion frame gives for  $k \sim k_{\perp}$

$$\Delta_{\mathbf{k}} = \frac{\rho_{\mathbf{k}}^N}{\rho_{\mathbf{k}}^L} = \frac{Z_d w}{\sqrt{\pi} (4\pi)^2 n_i \lambda_{Di}^3 k_{\perp} \lambda_D} I(w, t_{21}), \quad (6.51)$$

where

$$\begin{aligned} I(w, t_{21}) = & \int_0^{\infty} dx \int_0^{\infty} ds \frac{x^2 s^4}{|x^2 s^2 + s^2 + 4x^2 W(w, t_{21}) / (1 + \sqrt{t_{21}})^2|^2} \\ & \times \left[ \int_0^{\infty} y dy \exp[-y^2 - s^2(y - w)^2 / x^2] \right. \\ & \left. \times -\sqrt{t_{21}} \int_0^{\infty} y dy \exp[-(y^2 / t_{21}) - s^2(y + w)^2 / x^2] \right]. \end{aligned} \quad (6.52)$$

Numerical calculations give  $I(1/2, 1/2) = 0.819$  and  $I(1, 1/2) = 1.362$ . The condition that the nonlinearity in the direction of the ion flow is small (with  $k_{\perp} \sim 2\pi/r$ ) thus becomes

$$Z_d \ll \alpha (2\pi)^2 n_i \lambda_{Di}^3 \frac{\lambda_D}{r}, \quad (6.53)$$

where  $\alpha \approx 5$  for  $w = 1/2$  and  $t_{21} = 1/2$ , and  $\alpha \approx 1.5$  for  $w = 1$  and  $t_{21} = 1/2$ . For  $r \approx 6\lambda_D$  (which is the approximate position of the minimum of the potential well according to the numerical results),  $n_i \approx 2 \times 10^9 \text{ cm}^{-3}$  and  $\lambda_{Di} \approx 5 \times 10^{-3} \text{ cm}$ . Then the right-hand side of (6.53) is of the order of  $10^3$ , which can correspond to the charges observed for not too large dust particles.

The results given above can thus be considered as the first approach to the problem since the nonlinearities in the dust particle shielding could be important, especially for larger particles. The linear approach can still have a range of applicability in the sheath where the ion flow is mainly regulated by the potential in the sheath. The change of the ion flow produced by a single dust particle is small for the dust particles of a small size as compared to the size of the wall producing the sheath. However, this statement is incorrect if the distance between the dust particle and the position of the minimum of the potential well is much less than the distance between the dust particle and the wall (electrode). For a more detailed description it is necessary to take into account the dependence of the ion flow velocity on the position of the dust particle with respect to the wall. This effect

can be especially important in the case when the flow velocity at the position of the dust particle significantly differs from the velocity of the flow at the wall.

### 6.6. *Simulations on plasma wakes*

As has already been demonstrated above, the ion flow provides not only a direct kinetic (dragging) influence (supporting, e.g., the formation of dust voids [234]), but is also responsible for the generation of associated collective plasma processes which can strongly affect the vertical arrangement of dust grains [254–256,324,325,359,360]. The problem of plasma kinetics in the presence of a macroscopic body is also related to the charging of the body. For a typical situation of a low-temperature laboratory dusty plasma, the macro-particle charge appears as a result of charging plasma currents onto the particle surface [3]. Several models of particle charging were developed, the Orbit Motion Limited theory (OML) being the basic one [44]. Also, a number of experiments [214–217,350] have been performed to elucidate the character of the charge of an isolated particle; most of experimental techniques are complicated, requiring special measurement procedures, and, on the other hand, do not always give the precise results. Moreover, it is especially difficult to determine the particle charges for two particles, especially in the sheath region in the presence of the ion flow. In this case, the *ab initio* numerical simulation, being one of the most complete model description, can provide very important information on the character of the plasma kinetics and particles' charging. We note here that the complete problem of plasma dynamics around a macroscopic body in the presence of plasma flows is highly nonlinear and therefore its numerical analysis is of a major importance. Among various numerical methods, direct integration of the equations of motions of plasma particles represents a numerical experiment whose significance approaches experiments in the laboratory.

Various models of dust in the presence of plasma flows were numerically considered, see, e.g., [243–245,325,330,360]. Note that most of the models considered deal with the fluid description of a plasma [360], the kinetic (i.e., coupled Poisson–Vlasov equations) case [245] without collisions in the vicinity of a dust grain, as well as with particle-in-cell simulations [244] of a uniform, steady state DC discharge plasma where plasma particle losses are assumed to be exactly balanced by a constant ionization source, or a hybrid model [243] combining Monte Carlo with fluid simulation, with the latter ignoring the equations of motion of the plasma particles. In a non-self-consistent three-dimensional description [325], the ion–ion interactions were neglected and the charge of the particle was fixed. In PIC simulation [330], the structure of the wake potential behind a stationary point-like grain with a constant charge was studied on ion time scales using particle-in-cell simulation methods; the ion dynamics (on a background of Boltzmann distributed electrons) was studied in one and two dimensions.

The first report on the self-consistent three-dimensional molecular dynamics simulation [361] of plasma kinetics around a single stationary grain demonstrated a strong ion focusing, with the ion density in the focus exceeding the ion density in the flow by a factor of 5–6. Thus the charging of the second dust grain located behind the first one, will be strongly affected by this (highly nonlinear) effect. On the other hand, the plasma dynamics around and behind the second particle is a function of its charge, and therefore the full self-consistent simulation of such an arrangement should necessarily take into account the charging of the second dust particle in the wake of the first one. It is natural to expect that the charge of this second particle will therefore differ from the charge of the first particle. Here, we note that the anisotropy of the forces appearing, e.g., in two-dimensional chains,

Table 6.1

The initial values for the dust grain and plasma particles.  $m_p = 1842m_e$  is the proton mass,  $m_e$  is the electron mass,  $e$  is the (absolute) electron charge [361]

|             | Macroparticle | Ions     | Electrons |
|-------------|---------------|----------|-----------|
| Charge      | $-1000e$      | $e$      | $-e$      |
| Mass        | $\infty$      | $4m_p$   | $100m_e$  |
| Number      | 1             | 10 000   | 9000      |
| Temperature | n/a           | 0.025 eV | 1 eV      |

is important for the proper modeling of processes in these structures levitating in the flow [248,362]; also, the ion charge accumulated behind dust grains, associated with the plasma wake, can also drive some instabilities in the dust chains [347]; on the other hand, the analytical modeling can hardly provide the relevant number because of the high nonlinearity of the processes involved.

In this section, we first present the kinetics of plasma particles around a single stationary grain in the presence of an ion flow studied using a three-dimensional molecular dynamics simulation method [361]. The model is self-consistent, involving the dynamics of plasma electrons and ions as well as charging of the dust grain. The effect of ion focusing is investigated as a function of the ion flow velocity, and distributions of electron and ion number densities, and electrostatic plasma potential, are presented. Furthermore, the characteristics of plasma particle kinetics in the presence of ions flowing around two stationary grains aligned in the direction of the flow are studied using a three-dimensional molecular dynamics simulation code [332]. The dynamics of plasma electrons and ions as well as the charging process of the dust grain are simulated self-consistently. Distributions of electron and ion number densities, and the electrostatic plasma potential are obtained for various intergrain distances, including those much less, of the order of, and more than the electron Debye length.

#### 6.6.1. Wake of a single test particle

Here, we present the results [361] of a self-consistent molecular dynamics (MD) three-dimensional (3D) simulation of the kinetics of plasma particles (electrons and ions) around a grain, taking into account the grain charging. The technique of studying the properties of a classical Coulomb plasma involving numerical integration of the equations of multi-particle dynamics used in this work is described also in Refs. [363,364]. The core of the method includes the consideration of the time evolution of the system consisting of  $N_i$  positively (“ions” with  $Z_i=1$ ) and  $N_e$  negatively (“electrons”) charged plasma particles confined in a region  $0 < x < L_x$ ,  $-L_y/2 < y < L_y/2$ ,  $-L_y/2 < z < L_z/2$ , together with a macroscopic absorbing grain of the radius  $a$  with the infinite mass and an initial (negative) charge  $Q = -Z_d e$ , where  $-e$  is the electron charge. The grain is placed at  $x = 5h_x$ ,  $y = 0$ , and  $z = 0$ . For the characteristic lengths we have (for most calculations unless otherwise specified)  $L_x/4 = L_y = L_z = 10h_x$ , with the characteristic grid step in the presented results  $h_x = 4h_y = 4h_z = 1.077 \mu\text{m}$ . Other initial values are summarized in Table 6.1. The walls bounding the simulation region are elastic for electrons; for ions, they are elastic in the  $y$  and  $z$  directions, i.e. at  $y = (-L_y/2, L_y/2)$  and  $z = (-L_z/2, L_z/2)$ . For the given values, the characteristic lengths in the plasma are: the electron Debye length  $\lambda_{De} = 5.256 \mu\text{m}$ , the ion Debye length  $\lambda_{Di} = 0.831 \mu\text{m}$ , and the Landau length for scattering



of the ions on the dust particle by the angle  $\pi/2$  is  $r_L \equiv Z_d e^2 / m_i v_0^2$ ; for the above parameters  $r_L = 0.6/M^2 \mu\text{m}$ . The ions are introduced in the system at the plane  $x = 0$  as a uniform flow with the Mach number  $M = v_0/v_s$  ( $v_0 > 0$ ) and the temperature  $T_i$ ; at  $x = L_x$  the ions are removed from the system. The paths of the ions and electrons are determined through numerical integration of the equations of motion:  $d^2\mathbf{r}_k/dt^2 = \mathbf{F}_k/m_k$ , where  $\mathbf{F}_k = \sum_1^{1+N_i+N_e} \mathbf{f}_{kl}$  and the Coulomb force is given by  $\mathbf{f}_{kl} = q_k q_l \mathbf{r}_{kl} / |\mathbf{r}_{kl}|^3$ .

The direct particle–particle interaction is in the core of the most appropriate method for the numerical integration of the equations of motion in studies of basic plasma kinetics. The particle–particle integration method is flexible enough but involves a high computational cost. In an implementation of this technique, an algorithm taking advantage of the specific properties of classical Coulomb plasmas was elaborated to significantly decrease the number of arithmetic operations. Central to the method is the determination of the particles nearest to every particle and inclusion of their interaction by using a computational scheme of high-order accuracy (Runge–Kutta of the 4th order with an automatically chosen time step). The code realizing the outlined algorithm was written in Fortran-90.

Simulating the charging process, the real electron/ion mass ratio is effectively taken into account (note that in the computational model the electron mass was assumed to be  $100m_e$ , see Table 6.1) by renormalizing the absorbed charge in the process of the electron–dust charging collision, so that the charge appearing on the grain corresponds to its value for the real electron/ion mass ratio. In the simulation, the ion number density was calculated by averaging within the spherical layer around the macro-particle. The total simulation time of the computed physical processes is  $3.36 \times 10^{-9}$  s which is approximately equal to the half of the oscillation period of plasma ions oscillating with the ion plasma frequency  $\tau_{pi} = 6.76 \times 10^{-9}$  s. The charge of the dust particle was found to fluctuate around  $Z_d \approx 1000$ –1100 weakly depending on the ion flow velocity.

In Fig. 36, the contour plots of the ion density  $n_i$  normalized to  $n_0 = N_i/L_x L_y L_z$ , are presented for three values of the velocity of the ion flow (one is subsonic with  $M^2 = 0.6$ , and two supersonic, with  $M^2 = 1.2$  and  $M^2 = 2.4$ ). For better visualization, parts of the simulation volume where  $n_i/n_0 < 1$  and  $n_i/n_0 > 1$ , respectively, are presented in the (grayscale) topograph style. A strong ion focus, with  $n_i/n_0 \sim 6.5$  at the maximum, is formed at the distance of a fraction of the electron Debye length behind the dust grain. The maximum value of the density at the ion focus is almost independent of the flow velocity, whereas the characteristic distance of the ion focus from the dust grain increases with increasing flow velocity, being approximately equal to  $0.5\lambda_{De}$  for  $M^2 = 2.4$ . This characteristic spacing corresponds to an ion focus effect in the near zone of the dust grain, which is a purely kinetic effect [324] not associated with the collective wake field formation. Note that the oscillating wake field in the wave zone behind the grain cannot form here for the considered simulation time (half of the period of the ion oscillations). Another kinetic effect seen from Figs. 36 is the appearance of precursors in front of the dust grain, which can be attributed to those ions reflected backwards within the radius (around the  $x$ -axis) of the order of the Landau length.

### 6.6.2. Wake of two particles

Here, we present the results of a self-consistent molecular dynamics (MD) three-dimensional (3D) simulation of the kinetics of plasma electrons and ions around two aligned (in the direction of the flow) dust grains, taking into account the dust charging and the supersonic ion flow [332]. The

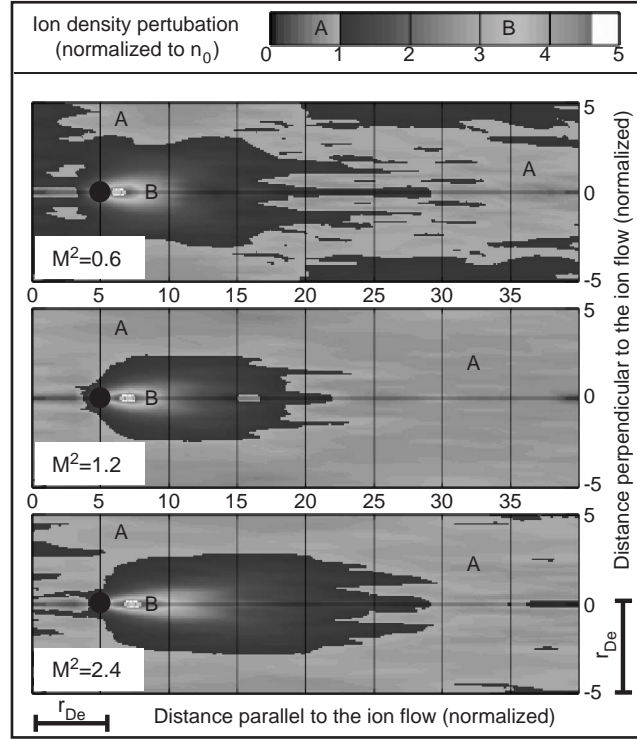


Fig. 36. Contour plot of the ion density, showing ion focusing, for three different velocities of ion flow. The plot is presented in the grayscale topograph style; regions A correspond to the normalized ion densities below 1, and regions B correspond to the normalized ion densities above 1. The ions are focusing behind the grain thus forming the region with the highly enhanced ion density. The distances are given in the units of  $h_x \approx 1.077 \mu\text{m}$  used in the calculation; the physical distance corresponding to the electron Debye length  $\lambda_{De}$  ( $r_{De}$  in the figure) is presented. Reprinted from Ref. [361].

details of the technique used for the numerical integration of the equations of multi-particle dynamics are described above (see also [332,361,363]). The numerical method used involves the simulation of the time evolution of the fully ionized (with the singly charged ions) plasma consisting of  $N_i$  positively (ions) and  $N_e$  negatively (electrons) charged plasma particles confined in a simulation box  $0 < x < L_x$ ,  $0 < y < L_y$ ,  $0 < z < L_z$ , together with two macroscopic absorbing grains (dust particles), each of the radius  $a = 0.5 \mu\text{m}$ , with infinite masses and the initial (negative) charges  $Q_{1,2} = -Z_{d1,2}e$ , where  $-e$  is the electron charge. The details are given in Table 6.2.

As in the previous section, the electron mass is assumed to be  $100m_e$ , see Table 6.2, but the real electron/ion mass ratio is taken into account by renormalizing the electron current and therefore the absorbed charge in the process of the electron–dust charging collision, so that the charges appearing on the grains correspond to their values for the real electron/ion mass ratio, see for details [332,361]. The ions were introduced in the system at the plane  $x=0$  as a uniform flow in the  $x$ -direction with the Mach number  $M = v_0/V_s$  ( $v_0 > 0$ ) and the temperature  $T_i$ ; at  $x=L_x$  the ions are removed from the system. The walls bounding the simulation region are elastic for electrons; for ions, they are elastic in the  $y$  and  $z$  directions, i.e. at  $y = (0, L_y)$  and  $z = (0, L_z)$ . This means that electrons are

Table 6.2

The initial values for the dust grain and plasma particles [332]

|             | Macroparticles | Ions     | Electrons |
|-------------|----------------|----------|-----------|
| Charge      | $-1250e$       | $e$      | $-e$      |
| Mass        | $\infty$       | $4m_p$   | $100m_e$  |
| Number      | 1              | 5000     | 2500      |
| Temperature | n/a            | 0.025 eV | 1 eV      |

specularly reflected from the walls in all directions; on the other hand, since the ions are moving in the  $x$  direction, for them the specular reflection condition applies in the  $y$  and  $z$  directions.

The total numbers of the electrons and ions in the system are fixed; it is chosen on the basis of a test simulation runs to satisfy the given number densities and to make sure that the system is neutral as a time average. In the place of the ion absorbed by the dust grains (or at the back wall of the simulation box), a new one is introduced at a random point on the front wall with the chosen velocity distribution function (the latter is assumed to be shifted Maxwellian). The dust grains are placed at  $x = x_0 = L_x/4$  and  $x = x_0 + D$ , such that  $D$  is the distance between the grains, with the other coordinates being  $y = y_0 = L_y/2$  and  $z = z_0 = L_z/2$ ; thus the grains are aligned in the direction parallel to the ion flow.

The initial distributions of the coordinates of the plasma electrons and ions are chosen to be homogeneous within the simulation box; the initial velocity distributions correspond to Maxwellian for electrons and shifted Maxwellian for ions at infinity. Depending on the distance to the colloidal particles, the distributions are distorted because of the interactions with the macroparticles. Thus the initial distributions do not include finite ion orbits which can strongly affect the kinetic characteristics under certain circumstances [365]. The trajectories of the plasma electrons and ions are determined through numerical integration of the equations of motion. For the Coulomb force at very small distances we used the corresponding expression for finite (small) size mutually penetrating spheres [363].

The equations of motion are solved by the Runge–Kutta method of the fourth order with an automatically chosen time step. For the characteristic lengths we have (for most calculations unless otherwise specified)  $L_x/2 = L_y = L_z = 20h_x$  with the spacing  $h_x = 2h_y = 2h_z = 0.5375 \mu\text{m}$ . For the given values, the characteristic lengths in the plasma are: the electron Debye length  $\lambda_{De} = 5.256 \mu\text{m}$  and the ion Debye length  $\lambda_{Di} = 0.831 \mu\text{m}$ . The ion number density is  $n_i = 2 \times 10^{12} \text{ cm}^{-3}$ , and hence the ion Debye length in term of the average ion–ion distance  $\lambda_{Di}n_i^{1/3} = 1.06$ ; the number of ions in the ion Debye sphere is approximately 5. Note that since the ions are supersonic, their energy exceeds  $T_e$  and they are really weakly coupled. For electrons, we have  $\lambda_{De}n_e^{1/3} = 5.25$ , which corresponds to more than 500 electrons in the electron Debye sphere, and the electron-ion system can be considered as an ideal plasma. Finally, the electron and ion number densities are chosen to be higher than those in real experiments for numerical reasons (to decrease the plasma Debye length).

The total simulated time of the physical processes is  $9.2 \times 10^{-9} \text{ s}$  which should be compared with the inverse ion plasma frequency  $\tau_{pi} = 1/\omega_{pi} = 3.4 \times 10^{-9} \text{ s}$ . The time step of the numerical simulation is  $4 \times 10^{-12} \text{ s}$  which is not only much less than the inverse ion plasma frequency, but is also much less than the electron plasma frequency  $\tau_{pe} = 1/\omega_{pe} = 8 \times 10^{-10} \text{ s}$ . The speed of the

Table 6.3

The charges on the dust grains depending on the distance between them [362]

| Distance $D$                 | Charge $ Q_1 $ | Charge $ Q_2 $ |
|------------------------------|----------------|----------------|
| $0.06L_x = 0.25\lambda_{De}$ | 1390           | 840            |
| $0.10L_x = 0.41\lambda_{De}$ | 1420           | 860            |
| $0.15L_x = 0.62\lambda_{De}$ | 1390           | 840            |
| $0.20L_x = 0.82\lambda_{De}$ | 1430           | 1010           |
| $0.25L_x = 1.03\lambda_{De}$ | 1470           | 1040           |
| $0.35L_x = 1.45\lambda_{De}$ | 1500           | 1080           |
| $0.40L_x = 1.64\lambda_{De}$ | 1410           | 1020           |
| $0.50L_x = 2.05\lambda_{De}$ | 1480           | 1130           |
| $0.60L_x = 2.46\lambda_{De}$ | 1450           | 1230           |
| $0.65L_x = 2.67\lambda_{De}$ | 1430           | 1180           |
| $1.00L_x = 4.10\lambda_{De}$ | 1460           | 1200           |
| $\infty$                     | 1450           | n/a            |

ion flow corresponds to the Mach number  $M^2 = 2$ . Table 6.3 demonstrates the dependence of the charges accumulated on the dust grains as functions of the intergrain distance. When the particles are very close to each other, their charges are influenced by the presence of the other particle. This influence is especially strong for the second (i.e., downstream) particle; its charge is significantly (typically, 40%) less than the charge of an isolated particle (see the last line of the table). As soon as the distance between the particles is increased, the second charge exhibits a noticeable increase; it is interesting to note that the first charge is increased, too, although by a lesser value. We also see that when the interparticle separation exceeds the electron Debye length ( $D = 1.03\lambda_{De} - 1.45\lambda_{De}$ ), the increase of the charge of the first particle stops; on the other hand, the increase of the charge accumulated on the second particle located downstream continues to grow until the distance exceeds two electron Debye lengths ( $D = 2.46\lambda_{De}$ ). We can attribute this phenomenon to the fact that the ion wake of the first particle is spreading at distances significantly exceeding the electron Debye length; on the other hand, the influence of the second (i.e., downstream) particle on the charge of the first one in the simplest approximation is limited to distances of the order of the electron Debye length. Note that other charge variations express fluctuations always present in the particle charges as well as the plasma parameters, see also [331]. Another interesting phenomenon is that the charge of the second particle, at the considered distances (up to  $D = 4.1\lambda_{De}$ ), is always less than the charge of the first particle, thus confirming the long-range influence of the ion wake.

To compare the results for two particles with the case of an isolated particle, in the last line of Table 6.3 the result of the special simulation run for the charge of the first particle when the second particle is removed from the system ( $D = \infty$ ) is presented. The particle charge in this case ( $Q = 1450e$ ) coincides with other numerical MD [361] as well as PIC [331] simulations; moreover, this result also agrees to the model OML calculation for a particle levitating in the sheath region in the presence of the ion flow [247].

In Fig. 37, the surface plots of the ion density  $n_i$  normalized to  $n_{i0} = N_i/L_x L_y L_z$ , for three different distances between the charged colloidal particles are presented: the first one (Fig. 37(a)) corresponds to the short distance of  $D = 0.25\lambda_{De}$ , the second one (Fig. 37(b)) is of order the electron Debye length:

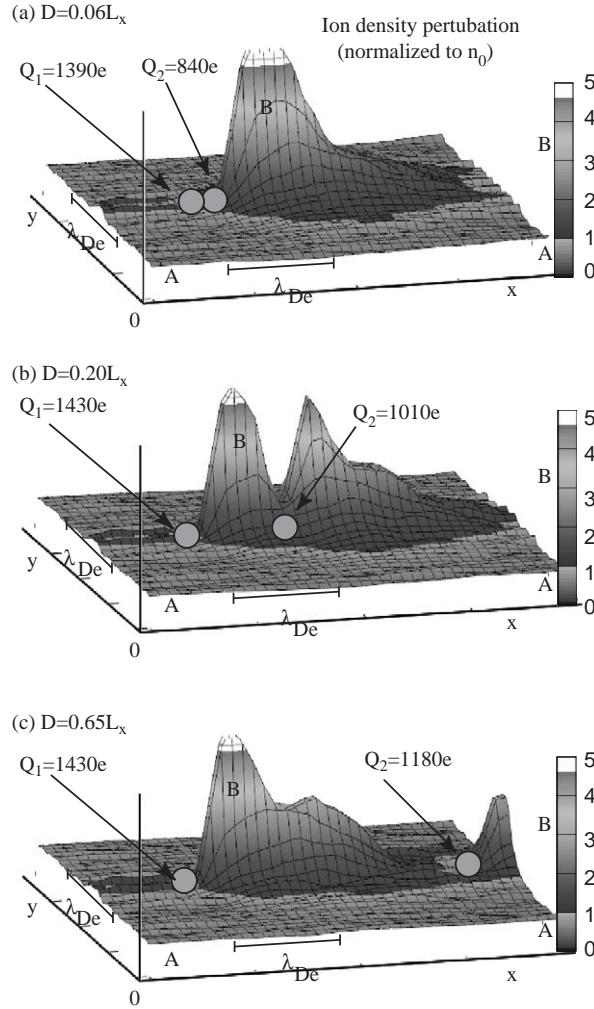


Fig. 37. Surface plot of the normalized ion density, showing ion focusing, for three different separations  $D$  between two dust grains. The plot is presented in the grayscale topograph style; regions A correspond to the normalized (to the unperturbed ion density  $n_{i0}$ ) ion densities below 1, and regions B correspond to the normalized ion densities above 1. The distances are given in the units of the total length of the simulation box in the direction of the ion flow  $L_x \approx 4.1\lambda_{De}$  used in the calculation; the physical distance corresponding to the electron Debye length  $\lambda_{De}$  is also presented. Reprinted from Ref. [332].

$D = 0.82\lambda_{De}$ , and the third one (Fig. 37(c)) corresponds to the relatively large distance exceeding the electron Debye length:  $D = 2.7\lambda_{De}$ . For better visualization, parts of the simulation volume where  $n_i/n_{i0} < 1$  and  $n_i/n_{i0} > 1$ , respectively, are presented in the (grayscale) topograph style, i.e. part A is for  $n_i/n_{i0} < 1$  and part B is for  $n_i/n_{i0} > 1$ , so that the change from lower (with respect to  $n_{i0}$ ) to higher densities is clearly seen. A strong ion focus is formed at the distance of a fraction of the electron Debye length behind the first dust grain; depending on the position of the second grain, the wake maxima are either combined, see Fig. 37(a), or clearly separated, see Fig. 37(c).

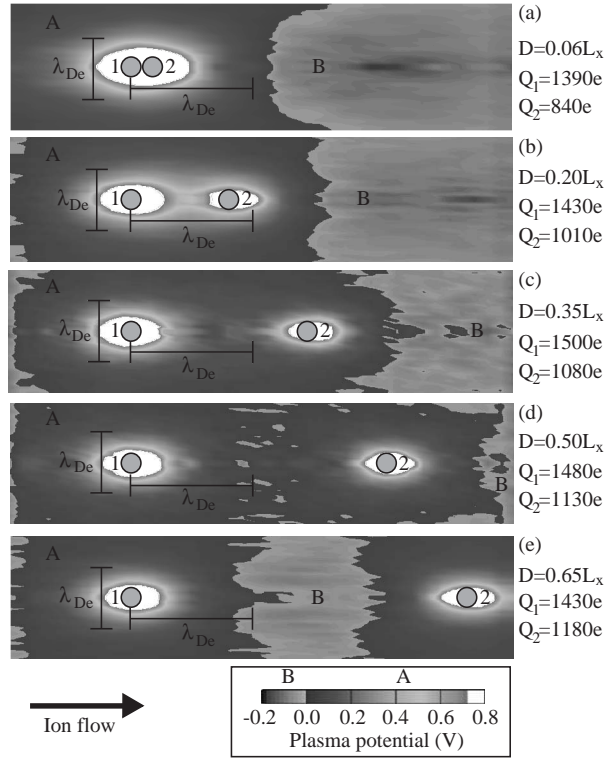


Fig. 38. Contour plot of the plasma potential for five different distances between two dust grains. The plot is presented in the greyscale topograph style. Note that the potential well (region B) is formed behind the dust grain and starts to form between the grains when the separation exceeds the electron Debye length. Reprinted from Ref. [332].

Fig. 38 gives the contour plot of the plasma potential (in V) for five different distances between the grains: (a) corresponds to a short distance which is much less than the electron Debye length,  $D=0.25\lambda_{De}$ , (b) is for the increased distance  $D=0.82\lambda_{De}$ , (c) is for  $D=1.43\lambda_{De}$ , (d) is for  $D=2.1\lambda_{De}$ , and (e) is for a distance relatively large with respect to the electron Debye length  $D=2.7\lambda_{De}$ . For short distances (Figs. 38(a) and 38(b)), the wake is almost the same as that of one (combined) particle; on the other hand, for distances of the order of (Fig. 38(d)), or more than (Fig. 38(e)) the electron Debye length, the formation of quasi-wake features can be seen after the first grain, i.e., before the second one. The characteristic distance for the region of the attractive potential to appear in the  $x$ -direction is of the order of the electron Debye length, thus coinciding with the linear theory [254].

To conclude this section, we stress that the ion wake strongly influences the charge of the second grain located downstream with respect to the first particle. This influence is especially strong for the intergrain distances small compared to the electron Debye length. It is interesting that there is also an influence of the downstream particle on the charge of the particle located upstream; this influence, however, is limited to distances of the order of the electron Debye length, in agreement with the Debye approximation. The charge of the second particle, for the distances considered (up to four



electron Debye lengths), is always less than the charge of the first particle, and this is attributed to the long-range influence of the plasma wake. The simulated plasma electron and ion densities as well as their cross-sections provide details of the corresponding distributions within and outside the wake. Finally, we note that in Ref. [333], MD simulations of the wake behind two particles aligned perpendicular to the ion flow were presented.

## 7. Collective plasma waves in open complex plasma systems

From the previous parts of this review we recall that the presence of highly charged dust particles can significantly affect a multi-component ionized gas system since the dust carries a considerable proportion of the total negative charge of the plasma. In particular, most of collective phenomena in such plasmas are affected by the dust. Since the charge on fine particles, being determined by the plasma currents, is not constant and varies in time and space, a principally new channel of wave dissipation due to the excitation of purely damped oscillations originating due to the dust charge relaxation process appears [10,12]. The dust-charge fluctuations take their origin from instantaneous modifications of the charging currents and the plasma modes become coupled to the dust charge fluctuations. This opens up an extra power loss channel and complements the variety of collisional effects in dusty plasmas, the latter include but are not limited to collisions between the electrons and ions, neutrals, or other electrons, as well as the elastic and inelastic (the dust-charging) collisions between the electrons and the dust. These processes exist in most complex plasma systems, which are usually of low temperature and partially ionized. In fact, the dust-charge fluctuations are themselves closely associated with the ionization and diffusion/recombination; these processes maintain the averaged background particle number densities self-consistently by dynamically acting as sources and sinks. The dynamic balance between the particle sources and sinks also defines the equilibrium, or steady, state of the entire plasma discharge, where the wave process in question develops. From the point of view of plasma waves and oscillations, the effects originating due to dust charging (and, e.g., the electron capture) result in the changes of the effective wave damping. The latter are normally much higher than in the constant dust charge case. In Section 7.1, by considering the basics of the dust charging, we demonstrate that this process can be regarded as a new channel of the wave power dissipation. In Sections 7.2–7.5 it will be shown, on several examples for the wave processes developing at electron, ion, and dust time scales, that the above dissipative processes lead to a net damping of the plasma collective waves and significantly affect the common plasma instabilities in typical complex plasma systems.

### 7.1. Dust charging—a new channel of wave dissipation

Here, we revisit the basics of the dust charging process discussed in Section 4.1 and reveal that this process opens up a new and unusual channel of power dissipation in a number of collective waves and oscillations in complex plasma systems. Let us consider the basic charging equation

$$\frac{dQ}{dt} = I(q) ,$$

where  $Q$  is the charge residing on a dust grain, and the current  $I$  on the dust particle is a sum of electron and ion plasma currents. In the state of equilibrium, we have

$$I^{\text{eq}}(Q^{\text{eq}}) \equiv I_e^{\text{eq}}(Q^{\text{eq}}) + I_i^{\text{eq}}(Q^{\text{eq}}) = 0 .$$

The charging dissipative process is characterized by the charging frequency  $\nu_d$

$$\nu_d \equiv - \frac{\partial I(Q)}{\partial Q} \bigg|_{Q=Z_d e} = \frac{1}{\sqrt{2\pi}} \frac{\omega_{pi}^2 a}{v_{Ti}} \left( 1 + \frac{T_i}{T_e} + \frac{Z_d e^2}{a T_e} \right) , \quad (7.1)$$

which is a characteristic of the process of charging of the dust particles when the deviations from the equilibrium are small. Naturally, Eq. (7.1) contains contributions from both the plasma electrons and ions. Comparison of rate (7.1) with the plasma collision frequencies reveals that the charging process is one of the most important dissipative process in complex (dusty) plasmas. Another characteristic is the rate of capture of the plasma electrons by the dust grains:

$$\nu_{ed}^{\text{eq}} = \nu_d \frac{n_d}{n_e} \frac{a T_e}{e^2} \left( \frac{T_i}{T_e} + \frac{Z_d e^2}{a T_e} \right) \left( 1 + \frac{T_i}{T_e} + \frac{Z_d e^2}{a T_e} \right)^{-1} , \quad (7.2)$$

which is particularly important when the ion contribution can be neglected [12].

The kinetic theory of dusty plasmas with variable charges on fine particles has been developed [12,366] by involving the dust charge as an additional dynamic variable. Specifically, introducing the distribution function of dust grains

$$f_d = f_d(q, \mathbf{r}, t) ,$$

where the electrostatic charge  $q$  is included as an additional independent variable. The first momentum of the distribution function

$$n_d = \int f_d \, dq = \text{const} , \quad (7.3)$$

gives the density of dust particles, and

$$Q = \frac{1}{n_d} \int q f_d \, dq \quad (7.4)$$

is the averaged charge on a dust grain. The corresponding kinetic equation can be written as

$$\frac{\partial f_d}{\partial t} + \frac{\partial}{\partial q} I(q) f_d = 0 , \quad (7.5)$$

where it was assumed that the grains have infinite masses and, hence their velocity is negligible ( $v_d = 0$ ). The next momentum of the distribution function

$$J = \frac{1}{n_d} \int I(q) f_d \, dq \quad (7.6)$$

yields the averaged current flowing onto the particle surface. From (7.4) and (7.6) it is easily seen that

$$\frac{dQ}{dt} = J(Q) , \quad (7.7)$$

which in the equilibrium state transforms to

$$J(Q = -Z_d e) = 0, \quad (7.8)$$

where the equilibrium state is described by the equilibrium distribution function  $f_d^{\text{eq}}$  of charges on dust particles.

The corresponding kinetic equations for the electrons or ions taking into account charging collisions is given by

$$\frac{\partial f_\alpha}{\partial t} + \mathbf{v} \cdot \frac{\partial f_\alpha}{\partial \mathbf{r}} + \frac{e_\alpha}{m_\alpha} \left[ \mathbf{E} + \left( \frac{\mathbf{v}}{c} \times \mathbf{B} \right) \right] \cdot \frac{\partial f_\alpha}{\partial \mathbf{v}} = - \int \sigma_\alpha v f_d f_\alpha d\mathbf{q},$$

where  $f_\alpha$  is the electron/ion distribution function. In the equilibrium state, one has the equilibrium electron (ion) distribution  $f_\alpha^{\text{eq}}$ .

Now, introducing (small) perturbations of the above distribution functions

$$f_d = f_d^{\text{eq}} + \delta f_d, \quad f_\alpha = f_\alpha^{\text{eq}} + \delta f_\alpha,$$

where  $|\delta f_d| \ll |f_d|$ ,  $|\delta f_\alpha| \ll |f_\alpha|$ , and assuming that the capture of electrons and ions by the dust particles is compensated (in the zero-order approximation) by external sources, one can linearize kinetic equations (7.5) and (7.6) with respect to these perturbations and obtain the following equation

$$\frac{\partial \delta f_d}{\partial t} + \frac{\partial}{\partial q} [I^{\text{eq}}(q) \delta f_d] + \frac{\partial}{\partial q} [\delta I(q) f_d^{\text{eq}}] = 0, \quad (7.9)$$

for the dust particle distribution function, where

$$I(q) = I^{\text{eq}}(q) + \delta I(q), \quad \int I^{\text{eq}}(q) f_d d\mathbf{q} = 0, \quad \delta I(q) = \sum_\alpha \int d\mathbf{v} e_\alpha \sigma_\alpha v \delta f_\alpha. \quad (7.10)$$

For the electron (ion) distributions one obtains

$$\frac{\partial \delta f_\alpha}{\partial t} + \mathbf{v} \cdot \frac{\partial \delta f_\alpha}{\partial \mathbf{r}} + \frac{e_\alpha}{m_\alpha} \left[ \mathbf{E} + \left( \frac{\mathbf{v}}{c} \times \mathbf{B} \right) \right] \cdot \frac{\partial f_\alpha^{\text{eq}}}{\partial \mathbf{v}} = -v_{\alpha d}^{\text{eq}} \delta f_\alpha - \delta v_{\alpha d} f_\alpha^{\text{eq}}, \quad (7.11)$$

where  $v_{\alpha d}$  is the rate of electron (ion) capture,

$$v_{\alpha d}^{\text{eq}} = \int \sigma_\alpha v f_d^{\text{eq}} d\mathbf{q}, \quad \delta v_{\alpha d} = \int \sigma_\alpha v \delta f_d d\mathbf{q}. \quad (7.12)$$

After Fourier-transform

$$A_{\mathbf{k}\omega} = \frac{1}{(2\pi)^4} \int A(\mathbf{r}, t) \exp(-i\mathbf{k} \cdot \mathbf{r} + i\omega t) d\mathbf{r} dt,$$

one finds from (7.11) that

$$\delta f_{\alpha, \mathbf{k}\omega} = \frac{-i}{\omega - \mathbf{k} \cdot \mathbf{v} + i v_{\alpha d}^{\text{eq}}} \left\{ \frac{e_\alpha}{m_\alpha} \left[ \mathbf{E}_{\mathbf{k}\omega} + \left( \frac{\mathbf{v}}{c} \times \mathbf{B}_{\mathbf{k}\omega} \right) \right] \cdot \frac{\partial f_\alpha^{\text{eq}}}{\partial \mathbf{v}} + \int \sigma_\alpha v \delta f_{d, \mathbf{k}\omega} d\mathbf{q} \right\}. \quad (7.13)$$

Now, Eq. (7.9) can be integrated over the charge domain to obtain

$$\int \delta f_d dq = 0 , \quad (7.14)$$

which is consistent with  $n_d = \text{const.}$  Furthermore, one can multiply (7.9) by  $q$  and integrate over  $q$  to find

$$\begin{aligned} -i\omega n_d \delta Q_{k\omega} &= \int I^{\text{eq}}(q) \delta f_{d,k\omega} dq + \int \delta I(q)_{k\omega} f_d^{\text{eq}} dq \\ &= -v_d^{\text{eq}} n_d \delta Q_{k\omega} + \int \delta I(q)_{k\omega} f_d^{\text{eq}} dq , \end{aligned} \quad (7.15)$$

where  $v_d^{\text{eq}}$  is the charging frequency (7.1). To obtain the last expression in the r.h.s. of (7.15), the particular dependence of the cross-section  $\sigma$  on  $v$  was used [12]. Therefore, the last equality of (7.15) is correct only for those  $\sigma$  which are linear functions of  $v$ .

To calculate the last term in the r.h.s. of (7.15), the perturbed charging current  $\delta I(q)$  can be split into the two parts

$$\delta I(q) = \delta I^{(1)}(q) + \delta I^{(2)}(q) ,$$

where

$$\delta I_{k\omega}^{(1)}(q) = \sum_{\alpha} \int d\mathbf{v} \frac{-ie_{\alpha} \sigma_{\alpha} v}{\omega - \mathbf{k} \cdot \mathbf{v} + i\nu_{\alpha d}^{\text{eq}}} \left\{ \frac{e_{\alpha}}{m_{\alpha}} \left[ \mathbf{E}_{k\omega} + \left( \frac{\mathbf{v}}{c} \times \mathbf{B}_{k\omega} \right) \right] \cdot \frac{\partial f_{\alpha}^{\text{eq}}}{\partial \mathbf{v}} \right\} ,$$

and

$$\begin{aligned} \delta I_{k\omega}^{(2)}(q) &= \sum_{\alpha} \int d\mathbf{v} \frac{-ie_{\alpha} \sigma_{\alpha} v}{\omega - \mathbf{k} \cdot \mathbf{v} + i\nu_{\alpha d}^{\text{eq}}} \int \sigma_{\alpha}(q') v \delta f_{d,k\omega}(q') dq' \\ &= n_d \delta Q_{k\omega} \sum_{\alpha} \int d\mathbf{v} \frac{-ie_{\alpha} \sigma_{\alpha} \sigma'_{\alpha} v^2 f_{\alpha}^{\text{eq}}}{\omega - \mathbf{k} \cdot \mathbf{v} + i\nu_{\alpha d}^{\text{eq}}} , \end{aligned} \quad (7.16)$$

where

$$\sigma'_{\alpha} \equiv \frac{\partial \sigma_{\alpha}(q)}{\partial q} = \text{const}(q) . \quad (7.17)$$

In deriving the last equality in the r.h.s. of (7.16), we again have used the linear dependence of  $\sigma$  on  $v$ . This is the reason for the factor  $\sigma'$  [given by Eq. (7.17)] to appear in Eq. (7.16).

Thus, for the perturbation of the averaged charge on dust grains one obtains

$$\delta Q_{k\omega} = \frac{-i}{\omega + i\nu_d^{\text{eq}}} \frac{1}{n_d G_{k\omega}} \int \delta I_{k\omega}^{(1)}(q) f_d^{\text{eq}} dq , \quad (7.18)$$

where the factor  $G_{k\omega}$  in (7.18) is given by

$$G_{k\omega} = -1 + \frac{n_d}{\omega + i\nu_d^{\text{eq}}} \sum_{\alpha} \int d\mathbf{v} \frac{e_{\alpha} \sigma_{\alpha}^{\text{eq}} \sigma'_{\alpha} v^2 f_{\alpha}^{\text{eq}}}{\omega - \mathbf{k} \cdot \mathbf{v} + i\nu_{\alpha d}^{\text{eq}}}$$

$$= -1 + \frac{1}{\omega + i\nu_d^{\text{eq}}} \sum_{\alpha} \int d\mathbf{v} \frac{\nu_{\alpha d}^{\text{eq}} e_{\alpha} \sigma'_{\alpha} v f_{\alpha}^{\text{eq}}}{\omega - \mathbf{k} \cdot \mathbf{v} + i\nu_{\alpha d}^{\text{eq}}} , \quad (7.19)$$

and we have used (7.12),

$$\sigma_{\alpha}^{\text{eq}} = \frac{1}{n_d} \int \sigma_{\alpha}(q) f_d^{\text{eq}} dq = \sigma_{\alpha}(q) \Big|_{q=Q^{\text{eq}}} ,$$

and  $Q^{\text{eq}} = -Z_d e$  is the equilibrium charge of a dust particle.

Finally, for the linear perturbation of the electron (ion) distribution function one finds

$$\begin{aligned} \delta f_{\alpha, \mathbf{k}\omega} = & -\frac{ie_{\alpha}/m_{\alpha}}{\omega - \mathbf{k} \cdot \mathbf{v} + i\nu_{\alpha d}^{\text{eq}}} \left[ \mathbf{E}_{\mathbf{k}\omega} + \left( \frac{\mathbf{v}}{c} \times \mathbf{B}_{\mathbf{k}\omega} \right) \right] \cdot \frac{\partial f_{\alpha}^{\text{eq}}}{\partial \mathbf{v}} \\ & - \frac{1}{G_{\mathbf{k}\omega}} \frac{1}{\omega + i\nu_d^{\text{eq}}} \frac{\sigma'_{\alpha} v f_{\alpha}^{\text{eq}}}{\omega - \mathbf{k} \cdot \mathbf{v} + i\nu_{\alpha d}^{\text{eq}}} \int \delta I_{\mathbf{k}\omega}^{(1)}(q) f_d^{\text{eq}} dq . \end{aligned} \quad (7.20)$$

Expressions (7.18) and (7.20) contain all the necessary information for further calculation of the linear dielectric permittivity and other parameters of dusty plasmas with variable charges on fine particles. The resulting dielectric functions feature the imaginary parts related to the grain charging process and do not persist in the constant dust charge approximation.

## 7.2. Langmuir waves

In this section, we consider propagation of Langmuir waves in a self-consistent closed system that includes a nonisothermal plasma and fine particles with a variable charge. Following the original work [367], we take into account the dust charge relaxation process, the plasma ionization and recombination, as well as the collisional dissipation and show that the otherwise unstable coupling of the Langmuir and dust-charge relaxation modes becomes stable and the Langmuir waves become frequency-downshifted. In the absence of the ionization, recombination and collisional dissipation, it was found [368] that Langmuir waves can be unstable because of their coupling to the dust charge relaxation process. The problem of linear Langmuir wave propagation in nonisothermal dusty plasmas with dust charge variation as well as the collisional effects has also been reconsidered [367]. It was also shown that these dissipative processes lead to a net damping of the Langmuir waves in typical dusty plasma systems.

In Ref. [367], propagation of linear Langmuir waves in a nonisothermal ( $T_e \gg T_i$ , where  $T_e$  and  $T_i$  are the electron and ion temperatures) plasma was considered. The size of the dust grains was assumed to be much less than the inter-grain distance, the electron Debye radius, as well as the wavelength, so that they can be treated as heavy point masses. The charge of a dust grain varies because of the microscopic electron and ion currents flowing onto the grain due to the potential difference between the dust surface and the adjacent plasma. The dust particles were treated as an immobile background since the time scale of charge variation is much smaller than that of the dust motion [366].

Equations describing the propagation of Langmuir waves are

$$\partial_t n_e + \nabla \cdot (n_e \mathbf{v}_e) = S , \quad (7.21)$$

$$\partial_t \mathbf{v}_e + v_{\text{eff}} \mathbf{v}_e = (e/m_e) \nabla \varphi - \gamma_e v_{Te}^2 \nabla n_e / n_{e0} , \quad (7.22)$$

$$\nabla^2 \varphi = -4\pi e (Z_i n_i - n_e - |Z_d| n_d) , \quad (7.23)$$

where  $\varphi$  is the electrostatic potential,  $m_j$ ,  $n_j$  (including the stationary value  $n_{0j}$ ), and  $\mathbf{v}_j$  are the mass, density, and fluid velocity of the species  $j = e, i, d$  for electron, ion, and dust grains, respectively. Furthermore,  $Z_i e$  and  $-|Z_d|e$  are the charges of the ions and dust particles,  $\gamma_e$  is the adiabatic constant, and  $v_{Te} = (T_e/m_e)^{1/2}$  is the electron thermal velocity. Likewise,  $S = -v_{ed}n_e + v_i n_e - \beta_r n_e^2 + \beta_{si} n_e^2 + \nabla \cdot (D_a \nabla n_e)$ , where  $v_{ed}$  is the collection rate of the plasma electrons by the dust grains,  $v_i$  is the ionization rate,  $\beta_r$  is the volume recombination rate,  $\beta_{si}$  is the step-wise ionization rate, and  $D_a$  is the ambipolar diffusion coefficient. The effective electron collision frequency is  $v_{\text{eff}} = v_e + v_e^{\text{el}} + v_e^{\text{ch}}$ , where  $v_e$  is the rate of electron collisions with the neutrals and plasma particles,  $v_e^{\text{el}}$  is the rate of elastic (Coulomb) electron–dust collisions, and  $v_e^{\text{ch}}$  is the effective rate of collection of the plasma particles by the dust.

Following Ref. [367], we shall assume that the wave perturbations behave like  $\sim \exp[i(kz - \omega t)]$  and use the Orbit Motion Limited model for the dust charging (see Section 4.1). In the absence of the perturbations, the system is assumed quasi-neutral. For Langmuir waves, the contribution of the perturbed (by the wave process) ion current  $I_{i1}$  is negligible with respect to the perturbed electron one  $I_{e1}$ , since it is on the slower ion time scale. The perturbed dust charge can then be described by

$$d_t q_{d1} + v_{\text{ch}} q_{d1} = -|I_{e0}| n_{e1} / n_{e0} , \quad (7.24)$$

where  $v_{\text{ch}} = a\omega_{pi}^2 \mathcal{A} / \sqrt{2\pi} v_{Ti}$  is the charging rate of the dust particle defined by the equilibrium electron and ion microscopic currents (see Sections 4.1 and 7.1). Here,  $v_{Ti}$  is the ion thermal velocity,  $\tau = T_i / T_e$ ,  $\mathcal{A} = 1 + \tau + \mathcal{Z}$ , and  $\mathcal{Z} = Z_d e^2 / a T_e$ . The effective charging rate is  $v_e^{\text{ch}} = v_{\text{ch}} P_e (4 + \mathcal{Z})(\tau + \mathcal{Z}) / \mathcal{A} \mathcal{Z}$ , and the electron capture rate (7.2) at the grain surface is [12,366,369]:  $v_{ed} = v_{\text{ch}} P_e (\tau + \mathcal{Z}) / \mathcal{A} \mathcal{Z}$ , and  $P_e = Z_d n_{d0} / n_{e0}$ . The rate of elastic electron–dust collisions is [369]  $v_{el} = 4\sqrt{2\pi} Z_d^2 n_d e^4 \Lambda / 3m_e^2 v_{Te}^3$ , where  $\Lambda = \ln(\lambda_{De} / a)$  is the Coulomb logarithm. The expressions for the rate  $v_e$  of electron collisions as well as for  $v_i$ ,  $\beta_r$ ,  $\beta_{si}$  and  $D_a$  can be found in Ref. [370]. Eqs. (7.21)–(7.23) and (7.24) describe the coupling between the high-frequency electrostatic Langmuir waves and the dust charge relaxation process.

To determine the stationary electron plasma density it was assumed that the pressure is not too low, such that recombination losses prevail over diffusion losses. The last term in  $S$  can then be ignored. From (7.21) the lowest order (steady state) electron plasma density  $n_{e0} = (v_i - v_{ed}) / \beta_{\text{eff}}$  can then be obtained, where  $\beta_{\text{eff}} = \beta_r - \beta_{si}$ . We note that the ionization rate must be high enough such that  $v_i > v_{ed}$ , otherwise no self-consistent stationary state exists [367].

Linearizing with respect to the wave perturbations, and combining the above equations, we obtain the following dispersion relation of the Langmuir waves

$$D(\omega, k) = i\tilde{v} \frac{\omega + i v_{\text{eff}}}{\omega + i v_{\text{ch}}^*} \left[ \eta_{e0} + i \frac{n_{e0}}{n_{d0}} (\partial_{Z_d} v_{ed})_{Z_{d0}} \right] , \quad (7.25)$$

where  $D(\omega, k) = (\omega + i v_{\text{eff}}) \eta_{e0} - \omega_{pe}^2$ ,  $\eta_{e0} = \omega - i v_{ed} + i \xi_2 v_i - \gamma_e k^2 v_{Te}^2 / (\omega + i v_{\text{eff}})$ , and  $\xi_2 = 2 - \xi_1$ ,  $\omega_{pe}$  is the electron plasma frequency. Here, the two models, namely, that of a density-fluctuation



independent ionization rate, with  $\xi_1 = 0$ , and that of density-fluctuation dependent ionization rate, with  $\xi_1 = 1$ , are considered. Eq. (7.25) describes the linear coupling of the high-frequency Langmuir plasma waves with the dust charge relaxation process  $\omega = -iv'_{\text{ch}}$ . It can be solved numerically for any given set of parameters. We also note that if  $v_e^{\text{el}}$ ,  $v_e^{\text{ch}}$ ,  $v_{ed}$  and  $(\partial v_{ed}/\partial Z_d)_{Z_{d0}}$  are set to zero in (7.25), one recovers the coupling equation of Ref. [368].

It is instructive to estimate the effect of electron capture (by the dust grain) and dissipative collisions on the Langmuir waves. For this purpose it is convenient to make the Ansatz  $\omega \gg (v_{\text{eff}}, v_{ed}, v_{\text{ch}}^*)$ . Setting  $\omega = \omega_1 + \delta'_1 + i\delta''_1$ , where  $\omega_1^2 = \omega_{pe}^2 + \gamma_e k^2 v_{Te}^2$  one finds from (7.25)

$$\delta'_1 = -(\omega_{pe}^2 \tilde{v} \omega_1^2 - \mathcal{B}) \tilde{v} / 2\omega_1, \quad (7.26)$$

where  $\mathcal{B} = a^3 n_{i0} \omega_{pi}^2 \mathcal{A} / v_{\text{ch}}$ , and

$$2\delta''_1 = \omega_{pe}^2 \tilde{v} / \omega_1^2 - v_{\text{eff}} - \xi_2 v_i + v_{ed} + \tilde{v} v_{\text{eff}} \mathcal{B} / \omega_1^2, \quad (7.27)$$

so that the frequency of the Langmuir waves is down shifted, and the waves are damped by most of the collisional processes included here. In the absence of the latter processes, the first term in (7.27) remains and it leads to the Langmuir wave instability discussed earlier [368]. Although the rate  $v_{ed}$  of electron capture by the dust also has a positive sign, it is always smaller than the term  $-\xi_2 v_i$  involving the plasma ionization because  $v_i > v_{ed}$  (required by the existence condition for the stationary state) and  $\xi_2 > 1$ . For the charge relaxation, we let  $\omega = -iv_{\text{ch}}^* + i\delta_2$ . From (7.25) one then obtains

$$\delta_2 \omega^2 / \tilde{v} = 3k^2 v_{Te}^2 + (v_{\text{ch}}^* - v_{\text{eff}})(v_{\text{ch}}^* + \xi_2 v_i - v_{ed} - \mathcal{B}), \quad (7.28)$$

which shows that the dust charging rate is slightly reduced by the coupling with Langmuir waves.

One can now estimate the average dust charge and the dissipation parameters  $v_{\text{eff}}$ ,  $v_{ed}$ ,  $v_{\text{ch}}^*$  and  $\tilde{v}$  for typical dusty plasmas. The factor  $e\Delta\phi_g/T_e$ , which defines the average charge on a dust grain and can strongly affect the density ratio  $n_{d0}/n_{e0}$  through the quasineutrality condition, can be found from the condition of the zero total current flowing onto the grain in the absence of the high-frequency perturbations. For a typical dusty argon plasma, we have  $T_e \sim 10$  eV,  $T_i \sim 1$  eV,  $a \sim 5$   $\mu\text{m}$ ,  $n_{e0} \sim 5 \times 10^{10} \text{ cm}^{-3}$ , and  $n_{i0}/n_{e0} = 10$ . One then obtains  $e\Delta\phi_g/T_e = -1.71$ ,  $Z_{d0} = -6.12 \times 10^4$ , and  $n_{d0}/n_{e0} \approx 1.74 \times 10^{-4}$ . One can also show that the inequality  $\tilde{v} \ll \omega$ , where  $\tilde{v} = (v_{\text{eff}}, v_{ed}, v_{\text{ch}}^*, \tilde{v})$  represents the dissipative effects invoked here, is satisfied. In fact,  $\tilde{v} \sim 3 \times 10^7 - 5 \times 10^8 \text{ s}^{-1}$  and  $\omega \sim 10^{10} \text{ s}^{-1}$ , which validate the Ansatz.

It is also necessary to verify the existence condition  $v_i > v_{ed}$  for the stationary state with the equilibrium density  $n_{e0} = (v_i - v_{ed})/\beta_{\text{eff}}$ , which imposes the existence of the minimal electron temperature threshold, allowing for the stationary state to exist. Indeed, a decrease of  $T_e$  would lead to a decrease of the ionization rate, and hence the existence condition for the stationary state can be violated. We note that  $T_e^{\text{thres}}$  depends weakly on the ion density. Furthermore, the threshold is affected by the degree of ionization (an increase of  $n_{i0}/n_n$  would lead to a downshift of  $T_e^{\text{thres}}$ ), the dust size and charge ( $T_e^{\text{thres}}$  increases with  $a$  and  $Z_{d0}$ ), as well as by the amount of electrons in the system ( $T_e^{\text{thres}}$  increases when  $n_{e0}/n_{i0}$  decreases). Furthermore, the threshold temperature can be decreased in cases when multi-step ionization processes become important. For further details, the reader can be referred to the original article [367].

To conclude this section, we recall that if the ionization, recombination, and other dissipative processes are included, the linear coupling of the fluctuations and Langmuir waves leads to a damping and a frequency downshift of the waves. This result differs considerably from that where a uniform source is invoked to replace the electrons and ions lost to dust charging [368]. Thus, the actual ionization and recombination processes that maintain the total charge balance of a dusty plasma system can be important in investigations of other waves and instabilities in dusty plasmas (also occurring at much slower, ionic and dust time scales), which will be further evidenced in the following sections.

### 7.3. Ion–acoustic waves

We now discuss the key points of the self-consistent theory of ion-acoustic waves in dusty gas discharge plasmas with variable-charge dust particles [371]. The stationary state of the plasma and the dispersion and damping characteristics of the waves on the ionic temporal scales will also be determined. The major dissipative and plasma particle–dust interaction processes are accounted for in a manner similar to Section 7.2.

The effect of dust on acoustic waves in space and laboratory plasmas was studied by many authors (see e.g. [372–375]). However, most theoretical models consider dust-charge variation without properly taking into account the change of the plasma particle number density arising from their capture (and release) by the dust grains, as was discussed in Sections 7.1 and 7.2.

For the relatively high frequency Langmuir waves considered in Section 7.2, the ion motion is unimportant [367]. However, for the lower-frequency ion-acoustic waves (IAWs), a self-consistent theory should include a proper account of the ion dynamics. In this section, the effect of variable-charge dust grains on the propagation and damping of the ion-acoustic waves in gas discharge plasmas is reviewed following the original work [371], where the process is investigated self-consistently by including both electron and ion sub-systems with elastic and charging interactions and taking into account the overall particle balance.

Thus, the linear propagation of ion-acoustic waves in the plasma with finite electron ( $T_e$ ) and ion ( $T_i$ ) temperatures is concerned. Most of the basic assumptions are similar to the ones used in Section 7.2 and the basic set of equations is to be complemented by the following equations describing the balance and dynamics of the plasma ions:

$$\partial_t n_i + \nabla \cdot (n_i v_i) = -v_{id} n_i + v_{ion} n_e - \beta_{eff} n_e^2, \quad (7.29)$$

$$\partial_t v_i + v_i^{eff} v_i + \frac{T_i}{m_i n_i} \partial_x n_i = \frac{e}{m_e} E, \quad (7.30)$$

where  $E = -\nabla \varphi$  is the electric field of the ion-acoustic waves,  $\varphi$  is the electrostatic potential,  $m_i$  and  $n_i$  are the mass and number density of the ions, respectively. Other notations are similar to those used in Section 7.2. The effective frequency of ion collisions can be presented as  $v_i^{eff} = v_i + v_i^{el} + v_i^{ch}$ , where  $v_i = v_{in} + v_{ie}$  is the rate of ion collisions with the neutrals and plasma particles.

The relation between the electron/ion charging collisions is

$$v_e^{ch} = \frac{3}{2} v_i^{ch} \frac{n_{i0}}{n_{e0}} \frac{\alpha_1 \sigma_1}{T_i/T_e + \alpha_1} = v_d^{ch} \frac{\alpha_1 \gamma_1 \sigma_1}{\mathcal{A}}, \quad (7.31)$$

while the rate of electron and ion capture by the grains is given by

$$v_{ed} = \frac{n_{i0}}{n_{e0}} v_{id} = v_d^{\text{ch}} \frac{\alpha_1 \gamma_1}{\mathcal{A}}, \quad (7.32)$$

where  $\alpha_1 = \mathcal{A} - 1$ ,  $\gamma_1 = (Z_{d0} n_{d0} / n_{e0}) \varphi_e^{\text{th}} / \varphi_d^{\text{el}}$ , and  $\sigma_1 = 4 + \varphi_d^{\text{el}} / \varphi_e^{\text{th}}$ . Here,  $v_d^{\text{ch}} = a \omega_{pi}^2 \mathcal{A} / \sqrt{2\pi} v_{Ti}$  is the dust charging rate, and we have defined  $\mathcal{A} = 1 + (T_i / T_e) + (\varphi_d^{\text{el}} / \varphi_e^{\text{th}})$ ,  $\varphi_d^{\text{el}} = Z_d e / a$ ,  $\varphi_e^{\text{th}} = T_e / e$ ;  $v_{Ti} = (T_i / m_i)^{1/2}$  is the ion thermal velocity,  $\omega_{pi}$  is the ion plasma frequency.

The rates of the elastic electron– and ion–dust Coulomb collisions are

$$v_e^{\text{el}} = v_i^{\text{el}} \frac{T_i}{T_e} \frac{n_{i0}}{n_{e0}} \alpha_1 \exp\left(\frac{\varphi_d^{\text{el}}}{\varphi_e^{\text{th}}}\right) = \frac{2}{3} v_d^{\text{ch}} \frac{\alpha_1 \gamma_1 \mathcal{A}}{\mathcal{A}} \exp\left(\frac{\varphi_d^{\text{el}}}{\varphi_e^{\text{th}}}\right), \quad (7.33)$$

where  $\mathcal{A}$  is the Coulomb logarithm. The electron– and ion–neutral, electron–ion and ion–electron collision rates (also ionization and recombination) are standard and can be found e.g. in Refs. [237,370]. The equilibrium electron density  $n_{e0} = (v_{\text{ion}} - v_{ed}) / \beta_{\text{eff}}$  has the same form as in Section 7.2. For the equilibrium ion density, one obtains  $n_{i0} = (v_{ed} / v_{id}) n_{e0}$ . It is remarkable that the equilibrium electron and ion densities are different and are inversely proportional to the rates of electron and ion capture by dust. The same result follows from (7.32) and the overall charge neutrality condition.

The dispersion relation of the ion-acoustic waves in variable-charge plasmas is [371]

$$1 - i \frac{v_{ed}}{\omega + i \tilde{v}_d^{\text{ch}}} - \frac{\omega_{pe}^2}{\eta_e (\omega + i v_e^{\text{eff}})} - \frac{\omega_{pi}^2}{\eta_i (\omega + i v_i^{\text{eff}})} \left( 1 - i \frac{Z_d n_{d0}}{n_{i0}} \frac{v_{ed}}{\omega + i \tilde{v}_d^{\text{ch}}} \right) (1 - i \mathcal{G}) = 0, \quad (7.34)$$

where

$$\mathcal{G} = \frac{n_{e0}}{n_{i0}} \frac{m_i}{m_e} \frac{\omega + i v_i^{\text{eff}}}{\omega + i v_e^{\text{eff}}} \frac{2v_{ed} - v_{\text{ion}}}{\eta_e},$$

$\eta_e = \omega + i(v_{\text{ion}} - v_{ed}) - k^2 v_{Te}^2 / (\omega + i v_e^{\text{eff}})$ , and  $\eta_i = \omega + i v_{id} - k^2 v_{Ti}^2 / (\omega + i v_i^{\text{eff}})$ .

In the absence of the dissipation and the dust-charge variation we have from (7.34)  $\omega = k v_{\text{SD}}$ , where  $v_{\text{SD}} = \sqrt{(T_e / m_i)(n_{i0} / n_{e0}) + T_i / m_i}$  is the ion-acoustic speed in a dissipationless plasma with the constant-charge dust particles. If  $k^2 v_{Te}^2 \gg [\omega^2, v_e^{\text{eff}}(v_{\text{ion}} - v_{id})]$ , which is usually valid for ion-acoustic waves, from (7.34) follows

$$\begin{aligned} & (\omega + i \tilde{v}_d^{\text{ch}}) \{ (\omega + i v_i^{\text{eff}})(\omega + i v^*) - k^2 v_{\text{SD}}^2 \} \\ & = -i \frac{v_{ed} Z_d n_{d0}}{n_{i0}} [k^2 (v_{\text{SD}}^2 - v_{Ti}^2) + i(2v_{ed} - v_{\text{ion}})(\omega + i v_i^{\text{eff}})], \end{aligned} \quad (7.35)$$

where  $v^* = v_{id} + v_{\text{ion}} - 2v_{ed}$ . If the dust-charging terms and the usual electron– and ion–neutral collisions are retained only in (7.35), one obtains the coupling equation similar to that for the ion-acoustic surface waves [375].

To solve the dispersion relation (7.35), it was assumed that the wave frequency is real and a complex wave number  $k = k' + i k''$  was derived [371]. This solution is valid when the frequency

of the ion-acoustic waves is of the order of or less than the capture rate of the plasma electrons by the dust grains.

For high frequencies ( $\omega \gg v_{ed} Z_d n_{d0} / n_{i0}$ ), relation (7.35) describes the coupling of the ion-acoustic waves and the dust-charge relaxation process. One can then obtain the two equations, namely  $D_1(\omega, k) = (\omega + i v_i^{\text{eff}})(\omega + i v^\star) - k^2 v_{SD}^2 = 0$  for the ion-acoustic waves, and  $D_2(\omega, k) = \omega + i \tilde{v}_d^{\text{ch}} = 0$  for the dust-charge relaxation process. The solution of the dispersion equation  $D_1(\omega, k) = 0$  is

$$\omega = -i \frac{v_i^{\text{eff}} + v^\star}{2} \pm \left[ k^2 v_{SD}^2 - \frac{(v_i^{\text{eff}} + v^\star)^2}{4} \right]^{1/2}, \quad (7.36)$$

which describes damped ion-acoustic waves in a low-temperature dusty plasma. From (7.36) it follows that propagating waves exist if  $k v_{SD} > (v_i^{\text{eff}} + v^\star)/2$ . The real and imaginary parts of the frequency are  $\omega'_{IA} = [k^2 v_{SD}^2 - (v_i^{\text{eff}} + v^\star)^2/4]^{1/2}$ , and  $\omega''_{IA} = -(v_i^{\text{eff}} + v^\star)/2$ . However, if  $k v_{SD} < (v_i^{\text{eff}} + v^\star)/2$ , the solution is purely damped. The coupling with the dust-charge relaxation process leads to the variation  $\delta\omega_{IA}$  of the IAW eigenfrequency

$$\delta\omega_{IA} = -i \frac{v_{ed}}{\omega_{IA} + i \tilde{v}_d^{\text{ch}}} \frac{Z_{d0} n_d}{n_{i0}} \frac{\mathcal{E}_{IA}}{2\omega'_{IA}}, \quad (7.37)$$

where  $\mathcal{E}_{IA} = k^2(v_{SD}^2 - v_{Ti}^2) + i(2v_{ed} - v_{ion})(\omega_{IA} + i v_i^{\text{eff}})$ . From (7.37) one can see that the coupling of IAWs to the dust-charge fluctuations leads to a frequency downshift and an increase of the damping decrement. The corresponding solution for the dust charge relaxation process is  $\omega_D = -i \tilde{v}_d^{\text{ch}} + \delta\omega_D$ , where

$$\delta\omega_D = i v_{ed} \frac{Z_{d0} n_d}{n_{i0}} \frac{\mathcal{B}}{\mathcal{D}},$$

$\mathcal{B} = k^2(v_{SD}^2 - v_{Ti}^2) + (2v_{ed} - v_{ion})(v_i^{\text{eff}} - \tilde{v}_d^{\text{ch}})$ , and  $\mathcal{D} = k^2 v_{SD}^2 + (v_i^{\text{eff}} - \tilde{v}_d^{\text{ch}})(v^\star - \tilde{v}_d^{\text{ch}})$ . We note here that the dust charge relaxation rate is reduced due to coupling with the ion-acoustic waves.

Expressions (7.28)–(7.37) describe propagation of ion-acoustic waves in a plasma with variable-charge colloidal particles for a wide range of parameters of interest. The frequency of the IAWs should not be too low, otherwise inclusion of temperature fluctuations and use of the full Braginski's equations for strongly collisional plasmas would be necessary [376]. This is especially true if the frequency of IAWs is less than the effective rate of ion collisions. Further details on the applicability of the above self-consistent theory to the experiments on low-frequency (in the ion frequency range) waves and instabilities in dusty plasmas [373] can be found in Ref. [371]. Finally, we note that the theory of the ion-acoustic waves reviewed in this section has recently been extended to multicomponent chemically active plasmas with negative ions [377].

#### 7.4. Dust-acoustic waves

In this section, we present a self-consistent theory of low-frequency dust-acoustic waves in low-temperature collisional plasmas containing variable-charge dust grains [13]. The generalized dispersion relation describing propagation and damping of the dust-acoustic waves is derived and analyzed.

The presence of the massive and highly charged dust particles introduces new processes such as charge relaxation as well as new, very long time scale phenomena associated with the dust motion.

In particular, a new low-frequency mode, namely the electrostatic dust-acoustic waves (DAWs), has been demonstrated theoretically and experimentally [213,373,378,379].

In the earlier studies on DAWs the constant-charge approximation was often used (see, e.g., [378]). In this approximation, DAWs are similar to ion acoustic waves propagating in multi-component plasmas with negative ions. However, the charge on a dust grain can vary according to the local plasma potential, and electrons and ions can be captured or released by the dust grain. There is thus a corresponding variation in the electron and ion densities. However, a realistic description of DAWs necessarily requires the inclusion of the electron/ion capture/release by the dust particles, as well as the relevant dissipative processes.

Following the original work [13], we now show that the DAWs can be strongly affected by the particle creation and loss mechanisms. Basic assumptions are similar to Sections 7.2 and 7.3, and the corresponding electron and ion balance/motion equations (with time-dependent terms dropped here due to much slower, dust motion time scales) are to be complemented by the following equations for the dust and neutrals:

$$\frac{\partial n_d}{\partial t} + \nabla \cdot (n_d v_d) = 0, \quad (7.38)$$

$$\frac{\partial v_d}{\partial t} + v_{dn}(v_d - v_n) + \frac{T_d}{m_d n_d} \frac{\partial n_d}{\partial x} = -\frac{Z_d e}{m_d} E, \quad (7.39)$$

$$\frac{\partial v_n}{\partial t} + v_{nd}(v_n - v_d) = 0, \quad (7.40)$$

where  $E = -\nabla \varphi$  is the electric field of the dust-acoustic waves,  $v_{dn} \approx 4m_n n_n a^2 v_{Tn}/m_d$  is the effective frequency of the dust–neutral collisions, and  $v_{Tn}$  is the thermal velocity of neutrals. The frequency of the neutral–dust collisions appearing in Eq. (7.40) is given by  $v_{nd} \approx (n_d m_d / n_n m_n) v_{dn}$ . Other electron/ion rates entering the basic set of equations for DAWs, are similar to those used in Sections 7.2 and 7.3. In the intermediate pressure range, when the plasma particle loss is predominantly controlled by the volume recombination, the equilibrium values of the electron/ion number densities appear to be the same as described in Sections 7.2 and 7.3.

The dispersion equation of the dust-acoustic waves can be written as follows [13]

$$\epsilon_{pd} + \frac{\omega_{pi}^2}{\eta_i} \zeta_1 + \frac{\omega_{pe}^2}{\eta_e} \zeta_2 = 0, \quad (7.41)$$

where  $\epsilon_{pd} = 1 - \omega_{pd}^2(\omega + i v_{nd})/\omega^2[\omega + i(v_{dn} + v_{nd})]$ ,  $\zeta_1 = 1 + n_{e0} v_{ed}/n_{i0} \tilde{v}_d^{\text{ch}}$ ,  $\zeta_2 = 1 + v_{ed}/\tilde{v}_d^{\text{ch}} - v_i^{\text{eff}} \zeta_1 (2v_{ed} - v_{\text{ion}})/\eta_i$ , and we have assumed  $T_d \ll T_i, T_e$ . Here,  $\eta_e = v_e^{\text{eff}}(v_{\text{ion}} - v_{ed}) + k^2 v_{Te}^2$ , and  $\eta_i = v_{id} v_i^{\text{eff}} + k^2 v_{Ti}^2$ . The three terms on the l.h.s. of (7.41) are the effective dielectric functions of the dust particles, electrons and ions, respectively.

From Eq. (7.41) one can obtain the DAW eigenfrequency  $\omega = \omega' + i\omega''$ , where

$$\omega' = \omega_{pd} \left( 1 + \frac{\omega_{pe}^2}{\eta_e} \zeta_2 + \frac{\omega_{pi}^2}{\eta_i} \zeta_1 \right)^{-1/2}, \quad (7.42)$$

$\omega'' = -v_{dn}/2$ , and it was assumed that  $\omega \gg v_{dn}, v_{nd}$ . The dispersion relation (7.41) also allows for simpler solutions in several limiting cases. For example, if  $k^2 v_{Te}^2 \gg v_e^{\text{eff}}(v_{\text{ion}} - v_{ed})$  and  $k^2 \lambda_{De}^2 \ll 1$ ,

it follows that

$$\frac{\omega'}{k} = \left( \frac{1}{m_d} \frac{n_{d0} Z_{d0}^2 T_e T_i \delta_1}{n_{e0} T_i \delta_1 \xi_2 + n_{i0} T_e \xi_1} \right)^{1/2}, \quad (7.43)$$

where  $\delta_1 = 1 + v_i^{\text{eff}} v_{id} / k^2 v_{Ti}^2$ . If  $k^2 v_{Ti}^2 \gg v_i^{\text{eff}} v_{id}$ , the expression (7.43) can be simplified by noting  $\delta_1 \approx 1$ . In the latter case, neglecting the effects of dust–charge relaxation as well as the ionization–recombination balance of the electrons and ions in dusty plasmas, i.e., letting  $\xi_{1,2} = 1$ , one can recover the DAW dispersion relation of Rao et al. [378]. In the strongly nonisothermal limit we obtain under the same conditions

$$\omega = k \left( \frac{n_{d0} Z_{d0}^2}{n_{i0}} \frac{T_i}{m_d} \right)^{1/2},$$

which is valid if  $T_e \gg T_i$ .

For long-wavelength DAWs satisfying  $k^2 \lambda_{De}^2 \ll v_e^{\text{eff}} (v_{\text{ion}} - v_{ed}) / \omega_{pe}^2$  and  $k^2 \lambda_{Di}^2 \ll v_i^{\text{eff}} v_{id} / \omega_{pi}^2$ , one can obtain  $\omega' = \omega_c$  for the real part of the frequency, where

$$\omega_c = \omega_{pd} \left[ 1 + \mathcal{B} + \frac{\omega_{pe}^2 \xi_2}{v_e^{\text{eff}} (v_{\text{ion}} - v_{ed})} \right]^{-1/2} \quad (7.44)$$

and  $\mathcal{B} = \omega_{pi}^2 \xi_1 / v_{id} v_i^{\text{eff}}$ . It is of interest to note that  $\omega_c$  is a (lower) cutoff frequency of the DAWs in the presence of sources/sinks and dissipation of ions and electrons. We note that usually  $\omega_{pe}^2 \gg v_e^{\text{eff}} (v_{\text{ion}} - v_{ed})$ , and the unity in (7.44) can be neglected. Thus, the cutoff frequency is much less than the dust plasma frequency, or

$$\frac{\omega_c}{\omega_{pd}} \sim \frac{[v_e^{\text{eff}} (v_{\text{ion}} - v_{ed})]^{1/2}}{\omega_{pe}} \ll 1, \quad (7.45)$$

which can be attributed to an imbalance of charge densities due to the creation and dissipation of the electrons and ions in the DAW motion.

Another interesting case is for  $k^2 v_{Te}^2 \gg v_e^{\text{eff}} (v_{\text{ion}} - v_{ed})$ , but  $k^2 v_{Ti}^2 \ll v_{id} v_i^{\text{eff}}$ . This situation is realized in e.g., strongly nonisothermal plasmas or plasmas with large ion mass (such as argon or potassium). Accordingly,

$$\omega' = \omega_{pd} \left( 1 + \mathcal{B} + \frac{\xi_2}{k^2 \lambda_{De}^2} \right)^{-1/2} \quad (7.46)$$

is the real part of the DAW frequency. Note that in Eqs. (7.42)–(7.46) the frequency of DAWs satisfies  $\omega < \omega_{pd}$  and  $\omega \ll k v_{Ti}$ .

Fig. 39 presents the dependence of the normalized eigenfrequency of the dust–acoustic waves on the normalized wavenumber in hydrogen plasma. For other parameter regimes the numerical DAW dispersion curves, as well as a general analytical solution of Eq. (7.41) in the wavenumber domain can be found in Ref. [13]. The numerical results suggest that the frequency of the DAWs increases with the electron-to-ion temperature ratio and that the lower cutoff is much lower in the heavy-ion (argon) plasma. In argon plasmas the above cutoff depends weakly on the electron-to-ion temperature



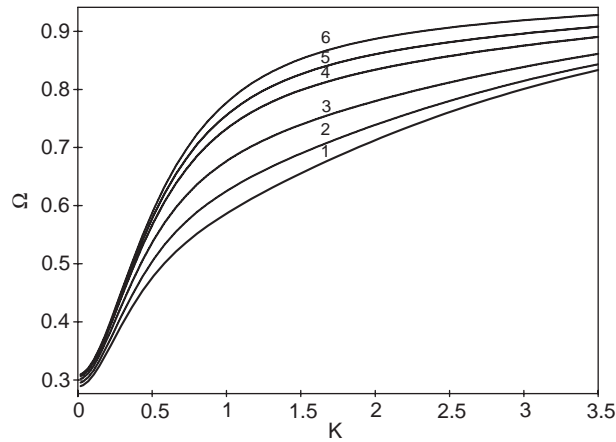


Fig. 39. Dependence of the non-dimensional frequency of the DAWs  $\Omega = \omega/\omega_{pd}$  on the non-dimensional wave number  $K = k\lambda_{De}$  in hydrogen plasmas for  $Z_{d0}n_{d0}/n_{e0} = 0.3$ ,  $v_{ed}/v_d^{\text{ch}} = 0.1$ ,  $v_{\text{ion}}/v_{ed} = 1.5$ ,  $v_e^{\text{eff}}/v_i^{\text{eff}} = 25$ ,  $v_i^{\text{eff}}/\omega_{pi} = 2$ , and  $v_{id}/\omega_{pi} = 0.5$ . Curves 1–6 correspond to  $T_e/T_i = 1.05, 1.5, 2.5, 5.0, 7.5$ , and  $12.5$ , respectively [13].

ratio. This is expected since the cutoff originates from the dynamical wave-induced charge imbalance for which the thermal motion of the ions plays a role.

In this model, the cutoff frequency (7.44) appears because of the charge imbalance of the light particles in the process of particle creation and momentum dissipation. We recall here that for low-frequency Alfvén waves in dusty plasmas a similar imbalance leads to uncompensated electron and ion Hall currents. The latter give rise to the low-frequency cutoff of the Alfvén wave dispersion [380]. Furthermore, we note that the model in question implies that the ionization source is unaffected by the wave oscillations.

### 7.5. Dust–acoustic and other instabilities

Here, we demonstrate how the open character of dust–plasma system affects the current-driven dust–acoustic wave instability in a collisional plasma with variable-charge fine particles. The instability thresholds affected by a number of particle source and sink, as well as numerous dissipative mechanisms, will be obtained following the original work [381]. In particular, it will be shown that the current-driven instability is relevant to dust cloud filamentation at the initial stages of void formation in dusty RF discharge experiments discussed in Section 5.2.

In many space and laboratory environments complex plasmas are affected by external DC electric fields, such as that in the sheath/pre-sheath regions, or that additionally introduced for electrode biasing, ion extraction, etc. In such cases the occurrence of directed plasma flows is unavoidable. The latter can give rise to current-driven instabilities which develop at the dust–acoustic [373,382,383] or dust–ion-acoustic [373,384] time scales.

As was shown above in Sections 7.1–7.4, the electron and ion capture/release by the dust grains, usually occurring at the same time scale as that of dust charge variation, can strongly affect various collective phenomena in dusty plasmas. On the dust–acoustic time scale, the effects mentioned can affect the dispersion properties and stability of the dust–acoustic waves. It has also been demonstrated

that ion drag on the dust grains is important for the instability and can lead to the formation of regions void of dust in the plasma (see Section 5.2). Below, we review the effects of plasma particle capture/release by the dust particles as well as the ion drag on the development of the current-driven instability at the dust–acoustic time scale and relate the results to void formation, dust cloud filamentation, and instabilities in low-temperature RF complex plasmas.

Consider a three-component plasma in an external DC electric field  $E_0\hat{x}$ . The external DC electric field causes the electrons and dust particles to drift with different velocities in a direction opposite to the ions. Here, we list only those of the fluid continuity and momentum equations that differ from the basic set of Section 7.3:

$$v_i \frac{\partial v_i}{\partial x} + v_i^{\text{eff}} v_i + \frac{T_i}{n_i m_i} \frac{\partial n_i}{\partial x} = \frac{e}{m_i} E, \quad (7.47)$$

$$\frac{\partial v_d}{\partial t} + v_d \frac{\partial v_d}{\partial x} + v_{dn} v_d + \frac{T_d}{n_d m_d} \frac{\partial n_d}{\partial x} + \mu_{\text{drag}}^i (v_d - v_i) = -\frac{Z_d e}{m_d} E, \quad (7.48)$$

$$\frac{\partial n_d}{\partial t} + \frac{\partial (n_d v_d)}{\partial x} = 0, \quad (7.49)$$

where  $E$  is the total electric field in the plasma including the steady-state (zero-order) field  $E_0$ , and other equations and notations are similar to the ones used in Sections 7.2–7.4. In (7.48) the term  $\mu_{\text{drag}}^i (v_d - v_i)$  corresponds to the ion drag force acting on dust particles. In the standard OML theory expressions for the microscopic ion currents on the dust particles, the contributions of the steady-state ion flow  $v_0 = eE_0/m_i v_i^{\text{eff}}$  has been accounted for. For the electrons, the thermal energy is much larger than the directed energy associated the steady electron flow  $v_{e0} = -eE_0/m_e v_e^{\text{eff}}$  due to the external field, so that the effect of the latter in the electron charging equation has been ignored.

In (7.48) there are two dissipative terms that affect the dust dynamics, namely the rate of dust–neutral collisions  $v_{dn} v_d$  of Section 7.3, and the ion drag term  $\mu_{\text{drag}}^i (v_d - v_i)$ , where

$$\mu_{\text{drag}}^i \sim 4m_i n_{0i} b_i^2 v_S / m_d,$$

is the ion drag coefficient,  $b_i \sim a\sqrt{\pi}(1 - \Delta\phi_g/T_i)$  is the ion-collection impact parameter (see Section 4.2), and  $v_S$  is the ion-acoustic velocity.

For the stationary dust drift velocity, one obtains

$$v_{d0} = -\frac{Z_{d0} e E_0 (1 - 1/\mathcal{A})}{m_d (v_{dn} + \mu_{\text{drag}}^i)}, \quad (7.50)$$

where  $\mathcal{A} = Z_{d0} m_i v_i^{\text{eff}} / m_d \mu_{\text{drag}}^i$ . Note that since  $v_{(i,e)}^{\text{eff}} > (v_{en}, v_{in})$  the magnitudes of the electron and ion drift velocities are lower than those under the constant charge approximation. The second term in (7.50) is responsible for the pushing of the dust particles in a direction opposite to the electric force acting on the negatively charged dust particles. Thus, if the ion drag is weak, the dust particles drift in the negative  $x$  direction, and if the ion drag is sufficiently strong, they drift in the opposite

direction. In particular, if  $\mathcal{A} > 1$ , the negatively charged dust particles drift in the same direction as the plasma electrons. Otherwise the dust particles and electrons drift in the opposite directions.

The dispersion relation of the unstable dust–acoustic mode can be presented as [381]

$$\begin{aligned} & \frac{\omega_{pe}^2}{\eta_e v_e^{\text{eff}}} \left( 1 + \frac{v_{ed}}{v_d^{\text{ch}}} \right) + \frac{\omega_{pi}^2}{\eta_i v_i^{\text{eff}}} \left( 1 + \frac{n_{e0} v_{ed}}{n_{i0} v_d^{\text{ch}}} \right) \\ & + \frac{i\omega_{pd}^2}{\Omega_{d0}[\Omega_{d0} + i(v_{dn} + \mu_{\text{drag}}^i)]} \left( 1 - \frac{\Omega_{i0} + i v_{id}}{\eta_i \mathcal{A}} \right) = 0, \end{aligned} \quad (7.51)$$

where  $\Omega_{e0} = \Omega_{d0} - k\vartheta_e$ ,  $\Omega_{i0} = \Omega_{d0} - k\vartheta_i$ ,  $\vartheta_e = v_{e0} - v_{d0}$ , and  $\vartheta_i = v_{i0} - v_{d0}$ . Here,  $\eta_e = \Omega_{e0} + i(v_{\text{ion}} - v_{ed} + k^2 v_{Te}^2 / v_e^{\text{eff}})$  and  $\eta_i = \Omega_{i0} + i(v_{id} + k^2 v_{Ti}^2 / v_i^{\text{eff}})$ .

In the limiting case of negligible dust-specific electron and ion dissipation (by formally setting  $v_{(i,e)}^{\text{eff}} \rightarrow v_{(i,e)n}$  and  $v_{(i,e)d} \rightarrow 0$ ), dust–charge variations ( $v_d^{\text{ch}} \rightarrow 0$ ), as well as the ion drag force ( $\mu_{\text{drag}}^i \rightarrow 0$ ), the dispersion relation (7.51) is reduced to Eq. (7) of Ref. [382]. The analytical solutions for the frequency of the unstable mode can be obtained in the case when the equilibrium density of the ions much exceeds that of the electrons ( $n_{i0} \gg n_{e0}$ ). This may happen at the initial stage of the filamentary mode development [233], when the charge density  $Z_{d0} n_{d0}$  of the dust particles constitutes a significant proportion of total plasma negative charge density.

Letting  $\Omega_d = \Omega'_d + i\Omega''_d$  and separating the real and imaginary parts of (7.51), one can obtain

$$\Omega''_d = -\frac{v_{dn}}{2} \left[ 1 + \mathcal{B} \left( 1 - \frac{k v_i}{\Omega'_d} \right) + \frac{\mu_{\text{drag}}^i}{v_{dn}} \frac{k \vartheta_i}{\Omega'_d} \right] \quad (7.52)$$

for the imaginary part of the frequency in a dust frame, where  $\mathcal{B} = Z_{d0} m_i v_i^{\text{eff}} / m_d v_{dn}$ . It is seen from (7.52) that there is no instability if  $k\vartheta_i < \Omega'_d$ . If, however, the relative ion-to-dust drift in the external electric field is such that  $\vartheta_i > \Omega'_d/k$ , the instability of the dust–acoustic waves becomes possible.

The condition for the instability strongly depends on the direction of the stationary dust drift in the external electric field (7.50). As already mentioned, one can see that the dust grains drift in the direction of the electric force (opposite to the ion drift) when the inequality  $\mathcal{A} > 1$  is satisfied. This means that the effect of the steady electric force on the dust particles overcomes that of the ion drag force. If the opposite inequality holds, the dust grains are pushed by the ion drag force and move in the same direction with the ions. Note that the inequality varies continuously when the fine particles are growing (see Sections 2.1–2.3). It is possible that  $\mathcal{A} > 1$  is satisfied for initially small grains, and when the grains becoming sufficiently large the condition becomes eventually violated. The two relevant cases of the weak and strong ion drag are considered in detail in Ref. [381].

We now examine the conditions for the current-driven dust–acoustic instability derived in Ref. [381]. One can see that the terms in (7.52) leading to the instability are proportional to the effective frequency of the ion collisions. This means that the ion collisions have a destabilizing effect on the dust–acoustic waves. It is worth mentioning that the electron–neutral collisions in a dust-free plasma lead to resistive ion–acoustic instability in a similar manner. We emphasize that the competition between the electrostatic and ion drag forces on dust grains strongly affects the conditions for the instability. The ratio of these forces is  $\mathcal{A}$ , which can be greater or less than unity. In fact, as shown in Ref. [381], this ratio has a rather broad range from  $\sim 10^{-4}$  to  $\sim 2.5 \times 10^4$ .

The conditions for the instability strongly depend on the value of parameter  $\mathcal{B}$ . If it is small compared with unity but still large compared with  $\mu_{\text{drag}}^i/v_{dn}$ , then the relative ion-to-dust drift should be large such that  $\vartheta_i^{\text{thres}} \sim \Omega'_d/k\mathcal{B} \gg \Omega'_d/k$ . In this case we face the situation that the destabilizing effect of ion collisions is small, but the effect of the ion drag is even smaller. If the opposite inequality,  $\mathcal{B} \gg 1$ , holds,  $\vartheta_i$  should simply exceed  $\Omega'_d/k$ , as is the case in the constant dust charge approximation [382]. This conclusion is expected since the ion drag then becomes unimportant.

For conditions representative of the experiments in Refs. [373,382], namely  $m_i/m_e \sim 51\,600$ ,  $m_i/m_d \sim 4.7 \times 10^{-14}$ ,  $n_{i0} \sim 10^9 \text{ cm}^{-3}$ ,  $v_{in} \sim 8.8 \times 10^4 \text{ s}^{-1}$ ,  $n_n \sim 3 \times 10^{15} \text{ cm}^{-3}$ ,  $T_e \sim 3 \text{ eV}$ ,  $T_i \sim 0.1 \text{ eV}$ ,  $T_n \sim 0.025 \text{ eV}$ , and  $a \sim 5 \text{ }\mu\text{m}$ , one can obtain  $\mathcal{A} \sim 10^2$ . Therefore, the effect of ion drag can be neglected and the instability seems to follow the weak ion drag scenario. On the other hand, one also obtains  $\mathcal{B} \sim 10^{-1}$ . Thus,  $\vartheta_i$  must exceed  $10\Omega'_d/k$  for the dust-acoustic wave instability to be realized [381].

We now discuss the relevance of the original results of Ref. [381] to the dust-void experiments [233] (see also Section 5.2). In Ref. [381], it was assumed that the electric field is externally applied and uniform. Clearly, from the Poisson's equation it follows that electric fields sufficiently strong for the development of the instability can be generated because of charge fluctuations in the pristine dusty plasmas. Namely, for  $n_{e0} \sim 10^{10}\text{--}10^{12} \text{ cm}^{-3}$ ,  $\tilde{n}_e/n_{e0} \sim 10^{-3}\text{--}10^{-4}$ , and the characteristic filament size  $L \sim 1 \text{ cm}$ , an electric field  $E_0 \sim 1.5\text{--}150 \text{ V/cm}$  can be generated. It is remarkable that the measurements near the instability threshold clearly indicate the presence of the DC electric field of  $E_0 \sim 20 \text{ V/cm}$  [233].

An important feature of the experiment of Ref. [233] is a relatively high operating gas pressure (400 mTorr), which corresponds to a large neutral gas density  $n_n \sim 1.4 \times 10^{16} \text{ cm}^{-3}$ . In this case the assumption of the volume recombination controlled regime would seem to be valid. For lower operating gas pressures the diffusion terms in the particle balance equations (7.21) and (7.23) should be taken into account. The high density of neutrals yields a relatively large rate  $v_{in} \sim 10^7 \text{ s}^{-1}$  of ion-neutral collisions in argon at  $p_0=400 \text{ mTorr}$ . This rate appears larger than the frequencies of ion-dust Coulomb ( $v_i^{\text{el}}$ ) and charging ( $v_i^{\text{ch}}$ ) collisions. For  $E_0 \sim 20 \text{ V/cm}$ ,  $T_e \sim 3 \text{ eV}$ , and  $T_i \sim 0.05 T_e$ , the characteristic ion drift velocity is  $v_0 \sim 4.4 \times 10^4 \text{ cm/s}$ . For this value of  $v_0$  and the spatial scale  $\sim 1 \text{ cm}$  of the filamentation, the nonlinear term  $v_i \partial v_i / \partial x$  in Eq. (7.47) is ignorable. However, this is valid only at the initial stage of the instability. At later stages the nonlinear term can be crucial in the description of self-organized nonlinear dissipative structures of the dust void (see also Section 5.2). Furthermore, near the filamentation threshold, assuming  $a \sim 0.13 \text{ }\mu\text{m}$  one can estimate the dust mass  $m_d \sim 9.2 \times 10^{-15} \text{ g}$ . From the condition of the equality of the equilibrium electron and ion grains currents on the dust particle we have  $Z_{d0} \sim 250$ . For  $n_d \sim 10^8 \text{ cm}^{-3}$  and  $T_n \sim 0.1 T_i$ , it follows that the dust-neutral collision frequency  $v_{dn}$  is approximately  $1.31 \times 10^3 \text{ s}^{-1}$ . We remark that the latter exceeds that of the characteristic oscillations associated with the plasma striation at the initial stage of the instability [233].

Unfortunately, there is a fairly large uncertainty in determining the ion drag force, which depends strongly on the impact parameter  $b$  for ion collection entering the ion drag coefficient. Assuming a local potential difference  $\Delta\phi_g \sim 3 \text{ eV}$ , and  $T_i \sim 0.15 \text{ eV}$ , for the ion drag coefficient one obtains  $\mu_{\text{drag}}^i \sim 1.65 \times 10^3 \text{ s}^{-1}$  so that  $\mu_{\text{drag}}^i/v_{dn} \sim 1.26$ . For argon gas and 130 nm dust particles the key parameters are:  $Z_{d0}m_i/m_d = 1.95 \times 10^{-6}$ ,  $Z_{d0}m_i v_i^{\text{eff}}/m_d v_{dn} = 0.015$ , and  $Z_{d0}m_i v_i^{\text{eff}}/m_d \mu_{\text{drag}}^i = 0.01$ ,

respectively. This means that the effect of the ion drag on the current-driven dust–acoustic instability can really be important for the development of the filamentary mode in dust void experiments [233].

The sudden onset of the instability can be understood if we note that the threshold value of the electric field, appears to scale like  $E_0^{\text{thres}} \sim 1/a$  [381]. This means that for small dust grains the instability threshold cannot be reached. When the grains grow in size, the threshold is greatly decreased and the instability onset becomes possible.

To conclude this section, we emphasize that the conditions for the instability are very different for weak and strong ion drag. Furthermore, the threshold of the external electric field is larger for variable-charge dust grains compared to that for constant dust charge because of the large dissipation rate induced by the fine particles. Finally, we note that self-consistent plasma particle sources and sinks, as well as numerous dissipative processes strongly affect the onset and development of other plasma instabilities, including the drift wave [369] and ion-acoustic [385] instabilities.

## 8. Collective oscillations in arrays of colloid particles

Stability and arrangements of macroscopic particles as well as the properties of excitations propagating in strongly coupled particle structures (two-dimensional and three-dimensional dust–plasma crystals, one-dimensional chains of grains) observed in a complex plasma is a subject of a significant recent interest [7]. We remind that in the laboratory experiments, the micrometer-size highly charged grains usually levitate in the sheath region of the horizontal negatively biased electrode where there is balance between the gravitational and electrostatic forces acting in the vertical direction as well as externally imposed confining potential applied in the horizontal plane. In this region, arrangements of dust particles are also influenced by the strong ion flow, and the effects of the plasma wakes were extensively discussed above in Section 6.

The vertical confinement involving the gravity force and the electrostatic force acting on the dust particles with variable charges is a complex process exhibiting oscillations, disruptions and instabilities [247,251,362,386,387]. A characteristic feature of the particle confinement is also a strong influence of plasma collective processes such as the ion plasma wake. It was shown theoretically [347] that the ion focusing associated with the wake can induce instabilities in the horizontal chain of dust grain related to interaction of transverse and longitudinal modes via the plasma ions focused in the sheath below the levitating grains. However, an instability of particle equilibrium may appear even for two particles [387,388] when obviously we cannot relate it to any cooperative lattice mode.

It was theoretically predicted that vertical vibrations of dust particles in one-dimensional chains may cause propagation of specific modes with the acoustic-type [346] and the optical-type dispersion [246,389]. Observations of vertical motions of the dust are important for diagnostics of processes in the plasma sheath [348,350], especially in the case of several vertically arranged horizontal layers when vertical oscillations are affected by the parameters of the ion flow [249]. Note that the spontaneous excitation of vertical vibrations of dust grains was also experimentally observed [220,251], and driven vertical oscillations were studied in a separate series of experiments [214,218]. On the other hand, molecular dynamic simulations [250] clearly demonstrate a sequence of phase transitions associated with vertical arrangements of horizontal chains when the strength of the confining (in the vertical dimension) parabolic potential is changed. The vertical rearrangements of the dust grains are directly connected with the possible equilibria of the system [362].

At present, the mostly studied experimentally and theoretically cases of excitations in a dust-plasma crystal correspond to structures composed of spherical dust grains. However, there are recent experimental observations of the formation of colloidal structures composed of elongated (cylindrical) particles [205,334,335] levitating in the sheath region of a gas discharge plasma. The experiments demonstrate that there are various arrangements of such grains, levitating horizontally (i.e., oriented parallel to the lower electrode and perpendicular to the gravity force) and vertically (i.e., oriented perpendicular to the lower electrode and parallel to the gravity force). Theoretical papers [391,392] were devoted to the study of modes in lattices composed of such type of grains, and it was demonstrated that in the case of rod-like particles additional modes appear due to the new (rotational) degree of freedom. The “liquid crystal” lattices [335] composed of rods should therefore exhibit the rotational oscillation modes similar to those in liquid crystals. Excitation and interactions of all these modes lead to new types of phase transitions and affect those phase transitions existing also in lattices composed of spherical grains.

### 8.1. Oscillations of a particle in the plasma sheath

In this section, we consider vertical oscillations of a grain, taking into account the dependence of the particle charge on the local sheath potential. We show that the equilibrium of the dust grain close to the electrode can be disrupted by large amplitude vertical oscillations. Earlier analytical models considering the lattice vibrations [248,249,346], as well as numerical models studying the phase transitions [250] in the dust-plasma system, usually deal with the grains of a constant charge. However, as we already discussed above, the charge of dust particles, appearing as a result of electron and ion current onto the grain surfaces, strongly depends on the parameters of the surrounding plasma. Here, we demonstrate [247] that dependence of the dust particle charge on the sheath parameters has an important effect on the oscillations and equilibrium of dust grains in the vertical plane, leading to a disruption of the equilibrium position of the particle and the corresponding transition to a different vertical arrangement.

Consider vertical vibrations of a particle of mass  $m_d$  levitating in the sheath region. The charge  $Q$  of the dust particle is found, as usually, from the condition of a zero total plasma current onto the grain surface. Since we are interested in the collective processes on the time scale of the characteristic frequencies (of the order of a few times  $10\text{ s}^{-1}$ ), which are much lower than the charging frequency (of the order of  $10^5\text{ s}^{-1}$ ), assume that (re)charging of dust grains is practically instantaneous, and therefore neglect the charging dynamics. The plasma electrons are Boltzmann distributed. The discharge pressure is assumed to be low enough that ion collisions with the neutrals and other species can be neglected (this corresponds to experiments in a low-pressure discharge where a spontaneous excitation of vertical vibrations was observed [251]). Thus, in contrast to the electron distribution, we consider collisionless, ballistic ions in the sheath. The charge of a dust particle in the sheath region is then determined by Eq. (6.4). The sheath potential is found from the Poisson’s equation and defined by Eq. (6.1) (where the total charge contributed by the dust grains is neglected) and the sheath electric field is given by Eq. (6.2).

The balance of forces acting on the particles in the vertical direction (4.14) includes the gravity force and the sheath electrostatic force. Solution of this equation together with the charging equation (6.4) gives the dependence of the charge of the grain, levitating in the sheath electric field, as a function of its size, as shown in Fig. 30. There is no equilibrium solution for  $a > a_{\max} = 3.75\text{ }\mu\text{m}$ .



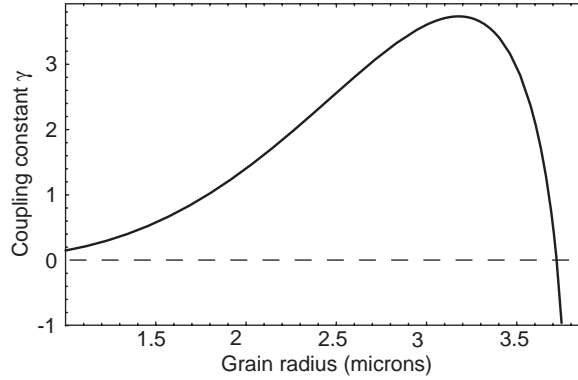


Fig. 40. Dependence of the coupling constant  $\gamma_c$  of the dust vertical vibration on the dust size. The critical radius when  $\gamma_c = 0$  is  $a_{cr} = 0.372 \times 10^{-3}$  cm [247].

Note also that the equilibrium solutions for positions closer than  $z_{min} = 1.64\lambda_{D0}$ , where the grain has a critical size  $a = a_{cr} < a_{max}$ , are unstable in relation to vertical oscillations, as we show now.

Consider small oscillations of an isolated dust grain around the equilibrium position. The equation of motion is given by

$$m_d \frac{d^2 \delta z}{dt^2} = -\gamma_c \delta z, \quad (8.1)$$

where the coupling constant is

$$\gamma_c = EQ \frac{dE}{d\phi} + E^2 \frac{dQ}{d\phi}. \quad (8.2)$$

Note that all the derivatives (as functions of the sheath potential  $\phi$  and the particle charge  $Q$ ) in Eq. (8.1) can be found analytically from Eqs. (6.4) and (6.2). It is also important to note that the second term on the right-hand side of Eq. (8.2) is negative and becomes dominant for larger dust size. The function  $\gamma_c(a)$  is presented in Fig. 40. We see that for  $a > a_{cr} = 3.72 \mu\text{m}$ , the coupling constant is negative and therefore no oscillations are possible. This case corresponds to an instability of the equilibrium levitation in the sheath field because the heavy (large) particle is positioned too close to the electrode where the charging by plasma electrons is insufficient because of the electron density depletion.

The equilibrium charge as well as the sheath potential and electric field at the position of the dust grain, and hence the derivatives in (8.2), can be found numerically by solving Eqs. (6.4) and (4.14) simultaneously. For example, with the parameters [247]  $\lambda_{D0} = 3 \times 10^{-2}$  cm,  $T_e = 1$  eV,  $M_0 = v_0/v_s = 1$ ,  $m_i/m_e = 40 \times 10^3$ ,  $\rho = 1$  g/cm<sup>3</sup> and  $a = 0.35 \times 10^{-3}$  cm, the resulting characteristic long-wavelength frequency is

$$f_{ch}(k=0) = \frac{1}{\sqrt{2\pi}} \sqrt{\frac{\gamma_c}{m_d}} \approx 12.2 \text{ Hz}, \quad (8.3)$$

and the equilibrium charge is  $\bar{q} = -(Q/e) \times 10^{-3} \approx 5.4$ . In general, the characteristic frequency of the dust vertical vibration is a function of the dust size, as shown in Fig. 41; the frequency becomes zero for  $a = a_{cr} = 3.72 \mu\text{m}$ .

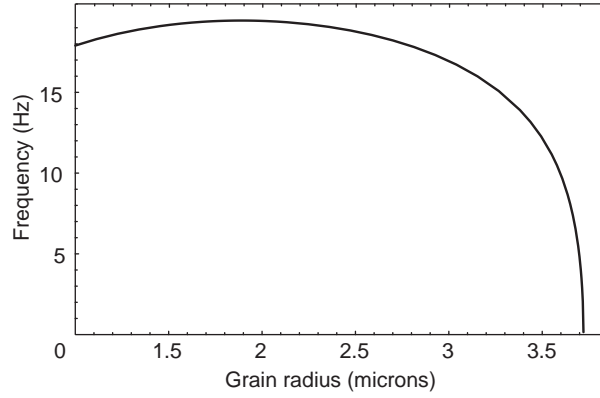


Fig. 41. Dependence of the characteristic frequency  $f_{ch}$  (in Hz) of the oscillation of dust on the size  $a$  (in microns) of the dust grain. The critical dust radius is  $a_{cr} = 0.372 \times 10^{-3}$  cm [247].

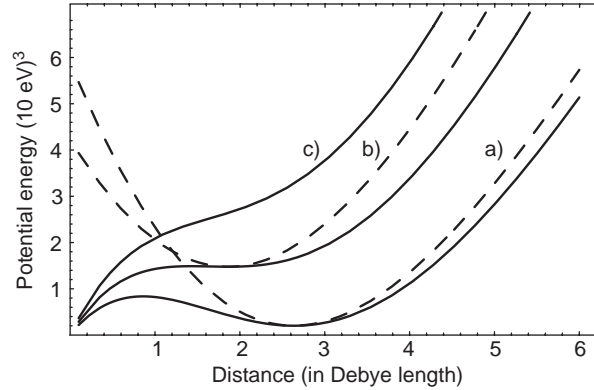


Fig. 42. The total interaction energy  $U_{tot}$  as a function of the distance  $h = z/\lambda_D$  from the electrode for the different sizes of a dust particle: (a)  $a = 0.35 \times 10^{-3}$  cm; (b)  $a = a_{cr} = 0.372 \times 10^{-3}$  cm; and (c)  $a = 0.4 \times 10^{-3}$  cm. The dashed lines correspond to the case of a constant charge at the equilibrium (or the marginal equilibrium) position: a)  $Q = -5.42e \times 10^3$  and (b)  $Q = -4.93e \times 10^3$ . Reprinted from Ref. [247].

It is also instructive to find the total “potential energy”, relative to the electrode position, of a single dust particle of a given size at the position  $z$  in the sheath electric field:

$$U_{tot}(z) = - \int_0^z dz' [Q(z')E(z') - m_d g] . \quad (8.4)$$

Note that the total energy in this case contains not only the electrostatic energy  $Q(z)\phi(z)$ , but also terms associated with  $dQ/d\phi$  which represent, because of the openness of the system, the work of external forces which change the dust charge. Solving Eqs. (6.4) and (6.2), the dependence of the total potential energy on the distance from the electrode can be found, as shown in Fig. 42. For comparison, in Fig. 42 the energy in the case of a constant  $Q$  placed at the same equilibrium (or marginal equilibrium) position is also plotted. The potential always has a minimum for the case of  $Q = const$ , but in the case of a variable charge there can be a maximum and a minimum,

corresponding to the two equilibrium positions. The minimum (the stable equilibrium) disappears if  $a > a_{\text{cr}}$  (the curve  $c$ ) in Fig. 42. A similar result has been found for the collisional sheath case [390]. Other effects which have been neglected here, such as an electron temperature increasing towards the electrode, may serve to increase the negative charge on a grain, and so preserve an equilibrium. The critical radius can be found numerically [247] by solving equations (6.4) and (4.14) simultaneously with the condition  $\omega = 0$ . For the parameters considered here, for  $a = a_{\text{cr}} = 0.372 \times 10^{-3}$  cm, the minimum disappears. This is close to the critical radius observed experimentally [251].

Thus for the collisionless sheath, for  $a$  less than the critical radius, there is an unstable equilibrium position deep inside the sheath, and a stable equilibrium position closer to the presheath [247]. For  $a$  greater than the critical radius there is no equilibrium position. Vertical oscillations about the stable equilibrium may develop high amplitudes (e.g., because of an instability in the background plasma). This may lead to a fall of the oscillating grain onto the electrode when the potential barrier (see the curve  $a$ ) in Fig. 42 is overcome. Such a disruption of the dust motion has been observed experimentally [220,251].

To conclude, we note that the charge, position, and vertical oscillations of a dust grain levitating in a collisionless sheath field of a horizontal negatively biased electrode strongly depend on the parameters of the sheath, in particular, the sheath potential. The dependence of the particle charge on the potential is also important for the characteristics of the oscillation mode as well as for the equilibrium of the dust particle. Large amplitude vertical oscillations of the dust grains may be responsible for experimentally observed disruptions of the equilibrium of the dust crystal as well as with numerically demonstrated phase transitions associated with vertical rearrangements of the grains.

## 8.2. Stability of dust particles confinement

The stability of the vertical and horizontal confinement of particles levitating in a complex plasma appears as a non-trivial interplay of the external confining forces as well as the particle interactions and plasma collective processes such as the wake formation. In particular, the stability of the combined vertical and horizontal confinement of two dust grains was studied [362]. Here, following [362], we demonstrate that the potentials confining particles in the directions perpendicular to the particle motions can disrupt the equilibrium and discuss qualitative consequences for the experiments.

Consider vibrations of two particles of mass  $m_{d1,d2}$  and charges  $Q_{1,2}$ , separated by the distance  $x_d$  horizontally (i.e., aligned along the  $x$ -axis), see Fig. 43a or  $z_d$  vertically (aligned along the  $z$ -axis), see Fig. 43b. In the simplest approximation, the particles interact via the screened Coulomb (Debye) potential  $\phi_D = Q_1 Q_2 \exp(-|\mathbf{r}|/\lambda_D)/|\mathbf{r}|$  where  $\lambda_D$  is the plasma Debye length. Here we note that for particles levitating in the plasma sheath, the interaction potential in the vertical direction is actually such that the forces between them are asymmetric because of the ions flowing towards the negatively charged electrode. However, it is also instructive to consider the case with Debye only interaction even in the vertical direction; there are two reasons for that. Firstly, in the microgravity experiments, such as those onboard of the International Space Station, the dust particles can levitate in the plasma bulk where the effects associated with the ion flow can be negligible. Secondly, consideration of the effects associated with the symmetric Debye screening allows us to elucidate the role of more complex asymmetric potentials.

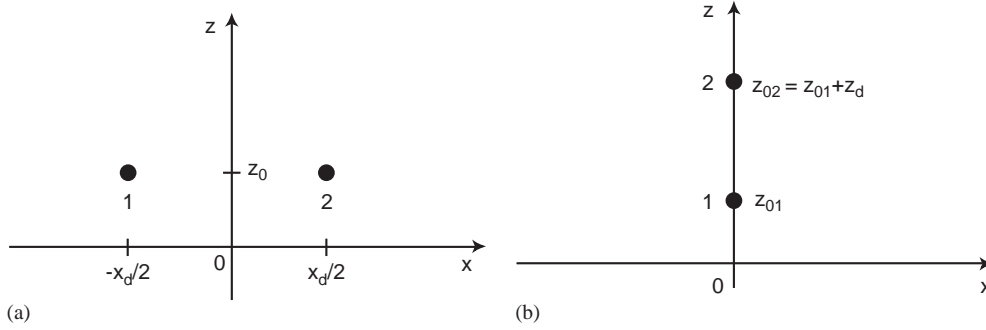


Fig. 43. Sketch of possible particle configurations for two confined particles [362].

Thus consider two cases of the interaction in the vertical direction: (1) when the interaction potential is symmetric of the screened Coulomb type; and (2) when the interaction potential is asymmetric. The latter can be of a different physical origin, here, it is sufficient to assume only that it can be parabolically approximated near the equilibrium. As an example of the asymmetric potential, the wake potential can be considered; it has the following approximate expression along the line (the  $z$ -axis) connecting two vertically oriented particles [254]:  $\Phi_W = 2Q \cos(|z|/L_s)/|z|(1 - v_s^2/v_0^2)$ , where  $v_0$  is the ion flow velocity,  $v_s$  is the ion-sound speed, and  $L_s = \lambda_D \sqrt{v_0^2/v_s^2 - 1}$ . Note that this expression is only applicable on the line behind the dust grain; generally, within the Mach cone the wake potential has more complex structure, see Section 6, while outside the Mach cone the particle potential can be approximated by the Debye formula. Therefore the potential acting on the upper particle due to the lower particle, see Fig. 43b, is a simple Debye repulsive potential.

The balance of forces in the horizontal direction involves the action of the external (horizontal) confining potential as well as the Debye repulsion. We note that in experiments, the symmetric horizontal potential can be obtained using the ring or disk electrodes. For example, the glass cylinder was used to create the “square well”, that is, the parabolic confining potential in Ref. [387]; in the experiment [386] the circle grid electrode was used for this purpose. In the experiment done at the University of Sydney [388], copper and glass rings were used. Thus for the external horizontal potential it is assumed that the external confining force acting in the  $x$ -direction can be written as  $F^{\text{ext}} = -\gamma_x(x - x_0)$ , where  $\gamma_x \sim Q dE_x^{\text{ext}}/dx$  is a constant and  $x_0$  is the equilibrium position of a single dust particle or two vertically aligned particles (Fig. 43b); for further convenience  $x_0 = 0$ . The equilibrium distance  $x_d$  for the case of two horizontally aligned particles, Fig. 43a, appears as a result of the action of the external confining and Debye repulsion forces (note that for the horizontal alignment of two levitating particles they should be identical, i.e.  $Q_1 = Q_2$  and  $m_{d1} = m_{d2} = m_d$ , see also below)

$$\frac{2Q^2}{x_d^2} \left(1 + \frac{x_d}{\lambda_D}\right) \exp\left(-\frac{x_d}{\lambda_D}\right) = \gamma_x x_d. \quad (8.5)$$

The balance of forces in the vertical direction, in addition to the electrostatic Debye and the wake potential forces, includes the gravitational force  $F_g = m_d g$  as well as the sheath electrostatic force  $F_E = QE_z^{\text{ext}}(z)$  acting on the grains. In equilibrium, the interparticle vertical distance  $z_d$  is assumed to be small compared with the distance between the lower particle and the electrode

(as well as small compared with the width of the sheath), therefore the sheath electric field in the range of distances near the position of the equilibrium can be linearly approximated so that we write  $F_E - m_d g = -\gamma_z(z - z_0)$ , where  $\gamma_z \sim Q dF_z^{\text{ext}}/dz$  is assumed to be a constant and  $z_0$  is the equilibrium position of a particle of mass  $m_d$  due to the forces  $m_d g$  and  $F_E$  only. We stress that  $z_0$  is the actual vertical position of the horizontally aligned two identical particles (see Fig. 43a,  $m_{d1} = m_{d2} = m_d$  and  $Q_1 = Q_2 = Q$ ); on the other hand, for the vertically aligned particles (Fig. 43b) the lower and upper equilibrium positions are  $z_{01}$  and  $z_{02} = z_{01} + z_d$ , respectively. In this case, the equilibrium balance of the forces in the vertical direction acting on the lower particle and the upper particle can be written as  $F_{E,1(2)}(z_{01(2)}) - m_{d1(2)}g + F_{1(2)}^{D,W}(z_{02} - z_{01}) = 0$ , where  $F_{1,2}^{D,W}$  are the forces of the interaction between the particles due to their interaction Debye and/or asymmetric (wake) potentials  $\Phi_D$  and/or  $\Phi_W$ , respectively:  $F_1^D(z_{02} - z_{01}) = Qd\Phi_D(|z|)/d|z||_{|z|=z_d}$ , and  $F_2^{D,W}(z_{02} - z_{01}) = -Qd\Phi_{D,W}(|z|)/d|z||_{|z|=z_d}$ . In the case of two identical particles and Debye only interaction between them, the equation similar to (8.5) is obtained

$$\frac{2Q^2}{z_d^2} \left(1 + \frac{z_d}{\lambda_D}\right) \exp\left(-\frac{z_d}{\lambda_D}\right) = \gamma_z z_d. \quad (8.6)$$

In the case of the asymmetric potential, the equilibrium condition for the levitation of two identical particles gives

$$\frac{Q^2}{z_d^2} \left(1 + \frac{z_d}{\lambda_D}\right) \exp\left(-\frac{z_d}{\lambda_D}\right) - \gamma_z^W(z_d - z_W) = \gamma_z z_d, \quad (8.7)$$

where  $z_W$  is the distance between the minimum of the asymmetric attracting potential characterized by  $\gamma_z$  and the upper particle (for the wake potential,  $z_W = \pi L_s$  and in the parabolic approximation, assuming that  $z_W$  is close to  $z_d$ ,  $\gamma_z^W = Q d^2\Phi^W/dz^2|_{z=z_W} = [2(\pi^2 - 2)Q^2/\pi^3\lambda_D^3]v_0^2v_s^3/(v_0^2 - v_s^2)^{5/2}$ ).

Now, consider the first case of two horizontally aligned particles located at the positions  $(-x_d/2, z_0)$  and  $(x_d/2, z_0)$ , see Fig. 43a. As we already noted, to achieve the horizontal alignment, the particles are assumed to be identical. First, introduce small horizontal perturbations  $\delta x_i$ , where  $i=1, 2$ , assume that the vertical displacements are zero (note that in the linear approximation the vertical and horizontal modes are decoupled) and include the phenomenological damping  $\beta_d$  due to the friction of particles with the neutral gas. Linearly expanding the interaction forces, two oscillation modes appear. Their frequencies are given by the frequency

$$\omega_{xx,1} = -\frac{i\beta_d}{2} + \left(\frac{\beta_d^2}{4} + \frac{\gamma_x}{m_d}\right)^{1/2}, \quad (8.8)$$

for the two particle oscillating in phase with equal amplitudes  $A_1 = A_2$ , and by the frequency

$$\omega_{xx,2} = -\frac{i\beta_d}{2} + \left[-\frac{\beta_d^2}{4} + \frac{\gamma_x}{m_d} \left(3 + \frac{x_d^2/\lambda_D^2}{1 + x_d/\lambda_D}\right)\right]^{1/2} \quad (8.9)$$

for the two particles oscillating counter phase with equal amplitudes ( $A_1 = -A_2$ ). The both modes are always stable. The counter phase mode provides (if excited) a good diagnostic tool to determine the plasma parameters (such as Debye length and the neutral friction): by knowing the experimental values of the in-phase and counter-phase frequencies, together with the equilibrium interparticle distance, we are able to determine the unknown plasma parameters (or at least their ratios).

The next case to consider involves vertical oscillations of two horizontally aligned particles, Fig. 43a. In this case, the two oscillation modes have the frequency

$$\omega_{xz,1} = -\frac{i\beta_d}{2} + \left( -\frac{\beta_d^2}{4} + \frac{\gamma_z}{m_d} \right)^{1/2}, \quad (8.10)$$

for the two particle oscillating in phase ( $A_1 = A_2$ ), and the frequency

$$\omega_{xz,2} = -\frac{i\beta_d}{2} + \left( \frac{\beta_d^2}{4} + \frac{\gamma_z}{m_d} - \frac{\gamma_x}{m_d} \right)^{1/2} \quad (8.11)$$

for the two particles oscillating counter phase ( $A_1 = -A_2$ ). We see that while the first mode is always stable, the counter phase mode can now be unstable, depending on the ratio  $\gamma_x/\gamma_z$ . We stress that this instability arises because of the action of the confining potential in the direction perpendicular to the direction of particle oscillations. This instability can lead to disruption of an initially stable horizontal arrangement in an experiment if the relative strength of the vertical to horizontal confining potentials is changed.

By introducing small vertical perturbations  $\delta z_i$  of the vertically aligned particles at equilibrium positions  $(0, z_{0i})$ , where  $i = 1, 2$ , and expanding the interaction forces, one obtains for the case of Debye only interactions the equations analogous to the first case of horizontal vibrations of horizontally aligned particles (for simplicity, the particles are again assumed to be identical; the corresponding generalization to the case of different charges/masses is trivial). There are two oscillations modes; the first one has the frequency (8.10) for the two particle oscillating in phase with equal amplitudes  $A_{1,2}$ , and the second mode's frequency is given by

$$\omega_{zz,2}^D = -\frac{i\beta_d}{2} + \left[ -\frac{\beta_d^2}{4} + \frac{\gamma_z}{m_d} \left( 3 + \frac{z_d^2/\lambda_D^2}{1 + z_d/\lambda_D} \right) \right]^{1/2}, \quad (8.12)$$

for the counter phase oscillations,  $A_1 = -A_2$ . Again, both modes are always stable and the counter phase mode provides (if excited) similar diagnostic tool to determine the plasma parameters (such as Debye length and the neutral friction).

If the asymmetry of the interaction potential (e.g., the plasma wake) is taken into account, the equation of the vertical motion of the upper particle (number 2) is in the Debye potential; motion of the lower particle now involves the wake potential. There are two oscillation modes in this case; the first one, for the particles moving in phase with equal amplitudes  $A_1 = A_2$ , has the frequency (8.10); the second frequency is now given by

$$\omega_{zz,2}^W = -\frac{i\beta_d}{2} + \left[ -\frac{\beta_d^2}{4} + \left( \frac{\gamma_z}{m_d} + \frac{\gamma_z^W}{m_d} \left( 1 - \frac{z_W}{z_d} \right) \right) \left( 3 + \frac{z_d^2/\lambda_D^2}{1 + z_d/\lambda_D} \right) + \frac{\gamma_z^W}{m_d} \frac{z_W}{z_d} \right]^{1/2} \quad (8.13)$$

for the counter phase oscillations; their amplitudes are not equal in magnitude and now related by

$$A_1 = - \left( 2 + \frac{z_d^2/\lambda_D^2}{1 + z_d/\lambda_D} \right) \left( 1 - \frac{z_W}{z_d} + \frac{\gamma_z}{\gamma_z^W} \right) A_2. \quad (8.14)$$

Again, both modes are always stable and the counter phase mode provides (if excited) a diagnostic tool to determine the plasma and the wake parameters (such as Debye length and the position of the



first potential minimum). A very useful information can also be obtained by measuring the amplitude ratio of this type of oscillations.

Now, consider horizontal oscillations of two vertically aligned particles. In the first case, when the particle interaction is symmetric (and of Debye type) the equations of motion are similar to the case of the vertical vibrations of the horizontally arranged particles (with the obvious change of  $z$  to  $x$ ). Thus, two modes of oscillations appear, the first one corresponds to (8.10), when the particles oscillate in phase (with equal amplitudes), and its frequency is equal to (8.8). The second one is similar to (8.11), with the frequency

$$\omega_{zx,2} = -\frac{i\beta_d}{2} + \left( -\frac{\beta_d^2}{4} + \frac{\gamma_x}{m_d} - \frac{\gamma_z}{m_d} \right)^{1/2}, \quad (8.15)$$

and  $A_1 = -A_2$ . While the first mode is always stable, the counter phase mode can be unstable, depending on the ratio  $\gamma_x/\gamma_z$ . The condition for this instability is opposite to the condition of the instability of the mode of vertical vibrations of two horizontally arranged particles, see (8.11).

Finally, consider the case of horizontal oscillations of two vertically aligned particles taking into account the plasma wake. The equation of horizontal motion of the upper particle in this case is the same as for the symmetric Debye only interaction, while the lower particle is oscillating in the wake potential characterized by  $\gamma_x^W$  which is its horizontal strength in the parabolic approximation. Here, it is sufficient to assume that  $\gamma_x^W$  is a positive constant of the order of (or slightly more than)  $\gamma_z^W$ , see, e.g., numerical simulations [361]. For the two oscillatory modes, the frequency of the first one coincides with (8.8) while the frequency of the second mode is given by

$$\omega_{zx,2} = -\frac{i\beta_d}{2} + \left[ -\frac{\beta_d^2}{4} + \frac{\gamma_x}{m_d} + \frac{\gamma_x^W}{m_d} - \frac{\gamma_z}{m_d} - \frac{\gamma_z^W}{m_d} \left( 1 - \frac{z_W}{z_d} \right) \right]^{1/2}. \quad (8.16)$$

Now, we see another important feature: the wake potential can stabilize the possible horizontal instability of two vertically aligned particles (this can be easily seen for the case  $\gamma_z^W = \gamma_x^W$ ); note that for the supersonic wake potential this stabilization occurs only within the Mach cone. The amplitudes of the second mode of oscillations are related by

$$A_1 = \frac{\gamma_x^W A_2}{\gamma_z + \gamma_z^W (1 - z_W/z_d)}. \quad (8.17)$$

Thus for the asymmetric interaction potential, the second mode of oscillations does not correspond to the counter phase motions: the vibrations of particles are in phase now, with unequal amplitudes. Here, we see another powerful experimental tool to determine the character of the interaction potential experimentally: for the pure symmetric interaction potential of repulsive Debye (or Coulomb) type, the oscillations of the second mode are counter phase, while for the asymmetric repulsive–attractive potential the oscillations are in phase (with unequal amplitudes).

The proposed mechanism can be related to experimentally observed phenomena, for example, for the two-particle system in planar rf-discharge [386–388], involving horizontal oscillations of two particles aligned in the vertical string [362] and hysteretic phenomena in the disruptions of the horizontal and vertical arrangements [362,387], see Fig. 44. For simplicity, in the analysis only symmetric Debye interactions of particles are considered, and the stability diagram for the two-particle system is presented in Fig. 45 [362]. There are two extreme regions: one is the region (I) where

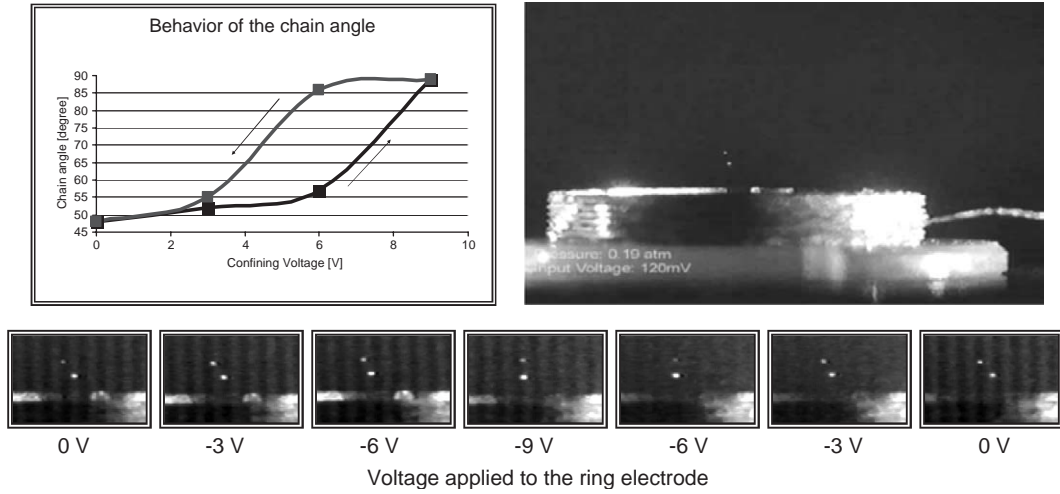


Fig. 44. Experiment at the University of Sydney [388]: levitation of two particles and change of arrangements [388].

$\gamma_z > \gamma_x + m_d \beta_d^2/4$ , corresponding to the vertical string unstable with respect to the horizontal motions of the particles, another is the region (III) where  $\gamma_x > \gamma_z + m_d \beta_d^2/4$  corresponding to the horizontal string unstable with respect to the vertical motions of the particles, as well as the central region (II) where both structures are stable. Realization of the particular arrangement depends on the initial conditions (for example on the particle's inserting technique).

Since for the sheath conditions of planar RF discharge  $\gamma_z \gg \gamma_x$  [362,387], the vertically aligned two-particle system is in this case in the region (I) of Fig. 45, and the instability with respect to the horizontal motions and stability with respect to the excitation of the vertical oscillations should be expected. Indeed, the self-excited horizontal but no vertical oscillations were observed in this case [388]. Also, it was observed that the decrease of the input power leads to the stabilization of the system with respect to the horizontal motions; according [387,388], the decreasing input power is accompanied by the decreasing strength of the vertical confinement  $\gamma_z$ , while the strength of the horizontal confinement  $\gamma_x$  does not change significantly; according to Fig. 44, this means that the system enters the stability region (II) [362].

The hysteretic phenomena in disruption of the vertical and/or horizontal alignment of two particles observed in experiments [386–388] can be qualitatively explained by Fig. 44 [362]. Let us start with the horizontally arranged particles under the conditions of the (stable) region (II). Then, if to decrease the input power and therefore decrease the ratio  $\gamma_z/\gamma_x$  the system enters (at the point  $\gamma_x = \gamma_z + m_d \beta_d^2/4$ ) the region (III), where only the vertical arrangement is stable, that is, the transition from the horizontal to the vertical arrangement takes place. When reversing the process, the transition from the vertical to the horizontal arrangement occurs only at the point  $\gamma_x = \gamma_z - m_d \beta_d^2/4$  and the hysteresis is observed. The strength of the hysteretic behavior  $\Delta\gamma_{x,z}$  can be written as (if the asymmetric wake potential is taken into account)  $\Delta\gamma_z + \Delta\gamma_x \sim m_d \beta_d^2 + 4[\gamma_x^W - \gamma_z^W(1 - z_W/z_d)]$  and can be used to estimate the plasma and confinement characteristics. An interesting observed phenomenon, a “particle jump” [387,388] can be attributed to the point where the particle changes the region from the repulsive symmetric Debye interaction potential to the region where asymmetry

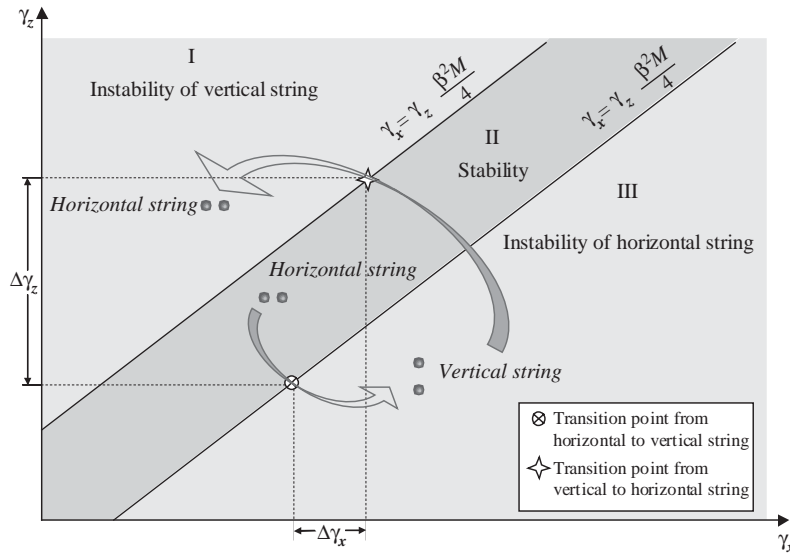


Fig. 45. Stability diagram of the particle arrangements for two confined particles. The mass of dust particle  $m_d$  is denoted as  $M$  in this figure. Reprinted from Ref. [362].

in the particle interaction exists—for example, crosses the boundary of the Mach cone of the wake potential.

### 8.3. Dust–lattice waves in the regular arrays of spherical particles

As we mentioned already, motion on the dust grains in the vertical direction can provide a useful tool for determining the grain charge. Here, we first demonstrate that oscillations of the grains in the vertical plane can lead to a low-frequency mode [247,248]. The mode is characterized by an optical-mode-like inverse dispersion (i.e., its frequency decreases with the growing wave number) if  $kr_0 \ll 1$  where  $k$  is the wave number,  $r_0$  is the interparticle distance in the chain, and only nearest-neighbour interactions are taken into account. As we have seen in Section 6.1, the charge of dust particles, appearing as a result of the electron and ion current onto the grain surfaces, strongly depends on the parameters of the surrounding plasma and therefore on the levitation height. Thus we also show here that the dependence of the dust particle charges on the sheath parameters has an important effect on the oscillations and equilibrium of the grains in the one-dimensional chain, leading to a disruptions of the equilibrium positions similar to the case of an isolated particle considered above in Section 8.1, and a corresponding transition to a different vertical arrangement, see Section 8.2.

In most of the experiments, the Coulomb dust lattices consist of a few layers of dust particles levitating above the electrode. Thus, in Ref. [249] it was predicted that there are two low-frequency modes associated with vertical oscillations in the Coulomb crystal of dust grains arranged in two horizontal chains in a sheath region of a low-temperature gas discharge plasma and the dispersion relations and characteristic frequencies of the modes were found. Here, we consider vertical oscillations of dust grains in two vertically ordered one-dimensional horizontal chains. Following [249],

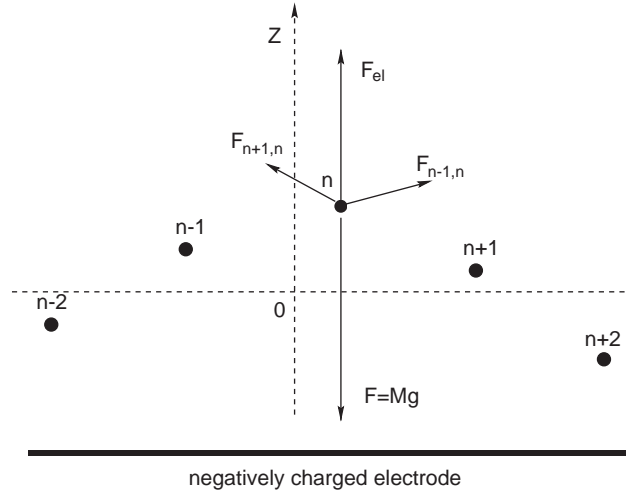


Fig. 46. Oscillations of dust particles in a one-dimensional chain. The mass of dust particle  $m_d$  is denoted as  $M$  in this figure. Reprinted from Ref. [248].

we demonstrate that two low-frequency modes (associated with the vertical vibrations of the dust) can propagate in such a system. Both of the modes are characterized by the optical-mode-like inverse dispersion (i.e., its frequency decreases with growing wave number) if  $kr_0 \ll 1$  and only the nearest-neighbour interactions are taken into account.

### 8.3.1. Oscillation modes in one-dimensional chains of particles

Consider vibrations of a one-dimensional horizontal chain of particulates of equal mass  $m_d$  separated by the distance  $r_0$ , see Fig. 46. We assume that the interaction potential between the particles can be approximated by the Debye law

$$\Phi = \frac{Q}{r} \exp\left(-\frac{r}{\lambda_D}\right). \quad (8.18)$$

In addition to the electrostatic Debye shielded force, the gravitational force  $m_d g$  and the sheath electrostatic force  $F_E = QE(z)$  act on the dust grains in the vertical direction  $z$ . The balance of forces in the linear approximation with respect to small perturbations  $\delta z$  of the equilibrium at  $z = 0$  gives the equation for the vertical oscillations

$$m_d \frac{d^2 \delta z_n}{dt^2} = \frac{Q^2}{r_0^3} e^{-r_0/\lambda_D} (1 + r_0/\lambda_D) (2\delta z_n - \delta z_{n-1} - \delta z_{n+1}) - m_d g + F_E. \quad (8.19)$$

Here

$$F_E - m_d g = -\gamma_s \delta z_n, \quad (8.20)$$

where  $\gamma_s$  is a constant assuming a linear variation of the sheath electric field, and  $\delta z_n$  is the vertical deviation of the  $n$ th particle from its equilibrium position. Note that although in general particles oscillate in the vertical as well as in horizontal direction, see Fig. 46, in the linear approximation

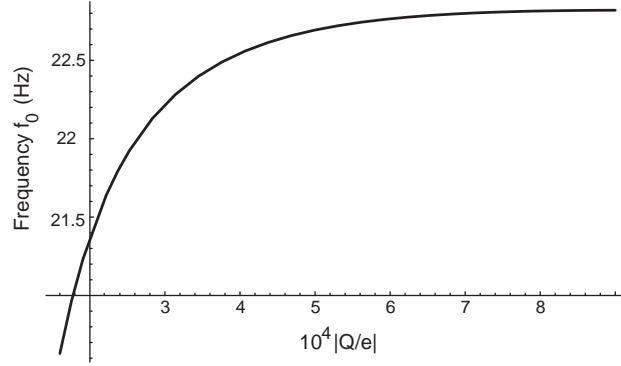


Fig. 47. Frequency  $f_0$  in Hz vs dust charge  $|Q/e| \times 10^{-4}$  for oscillations of particles with a constant charge in a one-dimensional chain [248].

their transverse and longitudinal vibrations are not coupled. Substituting  $\delta z_n = A \exp(-i\omega t + iknr_0)$  into (8.19) gives the dispersion of the vertical oscillations

$$\omega^2 = \frac{\gamma_s}{m_d} - \frac{4Q^2}{m_d r_0^3} e^{-r_0/\lambda_D} (1 + r_0/\lambda_D) \sin^2 \frac{kr_0}{2}. \quad (8.21)$$

For  $k = 0$ , the characteristic frequency is given by  $\omega^2 = \gamma_s/m_d$ , decreasing with the growing wave number when  $kr_0 \ll 1$ .

To estimate the effective width of the potential well  $\gamma_s$ , consider the standard model of the sheath with the Boltzmann distributed electrons and ballistic ions, see Section 6.1. When  $e\phi_0 \ll T_e$ , the characteristic frequency is approximately given by [248]

$$f_0 = \frac{1}{2\pi} \sqrt{\frac{\gamma_s}{m_d}} \approx \frac{1}{2\pi} \sqrt{\frac{g(1 - v_s^2/v_0^2)}{\lambda_D}} \simeq 20 \text{ Hz}, \quad (8.22)$$

where  $\lambda_D \approx (T_e/4\pi n_0 e^2)^{1/2} \sim 2 \times 10^{-2}$  cm and  $v_0^2/v_s^2 \sim 1.5$ . Fig. 47 presents the numerical result for the frequency  $f_0$  as a function of the dust charge  $Q$ . Thus vertical oscillations of a one-dimensional chain of dust grains with a constant charge levitating in the sheath field of a horizontal negatively biased electrode can give rise to a specific low-frequency mode which is characterized by inverse optic-mode-like dispersion when the wave lengths far exceed the intergrain distance.

Considering now the equilibrium and oscillations of a horizontal chain of dust grains with variable charges [247], we note that the parallel (to the electrode) component of the interaction force acting on the particle at the position  $n$  due to the particle at the position  $n - 1$  (see Fig. 46) can now be written as

$$\mathbf{F}_{\parallel, n, n-1} = \frac{\mathbf{R}_{\parallel} Q_n(z_n) Q_{n-1}(z_{n-1})}{|\mathbf{R}|^3} \left[ 1 + \frac{|\mathbf{R}|}{\lambda_D(z_{n-1})} \right] \exp \left[ -\frac{|\mathbf{R}|}{\lambda_D(z_{n-1})} \right], \quad (8.23)$$

where  $\lambda_D(z) = \lambda_{De}(z) = (T_e/4\pi n(z)e^2)^{1/2}$ . Note that now the dust charge  $Q$  and as well as the Debye length  $\lambda_D$  are functions of the vertical position of the dust particles. The component of the

interparticle force in the  $z$ -direction is given by

$$F_{z,n,n-1} = \frac{(z_n - z_{n-1})Q_n(z_n)Q_{n-1}(z_{n-1})}{|\mathbf{R}|^3} \left[ 1 + \frac{|\mathbf{R}|}{\lambda_D(z_{n-1})} \right] \exp \left[ -\frac{|\mathbf{R}|}{\lambda_D(z_{n-1})} \right]. \quad (8.24)$$

Assuming only the nearest neighbour interactions, a small perturbation  $\delta z$  of the equilibrium  $z = z_0$  gives the equation of motion for vertical oscillations of the grains in the linear approximation

$$m_d \frac{d^2 \delta z_n}{dt^2} = -\gamma_s \delta z_n + \frac{Q^2(z_0)}{r_0^3} e^{-r_0/\lambda_D(z_0)} \left[ 1 + \frac{r_0}{\lambda_D(z_0)} \right] (2\delta z_n - \delta z_{n-1} - \delta z_{n+1}), \quad (8.25)$$

where  $r_0$  is the particle separation in the horizontal plane and the coupling constant is defined by Eq. (8.2). Substituting  $\delta z_n \sim \exp(-i\omega t + iknr_0)$  into (8.25), the expression for the frequency of the mode associated with the vertical vibrations at the position  $z_0$  is obtained

$$\omega^2 = -\frac{4Q^2(z_0)\exp(-r_0/\lambda_D(z_0))}{m_d r_0^3} \left[ 1 + \frac{r_0}{\lambda_D(z_0)} \right] \sin^2 \frac{kr_0}{2} + \frac{\gamma_s}{m_d}. \quad (8.26)$$

This mode has an optical-mode-like dispersion similar to that studied above in the case of a constant grain charge. With the charge variation taken into account, the characteristics of the mode are strongly affected by the sheath parameters, in particular, by the sheath potential. Note that this equilibrium is stable only when the last term on the right hand side of (8.26) dominates over the first one. The case when both terms are equal to each other, corresponds to the phase transition associated with the vertical rearrangement of the type  $N \rightarrow N+1$ , where  $N$  is the number of the one-dimensional chains in the vertical dimension. This type of transition is similar to the change of particle arrangements of two particles, Section 8.2. Note that in the case of a horizontal chain of interacting dust particles, with a non-negligible negative first term on the right hand side of Eq. (8.26), the oscillation frequency can become zero (and hence the equilibrium can be disrupted) for even smaller dust sizes than  $a_{ct}$ , presented in Section 8.1.

### 8.3.2. Oscillation modes in two vertically arranged one-dimensional chains of colloid particles

Consider vibrations of the two one-dimensional horizontal chains of particulates of equal mass  $m_d$  separated by the distance  $r_0$  in the horizontal direction and  $d$  in the vertical direction, see Fig. 48 [249]. In the simplest approximation, the particles interact with their neighbors in horizontal as well as in the vertical direction. Interaction in the horizontal direction leads to the low-frequency modes associated with the horizontal and vertical vibrations of dust grains. An important feature in the consideration of the interaction potential between particles in the vertical direction is that the forces between them are asymmetric because of the wake potential.

Thus the (wake) potential in the vertical direction acting on the lower particle due to the upper one is given by [254,256]

$$\Phi_1 = \frac{Q}{|z|} \frac{2 \cos(|z|/L_s)}{1 - v_s^2/v_0^2}, \quad (8.27)$$

where  $|z|$  is the distance between the dust grains in the vertical direction. We remind that potential (8.27) is only applicable within the Mach cone while outside the Mach cone the particle potential



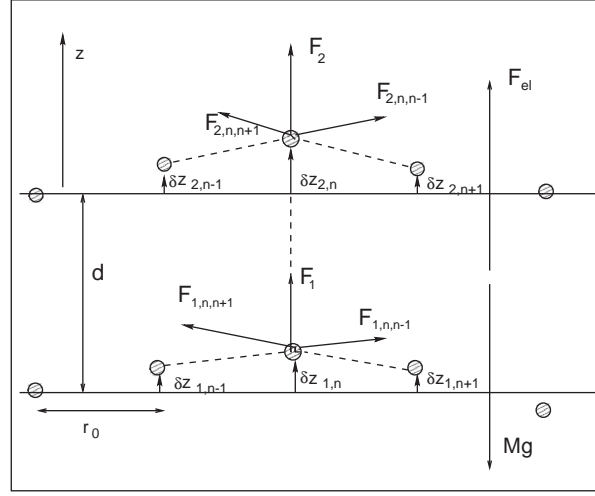


Fig. 48. Forces acting on dust particles in two one-dimensional horizontal chains: the gravitational and the sheath electric external fields, as well as the wake  $F_1$  and Debye  $F_2$  interaction fields. The mass of dust particle  $m_d$  is denoted as  $M$  in this figure. Reprinted from Ref. [249].

can be approximated by the Debye formula. Therefore the potential acting on the upper particle due to the lower particle (as well as the interaction potential between particles in the same chain) is the simple Debye repulsive potential

$$\Phi_2 = \frac{Q}{|z|} \exp\left(-\frac{|z|}{\lambda_D}\right).$$

The balance of forces in the vertical direction, in addition to the electrostatic Debye and the wake potential forces, includes the gravitational force  $F = m_d g$  as well as the sheath electrostatic force  $F_E = QE(z)$  acting on the dust grains. In equilibrium, since the interchain distance  $d$  is assumed to be small compared with the distance  $z_{01}$  of the lower chain from the electrode (as well as small compared with the width of the sheath), we can assume that the sheath electric field in the range of distances  $z_{01}$  to  $z_{02} = z_{01} + d$  can be linearly approximated as

$$F_E - m_d g = -\gamma_0(z - z_0), \quad (8.28)$$

where  $\gamma_0$  is a constant and  $z_0$  is the equilibrium position of a particle of mass  $m_d$  due to the forces  $m_d g$  and  $F_E$  only. We stress that the actual equilibrium positions of particles in lower and upper chains are  $z_{01}$  and  $z_{02}$ , respectively. The equilibrium balance of the forces in the vertical direction acting on the lower chain and the upper chain can be written as

$$F_{E,1}(z_{01}) - m_d g + F_1^0(z_{02} - z_{01}) = 0 \quad (8.29)$$

and

$$F_{E,2}(z_{02}) - m_d g + F_2^0(z_{02} - z_{01}) = 0, \quad (8.30)$$

where  $F_{1,2}^0$  are the forces of interaction between the chains due to the potentials  $\Phi_1$  and  $\Phi_2$ . Here, since  $z_{02} = z_{01} + d$ ,

$$F_1^0(z_{02} - z_{01}) = Q \frac{d\Phi_1(|z|)}{d|z|} \Big|_{|z|=d}, \quad F_2^0(z_{02} - z_{01}) = -Q \frac{d\Phi_2(|z|)}{d|z|} \Big|_{|z|=d}. \quad (8.31)$$

The equilibrium distance  $d$  can be found from the balance equations (8.29) and (8.30) after substituting (8.28) and (8.31)

$$F_2^0(d) - F_1^0(d) = \gamma_0 d.$$

By introducing small perturbations  $\delta z_{i,n}$  of the equilibrium at  $z_{0i}$ , where  $i = 1, 2$  for the lower and upper chains, respectively, and including interactions with nearest neighbors in each chain, one obtains

$$m_d \frac{d^2 \delta z_{1,n}}{dt^2} = B(2\delta z_{1,n} - \delta z_{1,n-1} - \delta z_{1,n+1}) - \gamma_0 \delta z_{1,n} + \gamma_1(\delta z_{2,n} - \delta z_{1,n}) \quad (8.32)$$

and

$$m_d \frac{d^2 \delta z_{2,n}}{dt^2} = B(2\delta z_{2,n} - \delta z_{2,n-1} - \delta z_{2,n+1}) - \gamma_0 \delta z_{2,n} + \gamma_2(\delta z_{2,n} - \delta z_{1,n}), \quad (8.33)$$

where

$$B = \frac{Q^2}{r_0^3} e^{-r_0/\lambda_D} (1 + r_0/\lambda_D)$$

and in the assumed linear approximation

$$\gamma_1 = Q \frac{d^2 \Phi_1(|z|)}{d|z|^2} \Big|_{|z|=d}, \quad \gamma_2 = -Q \frac{d^2 \Phi_2(|z|)}{d|z|^2} \Big|_{|z|=d}.$$

Substitution of  $\delta z_{i,n} = A_i \exp(-i\omega t + ikr_0)$  into Eqs. (8.32) and (8.33) gives the dispersion and amplitude relations for the two modes

$$\omega_1^2 = \frac{\gamma_0}{m_d} - \frac{4Q^2}{m_d r_0^3} e^{-r_0/\lambda_D} (1 + r_0/\lambda_D) \sin^2 \frac{kr_0}{2}, \quad A_1 = A_2, \quad (8.34)$$

and

$$\omega_2^2 = \frac{\gamma_0 + \gamma_1 - \gamma_2}{m_d} - \frac{4Q^2}{m_d r_0^3} e^{-r_0/\lambda_D} (1 + r_0/\lambda_D) \sin^2 \frac{kr_0}{2}, \quad A_1 = A_2 \frac{\gamma_1}{\gamma_2}. \quad (8.35)$$

For  $k = 0$  the characteristic frequencies are given by  $\omega_1^2 = \gamma_0/m_d$  and  $\omega_2^2 = (\gamma_0 + \gamma_1 - \gamma_2)/m_d$ , and they decrease with the wave number when  $kr_0 \ll 1$ .

To estimate the effective width of the electrode potential well  $\gamma_0$ , again the standard model of the sheath, which considers Boltzmann distributed electrons and ballistic cold ions, is employed. For simplicity, it is assumed that the sheath electric field near the position of the dust grains can be linearly approximated. The electric field is found taking into account the balance of the electric force and the gravity at  $z = z_0$ . Solutions for the sheath potential in the equilibrium position and for the equilibrium distance  $d$  in the vertical direction are found numerically [249]. Assuming  $\lambda_D \approx 2 \times 10^{-2}$  cm,  $v_0^2/v_s^2 \approx 1.5$ ,  $Q/e = 2 \times 10^4$ ,  $m_d = 0.6 \times 10^{-9}$  g, the equilibrium vertical distance

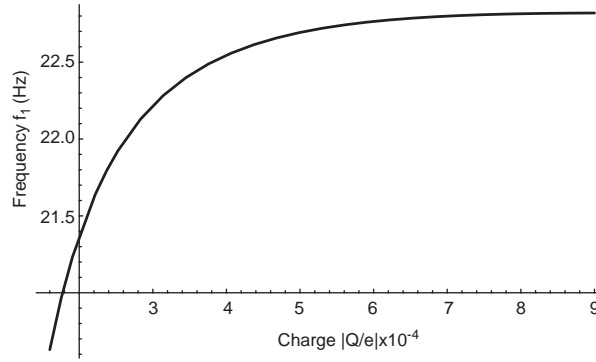


Fig. 49. Dependence of frequency  $f_1$  of the first mode (the amplitudes are the same and in phase for the vertically arranged grains in the first and in the second chains) vs the dimensionless grain charge  $q = |Q/e| \times 10^{-4}$  [249].

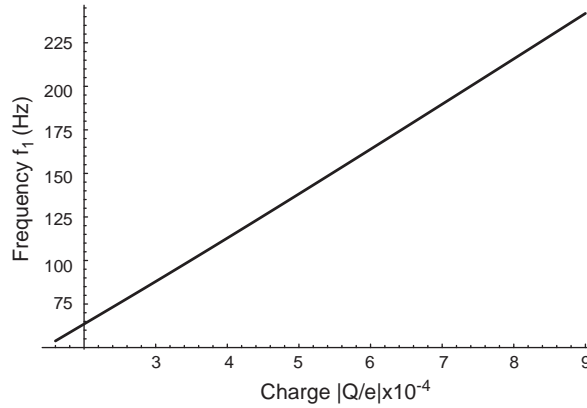


Fig. 50. Dependence of frequency  $f_2$  of the second mode (the amplitudes are different and in counter phase for the vertically arranged grains in the first and in the second chains) vs the dimensionless charge  $q = |Q/e| \times 10^{-4}$  [249].

is given by  $d = 1.75\lambda_D$ , and  $\gamma_1/\gamma_2 \approx -25.3$ . The characteristic frequencies of the two modes are approximately

$$f_1(k=0) = \frac{1}{2\pi} \sqrt{\frac{\gamma_0}{m_d}} \approx 21.3 \text{ Hz}, \quad f_2(k=0) = \frac{1}{2\pi} \sqrt{\frac{\gamma_0 + \gamma_1 - \gamma_2}{m_d}} \approx 63.5 \text{ Hz}.$$

Results of numerical calculation [249] of the frequencies  $f_1$  and  $f_2$  as functions of the dust charge  $Q$  are presented in Figs. 49 and 50. Since the equilibrium distance  $d$  between the chains is almost independent of  $Q$ , the frequency  $f_2$  is approximately directly proportional to  $Q$ . Note that the amplitude of dust grain oscillations in the lower chain for the second mode (when the grains oscillate with opposite phases) is much smaller than the amplitude of the oscillations in the upper chain,  $|A_1/A_2| = |\gamma_1/\gamma_2| \approx 25.3$ . For the first mode, the amplitudes are the same for the upper and the lower particles.

Thus the vertical oscillations of the two one-dimensional chains of dust grains levitating in the sheath field of a horizontal negatively biased electrode can give rise to two low-frequency modes which are characterized by the inverse optical-mode-like dispersion when the wave lengths far exceed the intergrain distance. The second mode can be especially useful for diagnostic purposes because its dispersion is almost directly proportional to the dust grain charge  $Q$  which in turn is a function of plasma parameters. We stress that while the interparticle distance  $d$  in the vertical direction is defined by the equilibrium balance of forces, the horizontal interparticle distance  $r_0$  is a free parameter in the presented theory; in real experiments, it is determined by many factors (including the horizontal confining potential) and usually is of the order of the Debye length  $\lambda_D$ . Finally, we note that the charge on a dust grain is strongly dependent on the grain size as well as on the ambient plasma parameters. Although grains in many experiments are usually geometrically identical, plasma parameters can differ in the position of the upper and the lower chains thus leading to different charges of particles  $Q_1$  and  $Q_2$  in the respective row. Different charges will change the coefficients  $\gamma_{0,1,2}$  for the upper and lower chains thus strongly affecting character of the modes. In particular, the first mode, corresponding to oscillations of upper and lower particles in phase with the same frequency  $f_1$ , will be split into two modes with close frequencies if the difference in charges  $Q_1 - Q_2$  is small compared with these charges.

#### 8.4. Waves in arrays of rod-like particles

Here, oscillations in the one-dimensional chain consisting of rotator-like particles levitating in a plasma are considered, following the original study [391]. We demonstrate that new oscillation modes associated with the rotational degrees of freedom appear for such a configuration. We also analyze dispersion characteristics of the modes and discuss collective oscillations and equilibrium in lattices composed of cylindrical particles in a plasma.

The simplest case corresponds to the rods with given (and static) charge distribution [337] along the rod length. More complicated is the case when the interaction of the rod-like particles between themselves and with the plasma is studied dynamically together with their charging, thus demanding that the problem of the charging of rods by the surrounding plasma should be first solved [205,206]. Here, following [391], we model the rod-like particle as the rotator having two charges (and masses) concentrated at the ends of the rod. For further simplicity, the charges are assumed to be fixed and the masses are equal. The rod of the length  $l_d$ , connecting these two charges, has zero radius and mass.

Consider the following geometry: the one-dimensional rod chain is along the  $x$ -axis, with the distance  $d$  between the centers of masses of the (unperturbed) rotators,  $\mathbf{R}^n$  is the radius-vector of the center of mass of the  $n$ th rotator (of equal masses  $m$  at the rod ends, the center of mass is located in the center of the rotator, at the distance  $l_d/2$  from its ends), the angle  $\Theta^n$  is between the  $n$ th rotator and the  $z$ -axis, and the angle  $\phi^n$  is between the  $x$ -axis and the projection of the  $n$ th rotator on the  $xy$ -plane. At the upper end of the  $n$ th rod, there is a spherical particle (coordinate  $\mathbf{a}^n$ ) with the charge  $Q_a$ , and mass  $m_a$ , and at the lower end of the same rod there is another spherical particle (coordinate  $\mathbf{b}^n$ ) with the charge  $Q_b$  and mass  $m_b$ . Furthermore, the masses of the particles are equal,  $m_a = m_b = m$  (the corresponding generalization to the case of unequal masses is trivial with the respective change of the position of the center of mass along the rotator).

The radius-vectors of the  $n$ th rod ends are  $\mathbf{a}^n = n d \mathbf{e}_x + \mathbf{R}^n + l_d \mathbf{S}^n / 2$  and  $\mathbf{b}^n = n d \mathbf{e}_x + \mathbf{R}^n - l_d \mathbf{S}^n / 2$ , where  $\mathbf{S}^n = (\cos \phi^n \sin \Theta^n, \sin \phi^n \sin \Theta^n, \cos \Theta^n)$ . The four distances between the ends of the  $n$ th and  $(n+1)$ th rotators are given by

$$\begin{aligned} \mathbf{r}_{a(b)a}^{n+} &= \mathbf{a}^n - \mathbf{a}(\mathbf{b})^{n+1} = -d \mathbf{e}_x + (\mathbf{R}^n - \mathbf{R}^{n+1}) + l_d (\mathbf{S}^n \mp \mathbf{S}^{n+1}) / 2, \\ \mathbf{r}_{b(a)b}^{n+} &= \mathbf{b}^n - \mathbf{a}(\mathbf{b})^{n+1} = -d \mathbf{e}_x + (\mathbf{R}^n - \mathbf{R}^{n+1}) - l_d (\mathbf{S}^n \mp \mathbf{S}^{n+1}) / 2. \end{aligned} \quad (8.36)$$

Here, the upper sign on the right hand side corresponds to  $\mathbf{r}_{aa}$  or  $\mathbf{r}_{bb}$ , and the lower sign on the right hand side corresponds to  $\mathbf{r}_{ba}$  or  $\mathbf{r}_{ab}$ , respectively. For the distances between the  $(n-1)$ th rod and the  $n$ th rod (e.g., for  $\mathbf{r}_{aa}^{n-}$ ), we have similar expressions with the simultaneous change  $(n+1) \rightarrow (n-1)$  and  $d \rightarrow -d$ .

Accounting for the oscillatory and rotational degrees of freedom and assuming the nearest neighbor interactions, the Lagrangian [393] of the system is written as

$$\begin{aligned} \mathcal{L} &= \frac{m}{2} \sum_n (\dot{\mathbf{R}}^n)^2 + \frac{I_0}{2} \sum_n [(\dot{\phi}^n)^2 \sin^2 \Theta^n + (\dot{\Theta}^n)^2] - Q_a \sum_n \Phi_{\text{ext}}(\mathbf{a}^n) - Q_b \sum_n \Phi_{\text{ext}}(\mathbf{b}^n) \\ &\quad - Q_a \sum_n [\Phi_a(\mathbf{r}_{aa}^{n+}) + \Phi_b(\mathbf{r}_{ba}^{n+})] - Q_b \sum_n [\Phi_a(\mathbf{r}_{ab}^{n+}) + \Phi_b(\mathbf{r}_{bb}^{n+})] \\ &\quad - Q_a \sum_n [\Phi_a(\mathbf{r}_{aa}^{n-}) + \Phi_b(\mathbf{r}_{ba}^{n-})] - Q_b \sum_n [\Phi_a(\mathbf{r}_{ab}^{n-}) + \Phi_b(\mathbf{r}_{bb}^{n-})], \end{aligned} \quad (8.37)$$

where  $I_0 = m l_d^2 / 2$  is the moment of inertia of the considered rotator,  $\Phi_a[\mathbf{r}_{aa}^{n+}]$  is the interaction potential between the  $n$ th and  $(n+1)$ th  $a$ -particles, etc., and  $\Phi_{\text{ext}}(\mathbf{r})$  is the external potential. Furthermore, the interaction potential is  $\Phi_a(\mathbf{r}) = (Q_a / |\mathbf{r}|) \exp(-|\mathbf{r}| / \lambda_D)$ , where  $\lambda_D$  is the plasma Debye length; the external potential is determined by the action of the gravity and the sheath electric field in the point of levitation, both fields act only along the  $z$ -axis.

The Lagrangian equations of motion are given by

$$\frac{d}{dt} \frac{\partial \mathcal{L}}{\partial \dot{s}} - \frac{\partial \mathcal{L}}{\partial s} = 0, \quad (8.38)$$

where  $s = (\mathbf{R}^i, \Theta^i, \phi^i)$ . General expressions for motion and rotation in all three dimensions are cumbersome and therefore further, for simplicity, only motions in the  $(x, z)$ -plane are considered such that  $\mathbf{S}^n = (S_x^n, 0, S_z^n) = (\sin \Theta^n, 0, \cos \Theta^n)$ ,  $\phi^n = 0$ , and  $\mathbf{R}^n = (x^n, 0, z^n)$ . Thus the motion of the center of mass in the  $x$ -direction is described by

$$\begin{aligned} 2m \ddot{\mathbf{R}}^n &= -Q_a \left[ \frac{\Phi'(\mathbf{r}_{aa}^{n+})}{|\mathbf{r}_{aa}^{n+}|} \mathbf{r}_{aa}^{n+} + \frac{\Phi'(\mathbf{r}_{aa}^{n-})}{|\mathbf{r}_{aa}^{n-}|} \mathbf{r}_{aa}^{n-} + \frac{\Phi'(\mathbf{r}_{ba}^{n+})}{|\mathbf{r}_{ba}^{n+}|} \mathbf{r}_{ba}^{n+} \right. \\ &\quad \left. + \frac{\Phi'(\mathbf{r}_{ba}^{n-})}{|\mathbf{r}_{ba}^{n-}|} \mathbf{r}_{ba}^{n-} + \frac{\partial \Phi_{\text{ext}}(\mathbf{a}^n)}{\partial \mathbf{R}^n} \right] - Q_b [\dots], \end{aligned} \quad (8.39)$$

where the dots stand for the terms analogous to those in the first square brackets (with the interchange  $a \leftrightarrow b$ ), and  $\Phi'_a(\mathbf{r}) \equiv d\Phi_a(\mathbf{r})/d|\mathbf{r}| = -(Q_a/|\mathbf{r}|)(\lambda_D^{-1} + |\mathbf{r}|^{-1}) \exp(-|\mathbf{r}|/\lambda_D)$  for Debye interaction potential.



Fig. 51. Rod-like micron-sized particles levitated in krypton plasmas. The dots are vertically aligned micro-rods [205].

Rotations on the angle  $\Theta$  are described by

$$\begin{aligned}
 I_0 \ddot{\Theta}^n = & -Q_a l_d \left\{ \frac{\Phi'(\mathbf{r}_{aa}^{n+})}{|\mathbf{r}_{aa}^{n+}|} [r_{aa,x}^{n+} \cos \Theta^n - r_{aa,z}^{n+} \sin \Theta^n] + \frac{\Phi'(\mathbf{r}_{aa}^{n-})}{|\mathbf{r}_{aa}^{n-}|} [r_{aa,x}^{n-} \cos \Theta^n - r_{aa,z}^{n-} \sin \Theta^n] \right. \\
 & + \frac{\Phi'(\mathbf{r}_{ba}^{n+})}{|\mathbf{r}_{ba}^{n+}|} [r_{ba,x}^{n+} \cos \Theta^n - r_{ba,z}^{n+} \sin \Theta^n] + \frac{\Phi'(\mathbf{r}_{ba}^{n-})}{|\mathbf{r}_{ba}^{n-}|} [r_{ba,x}^{n-} \cos \Theta^n - r_{ba,z}^{n-} \sin \Theta^n] \\
 & \left. + \frac{\partial \Phi_{\text{ext}}(\mathbf{a}^n)}{\partial \Theta^n} \right\} - Q_b l_d \{ \dots \} . \quad (8.40)
 \end{aligned}$$

General equations (8.39) and (8.40) can be used not only to obtain the dispersion relations for the small amplitude oscillations, but also to study mode interactions for larger amplitudes. For small deviations from the equilibrium, the oscillations decouple, and linear dispersion relations can be derived.

According to the experiments [205], there are two preferred equilibrium positions of levitating rod-like particles: when the rotators are oriented vertically (i.e., along the  $z$ -axis in our geometry) and when the rotators are oriented horizontally, see Fig. 51. Thus below we consider dispersion relations for the modes associated with small deviations around these two equilibrium positions.

If there are only small oscillations  $\delta x \ll \min(d, L)$  of the centers of mass of vertically oriented ( $\Theta = 0$ ) rotators in  $x$ -direction (which is horizontal), from Eq. (8.39) one can obtain

$$\begin{aligned}
 2m\delta\ddot{x}^n = & - \left\{ Q_a \left[ \Phi_a''(d) + \frac{\Phi_b'(L_d)}{L_d} + \frac{d^2}{L_d} \left[ \frac{\Phi_b'(r)}{r} \right]'_{L_d} \right] + Q_b[\dots] \right\} \\
 & \times (2\delta x^n - \delta x^{n+1} - \delta x^{n-1}) , \quad (8.41)
 \end{aligned}$$



where  $L_d = (d^2 + l_d^2)^{1/2}$ . For the perturbations propagating along the  $x$ -axis, Eq. (8.40) gives the following dispersion equation of the lattice-acoustic type

$$\omega^2 = \frac{4}{2m} \left[ Q_a \Phi_a''(d) + Q_b \Phi_b''(d) + 2Q_a \frac{d^2}{L_d^2} \Phi_b''(L_d) + 2Q_a \frac{L^2}{L_d^3} \Phi_b'(L_d) \right] \sin^2(kd/2), \quad (8.42)$$

Here, it is taken into account that for the Debye interaction potential  $Q_a \Phi_b = Q_b \Phi_a$ . In the limit  $l_d \ll d$  the standard dispersion relation for the lattice-acoustic wave [346] in the chain of particles with the charge  $Q_a + Q_b$  and the mass  $2m$  can be recovered from (8.42)

$$\omega^2 = 4 \frac{Q_a + Q_b}{2m} (\Phi_a''(d) + \Phi_b''(d)) \sin^2(kd/2), \quad (8.43)$$

where  $\Phi_a''(d) + \Phi_b''(d) = (Q_a + Q_b)(2 + 2d/\lambda_D + d^2/\lambda_D^2) \exp(-d/\lambda_D)/d^3$  for the interaction potential of the Debye type.

For the horizontally oriented rod chain ( $\Theta = \pi/2$ , note that in this case  $d > l_d$ ) the equation of motion is given by

$$\begin{aligned} 2m\delta\ddot{x}^n = & -[Q_a \Phi_a''(d) + Q_b \Phi_b''(d)](2\delta x^n - \delta x^{n+1} - \delta x^{n-1}) \\ & -[Q_a \Phi_b''(d - L) + Q_b \Phi_a''(d + l_d)](\delta x^n - \delta x^{n+1}) \\ & -[Q_a \Phi_b''(d + L) + Q_b \Phi_a''(d - l_d)](\delta x^n - \delta x^{n-1}). \end{aligned} \quad (8.44)$$

From Eq. (8.44) (noting that in the case of Debye interaction potential  $Q_a \Phi_b = Q_b \Phi_a$ ) the dispersion relation for the acoustic mode can be obtained

$$\omega^2 = \frac{4}{2m} [Q_a \Phi_a''(d) + Q_b \Phi_b''(d) + Q_a \Phi_b''(d - l_d) + Q_b \Phi_a''(d + l_d)] \sin^2(kd/2). \quad (8.45)$$

Again, in the limit  $l_d \ll d$ , Eq. (8.43) can be recovered from Eq. (8.45).

For small oscillations in the vertical direction of the vertically oriented rotators (i.e., parallel to the  $z$ -axis) the equation of motion is given by

$$\begin{aligned} 2m\delta\ddot{z}^n = & -Q_a \left\{ \left[ \frac{\Phi_a'(d)}{d} + \frac{\Phi_b'(L_d)}{L_d} + \frac{L^2}{L_d} \left[ \frac{\Phi_b'(r)}{r} \right]'_{L_d} \right] (2z^n - z^{n+1} - z^{n-1}) + \frac{\partial \Phi_{\text{ext}}(\mathbf{a}^n)}{\partial z^n} \right\} \\ & - Q_b \{ \dots \}. \end{aligned} \quad (8.46)$$

For the parabolic approximation of the external potential (depending only on  $z$ )  $Q_a \Phi_{\text{ext}}(\mathbf{a}^n) + Q_b \Phi_{\text{ext}}(\mathbf{b}^n) = \gamma_v(z^n - l_d/2)^2/2 + \gamma_v(z^n + l_d/2)^2/2$ , where  $\gamma_{a,b} > 0$ , for the wave propagating along the chain the following dispersion relation of the optical character is obtained

$$\omega^2 = \frac{\gamma_v}{m} + \frac{4}{2m} \left\{ Q_a \left[ \frac{\Phi_a'(d)}{d} + \frac{\Phi_b'(L_d)}{L_d} + \frac{L^2}{L_d} \left[ \frac{\Phi_b'(r)}{r} \right]'_{L_d} \right] + Q_b [\dots] \right\} \sin^2(kd/2). \quad (8.47)$$

In the limit  $l_d \ll d$ , the dispersion relation of the optical-like mode [248] propagating in the chain of particles can be recovered from (8.47):

$$\omega^2 = \frac{\gamma_v}{m} + 4 \frac{Q_a + Q_b}{2m} \left[ \frac{\Phi_a'(d)}{d} + \frac{\Phi_b'(d)}{d} \right] \sin^2(kd/2), \quad (8.48)$$

where  $\Phi'_a(d)/d + \Phi'_b(d)/d = -(Q_a + Q_b)(1 + d/\lambda_D)\exp(-d/\lambda_D)/d^3$  for the interaction potential of Debye type.

For vertical oscillations of horizontally oriented rotators (note that  $d > l_d$ ) the equation of motion is written as

$$\begin{aligned} 2m\delta\ddot{z}^n = & - \left[ Q_a \frac{\Phi'_a(d)}{d} + Q_b \frac{\Phi'_b(d)}{d} \right] (2\delta z^n - \delta z^{n+1} - \delta z^{n-1}) \\ & - \left[ Q_a \frac{\Phi'_b(d - l_d)}{d - l_d} + Q_b \frac{\Phi'_a(d + l_d)}{d + l_d} \right] (\delta z^n - \delta z^{n+1}) \\ & - \left[ Q_a \frac{\Phi'_b(d + l_d)}{d + l_d} + Q_b \frac{\Phi'_a(d - l_d)}{d - l_d} \right] (\delta z^n - \delta z^{n-1}) \\ & - Q_a \frac{\partial \Phi_{\text{ext}}(\mathbf{a}^n)}{\partial z^n} - Q_b \frac{\partial \Phi_{\text{ext}}(\mathbf{b}^n)}{\partial z^n} . \end{aligned} \quad (8.49)$$

For the parabolic external potential (note that in this case  $Q_a \Phi_{\text{ext}}(\mathbf{a}^n) + Q_b \Phi_{\text{ext}}(\mathbf{b}^n) = \gamma_h(z^n)^2$ ) and Debye interaction potential ( $Q_a \Phi_b = Q_b \Phi_a$ ), the dispersion relation for the optical mode can be obtained from Eq. (8.49)

$$\omega^2 = \frac{\gamma_h}{m} + \frac{4}{2m} \left[ Q_a \frac{\Phi'_a(d)}{d} + Q_b \frac{\Phi'_b(d)}{d} + Q_a \frac{\Phi'_b(d - l_d)}{d - l_d} + Q_b \frac{\Phi'_a(d + l_d)}{d + l_d} \right] \sin^2(kd/2) . \quad (8.50)$$

In the limit  $l_d \ll d$  equation similar to (8.48) can be recovered from Eq. (8.50). Note that a slightly different character of the external potential was assumed to allow for the cases of the stable vertically or horizontally oriented rotators, respectively.

Small rotating oscillations around  $\Theta = 0$  (i.e., for vertically oriented rotators) are described by

$$\begin{aligned} \frac{2I_0}{L^2} \delta\ddot{\Theta}^n = & -Q_a \left\{ \Phi''_a(d)(2\Theta^n - \Theta^{n+1} - \Theta^{n-1}) + \left[ \frac{\Phi'_b(L_d)}{L_d} + \frac{d^2}{L_d} \left[ \frac{\Phi'_b(r)}{r} \right]'_{L_d} \right] \right. \\ & \times (2\Theta^n + \Theta^{n+1} + \Theta^{n-1}) + \frac{2}{l_d} \frac{\partial \Phi_{\text{ext}}(\mathbf{a}^n)}{\partial \Theta^n} \left. \right\} - Q_b \{ \dots \} . \end{aligned} \quad (8.51)$$

Here, we note the changed character of the dispersion related to the nearest-neighbor interactions, as compared with the previous cases of oscillations of the rotators' centers of mass, see the term containing  $2\Theta^n + \Theta^{n+1} + \Theta^{n-1}$ . In the case of the external parabolic potential supporting the vertical orientation of the rotators (and accounting for  $Q_a \Phi_b = Q_b \Phi_a$ ), the following dispersion is obtained

$$\begin{aligned} \omega^2 = & \frac{2\gamma_v}{m} + \frac{8}{mL_d^3} [Q_a d^2 L_d \Phi''_b(L_d) + Q_a l_d^2 \Phi'_b(L_d)] \\ & + \frac{4}{m} \left[ Q_a \Phi''_a(d) + Q_b \Phi''_b(d) - 2Q_a \frac{d^2}{L_d^2} \Phi''_b(L_d) - 2Q_a \frac{l_d^2}{L_d^3} \Phi'_b(L_d) \right] \sin^2(kd/2) . \end{aligned} \quad (8.52)$$

Note that for Debye-type interaction potential, the factor at the oscillating term on the right hand side part of Eq. (8.52) is always positive. This means that although in general there is the frequency gap,

similar (but not equal) to that of the vertical oscillations of the center of mass of the rotators, the dispersion character is different as compared with the case of the vertical vibrations: because of the sign of the factor in front of the dispersion term in (8.52), there is no anomalous dispersion (i.e., the mode frequency increases with the increase of the wavenumber). Note also the second term on the right-hand side of (8.52): if positive, it allows rotational oscillations (in the  $xz$ -plane) in the chain of the vertically oriented rotators even in the absence of an external confining (in the  $z$ -direction) potential due to the interactions with the nearest neighbors. For the Debye screening potential, this term can be either positive or negative depending on the relations between  $l_d$ ,  $d$ , and the plasma Debye length  $\lambda_D$ . This indicates that the system can be unstable with respect to rotations of rods on the angle  $\Theta$ ; this can have important consequences for excitation of the corresponding mode and the related phase transition associated with the rotational (in)stability in the chains of rotators. Indeed, by changing the plasma characteristics, the originally stable vertically oriented equilibrium state of rotators can change its character and become unstable (and vice versa). Moreover, for marginally unstable equilibrium, because of the normal character of the wave dispersion, for some wavelengths the oscillations still can be stable (i.e. when the positive dispersive term exceeds the negative non-dispersive term).

Finally, consider rotational oscillations of horizontally oriented rotators (around  $\Theta = \pi/2$ ). If to assume  $\Theta = \pi/2 - \vartheta$ , one can obtain (compare with Eq. (8.49))

$$\begin{aligned}
 \frac{2I_0}{l_d^2} \delta \ddot{\vartheta}^n = & - \left[ Q_a \frac{\Phi'_a(d)}{d} + Q_b \frac{\Phi'_a(d)}{d} \right] (2\delta \vartheta^n - \delta \vartheta^{n+1} - \delta \vartheta^{n-1}) \\
 & + \left[ Q_a \frac{\Phi'_b(d-l_d)}{d-l_d} + Q_b \frac{\Phi'_a(d+l_d)}{d+l_d} \right] (\delta \vartheta^n - \delta \vartheta^{n+1}) \\
 & + \left[ Q_a \frac{\Phi'_b(d+l_d)}{d+l_d} + Q_b \frac{\Phi'_a(d-l_d)}{d-l_d} \right] (\delta \vartheta^n - \delta \vartheta^{n-1}) \\
 & - \frac{d}{l_d} \left[ Q_a \frac{\Phi'_b(d-l_d)}{d-l_d} + Q_b \frac{\Phi'_a(d-l_d)}{d-l_d} - Q_a \frac{\Phi'_b(d+l_d)}{d+l_d} - Q_b \frac{\Phi'_a(d-l_d)}{d-l_d} \right] \delta \vartheta^n \\
 & - \frac{2Q_a}{l_d} \frac{\partial \Phi_{\text{ext}}(\mathbf{a}^n)}{\partial \vartheta^n} - \frac{2Q_b}{l_d} \frac{\partial \Phi_{\text{ext}}(\mathbf{b}^n)}{\partial \vartheta^n} .
 \end{aligned} \tag{8.53}$$

For the external potential supporting the horizontal orientation of the rotators (and, as usual, taking into account that for the Debye interaction potential  $Q_a \Phi_b = Q_b \Phi_a$ ), the dispersion is given by

$$\begin{aligned}
 \omega^2 = & \frac{2\gamma_h}{m} + \frac{4}{ml_d} [Q_a \Phi'_b(d-l_d) - Q_a \Phi'_b(d+l_d)] \\
 & + \frac{4}{m} \left[ Q_a \frac{\Phi'_a(d)}{d} + Q_b \frac{\Phi'_b(d)}{d} + Q_a \frac{\Phi'_b(d-l_d)}{d-l_d} + Q_a \frac{\Phi'_b(d+l_d)}{d+l_d} \right] \sin^2(kd/2) .
 \end{aligned} \tag{8.54}$$

Again, note the second term on the right-hand side of Eq. (8.54) (originating from the nearest neighbor interactions): for the Debye interaction potential, it is always negative and can prevent

the stable equilibrium of the horizontally oriented rotators even in the case of the confining (in the  $z$ -direction) potential. Since the vertical confinement is usually associated with the properties of the plasma sheath (where the particles are levitated), the change of plasma parameters can lead to the change of the stability characteristics of the horizontally oriented rods. Depending on the particular character of the interaction (and on the plasma parameters), this feature can affect the excitation of the rotation modes of the horizontally oriented rotators and therefore the related phase transitions. In the limit  $l_d \rightarrow 0$ , dispersion (8.48) can be recovered from Eq. (8.54).

To conclude, we note that new modes associated with the rotational degrees of freedom can propagate in the chain of rotators interacting via the screened potential of Debye type and levitating in an external potential in a plasma [391,392]. New features related to the rotational modes include an interesting interplay of interactions of the rotators with a plasma (formalized above by the terms containing the external potential) and with themselves. Combination of these interactions strongly affects the equilibrium positions and orientations of the rotators and therefore will influence phase transitions associated with such rotating modes.

## 9. Conclusion

In this report, numerous physical phenomena in complex ionized gas systems have been reviewed. The spectrum of these phenomena is remarkably wide and includes the processes of dust generation, growth, self-organization into larger agglomerates and several ordered localized structures (e.g dust sheaths, voids, ordered particle arrays, etc.), charging, levitation, collective waves and oscillations, and many others. The state-of-the-art in the studies of such complex plasma systems is related to the unique capacity of fine particles to originate from molecular/radical precursors in reactive plasma environments, grow into nano-sized crystallites and larger agglomerates and further self-organize into fascinating ordered structures. Furthermore, individual dust grains, particulate clouds and more complex structures can be electrostatically confined in the discharge chamber, especially in the vicinity of the walls, internal electrodes or substrates. This opens up a wide horizon of numerous opportunities for the processing and modification of dust grains as well as controllable deposition of ultra-fine powders onto micro-/nano-patterned substrates.

In the above, we have reviewed a variety of problems related to micron- and nano-sized solid particles in laboratory low-temperature plasmas. The first aspect of problems considered (which, for simplicity, can be referred to “applied aspect”) deals with the origin, growth, characterization, and industrial applications of fine particulate matter. The problems highlighted in Sections 2 and 3 certainly do not completely cover the fascinating variety of the complex physical and chemical processes involved in the growth and self-organization of the fine particles in the reactive ionized gas phase. Nevertheless, we focused on the existing established models of the particulate growth, self-organization, discharge restructuring caused by rapid dust agglomeration processes, and many other interesting phenomena. We note that the research and application of fine powders in low-temperature plasma discharges is a rapidly growing area, with the key focus gradually shifting towards the recognition of nanometer-sized grains (fine crystallites) as the major structural elements in many advanced thin film fabrication technologies. Thus, adequate in situ detection and ex situ characterization methods (with the ultimate goal to eventually perform the basic powder characterization in situ) are becoming a vital necessity for the future studies in the area.

We emphasize that in the last two decades fine solid particles in plasma processing facilities have been considered from different points of view. On one hand, they have originally been deemed inevitably deleterious process contaminants in microelectronics. We thus reviewed a significant progress in the development of various methods of removal and suppression of dust from the plasma enhanced chemical vapor deposition systems. It has also been recently discovered that radioactive dust can appear in the active zone of the toroidal plasma devices and, moreover, be a serious hazard for the safety operation of the future nuclear fusion facilities. Most recently, the plasma-grown solid grains have become increasingly attractive for a number of thin-film technologies including but not limited to low-temperature self-assembly of ordered nanoparticle arrays, nanocrystalline and polymorphous silicon-based thin films for optoelectronic functionalities and devices, biocompatible calcium phosphate-based bio-ceramics for dental surgery and orthopaedic applications, hard wear-resistant, self-lubricated, UV-protecting and many other functional coatings. Several other aspects of applications of ultra-fine powder particulates and larger solid grains have been discussed in Section 3 of this review. We note that despite a notable progress in the industrial applications of the plasma-grown micro-/nanoparticles, some of them still remain at the research and development stage.

In view of the most recent advances in the science and applications of fine powders reviewed here, control and manipulation (and eventually the adequate control strategies) of the plasma-grown solid particles is becoming the matter of outmost importance. However, this aim cannot be achieved without a proper understanding of the underlying physics of the basics of plasma–fine particle interactions. For this reason, reviewing the second aspect of the problems involved (which can be termed as the “fundamental aspect”) we focused on the current status of research into the dynamics and self-organization of the particulate matter, as well as various collective processes in low-temperature plasma–dust systems (Sections 4–8). We emphasize that without proper understanding of the fundamentals of basic dust–plasma (and wherever applicable dust–solid substrate/wall) interactions, it is impossible to adequately understand and self-consistently describe the real processes in the complex plasma systems with the variable-size particulate matter of complex shapes and internal organization. On the other hand, the knowledge of the collective phenomena involving charged fine particles is important in the studies of self-organization and mode transition phenomena in gas discharges that sustain the origin and growth of the dust grains.

Even though many of the “signature” physical phenomena in complex plasmas do happen and have been observed in the chemically active environments of the plasma processing facilities, the overwhelming complexity (in particular, because of numerous polymerization/clustering processes involved in the origin and growth of fine powders) of the real systems makes the study of basic processes in chemically active plasmas rather complicated. Therefore, to elucidate the underlying physics of the particle–plasma interactions, most of the basic experimental complex plasma research is currently conducted using model systems that usually include the inert ambient gas as well as externally dispersed over the plasma volume organic (dielectric) or metal powder particles. In such a way, it becomes possible to investigate the fundamental physics of many of the particle–plasma and particle–plasma–wall interactions, collective phenomena and complex nonlinear plasma structures (shocks, solitons, sheaths, dust voids, ordered liquid and crystal-like structures, etc.). Most of the basic phenomena of dust–plasma interactions have been discussed in the present review.

In particular, the basics of charging processes of the colloidal particles in low-temperature plasmas can serve as a sound background for the description of a wide variety of self-organization and collective processes in the complex plasma systems. We stress that the understanding of the dynamic

charging processes is indispensable for the self-consistent description of dynamics (involving various forces acting on the dust), agglomeration, growth, and ordering (into one-, two-, or three-dimensional structures) of micron- and nano-sized solid particles in the complex ionized gas systems. In Section 4, we have also shown how the dust charging processes affect the dynamic force balance on the fine particles in the near-electrode areas of the discharges in inert and chemically active gas feedstock.

Likewise, it is worthwhile to mention that the investigation of the dynamic force balance (including the electrostatic, gravity, ion/neutral drag, thermophoretic and other forces) proved instrumental in the explanation of many complex phenomena such as the formation and stability of dust clouds and voids, oscillations in the ordered arrays of fine particles, levitation and confinement of dust grains in the near-electrode areas, and many other phenomena discussed above. Therefore, the knowledge on the charging processes and forces on the dust particles forms a background for the development of the adequate techniques for probing the particulate–surface interactions and in situ detection and characterization of the size-varying ultra-fine powders in the plasma processing facilities.

As we have mentioned above, the complex solid particle–plasma system possess an outstanding capacity to self-organize into a number of ordered structures discussed in Section 5. We note that the emerging structures are thermodynamically open and involve numerous processes of creation and sink of the plasma electrons and ions, in particular on the surfaces of the dust grains. The examples given in Section 5 include a number of dissipative self-organized structures (e.g. dust–plasma sheath), plasma regions free of dust (dust voids), ordered Coulomb crystal-like lattices, liquid-like and gas-like ordered structures, and some others. Some of the above plasma–dust structures can be regarded as model systems for the study of solid-state crystals, non-crystalline solids, and even some complex astrophysical objects. Furthermore, a reliable visualization of the ordering and oscillations of the dust particles in such systems is crucial for the understanding of various physical processes at the most fundamental kinetic (microscopic) level.

Meanwhile, the presence of the charged solid component does modify the existing and create a number of new collective phenomena in the background plasma. In particular, the established flows of positive ions in the near-electrode areas of low-temperature laboratory dusty plasmas result in the formation of the plasma wakes, which, in turn, dynamically affect the charging, ordering, interactions, and dynamics of the dust grains (Section 6). In the above, we have reviewed the basics of the plasma wake formation, behind the dust grains of different (spherical and non-spherical) morphologies. We recall that the ordering of fine particles in complex plasmas allows one to draw analogies with more complex solid systems. As an example, similar to the Cooper pairing of electrons in semiconductors, the negatively charged dust grains can be coupled in the presence of the plasma wake. It is also interesting that in the case of subsonic plasma wakes, the attraction of fine particles can be attributed to the inverse Landau damping, which is another important collective plasma process.

Meanwhile, most of the plasma collective phenomena (e.g. plasma waves and oscillations at various time scales) are strongly modified due to the presence of dust (Section 7). Furthermore, the presence of a charged heavy component in the plasma introduces a completely new time scale (with some new normal plasma modes) associated with the collective motion of the dust grains. It is remarkable that the dust charging opens up a new channel of power dissipation in the plasma. In this case the dust charge appears as a new dynamic variable in the kinetic description of a complex plasma. We also note that the plasma instabilities at dust time scales reviewed in



Section 7 are directly relevant to more complex phenomena in dusty plasmas such as dust void formation (Section 5).

We have also reviewed the collective oscillations in the ordered arrays (relevant to the strongly coupled Coulomb lattices) of dust particles in the near-electrode areas (Section 8). Again, study into the charging and levitation of dust in the sheath region is one of the most important milestones in the solution of the above complex problem. We emphasize that the parameters of the background plasmas as well as the external forces strongly affect the arrangements, equilibrium states and collective oscillations of the ordered fine particle arrays. We also note that vertical and horizontal arrangements of dust grains of different morphologies in the plasma sheath areas have a direct relevance to the controlled deposition of the ordered nanoparticle arrays discussed in Section 3.

We remark that the “applied” and “fundamental” aspects of the problems considered above are inseparably associated with each other. In the following, we will present our vision on how the above research components can interact and contribute to the solution of the challenging global problem of the development of control strategies and manipulation techniques of the complex plasma-nanoparticle systems.

Specifically, deposition of the plasma-grown building blocks onto pre-patterned substrates (see Sections 3.4 and 3.5) is a typical example of the problem that still requires a major conceptual advance in the near future. We now outline the major upcoming challenges in the study of the fundamental physics of multi-scale dynamic processes in self-organized gaseous plasma systems with nanometer sized clusters/particulates for the ordered nano-scale assemblies. These assemblies can be extremely important for the future optoelectronic/photonic applications and the development of advanced nano-structured materials. Technology using the ordered nano-structures, such as the fabrication of nanoelectronic and photonic devices, is anticipated to be extremely important in the coming years.

New approaches to the analysis of the behavior and manipulation of the complex plasma systems, based on advanced physical models of the interaction of nano-sized clusters/particulates with their ionized reactive plasma environments and nano-patterned substrate surfaces become a vital demand for the coming years. The ultimate aim of such research is to tailor the size, composition, and architecture of the gas-phase grown clusters/nanoparticles as building units for the assembly of ordered nanoparticle arrays and nanostructured materials. Specifically, we expect that the physical foundations of novel ordered nano-scale assembly concepts will employ reactive plasma-grown charged nanoparticles as building units and nanostructured materials as nanopatterned substrates. New control strategies for such systems are anticipated to advance the existing approaches to the development of new classes of nanoelectronic and photonic functionalities and devices.

The results reviewed here bring in a refreshing enthusiasm into a wider use of variety of the physical processes in the plasma enhanced chemical vapour deposition systems, which have recently been successfully applied for the fabrication and tailoring the structure and basic properties of the matter at length scales comparable to the sizes of large molecules, and to create nano-sized objects, such as nanoparticles, nanowires, nanotubes, quantum dots, and other structures with complex shapes. The ability to control function via tailoring the nano-object size makes them extremely attractive for technological applications in high-speed computing, data storage, high-performance displays, ultra-wide bandwidth and high-speed optical communications, quantum-dot lasers, etc. It is notable that the design of relevant devices requires not only strict control of the nanoparticle size but also assembly of ordered arrays of nano-sized objects. At present, the adequate results (which are

unfortunately outside the scope of this review) have been achieved in tailoring of the size, shape, and some other parameters of the structures, which are very important for certain applications including field emitters, nanoelectrode arrays and many others.

However, control of the nano-object ordering and site density over industrially viable surface areas remains a challenging task for the coming years and we anticipate that ordered arrays of the plasma-grown individual nanoparticles and complex structures can play a pivotal role in the solution of the above problem. Furthermore, the question of the fundamental physical mechanisms leading to the ordered self-assembly processes at nano-scales still remains open. Some of the key problems in this regard are related to the formation of the fundamental building blocks of the structures in the ionized gas phase, and the self-organization of them into the nano-sized ordered structures either in the plasma bulk or on the solid surface.

Another challenging problem is related to technological and economical limitations in lithographic technologies using optical, electron, or X-ray beams for the next stage of sub-100 nm ultra-large scale integration semiconductor devices. For this reason, it is expected that in the near future, the development of ULSI compatible self-organization methods for the assembly of nanostructures, which do not require artificial time and labor-consuming pattern delineation routines, will become a problem of the outmost importance.

We emphasize that chemically active ionized gas environments of PECVD systems reviewed here are good candidates for solution of all of the above problems. First, reactive plasmas are prone of the entire spectrum of the building units for the nano-assemblies, ranging from neutral/excited/ionized atoms and molecules, to nano-clusters and more complex nanoparticles. Second, the composition of the reactive species responsible for certain assemblies can be tailored to fit any specific conditions for the plasma–surface interaction. Above all, the complex system involving the plasma with colloidal nanometer-sized clusters/particles and solid substrate surface can self-organize to promote the efficient nanopatterning of the substrate, followed by the required ordered nanostructure growth.

However, the application of the plasma–particle systems to nano-scale processes is still at an early stage, and a number of fundamental physical problems at different dynamically coupled space and time scales are yet to be solved before the scheme can become industrially viable. First, the nanoassembly process will not be feasible without a precise control of the composition, size, and architecture of the plasma-grown building blocks. Furthermore, the building units have to be deposited on the nanopatterned substrate in a non-destructive fashion, preserving their unique features. The optimal parameters of the ionized gas phase allowing a predictable and controllable fabrication process have yet to be established and linked to the process control parameters. However, despite a notable recent progress in the growth of nanostructures, the working parameters of many nanoassembly experiments are still often chosen by trial and error. This practice should certainly be replaced in the near future by a number of highly-predictable (via appropriate modeling and simulation) processes.

We now briefly summarize the conceptual challenges still not adequately resolved in the most advanced existing models (some of them have been reviewed above). The existing knowledge of cluster/particulate dynamics in reactive plasmas is mostly limited to experimental detection, size measurement of particles, and attempts to growth control. The key obstacle in the self-consistent modeling of particle dynamics in near-substrate areas of chemically active environments lies in the appropriate treatment of plasma–particle and particle–surface interactions, involving flows of numerous reactive species onto the grain/substrate surface, secondary electrons, reactive chemical etching of the substrate surface, particle size and substrate surface morphology variation due to deposition/re-deposition

of thin films, etc. The relevant existing theories do not account for the chemical interactions of reactive species and the particle/substrate surfaces, and consider essentially stationary cases. However, the stationary models for particle–plasma interaction have a limited relevance to chemically active plasmas, as the balance between microscopic electron/ion/radical flows on the particle/substrate surface varies continuously. Above all, the existing models are not applicable to nano-objects approaching in size to large molecules, when the electron confinement effects come into play.

Thus, the complexity of the problem requires further conceptual advances in the description of the charging, dynamics, and interaction of nano-sized particles with nanostructured surfaces. Moreover, the appropriate models of the ordered nano-structure growth should properly address the open character of the complex plasma-nanostructured solid surface system and self-consistently account for the sources and sinks of all the particles involved. Therefore, novel methodologies that will eliminate the existing conceptual shortcomings outlined above and will advance the existing knowledge on the complex self-organized systems involving reactive plasmas with nano-colloidal particles and nano-structured substrates targeted for the ordered nano-assembly processes are highly warranted in the near future.

From the experimental point of view, the real-time detection, number density, size, and composition measurements still require a greater precision and reliability to be suitable for immediate industrial applications. Thus, the diagnostics of complex nanoparticle-loaded plasma systems should evolve into real-time, in situ monitoring of dynamic variations of grain size and elemental composition, alongside with the real-time diagnostic of the plasma species and other plasma parameters.

Finally, challenges in theoretical modeling and new fascinating industrial applications reviewed here do suggest that complex ionized gas systems have a remarkable future from both the fundamental knowledge and applications points of view and warrant further extensive theoretical and experimental efforts.

## Acknowledgements

The authors are deeply thankful to many of their colleagues, in particular to N.F. Cramer, V.E. Fortov, J. Goree, O. Ishihara, B. James, G. Morfill, M. Nambu, A. Samarian, L. Stenflo, H. Sugai, V.N. Tsytovich, O.S. Vaulina, S. Xu, and M. Yu (alphabetic order) for collaboration in some of the works discussed as well as many other colleagues for fruitful collaborations and discussions, all the authors of the original figures for their kind permissions for reproduction, and A. Samarian for providing unpublished optical images of dust structures. K.O. thanks C.H. Diong for stimulating discussions and support at Nanyang Technological University and R.G. Storer for hospitality at Flinders University. This work was partially supported by the Australian Research Council, the Agency for Science, Training, and Research of Singapore, Lee Kuan Yew Foundation, The University of Sydney, and the Flinders Institute for Research in Science and Technology.

## References

- [1] R.J. Gould, E.E. Salpeter, The interstellar abundance of the hydrogen molecule. I. Basic processes, *Astrophys. J.* 138 (1963) 393–412.
- [2] C.K. Goertz, Dusty plasmas in the solar system, *Rev. Geophys.* 27 (1989) 271–292.

- [3] E.C. Whipple, Potential of surfaces in space, *Rep. Prog. Phys.* 44 (1981) 1197–1250.
- [4] T.G. Northrop, Dusty plasmas, *Phys. Scr.* 45 (1992) 475–490.
- [5] A. Garscadden, B.N. Ganguly, P.D. Haaland, J. Williams, Overview of growth and behaviour of clusters and particles in plasmas, *Plasma Sources Sci. Technol.* 3 (1994) 239–245.
- [6] M. Shiratani, H. Kawasaki, T. Fukuzawa, H. Tsuruoka, T. Yoshioka, Y. Watanabe, Study on growth processes of particulates in helium-diluted silane rf plasmas using scanning electron microscopy, *Appl. Phys. Lett.* 65 (1994) 1900–1902.
- [7] H.M. Thomas, G.E. Morfill, Melting dynamics of a plasma crystal, *Nature (London)* 379 (1996) 806–809. \*\*
- [8] P. Jensen, Growth of nanostructures by cluster deposition: experiments and simple models, *Rev. Mod. Phys.* 71 (1999) 1695–1735.
- [9] N.M. Hwang, W.S. Cheong, D.Y. Yoon, D.Y. Kim, Growth of silicon nanowires by chemical vapor deposition: approach by charged cluster model, *J. Cryst. Growth* 218 (2000) 33–39. \*\*
- [10] V.N. Tsytovich, Dust plasma crystals, drops, and clouds, *Physics-Uspekhi* 40 (1997) 53–94 [*Usp. Fiz. Nauk* 167 (1997) 57–99].
- [11] V.N. Tsytovich, G.E. Morfill, H. Thomas, Complex plasmas: I. Complex plasmas as unusual state of matter, *Plasma Phys. Rep.* 28 (2002) 623–651 [*Fizika Plazmy* 28 (2002) 675–707].
- [12] S.V. Vladimirov, Propagation of waves in dusty plasmas with variable charges on dust particles, *Phys. Plasmas* 1 (1994) 2762–2767. \*\*\*
- [13] K.N. Ostrikov, S.V. Vladimirov, M.Y. Yu, G.E. Morfill, Low-frequency dispersion properties of plasmas with variable-charge impurities, *Phys. Plasmas* 7 (2000) 461–465. \*\*\*
- [14] L. Boufendi, A. Bouchoule, Particle nucleation and growth in a low-pressure argon–silane discharge, *Plasma Sources Sci. Technol.* 3 (1994) 262–267.
- [15] Ch. Hollenstein, The physics and chemistry of dusty plasma, *Plasma Phys. Contr. Fusion* 42 (2000) R93.
- [16] U. Kortshagen, U. Bhandarkar, Modeling of particulate coagulation in low pressure plasmas, *Phys. Rev. E* 60 (1999) 887–898. \*\*
- [17] A. Gallagher, Model of particle growth in silane discharges, *Phys. Rev. E* 62 (2000) 2690–2706.
- [18] U.V. Bhandarkar, M.T. Swihart, S.L. Girshik, U. Kortshagen, Modeling of silicon hydride clustering in a low-pressure silane plasma, *J. Phys. D: Appl. Phys.* 33 (2000) 2731–2746. \*
- [19] Y. Watanabe, M. Shiratani, K. Koga, Formation kinetics and control of dust particles in capacitively coupled reactive plasmas, *Phys. Scr. T* 89 (2001) 29–32.
- [20] Y. Watanabe, Dust phenomena in processing plasmas, *Plasma Phys. Control Fusion* 39 (1997) A59–A72.
- [21] K. Koga, Y. Matsuoka, K. Tanaka, M. Shiratani, Y. Watanabe, In situ observation of nucleation and subsequent growth of clusters in silane radio frequency discharge, *Appl. Phys. Lett.* 77 (2000) 196–198.
- [22] A. Leroux, W.M.M. Kessels, D.C. Schram, M.C.M. van de Sanden, Modeling of the formation of cationic silicon clusters in a remote Ar/H<sub>2</sub>/SiH<sub>4</sub> plasma, *J. Appl. Phys.* 88 (2000) 537–543.
- [23] S.J. Choi, M.J. Kushner, The role of negative ions in the formation of particles in low-pressure plasmas, *J. Appl. Phys.* 74 (1993) 853–861.
- [24] A.A. Howling, C. Courteille, J.L. Dorier, L. Sansonnens, C. Hollenstein, From molecules to particles in silane plasmas, *Pure Appl. Chem.* 68 (1996) 1017–1022.
- [25] A. Bouchoule, L. Boufendi, Particulate formation and dusty plasma behaviour in argon–silane RF discharge, *Plasma Sources Sci. Technol.* 2 (1993) 204–213.
- [26] A.A. Fridman, L. Boufendi, T. Hbid, B.N. Potapkin, A. Bouchoule, Dusty plasma formation: physics and critical phenomena, Theoretical approach, *J. Appl. Phys.* 79 (1996) 1303–1314. \*\*
- [27] L. Boufendi, A. Bouchoule, R.K. Porteous, J.Ph. Blondeau, A. Plain, C. Laure, Particle–particle interactions in dusty plasmas, *J. Appl. Phys.* 73 (1993) 2160–2162.
- [28] S. Stoykov, C. Eggs, U. Kortshagen, Plasma chemistry and growth of nanosized particles in a C<sub>2</sub>H<sub>2</sub> Rf discharge, *J. Phys. D: Appl. Phys.* 34 (2001) 2160–2173. \*
- [29] Ch. Deschenaux, A. Affolter, D. Magni, Ch. Hollenstein, P. Fayet, Investigations of CH<sub>4</sub>, C<sub>2</sub>H<sub>2</sub> and C<sub>2</sub>H<sub>4</sub> dusty RF plasmas by means of FTIR absorption spectroscopy and mass spectrometry, *J. Phys. D: Appl. Phys.* 32 (1999) 1876–1886.
- [30] S. Hong, J. Berndt, J. Winter, Study of dust particle formation and its applications in argon/methane and argon/acetylene mixtures, *Proceedings of the Third International Conference on Dusty Plasmas (ICDPD-2002)*, Durban, South Africa, 20–24 May 2002, C14.

- [31] E. Covacevic, I. Stefanovic, J. Berndt, J. Winter, Infrared fingerprints and periodic formation of nanoparticles in Ar/C<sub>2</sub>H<sub>2</sub> plasmas, *J. Appl. Phys.* 93 (2003) 2924–2930.
- [32] S. Hong, J. Berndt, J. Winter, Growth precursors and dynamics of dust particle formation in the Ar/CH<sub>4</sub> and Ar/C<sub>2</sub>H<sub>2</sub> plasmas, *Plasma Sources Sci. Technol.* 12 (2003) 46–52. \*\*
- [33] Z.L. Tsakadze, K. Ostrikov, J.D. Long, S. Xu, Self-assembly of large-area uniform carbon nanotip structures in chemically active inductively coupled plasmas: minimization of the growth temperature, *Diamond Relat. Mater.*, 2003, in press.
- [34] I.B. Denysenko, S. Xu, P.P. Rutkevych, J.D. Long, N.A. Azarenkov, K. Ostrikov, Modeling of inductively coupled Ar/CH<sub>4</sub>/H<sub>2</sub> plasmas in PECVD of ordered carbon nanotip structures, *J. Appl. Phys.* 95 (2004), in press.
- [35] Y.E. Lozovik, A.M. Popov, Formation mechanism of nanoparticles in arc discharge, *Molec. Cryst. Liq. Cryst. Sci. Technol. C—Molec. Mater.* 7 (1996) 89–92.
- [36] H. Kokura, S. Yoneda, K. Nakamura, N. Mitsuhiro, M. Nakamura, . Sugai, Diagnostic of surface wave plasma for oxide etching in comparison with inductive RF plasma, *Jpn. J. Appl. Phys. Part I* 38 (1999) 5256–5261.
- [37] R.J. Buss, W.A. Hareland, Gas phase particulate formation in radiofrequency fluorocarbon plasmas, *Plasma Sources Sci. Technol.* 3 (1994) 268–272.
- [38] K. Takahashi, K. Tachibana, Molecular composition of films and solid particles polymerized in fluorocarbon plasmas, *J. Appl. Phys.* 89 (2001) 893–899. \*
- [39] K. Takahashi, K. Tachibana, Solid particle production in fluorocarbon plasmas. I. Correlation with polymer film deposition, *J. Vac. Sci. Technol. A* 19 (2001) 2055–2060.
- [40] K. Takahashi, K. Tachibana, Solid particle production in fluorocarbon plasmas. II. Gas phase reactions for polymerization, *J. Vac. Sci. Technol. A* 20 (2002) 305–312.
- [41] L. Boufendi, A. Bouchoule, Industrial developments of scientific insights in dusty plasmas, *Plasma Sources Sci. Technol.* 11 (2002) A211–A218.
- [42] P. Roca i Cabarrocas, A. Fontcuberta i Morral, A.V. Kharchenko, S. Lebib, L. Boufendi, S. Huet, M. Mikikian, M. Jouanny, A. Bouchoule, Plasma grown particles: from injected gases to nanoparticles and nanomaterials, from injected particles to dust clouds in the PKE experiment, in: R. Bharuthram, et al., (Eds.), *AIP Conference Proceedings* 649, Dusty Plasmas in the New Millenium: Third International Conference on the Physics of Dusty Plasmas, American Institute of Physics, New York, 2002, pp. 45–52.
- [43] R. Bingham, V.N. Tsytovich, The criteria for dust agglomeration in plasmas, *IEEE Trans. Plasma Sci.* 29 (2001) 158–163.
- [44] J. Goree, Charging of particles in a plasma, *Plasma Sources Sci. Technol.* 3 (1994) 400–406. \*\*
- [45] M.S. Barnes, J.H. Keller, J.C. Forster, J.A. O'Neill, D.K. Coultas, Transport of dust particles in glow-discharge plasmas, *Phys. Rev. Lett.* 68 (1992) 313–316. \*\*\*
- [46] S. Ashida, C. Lee, M.A. Lieberman, Spatially averaged (global) model of time modulated high density argon plasmas, *J. Vac. Sci. Technol. A* 13 (1995) 2498–2507.
- [47] P.C. Reist, *Aerosol Science and Technology*, 2nd Edition, McGraw Hill, New York, 1993.
- [48] M.A. Lieberman, A.J. Lichtenberg, *Principles of Plasma Discharges and Materials Processing*, Wiley, New York, 1994.
- [49] A.V. Ivlev, G.E. Morfill, U. Konopka, Coagulation of charged microparticles in neutral gas and charge-induced gel transitions, *Phys. Rev. Lett.* 89 (2002) 195502/1-4.
- [50] S. Nonaka, S. Ikezawa, Y. Nakamura, K. Katoh, Typical characteristics of RF voltage thresholds for planar dusty RF discharges, in: R. Bharuthram, et al., (Eds.), *AIP Conference Proceedings* 649, Dusty Plasmas in the New Millenium: Third International Conference on the Physics of Dusty Plasmas, American Institute of Physics, New York, 2002, pp. 184–187.
- [51] D. Samsonov, J. Goree, Particle growth in a sputtering discharge, *J. Vac. Sci. Technol. A* 17 (1999) 2835–2840. \*
- [52] G. Selwyn, J. McKillop, K. Haller, J. Wu, In situ plasma contamination measurements by He–Ne laser light scattering: a case study, *J. Vac. Sci. Technol. A* 8 (1990) 1726–1731.
- [53] G.M. Jellum, J.E. Daugherty, D.B. Graves, Particle thermophoresis in low pressure glow discharges, *J. Appl. Phys.* 69 (1991) 6923–6934.
- [54] B. Ganguly, A. Garscadden, J. Williams, P. Haaland, Growth and morphology of carbon grains, *J. Vac. Sci. Technol. A* 11 (1993) 1119–1125.
- [55] F. Huang, M. Kushner, Shapes of agglomerates in plasma etching reactors, *J. Appl. Phys.* 81 (1997) 5960–5965.



- [56] G.S. Selwyn, C.A. Weiss, F. Sequeda, C. Huang, Particle contamination formation in magnetron sputtering processes, *J. Vac. Sci. Technol. A* 15 (1997) 2023–2028.
- [57] H.M. Anderson, S. Radovanov, J.L. Mock, P.J. Resnick, Particles in  $C_2F_6$ -CHF<sub>3</sub> and CF<sub>4</sub>-CHF<sub>3</sub> etching plasmas, *Plasma Sources Sci. Technol.* 3 (1994) 302–309.
- [58] I.I. Beilis, M. Keidar, R.L. Boxman, S. Goldsmith, Macroparticle separation and plasma collimation in positively biased ducts in filtered vacuum arc deposition systems, *J. Appl. Phys.* 85 (1999) 1358–1365.
- [59] M. Hirasawa, H. Shirakawa, H. Hamamura, Y. Egashira, H. Komiyama, Growth mechanism of nanoparticles prepared by radio frequency sputtering, *J. Appl. Phys.* 82 (1997) 1404–1407.
- [60] L. Boufendi, J. Gaudin, S. Huet, G. Viera, M. Dudemaine, Detection of particles of less than 5 nm in diameter formed in an argon–silane capacitively coupled radio-frequency discharge, *Appl. Phys. Lett.* 79 (2001) 4301–4303. \*
- [61] Kwang Soo Seol, Y. Tsutatani, T. Fujimoto, Y. Okada, New in situ measurement method for nanoparticles formed in a radio frequency plasma-enhanced chemical vapor deposition reactor, *J. Vac. Sci. Technol. B* 19 (2001) 1998–2000.
- [62] W.D. Reents Jr., S.W. Downey, A.B. Emerson, A.M. Mjtsce, A.J. Muller, D.J. Siconolfi, J.D. Sinclair, A.G. Swanson, Real-time compositional analysis of submicrometre particles, *Plasma Sources Sci. Technol.* 3 (1994) 369–372.
- [63] U. Kortshagen, On the use of dust plasma acoustic waves for the diagnostic of nanometer-sized contaminant particles in plasmas, *Appl. Phys. Lett.* 71 (1997) 208–210.
- [64] Ch. Hollenstein, W. Schwarzenbach, A.A. Howling, C. Courteille, J.-L. Dorier, L. Sansonnens, Anionic clusters in dusty hydrocarbon and silane plasmas, *J. Vac. Sci. Technol. A* 14 (1996) 535–539.
- [65] E. Bertran, J. Costa, G. Sardin, J. Campmany, J.L. Andujar, A. Canillas, Effects of plasma processing on the microstructural properties of silicon powders, *Plasma Sources Sci. Technol.* 3 (1994) 348–354.
- [66] R. Bingham, V.N. Tsytovich, Dust growth in astrophysical plasmas, in: R. Bharuthram, et al., (Eds.), *AIP Conference Proceedings 649, Dusty Plasmas in the New Millenium: Third International Conference on the Physics of Dusty Plasmas*, American Institute of Physics, New York, 2002, pp. 126–134.
- [67] J. Perrin, Ch. Hollenstein, Sources and growth of particles, in: A. Bouchoule (Ed.), *Dusty Plasmas: Physics, Chemistry, and Technological Impacts in Plasma Processing*, Wiley, Chichester UK, 1999.
- [68] The National Technology Roadmap for Semiconductors, Technical Report of the Semiconductor Industry Association, <http://notes.sematech.org/NTRS>.
- [69] G. Kroesen, Dusty plasmas in industry: from combustion to deposition, The Invited Topical Review Talk, Third International Conference on the Physics of Dusty Plasmas (ICPDP-2002), Durban, South Africa, 20–24 May 2002, Book of Abstracts, p. 12.
- [70] Y.J.T. Lii, Etching, in: C.Y. Chang, S.M. Sze (Eds.), *ULSI Technology*, McGraw-Hill, New York, 1996, pp. 329–370.
- [71] G.S. Selwyn, Optical characterization of particle traps, *Plasma Sources Sci. Technol.* 3 (1994) 340–347.
- [72] G. Lapenta, J.U. Brackbill, Simulation of dust particle dynamics for electrode design in plasma discharges, *Plasma Sources Sci. Technol.* 6 (1997) 61–69.
- [73] W. Boehme, W.E. Koehler, M. Roemheld, S. Veprek, R.J. Seeboeck, Observation of dust particle growth and fallout in RF-excited silane discharges, *IEEE Trans. Plasma Sci.* 22 (1994) 110–115.
- [74] H. Kersten, H. Deutsch, E. Stoffels, W.W. Stoffels, G.M.W. Kroesen, R. Hippler, Micro-disperse particles in plasmas: from disturbing side effects to new applications, *Contrib. Plasma Phys.* 41 (2001) 598–609. \*\*
- [75] G. Uchida, S. Iizuka, N. Sato, Fine-particle clouds controlled in a DC discharge plasma, *IEEE Trans. Plasma Sci.* 29 (2001) 274–278.
- [76] J. Perrin, P. Molinas-Mata, P. Belenguer, Ion drag and plasma-induced thermophoresis on particles in radiofrequency glow discharges, *J. Phys. D.: Appl. Phys.* 27 (1994) 2499–2507.
- [77] M. Klindworth, A. Melzer, A. Piel, Laser-excited intershell rotation of finite Coulomb clusters in a dusty plasma, *Phys. Rev. B* 61 (2000) 8404–8415.
- [78] J. Goree, T.E. Sheridan, Particulate release from surfaces exposed to a plasma, *J. Vac. Sci. Technol. A* 10 (1992) 3540–3544.
- [79] G.S. Selwyn, Particulate contamination removal from wafers using plasmas and mechanical agitation, US Patent No. 5,849,135 (1998).



- [80] H.H. Hwang, E.R. Keiter, M.J. Kushner, Consequences of three-dimensional physical and electromagnetic structures on dust particle trapping in high plasma density material processing discharges, *J. Vac. Sci. Technol. A* 16 (1998) 2454–2462.
- [81] S.E. Beck, S.M. Collins, J.F. O'Hanlon, A study of methods for moving particles in Rf processing plasmas, *IEEE Trans. Plasma Sci.* 22 (1994) 128–135.
- [82] H. Fujiyama, Y. Maemura, M. Ohtsu, Effects of crossed magnetic fields on silicon particles in plasma chemical vapor deposition process, *Jpn. J. Appl. Phys. Part 1* 38 (1999) 4550–4555.
- [83] M. Rosenberg, D.A. Mendis, Use of UV to reduce particle trapping in process plasmas, *IEEE Trans. Plasma Sci.* 24 (1996) 1133–1136.
- [84] M. Shiratani, S. Maeda, K. Koga, Y. Watanabe, Effects of gas temperature gradient, pulse discharge modulation, and hydrogen dilution on particle growth in silane RF discharges, *Jpn. J. Appl. Phys.* 39 (2000) 287–293.
- [85] Y. Watanabe, M. Shiratani, K. Koga, Nucleation and subsequent growth of clusters in reactive plasmas, *Plasma Sources Sci. Technol.* 11 (2002) A229–A233.
- [86] J. Winter, A.P. Fortov, A.P. Nefedov, Radioactive dust levitation and its consequences for fusion devices, *J. Nucl. Mater.* 290–293 (2001) 509–512.
- [87] J. Winter, Dust: a new challenge in nuclear fusion research?, *Phys. Plasmas* 7 (2000) 3862–3866. \*\*
- [88] J.P. Sharpe, B.J. Merrill, D.A. Petti, M.A. Bourham, J.G. Gilligan, Modeling of particulate production in the SIRENS plasma disruption simulator, *J. Nucl. Mater.* 290 (2001) 1128–1133.
- [89] V.E. Fortov, V.I. Vladimirov, L.V. Deputatova, A.P. Nefedov, V.A. Rykov, A.V. Khudyakov, Removal of dust particles from technological plants, *Dokl. Phys.* 47 (2002) 367–369.
- [90] T. Yokomine, A. Shimizu, M. Okuzono, The possibility of dust removal in fusion plasma device using thermophoretic force, *Fusion Technol.* 39 (2001) 1028–1032.
- [91] S. Iijima, Helical microtubules of graphitic carbon, *Nature (London)* 354 (1991) 56–58.
- [92] M. Meyyappan, Carbon nanotube based nanotechnology, *Bull. Amer. Phys. Soc.* 45 (2000) 65.
- [93] S. Iijima, T. Ichihashi, Single-shell carbon nanotubes of 1-nm diameter, *Nature (London)* 363 (1993) 603–605.
- [94] B. Wei, J. Zhang, J. Liang, D. Wu, The mechanism of phase transformation from carbon nanotube to diamond, *Carbon* 36 (1998) 997–1001.
- [95] L.J. Ci, B.Q. Wei, C.L. Xu, J. Liang, D.H. Wu, S.S. Xie, W.Y. Zhou, Y.B. Li, Z.Q. Liu, D.S. Tang, Crystallization behavior of the amorphous carbon nanotubes prepared by the CVD method, *J. Cryst. Growth* 233 (2001) 823–828.
- [96] M. Yudasako, Kikuchi Rie, Y. Ohki, E. Ota, S. Yoshimura, Behavior of Ni in carbon nanotube nucleation, *Appl. Phys. Lett.* 70 (1997) 1817–1819.
- [97] M.S. Dresselhaus, G. Dresselhaus, P.C. Eklund, *Science of Fullerenes and Carbon Nanotubes*, Academic Press, San Diego, 1996.
- [98] E.T. Thostenson, Z. Ren, T.W. Chou, Advances in the science and technology of carbon nanotubes and their composites: a review, *Compos. Sci. Technol.* 61 (2001) 1899–1912.
- [99] Z.F. Ren, A.P. Huang, J.W. Xu, J.H. Wang, P. Bushu, M.P. Siegal, P.N. Provencio, Synthesis of large arrays of well-aligned carbon nanotubes on glass, *Science* 282 (1998) 1005–1007.
- [100] M. Meyyappan, L. Delzeit, A. Cassel, D. Hash, Carbon nanotube growth by PECVD: a review, *Plasma Sources Sci. Technol.* 12 (2003) 205–216.
- [101] H. Murakami, M. Hirakawa, C. Tanaka, H. Yamakawa, Field emission from well-aligned, patterned, carbon nanotube emitters, *Appl. Phys. Lett.* 76 (2000) 1776–1778.
- [102] L. Delzeit, I. McIninch, B.A. Cruden, D. Hash, B. Chen, J. Han, M. Meyyappan, Growth of multiwall carbon nanotubes in an inductively coupled plasma reactor, *J. Appl. Phys.* 91 (2002) 6027–6033. \*
- [103] Y. Hayashi, T. Otoguro, M. Kawana, H. Hayashi, S. Nishino, Synthesis of carbon nanotubes by plasma chemical vapor deposition, XXV International Conference on Phenomena in Ionized Gases, July 17–22, 2001, Nagoya, Japan, Proceedings, Vol. 3, pp. 77–78.
- [104] H. Sugai, I. Ghanashev, M. Nagatsu, High-density flat plasma production based on surface waves, *Plasma Sources Sci. Technol.* 7 (1998) 192–205.
- [105] O.A. Louchev, J.R. Hester, Kinetic pathways of carbon nanotube nucleation from graphitic nanofragments, *J. Appl. Phys.* 94 (2003) 2002–2010.
- [106] D.B. Hash, M. Meyyappan, Model based comparison of thermal and plasma chemical vapor deposition of carbon nanotubes, *J. Appl. Phys.* 93 (2003) 750–752.

- [107] D. Hash, D. Bose, T.R. Govindan, M. Meyyappan, Simulation of the dc plasma in carbon nanotube growth, *J. Appl. Phys.* 93 (2003) 6284–6290.
- [108] S. Hofmann, C. Ducati, J. Robertson, B. Kleinsorge, Low-temperature growth of carbon nanotubes by plasma-enhanced chemical vapor deposition, *Appl. Phys. Lett.* 83 (2003) 135–137.
- [109] M. Tanemura, K. Iwata, K. Takahashi, Y. Fujimoto, F. Okuyama, H. Sugie, V. Filip, Growth of aligned carbon nanotubes by plasma-enhanced chemical vapor deposition: optimization of growth parameters, *J. Appl. Phys.* 90 (2001) 1529–1533.
- [110] P. Pomorski, C. Roland, H. Guo, J. Wang, First-principles investigation of carbon nanotube capacitance, *Phys. Rev. B* 67 (2003) 161404(R)/1–4.
- [111] J. Perrin, J. Schmidt, C. Hollenstein, A. Howling, L. Sansonnens, The physics of plasma-enhanced chemical vapour deposition for large-area coatings: industrial application to flat panel displays and solar cells, *Plasma Phys. Control. Fusion* 42 (2000) B353–B363.
- [112] G. Bruno, P. Capezutto, G. Cicala, in: G. Bruno, P. Capezutto, A. Madan (Eds.), *Amorphous Silicon Based Devices*, Academic Press, New York, 1995, pp. 1–57.
- [113] G.J. Nienhuis, W.J. Goedheer, E.A.G. Hamers, W.G.J.H.M. van Sark, J. Bezemer, A self-consistent fluid model for radio-frequency discharges in  $\text{SiH}_4\text{--H}_2$  compared to experiments, *J. Appl. Phys.* 82 (1997) 2060–2071.
- [114] A. Hadjadj, L. Boufendi, S. Huet, S. Schelz, P. Roca i Cabarrocas, H. Estrade-Szwarckopf, B. Rousseau, Role of the surface roughness in laser induced crystallization of nanostructured silicon films, *J. Vac. Sci. Technol. A* 18 (2000) 529–535.
- [115] R. Martins, H. Aguas, I. Ferreira, V. Silva, A. Cabrita, E. Fortunato, Role of ion bombardment and plasma impedance on the performances presented by undoped a-Si:H films, *Thin Solid Films* 383 (2001) 165–168.
- [116] R. Martins, H. Aguas, V. Silva, I. Ferreira, E. Fortunato, Nanostructured silicon films produced by PECVD, *Mater. Res. Soc. Symp. Proc.* 664 (2001) A9.6.1–A9.6.6. \*\*
- [117] G. Viera, M. Mikikian, E. Bertran, P. Roca i Cabarrocas, L. Boufendi, Atomic structure of the nanocrystalline Si particles appearing in nanostructured Si films produced in low-temperature radiofrequency plasmas, *J. Appl. Phys.* 92 (2002) 4684–4694.
- [118] E. Bertran, S.N. Sharma, G. Viera, J. Costa, P. St'ahel, P. Roca i Cabarrocas, Effect of the nanoparticles on the structure and crystallization of amorphous silicon films produced by RF glow discharge, *J. Mater. Res.* 13 (9) (1998) 2476–2479.
- [119] P. Roca i Cabarrocas, S. Hamma, S.N. Sharma, G. Viera, E. Bertran, J. Costa, Nanoparticle formation in low-pressure silane plasmas: bridging the gap between a-Si:H and  $\mu\text{c-Si}$  films, *J. Non-Cryst. Solids* 227–230 (1998) 871–875.
- [120] G. Viera, S. Huet, E. Bertran, L. Boufendi, Polymorphous Si thin films from radio frequency plasmas of  $\text{SiH}_4$  diluted in Ar: a study by transmission electron microscopy and Raman spectroscopy, *J. Appl. Phys.* 90 (2001) 4272–4280.
- [121] P. Roca i Cabarrocas, P. Gay, A. Hadjadj, Experimental evidence of nanoparticle deposition in continuous argon–silane plasmas: effects of nanoparticles on film properties, *J. Vac. Sci. Technol. A* 14 (1996) 655–659.
- [122] G. Viera, E. Garcia-Caurel, J. Costa, J.L. Andujar, E. Bertram, Nanoparticles of Si–C–N from low-temperature RF plasmas: selective size, composition and structure, *Appl. Surf. Sci.* 145 (1999) 702–707.
- [123] A. Bapat, C.R. Perrey, S.A. Campbell, C.B. Carter, U. Kortshagen, Synthesis of highly-oriented, single-crystal silicon nanoparticles in a low-pressure, inductively coupled plasma, *J. Appl. Phys.* 94 (2003) 1969–1974.
- [124] R. Tews, G. Suchaneck, A. Kottwitz, A model for high-rate film deposition from dusty Rf discharges, *Surf. Coat. Technol.* 97 (1997) 79–84.
- [125] J. Perrin, M. Shiratani, P. Kae-Nune, H. Videlot, J. Jolly, J. Guillon, Surface reaction probabilities and kinetics of H,  $\text{SiH}_3$ ,  $\text{Si}_2\text{H}_5$ ,  $\text{CH}_3$ , and  $\text{C}_2\text{H}_5$  during deposition of a-Si:H and a-C:H from  $\text{H}_2$ ,  $\text{SiH}_4$ , and  $\text{CH}_4$  discharges, *J. Vac. Sci. Technol. A* 16 (1998) 278–289.
- [126] R. Dewarrat, J. Robertson, Binding and surface diffusion of  $\text{SiH}_3$  radicals and the roughness of hydrogenated amorphous silicon, *Appl. Phys. Lett.* 82 (2003) 883–885.
- [127] A.H.M. Smets, W.M.M. Kessels, M.C.M. van de Sanden, Temperature dependence of the surface roughness evolution during hydrogenated amorphous silicon film growth, *Appl. Phys. Lett.* 82 (2003) 865–867.
- [128] M. Takai, T. Nishimoto, M. Kondo, A. Matsuda, Effect of higher-silane formation on electron temperature in a silane glow-discharge plasma, *Appl. Phys. Lett.* 77 (2000) 2828–2830. \*

- [129] Y. Hori, K. Ostrikov, H. Toyoda, and H. Sugai, Effect of fine particles on electron temperature in hydrogen plasmas, XXV International Conference on Phenomena in Ionized Gases, July 17–22, 2001, Nagoya, Japan, Proceedings, Vol. 3, pp. 25–26.
- [130] K.N. Ostrikov, M.Y. Yu, Effect of near-sheath dusts on a surface-wave sustained gas discharge, *J. Phys. D: Appl. Phys.* 32 (1999) 1650–1656.
- [131] K.N. Ostrikov, M.Y. Yu, H. Sugai, Standing surface waves in a dust-contaminated large-area planar plasma source, *J. Appl. Phys.* 86 (1999) 2425–2430.
- [132] K. Ostrikov, I.B. Denysenko, S.V. Vladimirov, S. Xu, H. Sugai, M.Y. Yu, Low-pressure diffusion equilibrium of electronegative complex plasmas, *Phys. Rev. E* 67 (2003) 056408/1–13.
- [133] M.R. Akdim, W.J. Goedheer, Modeling of dust in a silane/hydrogen plasma, *J. Appl. Phys.* 94 (2003) 104–109.
- [134] C.F. Lin, W.T. Tseng, M.S. Feng, Formation and characteristics of silicon nanocrystals in plasma-enhanced chemical vapor deposited silicon-rich oxide, *J. Appl. Phys.* 87 (2000) 2808–2815.
- [135] H.M. Jang, N.M. Hwang, Theory of the charged cluster formation in the low pressure synthesis of diamond: part I. Charge-induced nucleation, *J. Mater. Res.* 13 (1998) 3527–3535.
- [136] N.M. Hwang, Evidence of nanometer-sized charged carbon clusters in gas phase of the diamond chemical vapor deposition (CVD) process, *J. Cryst. Growth* 204 (1999) 85–90.
- [137] S.C. Lee, N.M. Hwang, B.D. Yu, D.Y. Kim, Molecular dynamics simulation on the deposition behavior of nanometer-sized Au clusters on a Au(001) surface, *J. Cryst. Growth* 223 (2001) 311–320.
- [138] E.E. Lin, On the cluster mechanism of diamond synthesis from different solid carbon films, *Phys. Sol. State* 42 (2000) 1946–1951.
- [139] J.D. Jackson, *Classical Electrodynamics*, Wiley, New York, 1967.
- [140] M. Adachi, K. Okuyama, T. Fujimoto, J. Sato, M. Muroyama, Morphology control of films formed by atmospheric-pressure chemical vapor deposition using tetraethylorthosilicate/ozone system, *Jpn. J. Appl. Phys.* 35 (1996) 4438–4443.
- [141] A. Perez, P. Mlinon, V. Dupuis, B. Prvel, L. Bardotti, J. Tuallion-Combes, B. Masenelli, M. Treilleux, M. Pellarin, J. Lerm, E. Cottancin, M. Broyer, M. Jamet, M. Ngrier, F. Tournus, M. Gaudry, Nanostructured materials from clusters: synthesis and properties, *Mater. Trans.* 42 (2001) 1460–1470.
- [142] N.C. Wu, M.S. Tsai, M.C. Wang, H.S. Liu, The morphology and formation mechanism of aluminum nitride nanocrystals synthesized by chemical vapor deposition, *J. Cryst. Growth* 208 (2000) 189–196.
- [143] P. Roca i Cabarrocas, Plasma enhanced chemical vapor deposition of amorphous, polymorphous and microcrystalline silicon films, *J. Non-Cryst. Solids* 266–269 (2000) 31–37. \*\*
- [144] P. Roca i Cabarrocas, Plasma production of nanocrystalline silicon particles. A new route for nanostructured silicon thin films, *Bull. Amer. Phys. Soc. GEM54* 46 (2001) 49.
- [145] N.P. Rao, H.J. Lee, M. Kelkar, D.J. Hansen, J.V.R. Heberlein, P.H. McMurtry, S.L. Girshick, Nanostructured materials production by hypersonic plasma particle deposition, *Nanostruct. Mater.* 9 (1997) 129–132.
- [146] E. Magnano, C. Cepek, M. Sancrotti, F. Siviero, S. Vinati, C. Lenardi, P. Piseri, E. Barborini, P. Milani, In situ growth and thermal treatment of nanostructured carbon produced by supersonic cluster beam deposition: an electron spectroscopy investigation, *Phys. Rev. B* 67, (2003) 125414/1-7.
- [147] J. Frantz, K. Nordlund, Mechanism of Co nanocluster burrowing on Cu(100), *Phys. Rev. B* 67 (2003) 075415/1-7.
- [148] M. Masi, Multiscale approach to material synthesis by gas phase deposition, *J. Phys. IV* 11 (2001) 117–128.
- [149] P. Mulvaney, Not all that's gold does glitter, *MRS Bulletin*, December 2001, pp. 1009–1014. \*
- [150] J. Zhao, J. Yang, J.G. Hou, Theoretical study of small two-dimensional gold clusters, *Phys. Rev. B* 67, (2003) 085404/1-6.
- [151] T. Hoshino, M. Hirokami, M. Hata, M. Tsuda, Theoretical analysis of charge confinement in metal microclusters, *Jpn. J. Appl. Phys., Part I* 40 (2001) 1906–1910.
- [152] S. Bednarek, B. Szafran, J. Adamowski, Theoretical description of electronic properties of vertical gated quantum dots, *Phys. Rev. B* 64 (2001) 5303–5322.
- [153] Y.M. Li, O. Voskoboynikov, C.P. Lee, S.M. Sze, Energy and coordinate dependent effective mass and confined electron states in quantum dots, *Solid State Commun.* 120 (2001) 79–83.
- [154] Y.M. Li, O. Voskoboynikov, C.P. Lee, S.M. Sze, Computer simulation of electron energy levels for different shape InAs/GaAs semiconductor quantum dots, *Comput. Phys. Commun.* 141 (2001) 66–72.

- [155] E.C. Niculescu, Energy levels in a spherical quantum dot with parabolic confinement under applied electric fields, *Mod. Phys. Lett. B* 15 (2001) 545–554.
- [156] N.A. Kotov, Ordered Layered Assemblies of Nanoparticles, *MRS Bull.* 26 (2001) 992–997.
- [157] V.I. Klimov, M.G. Bawendi, Ultrafast carrier dynamics, optical amplification, and lasing in nanocrystal quantum dots, *MRS Bull.* 26 (2001) 998–1004.
- [158] M. Shim, C. Wang, D.J. Norris, P. Guyot-Sionnest, Doping and charging in colloidal semiconductor nanocrystals, *MRS Bull.* 26 (2001) 1105–1008.
- [159] M.C. Roco, S. Williams, P. Alivisatos (Eds.), *Nanotechnology Research Directions: Vision for Nanotechnology Research and Development in the next Decade*, Kluwer Academic Publ., Amsterdam, 1999. See also: US National Nanotechnology Initiative, <http://www.nano.gov>.
- [160] E. Stoffels, H. Kersten, G.H.P.M. Swinkels, G.M.W. Kroesen, Surface processes of dust particles in low pressure plasma, *Phys. Scr.* T89 (2001) 168.
- [161] H. Kersten, P. Schmetz, G.M.W. Kroesen, Surface modification of powder particles by plasma deposition of thin metallic films, *Surf. Coat. Technol.* 108–109 (1998) 507–512. \*
- [162] W.W. Stoffels, E. Stoffels, G.H.P.M. Swinkels, M. Boufnichkel, G.M.W. Kroesen, Etching a single micrometer-size particle in a plasma, *Phys. Rev. E* 59 (1999) 2302–2304.
- [163] G. Thieme, M. Quaas, H. Kersten, H. Wulff, H. Hippler, On the modification of powder particles in a process plasma, *Third International Conference on Physics of Dusty Plasmas (ICPDP-2002)*, Durban, South Africa, 20–24 May 2002, Book of Abstracts, p. 33.
- [164] J. Cao, T. Matsoukas, Deposition kinetics on particles in a dusty plasma reactor, *J. Appl. Phys.* 92 (2002) 2916–2922.
- [165] D.M. Gruen, Ultrananocrystalline diamond in the laboratory and the Cosmos, *MRS Bull.* 26 (2001) 771–776.
- [166] V.I. Merkulov, D.H. Lowndes, L.R. Baylor, Field-emission studies of smooth and nanostructured carbon films, *Appl. Phys. Lett.* 75 (1999) 1228–1230.
- [167] W.P. Kang, T. Fisher, J.L. Davidson, Diamond microemitters—the new frontier of electron field emission and beyond, *New Diam. Front. Carb. Technol.* 11 (2001) 129–146.
- [168] R. Kumar, P. Cheang, K.A. Khor, RF plasma processing of ultra-fine hydroxyapatite powders, *J. Mater. Process. Technol.* 113 (2001) 456–462.
- [169] J.D. Long, S. Xu, J.W. Cai, N. Jiang, J.H. Lu, K.N. Ostrikov, C.H. Diong, Structure, bonding states, and in-vitro study of Ca-P-Ti films deposited on Ti–6Al–4V by RF magnetron sputtering, *Mater. Sci. Eng. C: Biomimetics and Supramolec. Syst.* 20 (2002) 175–180.
- [170] J.D. Long, S. Xu, J.H. Lu, K.N. Ostrikov, C.H. Diong, RF magnetron sputtering deposition of bioactive Ca–P-based coatings on Ti–6Al–4V orthopaedic alloy, *IEEE Trans. Plasma Sci.* 30 (Part I) (2002) 118–119.
- [171] C. Holt, N.M. Wahlgren, T. Drakenberg, Ability of beta-casein phosphopeptide to modulate the precipitation of calcium phosphate by forming amorphous dicalcium phosphate nanoclusters, *Biochem. J.* 314 (1996) 1035–1039.
- [172] J. Kreuter, Nanoparticle systems for brain delivery of drugs, *Adv. Drug Deliv. Rev.* 47 (2001) 65–81.
- [173] F.E. Kruis, H. Fissan, A. Peled, Synthesis of nanoparticles in the gas phase for electronic, optical and magnetic applications, *J. Aerosol Sci.* 29 (1998) 511–535.
- [174] U. Kogelshats, B. Eliasson, W. Egli, From ozone generators to flat television screens: history and future potential of dielectric-barrier discharges, *Pure Appl. Chem.* 71 (1999) 1819–1828.
- [175] S. Veprék, The search for novel, superhard materials, *J. Vac. Sci. Technol. A* 17 (1999) 2401–2420.
- [176] E. Stoffels, W.W. Stoffels, G. Ceccone, R. Hasnaoui, H. Keune, G. Wahl, F. Rossi, MoS<sub>2</sub> nanoparticle formation in a low pressure environment, *J. Appl. Phys.* 86 (1999) 3442.
- [177] Y. Wu, Y. Inoue, H. Sugimura, O. Takai, Low-temperature deposition of transparent ultra water-repellent thin films by microwave plasma enhanced chemical vapor deposition, in: S.C. Moss (Ed.), *Advanced Biomaterials—Characterization, Tissue Engineering and Complexity*, Materials Research Society Proceedings, Vol. 711, HH3.28, Materials Research Society, Warrendale, PA, 2002.
- [178] H. Thomas, G.E. Morfill, V. Demmel, J. Goree, B. Feuerbacher, D. Möhlmann, Plasma crystal: Coulomb crystallization in a dusty plasma, *Phys. Rev. Lett.* 73 (1994) 652–655. \*\*
- [179] J.H. Chu, Lin I, Direct observation of Coulomb crystals and liquids in strongly coupled rf dusty plasmas, *Phys. Rev. Lett.* 72 (1994) 4009–4012. \*\*

- [180] V.A. Schweigert, I.V. Schweigert, A. Melzer, A. Homann, A. Piel, Plasma crystal melting: a nonequilibrium phase transition, *Phys. Rev. Lett.* 80 (1998) 5345–5348.
- [181] A. Melzer, M. Klindworth, A. Piel, Normal modes of 2D finite clusters in complex plasmas, *Phys. Rev. Lett.* 87, (2001) 115002/1-4.
- [182] H. Totsuji, T. Kishimoto, Ch. Totsuji, K. Tsuruta, Competition between two forms of ordering in finite Coulomb clusters, *Phys. Rev. Lett.* 88, (2002) 125002/1-4.
- [183] O.S. Vulina, S.V. Vladimirov, O.F. Petrov, V.E. Fortov, Criteria of phase transitions in a complex plasma, *Phys. Rev. Lett.* 88, (2002) 245002/1-4. \* \* \*
- [184] F.F. Chen, Numerical computations for ion probe characteristics in a collisional plasma, *Plasma Phys.* 7 (1965) 47–67.
- [185] O. Havnes, T.K. Aanesen, F. Melandso, On dust charges and plasma potentials in a dusty plasma with dust size distribution, *J. Geophys. Res.* 95 (1990) 6581–6585. \*
- [186] F. Verheest, *Waves in Dusty Space Plasmas*, Kluwer, Dordrecht, 2000.
- [187] H. Ikezi, Coulomb solid of small particles in plasmas, *Phys. Fluids* 29 (1986) 1764–1766.
- [188] K. Avinash, A. Bhattacharjee, R. Merlino, Effect of charge reduction on shielding in dusty plasmas, *Phys. Plasmas* 10 (2003) 2663–2666.
- [189] K.N. Ostrikov, S. Kumar, H. Sugai, Equilibrium and relaxation of particulate charge in fluorocarbon plasmas, *J. Appl. Phys.* 89 (2001) 5919–5926.
- [190] K. N. Ostrikov, S. Kumar, H. Sugai, Charging and trapping of macroparticles in near-electrode regions of fluorocarbon plasmas with negative ions, *Phys. Plasmas* 8 (2001) 3490–3497. \* \* \*
- [191] V.W. Chow, D.A. Mendis, M. Rosenberg, Secondary emission from small dust grains at high electron energies, *IEEE Trans. Plasma Sci.* 22 (1994) 179–186.
- [192] M. Rosenberg, D.A. Mendis, UV-induced Coulomb crystallization in a dusty gas, *IEEE Trans. Plasma Sci.* 23 (1995) 177–179.
- [193] K.N. Ostrikov, M.Y. Yu, L. Stenflo, Surface waves in strongly irradiated dusty plasmas, *Phys. Rev. E* 61 (2000) 4314–4321.
- [194] M. Rosenberg, D.A. Mendis, D.P. Sheehan, Positively charged dust crystals induced by radiative heating, *IEEE Trans. Plasma Sci.* 27 (1999) 239–242.
- [195] A.A. Sickafoose, J.E. Colwell, M. Horanyi, S. Robertson, Photoelectric charging of dust particles in vacuum, *Phys. Rev. Lett.* 84 (2000) 6034–6037.
- [196] A. Barkan, N. D’Angelo, R.L. Merlino, Charging of dust grains in a plasma, *Phys. Rev. Lett.* 73 (1994) 3093–3096. \*
- [197] C. Chunshi, J. Goree, Fluctuations of the charge on a dust grain in a plasma, *IEEE Trans. Plasma Sci.* 22 (1994) 151.
- [198] T. Matsoukas, M. Russel, M. Smith, Stochastic charge fluctuations in dusty plasmas, *J. Vac. Sci. Technol.* 14 (1996) 624–630.
- [199] I.B. Denysenko, K. Ostrikov, S. Xu, M.Y. Yu, C.H. Diong, Nanopowder management and control of plasma parameters in electronegative SiH<sub>4</sub> plasmas, *J. Appl. Phys.* 94 (2003) 6097–6107. \*
- [200] V. Kasperovich, K. Wong, G. Tikhonov, V.V. Kresin, Electron capture by the image charge of a metal nanoparticle, *Phys. Rev. Lett.* 85 (2003) 2729–2732.
- [201] T. Baron, P. Gentile, N. Magnea, P. Mur, Single-electron charging effect in individual Si nanocrystals, *Appl. Phys. Lett.* 79 (2001) 1175–1177.
- [202] M. Krcmar, W.M. Saslow, A. Zangwill, Self-capacitance of a Thomas–Fermi nanosphere, *Appl. Phys. Lett.* 77 (2000) 3797–3799.
- [203] M. Krcmar, W.M. Saslow, A. Zangwill, Static screening by conducting nanospheres, *J. Appl. Phys.* 93 (2003) 3490–3494.
- [204] M. Krcmar, W.M. Saslow, A. Zangwill, Electrostatics of conducting nanocylinders, *J. Appl. Phys.* 93 (2003) 3495–3500.
- [205] B.M. Annaratone, A.G. Khrapak, A.V. Ivlev, G. Soellner, P. Bryant, R. Suetterlin, U. Konopka, K. Yoshino, M. Zuzic, H.M. Thomas, G.E. Morfill, Levitation of cylindrical particles in the sheath of Rf plasma, *Phys. Rev. E* 63, (2001) 036406/1-6.



- [206] A.V. Ivlev, A.G. Khrapak, S.A. Khrapak, B.M. Annaratone, G. Morfill, K. Yoshino, Rodlike particles in gas discharge plasmas: theoretical model, *Phys. Rev. E* 68, (2003) 026403/1–10.
- [207] J.G. Laframboise, L.J. Sonmor, Current collection by probes and electrodes in space magnetoplasmas: a review, *J. Geophys. Res.* 98 (A1) (1993) 337–357.
- [208] K.N. Ostrikov, M.Y. Yu, Comment on “The effect of dust charge fluctuations on ion cyclotron wave instability in the presence of an ion beam in a plasma cylinder”, [*Phys. Plasmas* 6 (1998) 444] *Phys. Plasmas* 6 (1999) 4127–4128.
- [209] G.E. Morfill, H.M. Thomas, B.M. Annaratone, A.V. Ivlev, R.A. Quinn, A.P. Nefedov, V.E. Fortov, PKE-Nefedov Team, Complex plasmas under microgravity conditions: first results from PKE-Nefedov, in: R. Bharuthram, et al., (Eds.), *AIP Conference Proceedings* 649, *Dusty Plasmas in the New Millenium: Third International Conference on the Physics of Dusty Plasmas*, American Institute of Physics, New York, 2002, pp. 91–109.
- [210] D.A. Mendis, Progress in the study of dusty plasmas, *Plasma Sources Sci. Technol.* 11 (2002) A219–A228.
- [211] C. Zafiu, A. Melzer, A. Piel, Measurement of the ion drag force on falling dust particles and its relation to the void formation in complex (dusty) plasmas, *Phys. Plasmas* 10 (2003) 1278–1282.
- [212] S.A. Khrapak, A.V. Ivlev, G.E. Morfill, H.M. Thomas, Ion drag in complex plasmas, in: R. Bharuthram, et al., (Eds.), *AIP Conference Proceedings* 649, *Dusty Plasmas in the New Millenium: Third International Conference on the Physics of Dusty Plasmas*, American Institute of Physics, New York, 2002, pp. 341–344.
- [213] J.B. Pieper, J. Goree, Dispersion of plasma dust–acoustic waves in the strong-coupling regime, *Phys. Rev. Lett.* 77 (1996) 3137.
- [214] A. Homann, A. Melzer, A. Piel, Measuring the charge on single particles by laser-excited resonances in plasma crystals, *Phys. Rev. E* 59 (1999) R3835–R3838. \*
- [215] U. Konopka, L. Ratke, H.M. Thomas, Central collisions of charged dust particles in a plasma, *Phys. Rev. Lett.* 79 (1997) 1269–1272.
- [216] E.B. Tomme, D.A. Law, B.M. Annaratone, J.E. Allen, Parabolic plasma sheath potentials and their implications for the charge on levitated dust particles, *Phys. Rev. Lett.* 85 (2000) 2518–2521.
- [217] V.E. Fortov, A.P. Nefedov, V.I. Molotkov, M.Y. Poustylnik, V.M. Torchinsky, Dependence of the dust-particle charge on its size in a glow-discharge plasma, *Phys. Rev. Lett.* 87, (2001) 205002/1–4.
- [218] C. Zafiu, A. Melzer, A. Piel, Nonlinear resonances of particles in a dusty plasma sheath, *Phys. Rev. E* 63, (2001) 066403/1–9.
- [219] A.A. Samarian, S.V. Vladimirov, Charge of a macroscopic particle in a plasma sheath, *Phys. Rev. E* 68, (2003) 066404/1–5. \*
- [220] A.A. Samarian, B.W. James, S.V. Vladimirov, N.F. Cramer, Self-excited vertical oscillations in an rf-discharge dusty plasma, *Phys. Rev. E* 64, (2001) 025402(R)/1–4.
- [221] A.A. Samarian, B.W. James, Sheath measurement in rf-discharge plasma with dust grains, *Phys. Lett. A* 287 (2001) 125–130.
- [222] E.B. Tomme, B.M. Annaratone, J.E. Allen, Damped dust oscillations as a plasma sheath diagnostic, *Plasma Sources Sci. Techn.* 9 (2000) 87–99.
- [223] A. Melzer, T. Trottenberg, A. Piel, Experimental determination of the charge on dust particles forming Coulomb lattices, *Phys. Lett. A* 191 (1994) 301–307.
- [224] S.V. Vladimirov, N.F. Cramer, Equilibrium and levitation of dust in a collisional plasma with ionization, *Phys. Rev. E* 62 (2000) 2754–2762. \* \* \*
- [225] A.V. Phelps, Z.L. Petrovic, Cold-cathode discharges and breakdown in argon: surface and gas phase production of secondary electrons, *Plasma Sources Sci. Technol.* 8 (1999) R21–R44.
- [226] D.M. Shaw, M. Watanabe, H. Uchiyama, G.J. Collins, Secondary electron energy spectra emitted from radio frequency biased plasma electrodes, *App. Phys. Lett.* 75 (1999) 34–36.
- [227] S. Takamura, T. Misawa, N. Ohno, S. Nunomura, M. Sawai, K. Asano, P.K. Kaw, Dynamic behaviors of dust particles in the plasma-sheath boundary, *Phys. Plasmas* 8 (2001) 1886–1895.
- [228] Y.P. Raizer, *Gas Discharge Physics*, Springer, Berlin, 1991.
- [229] J. Cobine, *Gaseous Conductors*, Dover, New York, 1958.
- [230] O. Havnes, T. Nitter, V. Tsytovich, G.E. Morfill, T. Hartquist, On the thermophoretic force close to walls in dusty plasma experiments, *Plasma Sources Sci. Technol.* 3 (1994) 448–457.
- [231] A.M. Ignatov, Sh.G. Amirashvili, Radiometric force in dusty plasmas, *Phys. Rev. E* 63, (2001) 017402/1–3.



- [232] E. Thomas Jr., B.M. Annaratone, G.E. Morfill, H. Rothermel, Measurements of forces on suspended microparticles in the void region of a complex plasma, *Phys. Rev. E* 66, (2002) 016405/1-7.
- [233] D. Samsonov, J. Goree, Instabilities in a dusty plasma with ion drag and ionization, *Phys. Rev. E* 59 (1999) 1047–1058. \* \* \*
- [234] J. Goree, G.E. Morfill, V.N. Tsytovich, S.V. Vladimirov, Theory of dust voids in plasmas, *Phys. Rev. E* 59 (1999) 7055–7067. \*
- [235] G.E. Morfill, H.M. Thomas, U. Konopka, H. Rothermel, M. Zuzic, A. Ivlev, J. Goree, Condensed plasmas under microgravity, *Phys. Rev. Lett.* 83 (1999) 1598–1602. \* \* \*
- [236] V.N. Tsytovich, S.V. Vladimirov, S. Benkadda, Dust–plasma sheath: a new self-organized structure, *Phys. Plasmas* 6 (1999) 2972–2975. \*
- [237] F.F. Chen, *Introduction to Plasma Physics and Controlled Fusion*, Plenum, New York, 1984.
- [238] M.A. Lieberman, Analytical solution for capacitive RF sheath, *IEEE Trans. Plasma Sci.* 16 (1988) 638–644.
- [239] V.A. Godyak, N. Sternberg, Smooth plasma-sheath transition in a hydrodynamic model, *IEEE Trans. Plasma Sci.* 18 (1990) 159–168.
- [240] T. Nitter, Levitation of dust in RF and DC glow discharges, *Plasma Sources Sci. Technol.* 5 (1996) 93–99.
- [241] T.E. Sheridan, J. Goree, Collisional plasma sheath model, *Phys. Fluids B* 3 (1991) 2796–2805.
- [242] J. Horwitz, P.M. Banks, Ion momentum and energy transfer rates for charge exchange collision, *Planet. Space Sci.* 21 (1973) 1975–1986.
- [243] T.J. Sommerer, M.S. Barnes, J.H. Keller, M.J. McCaughey, M.J. Kushner, Monte Carlo-fluid hybrid model of the accumulation of dust particles at sheath edges in radio-frequency discharges, *Appl. Phys. Lett.* 59 (1991) 638–640.
- [244] J.P. Boeuf, P. Belenguer, T. Hbid, Plasma particle interactions, *Plasma Sources Sci. Technol.* 3 (1994) 407–419.
- [245] D.B. Graves, J.E. Daugherty, M.D. Kilgore, R.K. Porteous, Charging, transport and heating of particles in radiofrequency and electron cyclotron resonance plasmas, *Plasma Sources Sci. Technol.* 3 (1994) 433–444.
- [246] J.X. Ma, J. Liu, M.Y. Yu, Fluid theory of the boundary of a dusty plasma, *Phys. Rev. E* 55 (1997) 4627–4633.
- [247] S.V. Vladimirov, N.F. Cramer, P.V. Shevchenko, Equilibrium and oscillations of grains in the dust–plasma crystal, *Phys. Rev. E* 60 (1999) 7369–7373.
- [248] S.V. Vladimirov, P.V. Shevchenko, N.F. Cramer, Vibrational modes in the dust–plasma crystal, *Phys. Rev. E* 56 (1997) R74–R76. \*\*
- [249] S.V. Vladimirov, P.V. Shevchenko, N.F. Cramer, Low-frequency modes in the dust–plasma Crystal, *Phys. Plasmas* 5 (1998) 4–6.
- [250] H. Totsuji, T. Kishimoto, Ch. Totsuji, Structure of confined Yukawa system (dusty plasma), *Phys. Rev. Lett.* 78 (1997) 3113–3116.
- [251] S. Nunomura, T. Misawa, N. Ohno, S. Takamura, Instability of dust particles in a Coulomb crystal due to delayed charging, *Phys. Rev. Lett.* 83 (1999) 1970–1973.
- [252] E.C. Whipple, T.G. Northrop, D.A. Mendis, The electrostatics of a dusty plasma, *J. Geophys. Res. A* 90 (1985) 7405–7422. \* \* \*
- [253] O. Havnes, C.K. Goertz, G.E. Morfill, E. Grün, W. Ip, Dust charges, cloud potential, and instabilities in a dust cloud embedded in a plasma, *J. Geophys. Res. A* 92 (1987) 2281–2293.
- [254] S.V. Vladimirov, M. Nambu, Attraction of charged particulates in plasmas with finite flows, *Phys. Rev. E* 52 (1995) R2172–R2174. \* \* \*
- [255] S.V. Vladimirov, O. Ishihara, On plasma crystal formation, *Phys. Plasmas* 3 (1996) 444–446. \*\*
- [256] O. Ishihara, S.V. Vladimirov, Wake potential of a dust grain in a plasma with ion flow, *Phys. Plasmas* 4 (1997) 69–74.
- [257] O. Ishihara, S.V. Vladimirov, Hamiltonian dynamics of dust–plasma interactions, *Phys. Rev. E* 57 (1998) 3392–3398.
- [258] R.J. Seeboeck, W. Boehme, W.E. Koehler, M. Roemheld, S. Veprek, The dynamics of dust particles in silane glow discharges between parallel plates, *Plasma Sources Sci. Technol.* 3 (1994) 359–368. \*
- [259] H. Sugai, K. Nakamura, T.H. Ahn, M. Nakamura, Diagnostics and control of high-density etching plasmas, *Mater. Res. Soc. Symp. Proc.* 406 (1996) 15–20.
- [260] A. Kono, K. Kato, Measurement of negative-ion density in high-density  $C_4F_8$  plasma using a laser photodetachment technique combined with a millimeter-wave open resonator, *Appl. Phys. Lett.* 77 (2000) 495–497.

- [261] A.J. Lichtenberg, V. Vahedi, M.A. Lieberman, T. Rognlien, Modeling electronegative plasma discharges, *J. Appl. Phys.* 75 (1994) 2339–2348.
- [262] C. Arnas, M. Mikikian, G. Bachet, F. Doveil, Sheath modification in the presence of dust particles, *Phys. Plasmas* 7 (2000) 4418–4423.
- [263] H. Kersten, H. Deutsch, M. Otte, G.H.P.M. Swinkels, G.M.W. Kroesen, Micro-disperse particles as probes for plasma surface interaction, *Thin Solid Films* 377–378 (2000) 530–536. \*
- [264] J.E. Daugherty, D.B. Graves, Particulate temperature in radio frequency glow discharges, *J. Vac. Sci. Technol. A* 11 (1993) 1126–1134.
- [265] T. Fukuzawa, K. Obata, H. Kawasaki, M. Shiratani, Y. Watanabe, Detection of particles in RF silane plasmas using photoemission method, *J. Appl. Phys.* 80 (1996) 3202–3209.
- [266] E. Stoffels, W.W. Stoffels, G.M.W. Kroesen, F.J. de Hoog, Dust formation and charging in an Ar/SiH<sub>4</sub> radio-frequency discharge, *J. Vac. Sci. Technol. A* 14 (1996) 556–565.
- [267] A. Melzer, S. Nunomura, D. Samsonov, Z.W. Ma, J. Goree, Laser-excited Mach cones in a dusty plasma crystal, *Phys. Rev. E* 62 (2000) 4162–4168.
- [268] A.A. Samarian, S.V. Vladimirov, Comment on “Dependence of the Dust-Particle Charge on Its Size in a Glow-Discharge Plasma”, *Phys. Rev. Lett.* 89 (2002) 229501. \*
- [269] M.A. Childs, A. Gallagher, Small particle growth in silane radio-frequency discharges, *J. Appl. Phys.* 87 (2000) 1076–1087.
- [270] N. Hayashi, Observation of submicron dust particles trapped in a diffused region of a low pressure radio-frequency plasma, *Phys. Plasmas* 8 (2001) 3051–3057.
- [271] C. Hollenstein, J.L. Dorier, J. Duta, L. Sansonnens, A.A. Howling, Diagnostics of particle genesis and growth in RF silane plasmas by ion mass spectrometry and light scattering, *Plasma Sources Sci. Technol.* 3 (1994) 278–289.
- [272] A. Bouchoule, L. Boufendi, J. Herman, A. Plain, T. Hbid, G.M.W. Kroesen, E. Stoffels, W.W. Stoffels, Formation of dense submicronic clouds in low-pressure argon–SiH<sub>4</sub> rf reactor: diagnostics and growth processes from monomers to large size particulates, *Pure Appl. Chem.* 68 (1996) 1121–1126.
- [273] N. Kaufman, *Characterization of Materials*, Wiley, New York, 2003.
- [274] M. Schabel, T. Peterson, J. Sinclair, D. Lynch, Characterisation of trapped particles in rf plasmas, *J. Appl. Phys.* 86 (1999) 1834–1842.
- [275] Y. Hayashi, S. Tachibana, Observation of coulomb-crystal formation from carbon particles grown in a methane plasma, *Jpn. J. Appl. Phys.* 33 (1994) L804–L806.
- [276] V.E. Fortov, A.P. Nefedov, O.F. Petrov, A.A. Samarian, A.V. Chernyshev, A.M. Lipaev, Experimental observation of Coulomb ordered structure in sprays of thermal dusty plasmas, *JETP Lett.* 63 (1996) 187–192.
- [277] V.E. Fortov, A.P. Nefedov, V.M. Torchinskii, V.I. Molotkov, A.G. Khrapak, O.F. Petrov, K.F. Volykhin, Crystallization of a dusty plasma in the positive column of a glow discharge, *JETP Lett.* 64 (1996) 92–98.
- [278] V.N. Tsytovich, G.E. Morfill, Collective attraction of equal-sign charged grains in plasmas, *Plasma Phys. Rep.* 28 (2002) 171–176 [*Fizika Plazmy* 28, 195–201 (2002)].
- [279] A.M. Ignatov, Lesage gravity in dusty plasmas, *Plasma Phys. Rep.* 22 (1996) 585–589.
- [280] G. Praburam, J. Goree, Experimental observation of very low-frequency macroscopic modes in a dusty plasma, *Phys. Plasmas* 3 (1996) 1212–1219.
- [281] A. Melzer, A. Homann, A. Piel, V.A. Schweigert, I.V. Schweigert, Laser-excited dust lattice waves and the nonequilibrium phase transitions of the plasma crystal, in: M. Horanyi, S. Robertson, B. Walch, (Eds.), *Physics of Dusty Plasmas*, AIP Conference Proceedings, Vol. 446, AIP, Woodbury, 1998, p. 167.
- [282] O. Havnes, U. de Angelis, R. Bingham, C.K. Goertz, G.E. Morfill, V.N. Tsytovich, On the role of dust in the summer mesopause, *J. Atmos. Terr. Phys.* 52 (1990) 637–643.
- [283] V.N. Tsytovich, S.V. Vladimirov, G.E. Morfill, J. Goree, Theory of collision-dominated dust voids in plasmas, *Phys. Rev. E* 63 (2001) 056609/1–11. \*
- [284] N. D’Angelo, Dusty plasma ionization instability with ion drag, *Phys. Plasmas* 5 (1998) 3155–3160.
- [285] J.P. Boeuf, Characteristics of a dusty nonthermal plasma from a particle-in-cell Monte Carlo simulation, *Phys. Rev. A* 46 (1992) 7910–7922.
- [286] P. Epstein, On the resistance experienced by spheres in their motion through gases, *Phys. Rev.* 23 (1924) 710–733.
- [287] L.S. Frost, Effect of variable ionic mobility on ambipolar diffusion, *Phys. Rev.* 105 (1957) 354–356.

- [288] A.V. Ivlev, D. Samsonov, J. Goree, G. Morfill, V.E. Fortov, Acoustic modes in a collisional dusty plasma, *Phys. Plasmas* 6 (1999) 741–750.
- [289] K. Avinash, Ionization instability of acoustic modes in dusty plasma with ion drag and charging dynamics, *Phys. Plasmas* 8 (2001) 351–357.
- [290] R.P. Dahiya, G.V. Paeva, W.W. Stoffels, E. Stoffels, G.M.W. Kroesen, K. Avinash, A. Bhattacharjee, Evolution of a dust void in a radio-frequency plasma sheath, *Phys. Rev. Lett.* 89 (2002) 125001/1–4.
- [291] B.M. Annaratone, S.A. Khrapak, P. Bryant, G.E. Morfill, H. Rothermel, H.M. Thomas, M. Zuzic, V.E. Fortov, V.I. Molotkov, A.P. Nefedov, S. Krikalev, Yu.P. Semenov, Complex-plasma boundaries, *Phys. Rev. E* 66 (2002) 056411/1–4.
- [292] H. Rothermel, T. Hagl, G.E. Morfill, M.H. Thoma, H.M. Thomas, Gravity compensation in complex plasmas by application of a temperature gradient, *Phys. Rev. Lett.* 89 (2002) 175001.
- [293] M. Mikikian, L. Boufendi, A. Bouchoule, H.M. Thomas, G.E. Morfill, A.P. Nefedov, V.E. Fortov, the PKE-Nefedov team, Formation and behaviour of dust particle clouds in a radio-frequency discharge: results in the laboratory and under microgravity conditions, *New J. Phys.* 5 (2003) 19.1–19.12.
- [294] A.P. Nefedov, G.E. Morfill, V.E. Fortov, H.M. Thomas, H. Rotherme, T. Hag, A.V. Ivlev, M. Zuzic, B.A. Klumov, A.M. Lipaev, V.I. Molotkov, O.F. Petrov, Y.P. Gidzenko, S.K. Krikalev, W. Shepherd, A.I. Ivanov, M. Roth, H. Binnenbruck, J.A. Goree, Y.P. Semenov, PKE-Nefedov: plasma crystal experiments on the International Space Station, *New J. Phys.* 5 (2003) 33.1–33.10.
- [295] O.S. Vaulina, S.V. Vladimirov, Diffusion and dynamics of macro-particles in a complex plasma, *Phys. Plasmas* 9 (2002) 835–840. \*
- [296] H.M. Van Horn, Crystallization of a classical, one-component Coulomb plasma, *Phys. Lett. A* 28 (1969) 706–707.
- [297] E.L. Ploolloc, J.P. Hansen, Statistical mechanics of dense ionized matter. II. Equilibrium properties and melting transition of the crystallized one-component plasma, *Phys. Rev. A* 8 (1973) 3110–3122.
- [298] W.L. Slattery, G.D. Doollen, H.E. DeWitt, Improved equation of state for the classical one-component plasma, *Phys. Rev. A* 21 (1980) 2087–2095.
- [299] S. Hamaguchi, R.T. Farouki, D.H.E. Dubin, Triple point of Yukawa systems, *Phys. Rev. E* 56 (1997) 4671–4682.
- [300] O.S. Vaulina, S.A. Khrapak, Scaling Law for the Fluid-Solid Phase Transition in Yukawa Systems (Dusty Plasmas), *JETP* 90 (2000) 287–289.
- [301] H. Lowen, T. Palberg, R. Simon, Dynamical criterion for freezing of colloidal liquids, *Phys. Rev. Lett.* 70 (1993) 1557–1560.
- [302] H. Ohta, S. Hamaguchi, Molecular dynamics evaluation of self-diffusion in Yukawa systems, *Phys. Plasmas* 7 (2000) 4506–4514.
- [303] W.T. Juan, L. I, Anomalous diffusion in strongly coupled quasi-2D dusty plasmas, *Phys. Rev. Lett.* 80 (1998) 3073–3076.
- [304] B.A. Carreras, W.E. Lynch, D.E. Newman, G.M. Zaslavsky, Anomalous diffusion in a running sandpile model, *Phys. Rev. E* 60 (1999) 4770–4778.
- [305] T.H. Solomon, E.R. Weeks, H.L. Swinney, Observation of anomalous diffusion and Levy flights in a two-dimensional rotating flow, *Phys. Rev. Lett.* 71 (1993) 3975–3978.
- [306] G.M. Zaslavsky, D. Stevens, H. Weitzner, Self-similar transport in incomplete chaos, *Phys. Rev. E* 48 (1993) 1683–1694.
- [307] Ya.I. Frenkel, *Kinetic Theory of Liquid*, Oxford University Press, Oxford, 1976.
- [308] O.S. Vaulina, S.A. Khrapak, Simulation of the dynamics of strongly interacting macroparticles in a weakly ionized plasma, *JETP* 92 (2001) 228–234.
- [309] H.L. Swinney, in: H.Z. Cummins, E.R. Pike (Eds.), *Photon Correlation and Light Beating Spectroscopy*, Plenum, New York, 1974, p. 331.
- [310] H.Z. Cummins, in: H.Z. Cummins, E.R. Pike (Eds.), *Photon Correlation and Light Beating Spectroscopy*, Plenum, New York, 1974, p. 285.
- [311] P.N. Pusey, in: H.Z. Cummins, E.R. Pike (Eds.), *Photon Correlation and Light Beating Spectroscopy*, Plenum, New York, 1974, p. 387.
- [312] J.M.A. Hofman, Y.J.H. Clercx, P.P.J. Schram, Effective viscosity of dense colloidal crystals, *Phys. Rev. E* 62 (2000) 8212–8233.

- [313] I.T. Yakubov, A.G. Khrapak, Thermophysical and electrophysical properties of low temperature plasma with condensed disperse phase, *Sov. Tech. Rev. B. Therm. Phys.* 2 (1989) 269–337.
- [314] R.T. Farouki, S. Hamaguchi, Phase transitions of dense systems of charged “dust” grains in plasmas, *App. Phys. Lett.* 61 (1992) 2973–2975. \*
- [315] O.S. Vulina, O.F. Petrov, M.V. Taranin, Diffraction of laser radiation and analysis of ordered grain structures in a nonideal thermal dusty plasma, *Plasma Phys. Rep.* 25 (1999) 281–283.
- [316] V.E. Fortov, A.P. Nefedov, O.S. Vulina, A.M. Lipaev, V.I. Molotkov, A.A. Samaryan, V.P. Nikitskii, A.I. Ivanov, S.F. Savin, A.V. Kalmykov, A.Ya. Solov’ev, P.V. Vinogradov, Dusty plasma induced by solar radiation under microgravitational conditions: an experiment on board the Mir orbiting space station, *JETP* 87 (1998) 1087–1097.
- [317] T. Maekawa, K. Ishii, S. Masuda, Temperature propagations and cluster structures in a near-critical fluid, *J. Jpn. Soc. Microgravity Appl.* 15 (1998) 130–135.
- [318] M.O. Robbins, K. Kremer, G.S. Grest, Phase diagram and dynamics of Yukawa systems, *J. Chem. Phys.* 88 (1988) 3286–3312.
- [319] E.J. Meijer, D. Frenkel, Melting line of Yukawa system by computer simulation, *J. Chem. Phys.* 94 (1991) 2269–2271.
- [320] M.J. Stevens, M.O. Robbins, Melting of Yukawa systems: A test of phenomenological melting criteria, *J. Chem. Phys.* 98 (1993) 2319–2324.
- [321] J.P. Hansen, L. Verlet, Phase transitions of the Lennard–Jones system, *Phys. Rev.* 184 (1969) 151–161.
- [322] W.G. Hoover, F.N. Ree, Melting transition and communal entropy for hard spheres, *J. Chem. Phys.* 49 (1968) 3609–3618.
- [323] J.H. Chu, J.B. Du, L. I, Coulomb solids and low-frequency fluctuations in RF dusty plasmas, *J. Phys. D: Appl. Phys.* 27 (1994) 296–300.
- [324] S. Benkadda, V.N. Tsytovich, S.V. Vladimirov, Shielding and charging of dust particles in a plasma sheath, *Phys. Rev. E* 60 (1999) 4708–4714. \*\*
- [325] V.A. Schweigert, I.V. Schweigert, A. Melzer, A. Homann, A. Piel, Alignment and instability of dust crystals in plasmas, *Phys. Rev. E* 54 (1996) 4155–4166.
- [326] D.S. Lemons, M.S. Murillo, W. Daughton, D. Winske, Two-dimensional wake potentials in sub- and supersonic dusty plasmas, *Phys. Plasmas* 7 (2000) 2306–2313.
- [327] M. Lampe, G. Joyce, G. Ganguli, V. Gavrilchaka, Interactions between dust grains in a dusty plasma, *Phys. Plasmas* 7 (2000) 3851–3861.
- [328] A.M. Ignatov, Interaction between dust grains near a conducting wall, *Plasma Phys. Rep.* 29 (2003) 296–299.
- [329] K. Takahashi, T. Oishi, K.I. Shimonai, Y. Hayashi, S. Nishino, Analyses of attractive forces between particles in Coulomb crystal of dusty plasmas by optical manipulations, *Phys. Rev. E* 58 (1998) 7805–7811. \*
- [330] D. Winske, W. Daughton, D.S. Lemons, M.S. Murillo, Ion kinetic effects on the wake potential behind a dust grain in a flowing plasma, *Phys. Plasmas* 7 (2000) 2320–2328.
- [331] S.V. Vladimirov, S.A. Maiorov, N.F. Cramer, Dynamics of the charging and motion of a macroparticle in a plasma flow, *Phys. Rev. E* 63 (2001) 045401/1–3. \*\*
- [332] S.V. Vladimirov, S.A. Maiorov, N.F. Cramer, Kinetics of plasma flowing around two stationary dust grains, *Phys. Rev. E* 67 (2003) 016407/1–6. \*\*
- [333] S.V. Vladimirov, S.A. Maiorov, O. Ishihara, Molecular dynamics simulation of plasma flow around two stationary dust grains, *Phys. Plasmas* 10 (2003) 3867–3873. \*\*
- [334] U. Mohideen, H.U. Rahman, M.A. Smith, M. Rosenberg, D.A. Mendis, Intergrain coupling in dusty-plasma coulomb crystals, *Phys. Rev. Lett.* 81 (1998) 349–352.
- [335] V.I. Molotkov, A.P. Nefedov, M.Yu. Pustynnik, V.M. Torchinsky, V.E. Fortov, A.G. Khrapak, K. Yoshino, Liquid plasma crystal: Coulomb crystallization of cylindrical macroscopic grains in a gas-discharge plasma, *JETP Lett.* 71 (2000) 102–105.
- [336] O. Ishihara, S.V. Vladimirov, N.F. Cramer, Effect of dipole moment on the wake potential of a dust grain, *Phys. Rev. E* 61 (2000) 7246–7248.
- [337] S.V. Vladimirov, M. Nambu, Interaction of a rod-like charged macroparticle with a flowing plasma, *Phys. Rev. E* 64 (2001) 026403/1–7.
- [338] M. Y. Yu, H. Saleem, H. Luo, Dusty plasma near a conducting boundary, *Phys. Fluids B* 4 (1992) 3427–3431.

- [339] S. Hamaguchi, R.T. Farouki, Plasma–particulate interactions in nonuniform plasmas with finite flows, *Phys. Plasmas* 1 (1994) 2110–2118.
- [340] J.-X. Ma, M.Y. Yu, Electrostatic sheath at the boundary of a dusty plasma, *Phys. Plasmas* 2 (1995) 1343–1348.
- [341] M. Nambu, S.V. Vladimirov, P.K. Shukla, Attractive forces between charged particulates in plasmas, *Phys. Lett. A* 203 (1995) 40–42.
- [342] P.G. de Gennes, *Superconductivity of Metals and Alloys*, Benjamin, New York, 1966, p. 102.
- [343] M. Nambu, H. Akama, Attractive potential between resonant electrons, *Phys. Fluids* 28 (1985) 2300–2301.
- [344] D. Pines, Superconductivity in the periodic system, *Phys. Rev.* 109 (1958) 280–287.
- [345] A.V. Ivlev, G. Morfill, V.E. Fortov, Potential of a dielectric particle in a flow of a collisionless plasma, *Phys. Plasmas* 6 (1999) 1415–1420.
- [346] F. Melandsø, Lattice waves in dust plasma crystals, *Phys. Plasmas* 3 (1996) 3890–3901.
- [347] A.V. Ivlev, G. Morfill, Anisotropic dust lattice modes, *Phys. Rev. E* 63 (2001) 016409/1–3.
- [348] A. Melzer, A. Homann, A. Piel, Experimental investigation of the melting transition of the plasma crystal, *Phys. Rev. E* 53 (1996) 2757–2766.
- [349] A. Melzer, V.A. Schweigert, I.V. Schweigert, A. Homann, S. Peters, A. Piel, Structure and stability of the plasma crystal, *Phys. Rev. E* 54 (1996) R46–R49.
- [350] S. Peters, A. Homann, A. Melzer, A. Piel, Measurement of dust particle shielding in a plasma from oscillations of a linear chain, *Phys. Lett. A* 223 (1996) 389–393. \*
- [351] N. Otani, A. Bhattacharjee, Debye shielding and particle correlations in strongly coupled dusty plasmas, *Phys. Rev. Lett.* 78 (1997) 1468–1471.
- [352] O. Ishihara, I. Alexeff, H.J. Doucet, W.D. Jones, Reflection and absorption of ion-acoustic waves in a density gradient, *Phys. Fluids* 21 (1978) 2211–2217.
- [353] D. Bohm, D. Pines, A collective description of electron interactions: III. Coulomb interactions in a degenerate electron gas, *Phys. Rev.* 92 (1953) 609–625.
- [354] M. Kitagawa, Y.H. Ohtsuki, Self-consistent treatment of the wake potential for fast ion pairs in metals, *Phys. Rev. B* 16 (1977) 5321–5325.
- [355] K.U. Riemann, The Bohm criterion and sheath formation, *J. Phys. D: Appl. Phys.* 24 (1991) 493–518.
- [356] J.E. Allen, Some researches on double-layers, *Plasma Phys. Control. Fusion* 27 (1985) 1343–1357.
- [357] G.A. Emmert, R.M. Wieland, A.T. Mense, J.M. Davidson, Electric sheath and pre-sheath in a collisionless, finite ion temperature plasma, *Phys. Fluids* 23 (1980) 803–812.
- [358] G. Bachet, L. Cherigier, F. Doveil, Ion velocity distribution function observations in a multipolar argon discharge, *Phys. Plasmas* 2 (1995) 1782–1788.
- [359] S.V. Vladimirov, O. Ishihara, Buneman-type streaming instability in a plasma with dust particulates, *Phys. Scr.* 60 (1999) 370–372.
- [360] F. Melandso, J. Goree, Polarized supersonic plasma flow simulation for charged bodies such as dust particles and spacecraft, *Phys. Rev. E* 52 (1995) 5312–5326.
- [361] S.A. Maiorov, S.V. Vladimirov, N.F. Cramer, Plasma kinetics around a dust grain in an ion flow, *Phys. Rev. E* 63 (2001) 017401/1–4.
- [362] S.V. Vladimirov, A.A. Samarian, Stability of particle arrangements in a complex plasma, *Phys. Rev. E* 65 (2002) 046416/1–4. \*\*
- [363] R.W. Hockney, J.W. Eastwood, *Computer Simulation Using Particles*, McGraw-Hill, New York, 1981.
- [364] S.A. Maiorov, A.N. Tkachev, S.I. Yakovlenko, Metastable state of supercooled plasma, *Phys. Scr.* 51 (1995) 498–516.
- [365] M. Lampe, V. Gavrilchaka, G. Ganguli, G. Joyce, Effect of trapped ions on shielding of a charged spherical object in a plasma, *Phys. Rev. Lett.* 86 (2001) 5278–5281.
- [366] V.N. Tsytovich, O. Havnes, Charging processes, dispersion properties and anomalous transport in dusty plasmas, *Commun. Plasma Phys. Contr. Fusion* 15 (1993) 267–290. \*\*
- [367] S.V. Vladimirov, K.N. Ostrikov, M.Y. Yu, L. Stenflo, Evolution of Langmuir waves in a plasma contaminated by variable-charge impurities, *Phys. Rev. E* 58 (1998) 8046–8048. \*
- [368] J.X. Ma, M.Y. Yu, Langmuir wave instability in a dusty plasma, *Phys. Rev. E* 50 (1994) R2431–R2434.
- [369] S.V. Vladimirov, V.N. Tsytovich, Dissipative drift waves in partially ionized plasmas containing high-Z impurities or dust, *Phys. Rev. E* 58 (1998) 2415–2423. \*\*



- [370] L.M. Biberman, V.S. Vorob'ev, I.T. Yakubov, *Kinetics of Non-equilibrium Low-temperature Plasmas*, Nauka, Moscow, 1982.
- [371] S.V. Vladimirov, K.N. Ostrikov, M.Y. Yu, Ion-acoustic waves in a dust-contaminated plasma, *Phys. Rev. E* 60 (1999) 3257–3261.
- [372] N. D'Angelo, Low-frequency electrostatic waves in dusty plasmas, *Planet. Space Sci.* 38 (1990) 1143–1146.
- [373] R.L. Merlino, A. Barkan, C. Thompson, N. D'Angelo, Experiments on waves and instabilities in dusty plasmas, *Plasma Phys. Control. Fusion* 39 (1997) A421–A429.
- [374] K.N. Ostrikov, M.Y. Yu, N.A. Azarenkov, Surface waves at the interface of a dusty plasma and a metallic wall, *Phys. Rev. E* 58 (1998) 2431–2435.
- [375] K.N. Ostrikov, M.Y. Yu, Ion-acoustic waves on a dusty plasma, *IEEE Trans. Plasma Sci.* 26 (1998) 100–104.
- [376] S.V. Vladimirov, M.Y. Yu, Nonlinear ion-acoustic waves in a collisional plasma, *Phys. Rev. E* 48 (1993) 2136–2139.
- [377] S.V. Vladimirov, K. Ostrikov, M.Y. Yu, G.E. Morfill, Ion-acoustic waves in a complex plasma with negative ions, *Phys. Rev. E* 67 (2003) 036406/1–10.
- [378] N.N. Rao, P.K. Shukla, M.Y. Yu, Dust-acoustic waves in dusty plasmas, *Planet. Space Sci.* 38 (1990) 543–546.
- [379] N. D'Angelo, Coulomb solids and low-frequency fluctuations in RF dusty plasmas, *J. Phys. D: Appl. Phys.* 28 (1995) 1009–1010.
- [380] N.F. Cramer, S.V. Vladimirov, The Alfvén resonance in a magnetized dusty plasma, *Phys. Scr.* 53 (1996) 586–590.
- [381] K.N. Ostrikov, S.V. Vladimirov, M.Y. Yu, G.E. Morfill, Dust-acoustic wave instabilities in collisional plasmas, *Phys. Rev. E* 61 (2000) 4315–4321. \* \* \*
- [382] N. D'Angelo, R.L. Merlino, Current-driven dust-acoustic instability in a collisional plasma, *Planet. Space Science* 44 (1996) 1593–1598.
- [383] M. Rosenberg, Ion-dust streaming instability in processing plasmas, *J. Vac. Sci. Technol. A* 14 (1996) 631–633.
- [384] R.L. Merlino, Current-driven dust ion-acoustic instability in a collisional dusty plasma, *IEEE Trans. Plasma Science* 25 (1997) 60–65.
- [385] K.N. Ostrikov, S.V. Vladimirov, M.Y. Yu, O. Ishihara, On the realization of the current-driven dust ion-acoustic instability, *Phys. Plasmas* 6 (1999) 737–740. \*
- [386] A. Melzer, V.A. Schweigert, A. Piel, Transition from attractive to repulsive forces between dust molecules in a plasma sheath, *Phys. Rev. Lett.* 83 (1999) 3194–3197.
- [387] V. Steinberg, R. Stterlin, A.V. Ivlev, G. Morfill, Vertical pairing of identical particles suspended in the plasma sheath, *Phys. Rev. Lett.* 86 (2001) 4540–4543.
- [388] S.V. Vladimirov, A.A. Samarian, B.W. James, Confining instability in a complex plasma, *Proceedings of the 29th EPS Conference on Plasma Physics and Controlled Fusion, Montreux, 2002, ECA Vol. 26B, P. O-4.27/1–4.*
- [389] S.V. Vladimirov, N.F. Cramer, Vibrations in vertical strings of dust grains, *Phys. Scr.* 58 (1998) 80–82.
- [390] S. Nunomura, N. Ohno, S. Takamura, Confinement and structure of electrostatically coupled dust clouds in a direct current plasma-sheath, *Phys. Plasmas* 5 (1998) 3517–3523.
- [391] S.V. Vladimirov, E.N. Tsoy, Oscillations in a chain of rod-shaped colloidal particles in a plasma, *Phys. Rev. E* 64 (2001) 035402(R)/1–4.
- [392] M.P. Hertzberg, S.V. Vladimirov, N.F. Cramer, Rotational modes of oscillation of rodlike dust grains in a plasma, *Phys. Rev. E* 68 (2003) 026402/1–8.
- [393] L.D. Landau, E.M. Lifshitz, *Mechanics*, Pergamon, Oxford, 1969.